



HAL
open science

New process of dry particle coating technology and numerical modelisation : preparation of clean solid catalysis for methanisation reaction

Hua Liu

► **To cite this version:**

Hua Liu. New process of dry particle coating technology and numerical modelisation : preparation of clean solid catalysis for methanisation reaction. Chemical engineering. Centrale Lille Institut, 2021. English. NNT : 2021CLIL0016 . tel-03997991

HAL Id: tel-03997991

<https://theses.hal.science/tel-03997991v1>

Submitted on 20 Feb 2023

HAL is a multi-disciplinary open access archive for the deposit and dissemination of scientific research documents, whether they are published or not. The documents may come from teaching and research institutions in France or abroad, or from public or private research centers.

L'archive ouverte pluridisciplinaire **HAL**, est destinée au dépôt et à la diffusion de documents scientifiques de niveau recherche, publiés ou non, émanant des établissements d'enseignement et de recherche français ou étrangers, des laboratoires publics ou privés.

CENTRALE LILLE

THÈSE

Présentée en vue
d'obtenir le grade de

DOCTEUR

En

Spécialité : Molécules et Matière Condensée

Par

HUA LIU

DOCTORAT DÉLIVRÉ PAR CENTRALE LILLE

**NEW PROCESS OF DRY PARTICLE COATING AND NUMERICAL MODELISATION:
PREPARATION OF CLEAN SOLID CATALYSIS FOR METHANATION**

**NOUVEAU PROCÉDÉ D'ENROBAGE DE PARTICULES EN VOIE SÈCHE ET
MODÉLISATION NUMÉRIQUE : PRÉPARATION DE CATALYSEUR SOLIDE PROPRE POUR
LA MÉTHANISATION**

Soutenue le 14 Octobre 2021 devant le jury d'examen

Président du jury : **Mr Aissa OULD-DRISS**, Professeur, Université de Technologie de Compiègne

Rapporteur : **Mme Claudia COGNE**, Maitre de Conférences, HDR, Université Claude Bernard Lyon1

Rapporteur : **Mr Aissa OULD-DRISS**, Professeur, Université de Technologie de Compiègne

Membre : **Mr Fabien DHAINAUT**, Maitre de Conférences, Centrale Lille Institut

Directeur : **Mme Nouria FATAH**, Professeur, Centrale Lille Institut

Thèse préparée dans le Laboratoire de l'Unité de Catalyse et Chimie du Solide (UCCS)

École Doctorale SMRE 104

Acknowledgement

During my PhD, I met many nice and important people who contributed to finish this thesis.

I want to thank everybody. First and foremost, I am extremely grateful to my supervisors, Prof. Nouria Fatah for her invaluable advice, continuous support, and patience during my PhD study. Under her tutelage, I learned how to be a competent researcher. Her immense knowledge and plentiful experience have encouraged me in all the time of my academic research and daily life. I thank her from the bottom of my heart and wish her happiness and prosperity in her future work and life.

Apart from my supervisor, I won't forget to express the gratitude to Dr. Fabien Dhainaut for his technical support on my simulation study and his help in revising my manuscript. I would also like to thank Dr. Andrei Khodakov, who has provided me with precious advice every time I have given a presentation. I would like to thank Dr. Rafeh Bechara for detailed explanations of the textural property. They all have played a major role in polishing my research writing skills. Their endless guidance is hard to forget throughout my life. I am grateful to UCCS (Unité de Catalyse et de Chimie du Solide) and Ecole Centrale de Lille for providing me with a valuable research platform, where I have spent three wonderful years of my PhD happily.

I am especially grateful to our techniques Johann Jezequel and Svetlana Heyte for their kind support of experiments. I would like to express my gratitude to Madame Catherine Candelier for her help in calcinating alumina. I would also like to thank Mr. Maxence Simonnet and Damien Creton for helping me prepare samples. I especially appreciate Madame Nora Djelal's help in analyzing my SEM samples and explaining my test results in detail and with patience. I would like to thank our secretarial staff, Madame Zohra Gueroui and Madame Vanessa Fleury, for their friendly help on administration staff.

I would like to thank all my dear colleagues. It is their kind help and support that have made my study and life in France a wonderful time.

Especially, I would like to express my inexhaustible gratitude to my parents, siblings. Without their tremendous understanding and encouragement in the past few years, it would be impossible for me to complete my study. I am very grateful to my fiancé Radoslav Kostadinov, in the past two years, regardless of sadness and happiness, he has been by my side, giving me not only life support, but more importantly, spiritual companionship, he is the best man I have ever met in my life. Besides that, he has contributed a lot in revising the grammar of my thesis almost every weekend, he made rigorously corrections! I also

Acknowledgement

want to thank my fiance's parents Dimka Racheva and Grasiel Gerasimov, for taking me to live with them for two months during the quarantine of the epidemic and taking care of me like my parents.

Finally, I especially want to thank my motherland and my sponsor, China Scholarship Council, for offering my scholarship and opportunity to come to France and finish my Ph.D. Without the support of my country, I probably would not have had the opportunity to study in France and meet so many wonderful people. The 3 years of my PhD were not smooth sailing, but I never regretted or doubted my choice.

Contents

Acknowledgement	2
Résumé	10
Abstract	13
Nomenclature	15
General Introduction	24
Chapter 1: Literature Review	28
1.1 Methanation reaction	28
1.2 Support of catalysts for the methanation reaction	29
1.2.1 Materials of support for methanation catalysis.....	30
1.2.2 Active metal for catalysis	31
1.3 Dry particle coating	35
1.3.1 Introduction	35
1.3.2 Principle of dry particle coating	36
1.3.3 Dry particle coating process	37
1.3.3.1 Mechanofusion	37
1.3.3.2 Hybridizer	38
1.3.3.3 Co Mill.....	38
1.3.3.4 Cyclomix	39
1.3.3.5 Magnetically Assisted Impaction Coater (MAIC).....	40
1.3.3.6 Turbula Mixer.....	40
1.3.3.7 High-shear mixer “Picomix”	41
1.3.3.8 Summary of dry particle coating devices	42
1.4 Coating catalysts.....	44
1.5 Nanomaterials/nanoparticles.....	47
1.5.1 Definition of Nanoparticles	47

Contents

1.5.2. Nanoparticle classification and dimension	47
1.5.2.1 Nanoparticle dimension	48
1.5.2.2 Nanoparticle morphology	48
1.5.2.3 Nanoparticle composition, uniformity and agglomeration	49
1.5.3 Agglomeration of nanoparticles	49
1.5.4 Measurements of nanoparticles	50
1.5.4.1 Transmission Electron Microscope (TEM)	50
1.5.4.2 Small Angle X-Ray Scattering (SAXS)	51
1.5.4.3 Dynamic Light Scattering (DLS).....	52
1.5.4.4 Specific Surface Area Method.....	53
1.5.4.5 Centrifugal Liquid Sedimentation (CLS)	54
1.5.4.6 Atomic Force Microscopy (AFM).....	55
1.5.4.7 Tunable Resistive Pulse Sensing (TRPS).....	56
1.5.4.8 Nanoparticle Tracking Analysis (NTA)	57
1.5.4.9 Laser Diffraction Analysis (LD).....	58
1.6 DEM modeling	62
1.6.1 Introduction	62
1.6.1.1 Hard Sphere	63
1.6.1.2 Soft sphere	63
1.6.2 Studies of DEM modeling	64
1.6.3 DEM modeling on dry particle coating	66
1.7 Different DEM model.....	68
1.7.1 Elastic contact model.....	69
1.7.1.1 Linear spring model.....	69
1.7.1.2 Hertz-Mindlin Model.....	70
1.7.1.3 Hertz-Mindlin + JKR model.....	71
1.7.1.4 DMT Model.....	73

Contents

1.7.2 Inelastic contact model	73
1.7.2.1 Linear spring-dashpot model	73
1.7.2.2 Hysteretic Model	74
1.7.2.3 Thornton Model	74
1.7.3 Non-contact model	74
1.7.4 Contact model used in this study	76
1.7.4.1 Governing equations	76
1.7.4.2 Summary of equations involved in these two models	78
1.7.4.3 Surface energy	79
1.8 Objectives of the thesis	83
Chapter 2: Experiments and Materials	85
2.1 Introduction	85
2.2 Materials and methodology	86
2.2.1 Materials	86
2.2.2 Supports preparation	86
2.2.2.1 New supports preparation	86
2.2.2.2 Picomix (high shearing mixer)	88
2.2.2.3 Coating layer calculation	89
2.3 Characterization methods	90
2.3.1. The characterization methods for nanopowder	90
2.3.1.1 Laser Diffraction analysis (LD)	90
2.3.1.2 Transmission electron microscope (TEM)	92
2.3.1.3 Dynamic Light Scattering (DLS)	95
2.3.1.4 Small Angle X-Ray Scattering (SAXS)	96
2.3.1.5 Specific surface area (BET)	97
2.3.2 Particle solid density	100
2.3.3 Scanning Electron Microscope (SEM)	101

Contents

4.5.2 Thickness of Zeolite/S.S316L, TiO ₂ /S.S316L, and SiO ₂ /S.S316L	141
4.6 Conclusions	148
Chapter 5: DEM Numerical Modelization	150
5.1 Introduction to EDEM	150
5.2 Modeling parameters	153
5.3 Geometry	155
5.3.1 Parameters analysis of Al ₂ O ₃	156
5.3.2 Parameters analysis of stainless steel (S.S316L) powders	158
5.3.3 Parameters used for modelisation	159
5.4 Data analysis	161
5.5 Conclusion	163
Chapter 6: Simulation Results and Discussions	165
6.1 Modeling the behavior of powders in the picomix: Mixing analysis of	165
γ -Al ₂ O ₃ and S.S316L	165
6.1.1 Analysis of stability calculation	167
6.1.2 The effect of young's modulus/shear modulus	168
6.1.2.1 Images snapshots analysis	169
6.1.2.2 Analysis of particle contact force and overlap	171
6.1.2.3 Particle velocity	172
6.1.2.4 Kinetic energy	173
6.1.2.5 Particle potential energy	175
6.1.3 The effect of particle size	176
6.1.3.1 Image snapshots analysis	176
6.1.3.2 Analysis of particle contact force and overlap	179
6.1.3.3 Particle velocity and energy	180
6.1.4 The effect of rotational speed	181
6.1.4.1 Images snapshot analysis	182

Contents

6.1.4.2 Particle force, velocity, and energy analysis	184
6.1.5 The effect of filling ratio	186
6.1.5.1 Images snapshot analysis.....	187
6.1.5.2 Particle force, velocity, and kinetic analysis	188
6.1.6 Partial conclusion	190
6.2 Modeling of the adhesion between particles: simulation of the coating phenomenon	192
6.2.1 Modeling parameters	192
6.2.2 Geometry of the used picomix.....	195
6.2.3 Analysis of the modeling by adhesion phenomenon between Al ₂ O ₃ and TiO ₂ particles....	196
6.2.3.1 Analysis of the modeling: Host particle: Al ₂ O ₃ -D _m -2.5 mm and guest particle: TiO ₂ -D _m -0.1 mm.....	197
6.2.3.2 Analysis of the modeling: Host particle: Al ₂ O ₃ -D _m -1.0 mm and guest particle: TiO ₂ -D _m -0.1 mm.....	200
6.2.3.2.1 Effect of interfacial energy	201
6.2.3.3 Analysis of the modeling: Host particle: Al ₂ O ₃ -D _m -1.0 mm and guest particle: TiO ₂ -D _m -0.04 mm.....	205
6.3 Conclusion.....	211
Conclusions	213
Perspectives.....	218
References	220
Appendix	249

Résumé

Dans ce travail de thèse, des travaux expérimentaux et de modélisation ont été réalisés pour étudier l'enrobage de particules en voie sèche ainsi que les interactions entre les particules pendant le processus d'enrobage. L'objectif de la partie expérimentale était de préparer de nouveaux supports de catalyseurs pour une réaction de méthanation via un mélangeur à haut cisaillement "Picomix". Suite à ce travail expérimental sur l'enrobage à sec et la préparation des supports et des catalyseurs, de nombreuses questions sont apparues sur les phénomènes de collisions et d'adhésions des particules dans le picomix, ainsi que sur la variation des différentes forces appliquées à la surface des particules et sur les vitesses des particules. Par conséquent, le travail de modélisation visait à révéler le mouvement des particules et à nous aider à mieux comprendre le processus de revêtement à sec.

Dans la partie expérimentale, les nouveaux supports $\text{TiO}_2/\gamma\text{-Al}_2\text{O}_3$, $\text{SiO}_2/\gamma\text{-Al}_2\text{O}_3$, Zeolite/ $\gamma\text{-Al}_2\text{O}_3$, $\text{TiO}_2/\text{S.S316L}$, $\text{SiO}_2/\text{S.S316L}$, et Zeolite/ S.S316L ont été préparés par force mécanique (force d'impact/compression/cisaillement) dans le picomix (Hosokawa Micro B.V) dans les conditions suivantes : 3500 rpm, 5 mins, taux de remplissage 40% (40 mL sur 100 mL). Cependant, ces poudres (Zeolite, SiO_2 , TiO_2) étaient très cohésives et formaient des agglomérats de tailles incontrôlables. Le processus d'enrobage requiert la taille des particules primaires et non celle des particules agglomérées. Par conséquent, 5 techniques ont été incluses : LD (diffraction laser), TEM (microscope électronique à transmission), DLS (diffusion dynamique de la lumière), SAXS (diffusion des rayons X aux petits angles), BET (surface spécifique) pour mesurer la taille des nanoparticules. Les trois techniques LD, TEM, DLS ont fourni des résultats qui ont été utilisés pour accomplir la préparation de nouveaux supports. En effet, BET n'est valable que pour des poudres sphériques, non poreuses, monodispersées et à surface lisse. Ce n'est pas le cas pour nos trois poudres : TiO_2 , SiO_2 et Zeolite. Ainsi, la taille donnée par BET n'a pas été appliquée dans l'étude expérimentale. SAXS donne théoriquement des mesures précises de la taille nanométrique, cependant nous n'avons pas ce type d'appareil dans notre laboratoire. Les nouveaux supports préparés ont été caractérisés par diverses méthodes pour indiquer la performance du revêtement en voie sèche.

Dans la partie numérique, la modélisation DEM a été utilisée pour explorer l'interaction des particules dans le mélangeur à haut cisaillement "Picomix". La modélisation numérique du revêtement de particules en voie sèche dans le picomix a été réalisée à l'aide d'un logiciel commercial de simulation DEM, EDEM 2018.3.0 et EDEM 2020.3.1 (licence académique avec 8 CPU, DEM solutions Ltd., Edinburgh, UK) avec le modèle de contact (sans glissement) de Hertz-Mindlin et le modèle cohésif de Hertz Mindlin + JKR. Trois ordinateurs ont été utilisés dans cette étude, deux d'entre eux sont équipés d'un processeur Intel(R)

Core(TM) i7-4790 CPU@3.60Hz, et 8.0Go de RAM ; un autre est équipé d'un processeur Intel(R) Xeon(R) CPU E5-1650 v2 @3.5GHz, et 32.0Go de RAM. Le modèle de contact de Hertz-Mindlin (sans glissement) a été utilisé pour étudier le mélange des deux particules hôtes ($\gamma\text{-Al}_2\text{O}_3$ et S.S316L) respectivement. Le modèle de cohésion Hertz-Mindlin avec JKR a été utilisé pour modéliser la cohésion entre les particules invitées (particules de TiO_2) et les particules hôtes (particules de $\gamma\text{-Al}_2\text{O}_3$).

Les effets de la taille des particules, du taux de remplissage, de la vitesse de rotation, du module de Young ont été simulés sur deux particules hôtes $\gamma\text{-Al}_2\text{O}_3$ et S.S316L, à l'aide du modèle de contact (sans glissement) de Hertz-Mindlin. Ensuite, la modélisation des particules hôtes (particules de $\gamma\text{-Al}_2\text{O}_3$) et des particules invitées (particules de TiO_2) a été réalisée, et l'influence de l'énergie de surface des particules hôtes/invitées a été étudiée par le modèle de cohésion Hertz-Mindlin avec JKR.

Dans l'étude expérimentale

1) Il a été constaté que parmi les cinq techniques d'analyse des nanopoudres, la technique LD fournissait la plus grande taille de particule pour la même quantité de nanopoudre, car elle mesurait les agglomérats. La DLS a donné une taille plus petite mais les particules forment toujours des agglomérats. Le TEM a indiqué le plus petit diamètre car cette technique permet de voir les particules et de les mesurer par traitement d'image. Il est intéressant de noter que les différences de taille des nanoparticules ont été déterminées par l'utilisation de différentes techniques. Ceci n'est pas dû à des erreurs de mesure, mais en fait à la spécificité de chaque technique. Le TEM mesure la taille géométrique des nanoparticules déposées sur la surface ; l'avantage du TEM est donc de pouvoir observer directement la morphologie et de déterminer la taille de la particule, ce qui offre une certaine intuitivité et crédibilité. Cependant, cette méthode est le résultat de l'observation de zones locales, elle présente donc certaines contingences et erreurs statistiques. La taille moyenne des nanoparticules peut être obtenue par la mesure et l'analyse statistique de la taille des particules avec un certain nombre de photos. Par conséquent, la différence entre les tailles des nanoparticules pour une même particule est due aux agglomérats.

2) La distribution de la taille des particules a indiqué que les particules invitées adhéraient aux particules hôtes, car les supports nouvellement préparés ont fourni presque la même distribution granulométrique que les particules hôtes. La taille des particules des nouveaux supports semble suivre l'ordre suivant : Zeolite^{LD}/S.S316L > Zeolite^{DLS}/S.S316L > Zeolite^{TEM}/S.S316L, ce qui est un très bon résultat, car il correspond à la taille originale des particules invitées Zeolite^{LD} > Zeolite^{DLS} > Zeolite^{TEM}.

3) Les morphologies de surface des images SEM ont démontré que pour les particules de TiO_2^{LD} , SiO_2^{LD} et Zeolite^{LD}, que le revêtement soit avec S.S316L ou $\gamma\text{-Al}_2\text{O}_3$, chaque particule hôte était couverte par des particules invitées et formait une couche de revêtement épaisse. De nombreuses particules invitées agglomérées (en raison de la forte force interparticulaire) peuvent être directement observées à la surface des particules hôtes. Lorsque $\text{TiO}_2^{\text{DLS}}$, $\text{SiO}_2^{\text{DLS}}$ et Zeolite^{DLS} sont déposées sur du S.S316L ou de $\gamma\text{-Al}_2\text{O}_3$, on note plutôt une surface lisse mais avec un petit nombre de débris (particules invitées agglomérées). En ce qui concerne les images obtenues par SEM, la taille TEM a fourni le meilleur revêtement avec une surface lisse sans aucun débris. C'est-à-dire que $\text{TiO}_2^{\text{TEM}}/\text{S.S316L}$, $\text{SiO}_2^{\text{TEM}}/\text{S.S316L}$ Zeolite^{TEM}/S.S316L, $\text{TiO}_2^{\text{TEM}}/\gamma\text{-Al}_2\text{O}_3$, $\text{SiO}_2^{\text{TEM}}/\gamma\text{-Al}_2\text{O}_3$, et Zeolite^{TEM}/ $\gamma\text{-Al}_2\text{O}_3$ ont présenté le meilleur revêtement.

4) Le calcul de l'épaisseur du revêtement a de nouveau validé directement les résultats des images MEB et l'analyse de la distribution de la taille des particules selon lesquels $\text{TiO}_2^{\text{TEM}}/\text{S.S316L}$, $\text{SiO}_2^{\text{TEM}}/\text{S.S316L}$, Zeolite^{TEM}/S.S316L, $\text{TiO}_2^{\text{TEM}}/\gamma\text{-Al}_2\text{O}_3$, $\text{SiO}_2^{\text{TEM}}/\gamma\text{-Al}_2\text{O}_3$ et Zeolite^{TEM}/ $\gamma\text{-Al}_2\text{O}_3$ ont présenté le meilleur revêtement. Néanmoins, une ou deux particules ont été prises en compte dans l'évaluation de l'épaisseur du revêtement. Ces valeurs manquaient d'un certain degré de fiabilité, et peut-être y avait-il une erreur entre elles et l'épaisseur réelle du revêtement.

5) Dans le calcul des particules invitées non enrobées, il a été constaté que toutes les particules invitées n'adhéraient pas aux particules hôtes, mais l'évaluation des particules invitées non enrobées a montré qu'il y avait beaucoup moins de petites particules invitées non enrobées pour S.S316L (la fraction en masse maximale pour une particule non enrobée est de 1.62% pour Zeolite^{LD}/S.S316L). Cependant, lors de l'enrobage avec $\gamma\text{-Al}_2\text{O}_3$, la fraction massique des particules non enrobées était relativement élevée quel que soit le type de particules avec lesquelles elles étaient enrobées, la fraction massique de zéolithe non enrobée pouvant atteindre 11.48 % (Zeolite^{LD}/ $\gamma\text{-Al}_2\text{O}_3$).

Dans l'étude de la modélisation

1) La modélisation des particules hôtes de mélange a révélé qu'au début du processus de mélange, les particules se sont déplacées du fond au sommet du picomix.

2) Les données de modélisation ont démontré que la taille des particules et la vitesse de rotation ont un effet significatif sur la vitesse des particules, les forces de contact, le chevauchement et l'énergie. L'effet du taux de remplissage et du module de Young sur le comportement des particules semble être partiel. Par exemple, la force de contact normale et le chevauchement normal sont sensible à l'augmentation du taux de remplissage, mais la vitesse des particules n'a pas montré de changement évident avec la variation du taux de remplissage. Puisque la l'amplitude du module de Young représente l'effet de la rigidité, les

forces de contact normales/tangentielles et le chevauchement normal/tangentiel sont associés à la rigidité et ont un effet significatif. Il convient de mentionner que la variation de tous les paramètres (taille des particules, vitesse de rotation, taux de remplissage et module de Young) a un effet plus important sur les particules de S.S316L que sur les particules de γ -Al₂O₃. Cela pourrait être dû à la propriété du matériau lui-même, comme la densité et la dureté du S.S316L, qui sont plus élevées que celles du γ -Al₂O₃.

3) L'énergie de surface de la particule est un paramètre clé à estimer et surtout, elle a un grand impact sur le modèle cohésif JKR de Hertz-Mindlin pour étudier le processus de revêtement. Lorsque le rapport de taille $D_{\text{host}}/D_{\text{guest}}=10$ (le diamètre du γ -Al₂O₃ était de 1.0 mm, le diamètre du TiO₂ de 0.1 mm), la force de contact normale/tangentielle moyenne, le chevauchement normal/tangentiel moyen, l'énergie cinétique translationnelle/rotationnelle moyenne, l'énergie potentielle moyenne et la vitesse moyenne ont tous augmenté avec l'augmentation de l'énergie interfaciale du γ -Al₂O₃-TiO₂. Lorsque le rapport de taille $D_{\text{host}}/D_{\text{guest}}=25$ (le diamètre de γ -Al₂O₃ était de 1.0 mm, le diamètre de TiO₂ était de 0.04 mm), le recouvrement normal moyen a commencé à augmenter avec l'augmentation de l'énergie interfaciale de γ -Al₂O₃-TiO₂, et le recouvrement normal moyen a atteint un maximum lorsque l'énergie interfaciale de γ -Al₂O₃-TiO₂ a atteint 20 J/m². Après cela, il a commencé à diminuer lorsque l'énergie interfaciale de TiO₂- γ -Al₂O₃ a augmenté, ce qui indique que l'énergie interfaciale de γ -Al₂O₃-TiO₂ de 20 J/m² est l'énergie interfaciale maximale requise pour le revêtement entre γ -Al₂O₃ et TiO₂ lorsque le diamètre de γ -Al₂O₃ était de 1.0 mm et le diamètre de TiO₂ de 0.04 mm. Le nombre de particules de TiO₂ déposées sur la particule de γ -Al₂O₃ a également prouvé que lorsque l'énergie interfaciale de γ -Al₂O₃-TiO₂ est de 20 J/m², 90% des particules de TiO₂ adhèrent à la particule de γ -Al₂O₃ (2442 particules de TiO₂ adhèrent à la particule de γ -Al₂O₃ sur 2704). L'effet de l'augmentation de l'énergie interfaciale de γ -Al₂O₃-TiO₂ sur la vitesse, l'énergie potentielle et l'énergie cinétique de translation n'était pas très évident.

D'une certaine manière, les données issues des simulations ont été corrélées avec les résultats des expériences. Dans les mêmes conditions expérimentales, avec les mêmes particules invitées, le revêtement de γ -Al₂O₃ n'était pas aussi bon que celui de S.S316L. Dans l'étude de simulation, il a été constaté que la variation de tous les paramètres (taille des particules, vitesse de rotation, taux de remplissage et module de Young) a un effet plus important sur les particules de S.S316L que sur les particules de γ -Al₂O₃. Cela pourrait être dû à la propriété du matériau lui-même, comme la densité et la dureté du S.S316L, qui sont plus élevées que celles du γ -Al₂O₃. Ou cela pourrait être dû au fait que le matériau du picomix est l'acier, ce qui signifie que les particules de S.S316L et le picomix sont également attractifs pour les particules.

Abstract

The objective of this thesis is to propose a new methodology – dry particle coating technique to prepare catalyst supports for the methanation reaction. Dry particle coating is considered as an environmentally friendly and low-cost technique. However, it is crucial to understand the mechanism of the dry coating process, the factors affect the coating performance, the evaluation of the coating quality, the large-scale production as well as the exploration of new application fields.

In this work, the method of preparing new catalyst supports is to coat γ -Al₂O₃ and 316L steel (S.S316L) particles with TiO₂, SiO₂, and Zeolite nanoparticles. However, these powders (TiO₂, SiO₂, and Zeolite) are highly cohesive and form agglomerates of uncontrollable sizes, the nanoscale of the powders poses a major problem in the accuracy of size measurements. The coating process requires analysis of the nanoparticles. Four analytical techniques were applied and compared. The basic principle of the dry particle coating process is the mixing of particles under mechanical force (impact/compression/shear force). Host particle: γ -Al₂O₃ and S.S316L have an average diameter of about 67 μ m and 98.3 μ m will be used as host particles to prepare new carriers. The guest particles: TiO₂, SiO₂ and Zeolite with nanosize will be used to coat the surface of γ -Al₂O₃ and S.S316L to prepare the new substrates (such as TiO₂/S.S316L, SiO₂/S.S316L, Zeolite/S.S316L and TiO₂/ γ -Al₂O₃, SiO₂/ γ -Al₂O₃, Zeolite/ γ -Al₂O₃,). The coating of particles in dry process is due to mechanical/shear forces and it depends on collisions, particle movements, interactions between particles and the impact of operating conditions (the rotation speed and coating time) in the mixer. A numerical modeling DEM (Discrete Element Method) has been implemented to answer and explain the phenomena and the coating process.

The results of the analysis of the nanoparticles showed that the technique of diffraction/laser scattering (LD) highlights a larger size of particle of the nanopowder (overestimation) on the other hand the dynamic diffusion of the light (DLS) shows a smaller size. Transmission electron microscopy (TEM) indicates the smaller diameter of the nanopowder. The coating results highlight a good coating by SiO₂, TiO₂, and Zeolite nanoparticles on the surface of γ -Al₂O₃ and S.S316L under 3500 rpm and 5 min. However, for the same guest particles with different host particles, the S.S316L coating shows excellent coating. Numerical modeling reveals that the main factors affecting the simulation are rotational speed and particle size. Simulation of the coating indicates that the interfacial energy between the host and the guest is the main parameter affecting the coating.

Keywords: Dry particle coating, High-shearing force, Picomix, Nanopowder, DEM modeling.

Nomenclature

Nomenclature

Letters	The meaning of letters	Units
A_m	Cross-sectional area of the adsorbate	nm ²
A	Hamaker constant	J
A_i	Hamaker constant of particle i	J
A_j	Hamaker constant of particle j	J
A_{ij}	Hamaker constant of particle i and j	J
B	Boltzmann's constant	J/K
C	Translational diffusion coefficient of particles	m ² /s
C_1	Center of particle 1	No
C_2	Center of particle 2	No
C_s	Constant of BET specific surface area test	No
D	Diameter of particle	mm or nm
D_m	Diameter of particle that has been used in the modelization	nm
D_{mhost}	Diameter of host particles that has been used in the modelization	mm
D_{mguest}	Diameter of guest particles that has been used in the modelization	mm
D_1	Rotation center to the surface of settlement media	mm or nm
D_2	Rotation center to the surface of light point transmittance	nm
D_{min}	Minimum separation distance	nm
d	Distance between the centers of particle i and j	mm or nm
d_t	Distance moved at time t	mm
$dp_{(3,2)}$	Mean diameter	μm or nm
d_i	Average dimension of the particle i in this class.	
E^*	Equivalent Young's modulus	GPa or Pa
E_i	Equivalent Young's modulus of particle i	Pa

Nomenclature

E_j	Equivalent Young's modulus of particle j	
$\overline{E_k}$	Particle kinetic energy	J
$\overline{E_r}$	Particle rotational kinetic energy	J
$\overline{E_t}$	Particle translational kinetic energy	J
$\overline{E_p}$	Particle potential energy	J
E_i	Impact energy of particle	J
E_t	Total energy of particle	J
e	Coefficient of Restitution	No
$F_{n,ij}/F_n$	Normal contact force between particle i and j	N
$F_{t,ij}/F_t$	Tangential contact force between particle i and j	N
$F_{cohesive}$	Cohesive force	N
F_c	Contact force	N
F_{nc}	No contact force	N
F_{vdw}	Van der Waals' force	N
F_{12}^e	Electrostatic Coulomb force between the charged particles 1 and 2	N
F_{cap}	Capillary force	N
F_{che}	Force of chemical bonds or acid-base interactions	N
F_{ad}	Adhesion force	N
F_i	Total force acting on particle i	N
F_{ij}^c	Contact force acting on particle i by its contacting particle j or walls	N
F_{ik}^{nc}	Non-contact force acting on particle i by its neighbor non-contacting particle k	N
F_i^g	Gravity force acting on particle i	N
F_i^f	Fluid interaction force acting on particle i	N
f_n	Collision frequency	s^{-1}
f_{max}	Maximum friction force	N
G	Shear modulus of particle	GPa

Nomenclature

g	Gravitational acceleration	m/s^2
h	Planck's constant	J/Hz
I_i	Moment of inertial of particle i	m^4
K_n	Spring constant of the particles involved in the normal contact	N/m
K_t	Spring constant of the particles involved in the tangential contact	N/m
K_B	Boltzman constant	J/K
\vec{k}_s	Incident wave vectors at angle 2θ	No
\vec{k}_t	Scattering wave vectors at angle 2θ	No
L_{av}	Avogadro's number	m^{-1}
M_i	Total torque acting on particle i	$\text{N}\cdot\text{m}$
M_{ij}	Torque acting on particle i by particle j	$\text{N}\cdot\text{m}$
M_v	Molar volume	m^3/mol
m_i	Mass of particle i	g
m_{host}	Mass of guest particles	g
m_{guest}	Mass of guest particles	g
$m_{vessel\ before\ mixing}$	Mass of the vessel of Picomix before mixing	g
$m_{rotor\ before\ mixing}$	Mass of the rotor of Picomix before mixing	g
$m_{rotor\ after\ mixing}$	Mass of the vessel of Picomix after mixing	g
$m_{rotor\ before\ mixing}$	Mass of the rotor of Picomix after mixing	g
$m_{particle's\ mass\ on\ the\ wall}$	Mass of the particle stayed on the wall of the vessel after mixing	g
$m_{particle's\ mass\ on\ the\ rotor}$	Mass of the particle stayed on the rotor of the vessel after mixing	g
N	Number of guest particles per host particle	No
N_i	Number of particles in class i	No
N_0	Modeling number of particles	No
$N_{collision}$	Number of collisions	No
$N_i\%$	Number of fractions in class i	No

Nomenclature

N_t	Number of data points for calculating the coating thicknesses	No
n	Moles	No
n_l	Refraction index of material	No
P	Pressure	Pa
P_0	Initial pressure of BET specific surface area test	Pa
q	Momentum transfer or scattering vector	No
q_1	Signed magnitudes of the charges of particles 1	No
q_2	Signed magnitudes of the charges of particles 2	No
R	Radius of the particles	mm
R^*	Equivalent radius	mm
R_1	Radius of the particle 1	mm
R_2	Radius of the particle 2	mm
S	Surface area	m ² /g
S_{BET}	Total BET specific surface area	m ² /g
S_l	Slope of the linear BET plot	m ² /g
T	Temperature	K/°C
Δt	Time step	μs
ΔT	Rayleigh time step	s
T_s	Simulation period time	s
T_σ	Tense stress	N/m ²
t	Modeling time	s
$t_{run\ time}$	The time takes of running a simulation	h
$t_{Rayleigh}$	Rayleigh time	s
V_n	Relative velocity on the normal direction	m/s
V_t	Relative velocity on the tangential direction	m/s
V_i	Translational velocity of particle i	m/s

Nomenclature

$V_{n,ij}$	Normal relative velocity between particles i and j	m/s
$V_{t,ij}$	Tangential relative velocity between particles i and j	m/s
V_j	Translational velocity of particle j	m/s
V_{it}	Translational velocities of particle i at time t	m/s
$V_{it+\Delta t}$	Translational velocities of particle i at time $t + \Delta t$	m/s
$\frac{dV_i}{dt}$	Acceleration of translational velocities of particle i	m/s ²
V_{total}	Total volume of particle	mm ³
V_0	Volume of individual particle	mm ³
V_{fi}	Volume of particle i	mm ³
$V_{fi}\%$	Volume fraction of particle i	No
W	Weight of the particle	g
W_a	Work to need to separate two adhered surfaces	N
W_{ii}	Work of adhesion between particle i and j	N
W_{ii}	Work of adhesion between particle i	N
W_{jj}	Work of adhesion between particle j	N
$w\%$	Mass fraction of the guest particles	No
X	Weight of nitrogen adsorbed at a given relative pressure (P/P_o)	g
X_m	Weight of nitrogen adsorbed of monolayer	g
\bar{X}	Average thickness of coating	nm
X_i	Thickness of coating of point i	nm
z	Surface's distance of the two particles (i and j)	nm
a	Radius of contact area	mm
a_c	Maximum radius of contact area.	mm
θ	Scattering angle	o
θ_1	Contact angle	o
ε_1	Dielectric constant of material	No

Nomenclature

ε_0	Permittivity of vacuum	F/m
ε	Strain or proportional deformation.	mm
ν_e	UV adsorptive frequency	cm ⁻¹
λ	Wavelength of the x-rays	nm
η	Viscosity	N·s/m ²
η_n	Normal damping coefficient	N·s/m
η_t	Tangential damping coefficient	N·s/m
σ	Standard deviation	No
ρ	Density of materials	kg/m ³
ρ_{bulk}	Bulk density of materials	kg/cm ³
ρ_{tap}	Tapped density of materials	kg/cm ³
ω	Angular velocity	rad/s
ω_i	Angular velocity of particle i	rad/s
ω_j	Angular velocity of particle j	rad/s
ω_{it}	Angular velocities of particle i at time t	rad/s
$\omega_{it+\Delta t}$	Angular velocities of particle i at time $t + \Delta t$	rad/s
$\frac{d\omega_i}{dt}$	Acceleration of angular velocities of particle i	rad/s ²
ν	Poisson ratio of particle	No
ν_i	Poisson's ratio of particle i	No
ν_j	Poisson's ratio of particle j	No
ρ_f	Density of subsidence medium	kg/m ³
δ	Overlap between particles	mm
δ_n	Overlap in the normal direction	mm
δ_t	Overlap in the tangential direction	mm
δ_c	Maximum overlap between particles	mm
γ	Surface energy	J/m ²

Nomenclature

γ_l	Surface tension of the liquid	J/m ²
γ_s	Surface energy of the solid	J/m ²
γ_{sl}	Interfacial surface between the liquid and solid	J/m
γ^d	Surface energy of dispersion component	J/m ²
γ^p	Surface energy of the polar	J/m ²
γ^i	Surface energy of the dipole	J/m ²
γ_s^d	Surface energy of dispersion component of solid	J/m ²
$\gamma_{s,i}^d$	Surface energy of dispersion component of solid of particle i	J/m ²
$\gamma_{s,j}^d$	Surface energy of dispersion component of solid of particle j	J/m ²
γ_l^d	Polar energy of liquid	J/m ²
γ_s^p	Dipole energy of solid	J/m ²
γ_l^p	Dipole energy of liquid	J/m ²
$\gamma_{s,i,j}$	Interfacial energy of two different solid particles	J/m ²
$\gamma_{s,i}$	Surface energy of the solid of particle i	J/m ²
$\gamma_{s,j}$	Surface energy of the solid of particle j	J/m ²
μ_f	Coefficient of rolling friction	No
μ_s	Coefficient of Static friction	No
u_{it}	Translational displacement of particle i at time t	mm
$u_{it+\Delta t}$	Translational displacement of particle i at time $t + \Delta t$	
φ_{it}	Angular displacement of particle i at time t	rad
$\varphi_{it+\Delta t}$	Angular displacement of particle i at time $t + \Delta t$	
$\varphi_{\%}$	Mass fraction of uncoated guest particles	No
$\varphi_{1\%}$	Mass fraction of particles that adhered on the wall and rotor	No
$\varphi_{2\%}$	Mass fraction of particles that size less than 63 μ m after sieving	No
$\tau_{rolling}$	Rolling friction torque	No
Ω	Rotation speed	rpm

Nomenclature

ϑ	Time per iteration per particle depends on hardware and number of licenses	μs
-------------	--	---------------

Abbreviations

AFM	Atomic force microscopy
API	Active pharmaceutical ingredient
AI	Absorption index
BET	Brunauer-Emmett-Teller
BJH	Barrett-Joyner-Halenda
CLS	Centrifugal liquid sedimentation
CsA	Herein cyclosporine
DLS	Dynamic light scattering
DMT	Derjaguin-Muller-Toporov
DEM	Discrete element modeling
DW	Demineralized water
DPI	Dry powder inhalers
FEM	Fluid energy mill
FT	Fischer Tropsch
HNPs	Hollow nanoparticles dispersion
HR	Hauser ratio
IC	ICarr's index
IUPAC	International Union of Pure and Applied Chemistry
JKR	Johnson-Kendall-Roberts
LD	Laser diffraction analysis
MAIC	Magnetically assisted impaction coater
NAT	Nanoparticle tracking analysis

Nomenclature

NOPD	Non-obstructive particle damping
OSC	Oxygen storage capacity
PEG	Polyethylene glycol
PE	Polyethylene
RI	Refractive index of particle
SCR	Selective catalytic reduction
SAXS	Small-angle X-ray scattering
SLM	Selective laser melting
SE	Secondary electrons
TRPS	Tunable resistive pulse sensing
TEM	Transmission electron microscopy

General Introduction

Methanation is a chemical reaction that converts carbon monoxide and/or carbon dioxide into methane and it is mainly used at industrial scale for methane production. Methanation is also considered to be a key technology to facilitate future manned space missions by recycling CO₂ from breathing or wasted H₂ from water electrolysis on the international space station [1-3]. Use of suitable catalyst is very important for methanation because catalysts can increase the reaction rate without getting consumed in the process. Usually, the catalyst support should be solid with large surface area, which can improve the catalyst activity [4-6]. Typically different kinds catalyst supports have been studied such as activated carbon, alumina, silica, and titanium oxide [4-8]. However, the methanation catalysts are usually prepared by wet-chemical methods, such as impregnation, sol-gel, etc. The disadvantage of these preparation methods is that use of excessive solvents and high temperatures, thus resulting in waste of solvents, waste of energy, and environmental pollution. Some studies [9-11] demonstrated that mechanical methods can be used to prepare catalysts for methanation.

As one of the mechanical methods, dry particle coating is considered to be an environmentally friendly and low-cost operating process method [12, 13]. In dry particle coating, fine particles (generally with nano-size) are mixed with relatively larger particles (generally with micron-level) by adhesion forces (van der Waals' force, shearing, and compression) without solvents. Because of its lower cost, reduced energy requirements, this technology can be found in many industries, such as pharmaceuticals, cosmetics, food, and ceramics [14, 15]. Nevertheless, due to a lack of adequate understanding of the knowledge in coating mechanism, this technology is still in the trial stage and is not commonly used in commercial. Several researchers [16-19] have tried to simulate the dry coating process by Discrete Element Method (DEM) and have demonstrated that DEM modeling can help us to gain further understanding of the mechanism of the dry coating process.

Therefore, the objective of this thesis is to apply the dry particle coating to prepare supports of catalysts for the methanation reaction. Besides, the DEM modeling will be used to investigate the interactions and collisions of the particles during the dry particle coating process.

In the experimental part, 5 supports: γ -Al₂O₃, S.S316L (Stainless steel), SiO₂, TiO₂ (Anatase titania), and Zeolite (Beta-zeolite) were chosen to prepare the catalysts for methanation reaction in a higher shear mixer "picomix" (Hosokawa Micron B.V). But unfortunately, TiO₂, SiO₂, and Zeolite are nanopowder, which cannot be directly mixed with another nanopowder to prepare the catalysts. Therefore, several processes

(granulation, pelletizing, and atomization) were carried out to try to get large diameters (80 μm). However, the particles obtained in these ways are particularly fragile and easily broken, and cannot be used in picomix at all. In this case, another idea was proposed, which was the preparation of supports. The new preparation used S.S316L and $\gamma\text{-Al}_2\text{O}_3$ as the host, the fine particles of SiO_2 , TiO_2 , and Zeolite were considered as the guest, and to form new supports: $\text{SiO}_2/\gamma\text{-Al}_2\text{O}_3$, $\text{TiO}_2/\gamma\text{-Al}_2\text{O}_3$, $\text{Zeolite}/\gamma\text{-Al}_2\text{O}_3$, $\text{SiO}_2/\text{S.S316L}$, $\text{TiO}_2/\text{S.S316L}$, and $\text{Zeolite}/\text{S.S316L}$. The specific experimental work happened as follows:

1) The particle size of three nanopowder (TiO_2 , SiO_2 , and Zeolite) were analyzed by five different techniques, such as LD (laser diffraction), TEM (Transmission electron microscope), DLS (dynamic light scattering), SAXS (small-angle X-ray scattering), and BET specific surface area. And the results of three of these analyses (LD, TEM, DLS) were used for dry particle coating investigation.

2) The effect of host and guest on dry particle coating were studied, such as using the different guest particles to coat the same host particle, e.g., $\text{SiO}_2/\gamma\text{-Al}_2\text{O}_3$, $\text{TiO}_2/\gamma\text{-Al}_2\text{O}_3$, and $\text{Zeolite}/\gamma\text{-Al}_2\text{O}_3$; or using the same guest particle to coat with different host particles, e.g., $\text{SiO}_2/\gamma\text{-Al}_2\text{O}_3$ and $\text{SiO}_2/\text{S.S316L}$.

3) The effect of adhesion force (van der Waals' force) was considered and calculated to explain the coating phenomena.

4) The prepared new supports (such as $\text{Zeolite}^{\text{LD}}/\gamma\text{-Al}_2\text{O}_3$, $\text{Zeolite}^{\text{DLS}}/\gamma\text{-Al}_2\text{O}_3$, $\text{Zeolite}^{\text{TEM}}/\gamma\text{-Al}_2\text{O}_3$) were characterized by a combination of particle size and SEM (scanning electron microscope). Besides, the coating thickness was roughly evaluated by cross-section sample to see the coating effect of different particles. Uncoated guest particles were calculated to measure the coating effect between different particles.

In the modeling part, it is aimed to learn the interactions and collisions of the particles in the picomix, particle's behavior was simulated by the DEM modeling to get a better understanding of the dry particle coating. This numerical modelization work was performed by a commercial DEM modeling software EDEM 2018.3.0 and EDEM 2020.3.1 (Academic license with 8 CPU, DEM solutions Ltd., Edinburgh, UK), both the Hertz-Mindlin (no-slip) contact model and Hertz-Mindlin + JKR (Johnson-Kendall-Roberts) cohesive model were applied to study the dry particle process. This modeling work includes the following two main sections:

1. Modelization of the two different host particles in the high shear mixer "picomix": the study of the mixing of $\gamma\text{-Al}_2\text{O}_3$ and S.S316L respectively.

1) The effect of young's modulus of two different host particles respectively (2.0×10^7 to 2.0×10^{11} Pa for S.S316L, 1.7×10^7 to 1.7×10^{10} Pa for γ -Al₂O₃) in the picomix on particle movement were studied. Because the young's modulus has a very significant effect on the time of simulation calculations, and in the DEM modeling, reducing the young's modulus to decrease the calculation time has been considered to be an acceptable approach ^[20, 21].

2) The effect of S.S316L and γ -Al₂O₃ on the particle size (0.6 - 2.0 mm in diameter), the filling ratio (10% - 40%), and the rotation speed (1500 - 5000 rpm) on particle interactions and motions in the picomix were investigated. To explore more possible factors that may influence the particle motion and its contact behavior.

2. Modeling of the adhesion of host particles (γ -Al₂O₃ particles) and guest particles (TiO₂ particles) in picomix under 3500 rpm of rotation speed was conducted, and the influence of surface energy of host/guest particles was investigated by the Hertz-Mindlin + JKR cohesion model.

This research work is divided into six chapters as follows:

Chapter 1: Firstly, the methanation reaction and its application, catalysts/supports/active metal selection are summarized; secondly, dry coating and its applications and commonly used equipment are summarized; thirdly, particle size analysis techniques of nanoparticles and their advantages and disadvantages are concluded, and finally, the model of DEM and its research literature on dry coating are summarized.

Chapter 2: Materials that have been used in this study will be listed, the experimental protocol will be described in detail, mainly including the calculation of the quantities required for the experimental process, equipment, and operating conditions. In addition, the principles of the characterization methods involved in the experiments are explained precisely.

Chapter 3: The results of the characterization of the raw materials will be presented including the analysis of three nanopowder (TiO₂, SiO₂, and Zeolite).

Chapter 4: The experimental results are displayed and discussed. Firstly, the adhesion between the particles is calculated in the form of van der Waals' forces to account for the agglomeration of nanoparticles and their effect on the coating. Secondly, guest particles that are not coated onto the host particles are roughly calculated to help understand the extent of the coating. Thirdly, the effect of host and guest on dry coating is investigated. Lastly, the thickness of the coating is roughly evaluated by cross-section samples to illustrate the results of the coating.

Chapter 5: A very detailed explanation of software EDEM is given. The material parameters related to the simulations are summarized by the analysis of the literature. The dimensions of the picomix are given

and the choice of the material parameters that will be used to simulate the study of dry coating are summarized.

Chapter 6: A large number of simulation data is presented and discussed. Firstly, the effect of modeling parameter (young's modulus) on two different host particle (S.S316L and γ -Al₂O₃) behavior in picomix is investigated. Secondly, the effects of particle size, rotation speed, and filling ratio on modeling of S.S316L and γ -Al₂O₃ behavior in picomix are compared. Finally, the coating of γ -Al₂O₃ (host particles) and TiO₂ (guest particles) are simulated, the effects of size ratio and interfacial energy of γ -Al₂O₃ - TiO₂ on coating are discussed.

Eventually, the general conclusion is made to summarize the key results in this thesis, some expectations for future studies are described as well.

Chapter 1: Literature Review

Renewable energies are playing and will continue to play a vital role in meeting current and future energy needs. As an energy carrier, methane has significant importance to the industry and transportation sectors worldwide [22]. Its existing distribution infrastructure in many countries makes it is a constitutive element of modern economies. Methane could be obtained from CO and CO₂ under atmospheric pressure by a reaction called methanation [23].

1.1 Methanation reaction

In 1902, Sabatier and Senderens discovered the methanation reaction of CO_x (x = 1 or 2), this discovery provided a very good and important promising solution for reducing anthropogenic gas emissions. Methanation is the conversion of CO_x into methane CH₄ through hydrogenation [24]. The history of methanation is presented in figure 1.1 [22, 25].

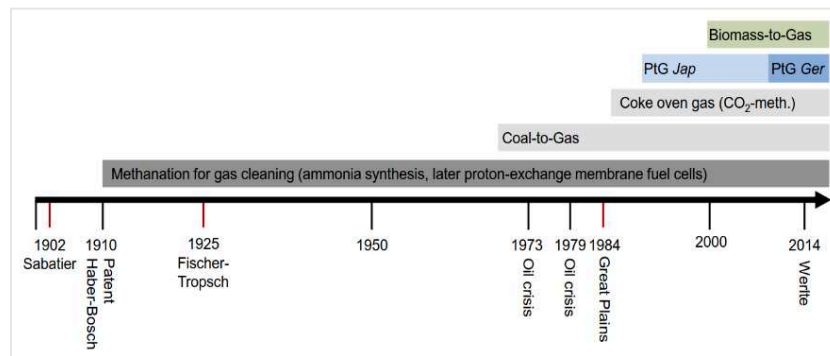


Fig.1.1 History of methanation; Abbreviations: Jap – Japan, Ger – Germany [22, 25].

Methanation is a chemical reaction that converts carbon monoxide and/or carbon dioxide to methane. The following reactions describe the methanation of carbon monoxide and carbon dioxide respectively [22, 26]:



Both reactions are exothermic, while the stoichiometric methanation of carbon monoxide releases 206 kJ heat per mole (see equation 1.1), the conversion of carbon dioxide releases 164 kJ per mole (see equation 1.2). Typically, operating temperature is between 200 °C and 450 °C but also depends on the catalyst (such

as Ni/Al₂O₃) and experimental conditions [27, 28], like pressure, catalytic activity, and concentration of CO and CO₂.

In the methanation reaction process, hydrogen is primarily produced by steam reforming of natural gas [29]. A small amount is obtained by water electrolysis and other sources, other major sources include gasification of coal and biomass, water splitting by high-temperature heat, photoelectrolysis, and biological processes [30]. CO₂ can be found in the atmosphere when fossil fuels are burned and when living organisms breathe or can be conveniently recovered from several industrial processes, such as biomass combustion and gasification, biogas facilities, and oil refineries [22, 30, 31]. CO gas mainly comes from coal or biomass gasification at synthetic fuel production plants [31, 32]. The methanation reaction is a reversible reaction, the produced water can be recycled by the methane steam reforming method [28, 33] and form CO and CO₂.

Methanation is mainly used at an industrial scale for large methane production. It is the final stage in the purification of synthesis gas and most modern ammonia plants plus some older hydrogen plants use the simple and convenient methanation reaction to remove traces of carbon oxides from the process gas [1, 34, 35]. Methanation is also considered to be a key technology to facilitate future manned space missions by the recycling of CO₂ from breathing or wasted H₂ from water electrolysis on the International Space Station [1-3].

Using a suitable catalyst is very important for methanation because catalysts can increase the reaction rate without getting consumed in the process, the catalyst support usually should be solid with a large surface area, which can improve the catalyst activity [4-6]. Typically various kinds of activated carbon, alumina, and silica, titanium oxide have been studied as supports to prepare the catalysts [4-8].

1.2 Support of catalysts for the methanation reaction

The selection of supported catalysts has a significant influence on the crystallite size, stability, dispersion, reducibility, and product selectivity of the methanation reaction. The main function of the support is to disperse and fix the active phase of metal nanoparticles, to improve the dispersion degree of active metal, increase the number of active sites, and prevent the sintering and loss of active components in the reaction process. The commonly used supports are alumina, silica, activated carbon, aluminum silicate, diatomite, clay, magnesium oxide, activated clay, etc. They can be powdered or granulated [36]. Alumina and silicon oxide supports are as easy to be wetted by aqueous solutions as most activated carbons with adsorptive

properties on their surfaces^[5]. The surface structure of catalyst depends on the surface structure of support particles, such as specific surface area, porosity, pore size, and other catalytic reaction rates.

1.2.1 Materials of support for methanation catalysis

The support type, such as pore structure, specific surface area, surface properties (acid-base, hydrophilic and hydrophobic), mechanical strength, hydrothermal stability, and the interaction between the support and metal all affect the structure and properties of the catalyst, changing the reaction activity, product selectivity, and reaction stability. The pore structure of the support affects the diffusion of the substrate and the product in the active center. The pH and hydrophilicity of the support will affect the selectivity of the product. Hydrothermal stability and mechanical strength affect the reaction stability of catalysts. The degree of reduction and dispersion of active metal is often determined by the interaction force between active metal and the support^[37]. The stronger the interaction force is, the higher the dispersion degree of active metal is, but meanwhile, the easier it is to form hard to reduce compounds with the support, thus reducing the reduction degree.

Silica (SiO_2) with a large specific surface area and pore volume are abundant solid in nature. Due to its easy to make, low cost, strong acid resistance, and heat resistance. It is the one of most commonly used supports to prepare the catalysts for methanation reaction^[38-40].

Alumina (Al_2O_3), especially $\gamma\text{-Al}_2\text{O}_3$ has a large specific surface area and the surface is acid and base center, which is more active than SiO_2 . Therefore, it has been used widely for preparing catalysts for the methanation process^[41-44].

Titanium dioxide (TiO_2) has strong selectivity and is suitable for loading non-inert metal oxides. TiO_2 is used as supported catalyst which were investigated by some researchers^[45-47]. Paraskevi et al.^[45, 46] prepared Ru/ TiO_2 catalyst to study the mechanism of selective methanation of CO/ CO_2 ; Zhou et al.^[46] studied the effect of the structure of Ni/ TiO_2 catalyst on CO_2 methanation; Wilbert et al.^[47] reported a strong promotional effect of Mn on Ni/ TiO_2 catalysts for CO_2 and CO methanation.

Besides supported catalysts, there are also unsupported kinds of methanation catalysts, such as Raney-Nickel^[48], but they also require large surface areas to reach a sufficient methanation activity. In recent years, quite a lot of results obtained for new kinds of catalyst supports were published, e.g., Zeolites^[49-52], and biochar^[53-55].

1.2.2 Active metal for catalysis

Catalysts are crucial for methanation processes. Not only is the reactor design influenced by the catalyst applied, but also are up - and downstream processes. In general, the active metal is supported to enlarge the catalyst surface area. A large surface area of a catalyst is obtained by supporting small particles of active metals on large surface-area supports [56].

For a metal that can be used as a catalyst, it is generally required to have more abundant electronic properties, such as a large and easily deformable electron cloud, which is conducive to contact with the reactants, while a loose electron cloud is also conducive to the departure of the reaction products. Therefore, transition metals (Ni, Pt, Pd, Ru) have better catalytic performance, while the main group metal as the activity center of the catalyst is less because the main group metal elements tend to lose or gain electrons to form a stable, relatively inert electronic structure, not conducive to the action with the reaction substrate. For example, Li, Na, K, Mg, Ca, etc., cannot be used as the main active components of catalysts.

In the early year, Sabatier and Senderens discovered that nickel was able to catalyze the reaction between carbon monoxide and hydrogen to form methane and water. Up to now, more than 100 years later, many metals mainly in groups 8-10 are active for methanation reaction (see figure 1.2), active metals for methanation are marked in gray [22].

24 Cr Chromium	25 Mn Manganese	26 Fe Iron	27 Co Cobalt	28 Ni Nickel	29 Cu Copper
42 Mo Molybdenum	43 Tc Technetium	44 Ru Ruthenium	45 Rh Rhodium	46 Pd Palladium	47 Ag Silver
74 W Tungsten	75 Re Rhenium	76 Os Osmium	77 Ir Iridium	78 Pt Platinum	79 Au Gold

Fig. 1.2 Excerpt from the periodic system of elements [22].

Catalyst activity and selectivity are regarded as two significant factors to evaluate the property of catalysts, some studies [57-59] were investigated to explore the activity and selectivity of metals. Table 1.1 summarized the activity and selectivity of the metal.

Chapter 1: Literature Review

Table 1.1 Metals activity and selectivity.

Articles	Activity	Selectivity
Fischer et al ^[57]	Ru > Ir > Rh > Ni > Co > Os > Pt > Fe > Mo > Pd > Ag	
Vannice et al ^[58]	Ru > Fe > Ni > Co > Rh > Pd > Pt > Ir;	Pd > Pt > Ir > Ni > Rh > Co > Fe > Ru
Mills and Steffgen ^[59]	Ru > Fe > Ni > Co > Mo	Ni > Co > Fe > Ru.

Among these metals, Ru is the most active metal for methanation, however, it is not industrially used because of its high price. Neglecting the price, Ru is the best choice, especially at low temperatures.

As one of the noble metals, Ru has catalytic activity and selectivity to CH₄. Some materials have supported Ru to form catalysts, such as Al₂O₃, TiO₂, SiO₂, MgO, MgAl₂O₄, and C. Pre-reduced 3% Ru/Al₂O₃ catalyst's activity is showing in Figure 1.3 ^[60]. This shows at 673 K, the catalyst presents the best catalytic performance with the high CO₂ conversion, CH₄ yield, and limited CO yield.

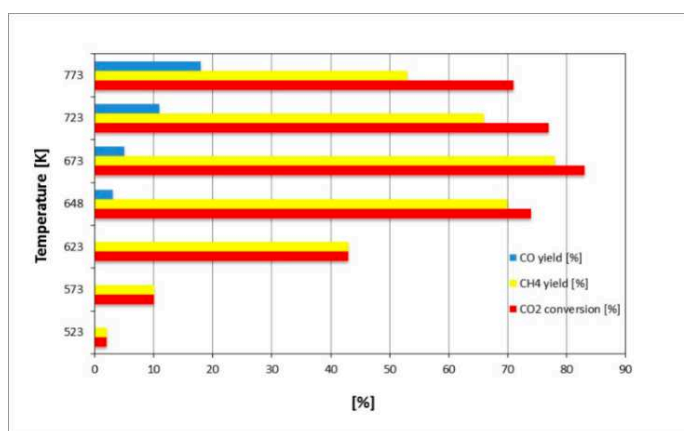


Fig.1.3 CO₂ conversion, CH₄ and CO yields on pre-reduced 3% Ru/Al₂O₃ catalyst at different temperature reactions ^[60].

In the presence of excess CO₂, Tada et al. ^[61] investigated the catalytic performance of supported Ru catalysts for the selective methanation of CO with respect to the loading (0.5 - 5.0 wt.%) and mean crystallite size (1.3 - 13.6 nm) of the metallic phase with the support (Al₂O₃, TiO₂, YSZ, CeO₂ and SiO₂). The temperature range is 170 - 470°C, 1% CO, 50% H₂, 15% CO₂ and 0 - 30% H₂O (balance He). The study illustrated that the conversion of CO₂ is completely suppressed until the conversion of CO reaches its maximum value for all catalysts investigated. The methane selectivity is higher than 70%, when increase temperature, it will become 100%. Increasing metal loading results in a significant shift of the

CO conversion curve toward lower temperatures, where the undesired reverse water-gas shift reaction becomes less significant.

As one of the noble metals, the hydrogenation of CO on supported Rh was investigated in a microreactor at atmospheric pressure [62]. The catalysts were prepared by impregnation of different supports with solutions of $\text{RhCl}_3 \cdot 3\text{H}_2\text{O}$, the ratio of $\text{H}_2/\text{CO} = 3:1$. The study demonstrated that the catalytic performance of Rh was influenced drastically by the support. Based on the specific activity (the rate of CH_4 formation per surface Rh sites), the most effective support was TiO_2 . The specific activities of Rh/MgO and Rh/ SiO_2 were lower by more than an order of magnitude.

Pd-based catalysts [63-65] have also been investigated and shown a good catalytic performance because Pd can dissociate molecular hydrogen. Vannice and Gartenl [66] reported that Pd/ Al_2O_3 catalysts exhibited a higher activity in the methanation reaction than unsupported Pd catalysts.

Cobalt (Co) catalysts exhibited a methanation activity similar to that of nickel, but cobalt the price is higher than nickel [67, 68]. Hence, Co is not that widely used for commercial applications as nickel catalysts [69].

Iron (Fe) catalysts are known to have high reactivity, but a very low selectivity towards methane. Thus, they are more often used in ammonia synthesis or in the Fischer–Tropsch process [70].

Because of the high efficiency in CH_4 production and low cost of the CO_2 methanation, Ni catalysts are the most widely investigated materials [71-74]. A lot of supports have been investigated for Ni catalysts, the catalytic performance strongly depends upon the nature and properties of the support. Table 1.2 summarizes some Ni-based catalysts for the methanation reaction in the literature.

Except Al_2O_3 , Zeolites, SiO_2 , and TiO_2 are used as supports, like CeO_2 [75], ZrO_2 [76], and Ce– ZrO_2 [77] also are applied as supports and showed good results and with particular emphasis on the role of promoters/modifiers in their catalytic performance in the reaction. Other materials were recently investigated as nickel supports, such as hydrotalcite [78], carbon nanotubes [79].

The preparation of supported catalysts mainly includes two methods (as summarized in the table 1.2): impregnation (dry/wet) and deposition precipitation. The sol-gel method is also used to synthesize the catalysts for methanation reaction.

The impregnation method can be identified to be a simple, easy and economical method, which is widely used to prepare supported catalysts, especially low-content precious metal supported catalysts [80]. The main weakness of the impregnation method is the lack of size control of metal particles except when the porous substrate has a narrow pore size distribution.

Chapter 1: Literature Review

Table 1.2 Ni-based catalysts for the methanation reaction.

Authors	Catalysts			Operation conditions				Ref.
	Preparation methods	Ni loading (wt./%)	Supports	Reactors	H ₂ :CO / H ₂ :CO ₂	Temperature (°C)	Pressure (bar)	
Hu et al.	Impregnation	20	Al ₂ O ₃	Continuous flow fixed-bed reactor	H ₂ /CO ≥3:1	300 - 550	30	[81]
Jwa et al.	Impregnation	0 - 10	Zeolite	Dielectric barrier discharge plasma reactor	H ₂ /CO ₂ = 4	180 - 360	Atmospheric pressure	[82]
Le et al.	Impregnation Precipitation	10 - 20	SiC, SiO ₂	Fixed-bed microreactor	H ₂ /CO ₂ = 4	140 - 450	Atmospheric pressure	[83]
Thien et al.	Impregnation	10	γ-Al ₂ O ₃ , SiO ₂ , TiO ₂	Continuous fixed bed reactor	1 mol% CO /CO ₂ , 50 mol% H ₂	500	Atmospheric pressure	[84]
Adrián et al.	Impregnation	10	Beta-zeolite	Downflow fixed bed reactor	H ₂ /CO ₂ =4	200 - 500	Atmospheric pressure	[51]
Cuili et al.	Impregnation	10	ZrO ₂ /Al ₂ O ₃	Stainless steel tubular microreactor	H ₂ /CO = 3	300 - 550	15	[85]
Jun et al.	Impregnation	10	(SiO ₂ , TiO ₂ , γ-Al ₂ O ₃)	Fixed-bed microreactor	H ₂ /CO = 3	190 - 600	10	[86]
Xiao et al.	Impregnation	10 - 30	SiO ₂	Quartz tubular reactor	5% CO/ 5% H ₂	500	Atmospheric pressure	[87]
Natalia et al.	Impregnation	10 - 15	Zeolite	Tubular quartz fixed-bed reactor	15% CO ₂ 60% H ₂	250 - 450	Atmospheric pressure	[88]
Thien et al.	Impregnation	10	γ-Al ₂ O ₃	Fixed-bed quartz reactor	1 mol% CO /CO ₂ , 50 mol% H ₂	140 - 450	Atmospheric pressure	[89]
Aziz et al.	Sol-gel method	5	SiO ₂ , γ-Al ₂ O ₃	Fixed-bed quartz reactor	H ₂ /CO ₂ =1-8	250 - 450	Atmospheric pressure	[90]
Tada et al.	Impregnation	10	TiO ₂	Fixed-bed tubular reactor	0.2% CO, 16.1% CO ₂ , 65.3% H ₂	200 - 450	Atmospheric pressure	[91]
Kohei	Impregnation	1- 30	TiO ₂	Continuous fixed bed flow tubular reactor	0.2% CO, 16.1% CO ₂ , 65.3% H ₂	350 - 650	Atmospheric pressure	[92]
Rui et al.	Impregnation	10	TiO ₂	Quartz tubular fixed-bed reactor	H ₂ /CO ₂ =4	250 - 500	Atmospheric pressure	[46]
Zhao et al.	Impregnation	10	SiO ₂	Fixed-bed quartz tube reactor	H ₂ /CO=3	300 - 460	Atmospheric pressure	[93]
Yan et al.	Impregnation	10 - 30	SiO ₂	Quartz tubular reactor	5% CO 5% H ₂	400 - 700	Atmospheric pressure	[94]

The deposition/precipitation method refers to add the precipitant into the metal salt solution, then aged, filtered, washed, dried, calcined and activated to produce catalysts or catalyst support [95]. The most important drawback of this method is the precipitating agent may cause the local concentration too high and produce agglomeration [95, 96].

The sol-gel method is a wet-chemical process that involves the formation of an inorganic colloidal suspension (sol) and gelation of the sol in a continuous liquid phase (gel) to form a three-dimensional network structure [97-99]. The sol-gel method has its disadvantages such as long processing time, relatively high cost of precursors, large shrinkage during processing, and possibility of the formation of agglomerates [98].

All these catalysts preparation methods involve solvents and catalyst pretreatments at higher temperature. A novel method - dry particle coating process was regarded as a promisingly alternative approach to prepare supported catalysts [100-104] because of its lower cost and reduced energy requirements.

1.3 Dry particle coating

1.3.1 Introduction

Dry particle coating is a solvent free method where fine “guest” particles (in size of 0.1-50 μm [104, 105]) adhere uniformly to the surface of a large “host” particle (in size of 1-500 μm [104, 105]) by strong adhesion forces (van der Waal’s force, shearing and compression) [15, 106]. Figure 1.4 illustrates the typical dry particle coating process. The host and the guest particles are mixed by mechanical forces, such as shearing and compression. Depending on the particle surface (roughness), mechanical energy and other properties of the particles, it is possible to obtain a discrete or a continuous coating [107].

In dry particle coating, small size “guest” particles are mixed with relatively larger size “host” particles by mechanical forces without solvent. A high number of collisions between the particles will occur, resulting in a coating of the guest particles on the surface of the host particles as the van der Waal’s forces are dominant in creating a strong cohesive bond between the host and the guest particles.

The dry particle coating technique is an environmentally-friendly and low-cost operation [12, 13], this technology can be found in many industries, such as in pharmaceuticals, cosmetics, food or ceramics areas [14]. However, more attention should be paid to the mechanism of the dry coating process, the factors that

affect coating performance, the evaluation of coating quality, the scale-up production as well as the exploration of novel application fields.

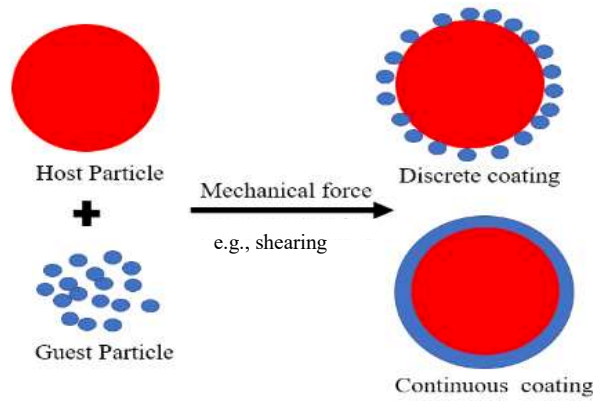


Fig.1.4 The schematic of a coating process.

1.3.2 Principle of dry particle coating

The purpose of the dry particle coating is to adhere the fine particles to the surface of big particles uniformly, with the help of strong adhesion forces. Dry particle is considered to be an ordered mixing ^[15], it is also an alternative to perfect mixing to achieve a more homogeneous mixture than that obtained by random mixing ^[105].

During the real mixing process, different steps in the process of ordered mixing are shown as figure 1.5. The principle of dry particle is based on the above three stages of the ordered mixing.

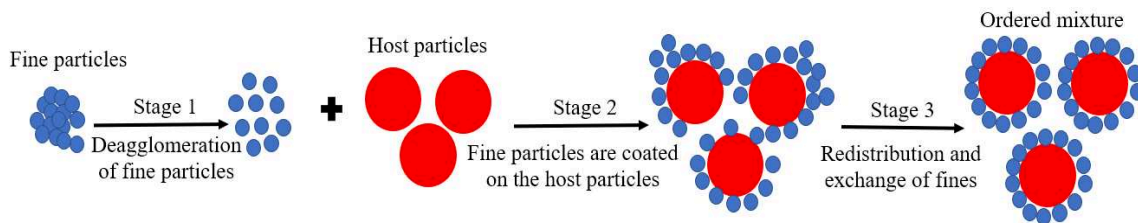


Fig.1.5 Various stages in the process of ordered mixing.

Agglomeration is a common phenomenon for fine particles because the action of the van der Waals' forces.

1.3.3 Dry particle coating process

There are different types of devices that have been used to study the dry particle coating process, these devices can supply mechanical force and efficiently promote the deagglomeration of the fine particles [13].

The dry particle coating devices are mainly consisted of low energy methods and high energy methods [104]. Common low energy devices include the magnetically assisted impaction coater (MAIC) [108-110], tubular mixer [111], V-blender [112], Cone mill [113] etc. High energy devices include the hybridizer, mechanofusion or high shear mixer “Cyclomix” and “Picomix”. A short introduction of these devices will be presented as follows.

1.3.3.1 Mechanofusion

Mechanical dry coating techniques (high shear mixer) were pioneered by Japanese scientists in 1970s to 1980s. Mechanofusion (see figure 1.6) this is one of the coating methods that consists of mixing fine and large particles and creating either a fusion of the fine particles that adhere to the large particles or a chemical reaction. Figure 1.6 shows the structure of a mechanofusion system from Hosokawa Micron, Japan [114]. The feed material is charged into a rotor using a fixed press head. The rotation of the rotor presses the powder against the rotor wall as a result of centrifugal force, the powder is transported to the fixed press head with the help of the rotor wall and is subjected to compression and shear forces several times. This force generates a particle with new attributes. Slits in the rotor wall allow the material to pass out and to be transported up by the circulation blades back to the top of the rotor in order to be processed again. The mechanofusion has been commonly used in pharmaceuticals to increase the solubility and the flowability by surface treatment [115-117].

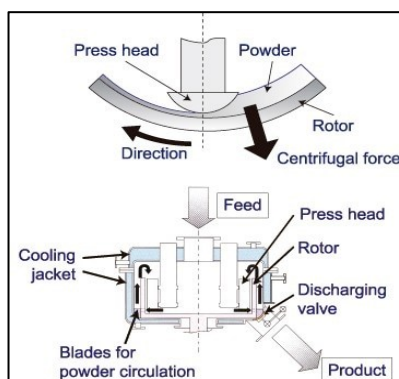


Fig.1.6 Schematic of mechanofusion system [114, 117].

1.3.3.2 Hybridizer

Hybridization system (Nara machinery Co. Ltd, Japan, see figure 1.7) is a technology for surface modification, preparation of composite materials of fine particles and precise mixing by dry powder process. The raw materials are dispersed in a high-speed air flow and processed by a mechanical impact force. Development of new materials or high improvement of conventional materials can be achieved by surface modification of particles or making powder composites. During hybridization processes, fine powder is applied onto or on the surface of a core powder. The main methods are embedding, penetrating, coating (micro-encapsulation) or rounding. The system works with mechanical forces like impact and shear.

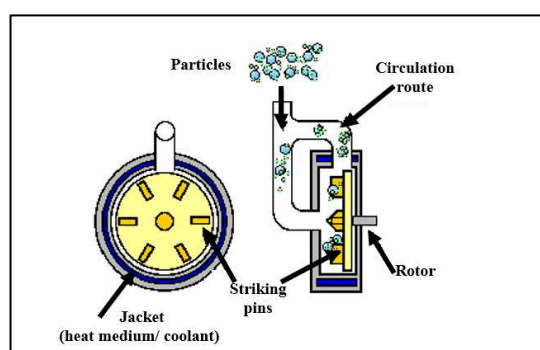


Fig.1.7 Schematic of Nara Hybridizer ^[118].

As figure 1.7 shows, the hybridizer has a high-speed rotor with 6 blades, a powder circulation route and a jacket cooling or heating system. The applications of hybridizer can be found in pharmaceuticals ^[117], cosmetics ^[119], coating ^[120] etc..

1.3.3.3 Co Mill

Co-Mill (Cone Mill, see figure 1.8) has a conical chamber where product enters through the feed hopper. Rotating impeller imparts a vortex flow to the product and centrifugal forces continuously force it to a zone between the impeller and a conical chamber screen. Particles become trapped between the screen and the impeller edge and experience high shear stress which causes de-agglomeration the guest particles. The experienced high shear stress causes the host and guest particles interaction and eventually lead to coating. Proper residence time ensures repeated collisions between host and guest particles and ensures uniform coating. The screen size ensures the desired size reduction and the finished product is discharged at the

bottom of the milling chamber. Kek (Kemutec schenck process group, USA) Cone Mills is mainly used for gentle grinding and deagglomeration, pharmaceutical industry for dry/wet granulation [121], food industry for coarse sugar grinding [122].

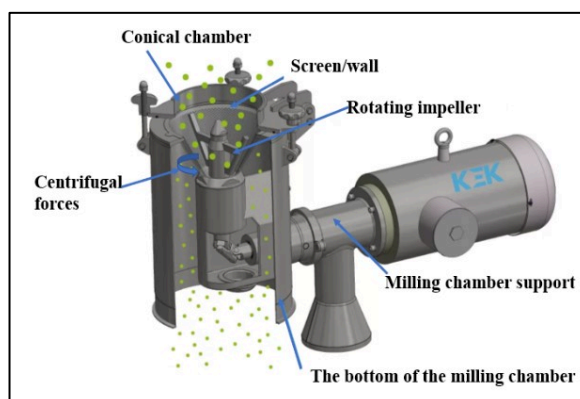


Fig.1.8 Schematic of a Kemutec Co-mill [123].

1.3.3.4 Cyclomix

Cyclomix (Hosokawa Micron, Japan) is a high-shear paddle mixer and agglomerator designed for mixing solid powders with liquids or to soften binders. Figure 1.9 shows the photo and schematic of a Cyclomix. It includes an inlet that's used to put a sample, a jacket to cool or heat, and a central rotor with four pairs of paddles, which combine high-impact and high-shear forces for mixing pastes, liquids and slurries. This mixer relies on a centrally placed high-speed rotating shaft that can be controlled from the mixer cover. The Cyclomix is a multi-purpose, high-shear impact mixer that is suitable for a variety of applications, such as dispersion of pigments [124], intensive mixing of cohesive powders [117], coating, grinding & deagglomeration [125] etc.



Fig.1.9 Photo (a) and schematic (b) of a Hosokawa Cyclomix [104, 105, 126].

1.3.3.5 Magnetically Assisted Impaction Coater (MAIC)

The principle of MAIC (see figure 1.10) regarding coating is that the guest particles adhere on the host particles assisted by impaction caused by magnetic assistance.

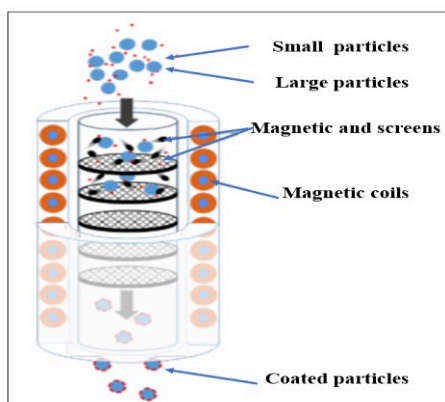


Fig.1.10 Schematic of a coating process performed by a AVEKA (Aveka technology, USA) MAIC [127].

The processing vessel is surrounded by a series of electromagnets. The magnetic field created by the electromagnets agitates the magnetic particles present in the vessel along with the powder. These agitated magnetic particles transfer their energy to the host and guest particles by collisions, hence promoting inter particle and particle wall collisions. These collisions cause deagglomeration and high energy impaction of guest particles on host particles leading to coating. Magnetic particles are generally coated to prevent contamination. In several key industries, e.g., pharmaceuticals, cosmetics and foods, surface modification processes are routinely used to MAIC change the physical and chemical surface properties of particulates [128].

1.3.3.6 Turbula Mixer

The Turbula mixer (T2F type) consists of a container which is placed in a mixing basket set by 2 stirrups at 2 rotary axes (see Figure 1.11). One of them drives the whole system by rotating at an adjustable speed. Turbula mixing is achieved by the harmonic interaction of rotation, translation and inversion throughout the mixing process. Turbula mixers are used for the homogeneous mixing of powdery substances with different specific weights and particle sizes [129]. In cosmetics, pharmaceuticals, and food industries, full stainless steel versions of the turbula mixers are available [130].

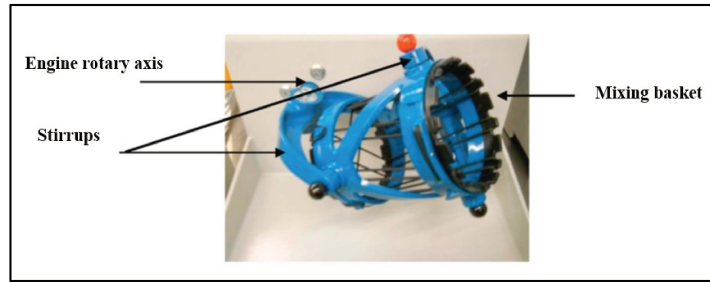


Fig.1.11 Photo of a Turbula mixer [130, 131].

1.3.3.7 High-shear mixer “Picomix”

Using the same system as Cyclomix, Picomix (Hosokawa Micron, Japan. See figure 1.12) is the Cyclomix with small volume (100 mL capacity) for dry coating powders. It offers very fast mixing with full discharge without loss of material. The rotating mixing takes place in a conical agitator vessel. The mixing efficiency is depending on the rotor speed (max. 6000 rpm), the mixing time (LCD screen) and the degree of filling. After filling the powder components into the agitator vessel, the machine is then closed. High-speed rotation of the paddles creates a centrifugal force and moves the particles from the bottom to the wall of the vessel. During mixing process, fine particles and host particle interact and collide under the high shearing/impacting force between the particles and the wall. Once the mixing process is completed, the vessel is removed from the machine and the mixture is emptied out. Picomix has been used in experimental studies to investigate dry particle coating by Lu et al. [101, 102, 131] and Liu et al. [103, 104].

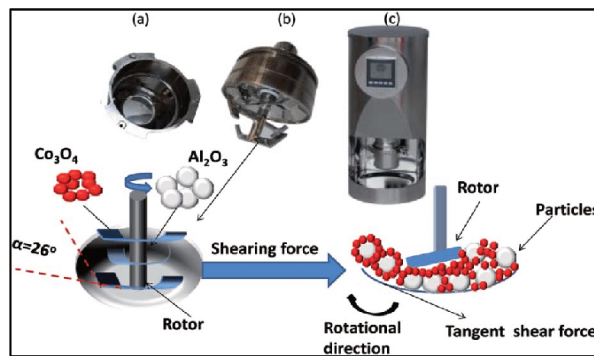


Fig.1.12 Picomix and its work principles [104, 132, 133].

Chapter 1: Literature Review

1.3.3.8 Summary of dry particle coating devices

The above-mentioned dry particle coating devices are summarized in table 1.3. The main advantages and disadvantages and limitation are listed in this table.

Table 1.3 Summary of dry particle coating devices.

Devices	Operator parameters	Advantages	Disadvantages or limitations
Mechano-fusion	<ul style="list-style-type: none"> ● Rotation speed ● Processing time 	<ul style="list-style-type: none"> ● Simple operation and strong mechanical energy; ● Control of particle shape (rounding, flattening); ● High degree of mixing; ● Wide range of capacities available; ● Control of material temperature possible with a cooling jacket; ● Processing in inert gas such as nitrogen and argon is possible. 	<ul style="list-style-type: none"> ● Strong mechanical force may break the host particles; ● Irregular fine particles are uneasily coated.
Hybridizer	<ul style="list-style-type: none"> ● Rotation speed ● Processing time 	<ul style="list-style-type: none"> ● High versatility, due the combinations of powder materials being infinite; ● Excellent dispersion of particles, since the particles are processed in a high-speed air flow; ● Closed system with inert gas to prevent oxidation of materials, e.g., metal fine particles are possible; ● High speeds up to 16,000 rpm can be achieved in a Hybridizer. 	<ul style="list-style-type: none"> ● The fragile host particles may be broken when the high speed is applied.
Co-Mill	<ul style="list-style-type: none"> ● Co-milling cycle ● Operating speed ● Powder filling ratio 	<ul style="list-style-type: none"> ● No substantial micronization; ● Prior blending preferred; ● Low temperature and low dust generation; ● The fines generated are on a lower side compared to other mills. 	<ul style="list-style-type: none"> ● The properties required for manufacturing tablets like compatibility showed no fixed trend.
Cyclomix	<ul style="list-style-type: none"> ● Rotation speed ● Rotation time ● Powder filling ratio ● Available change the clearance wall to paddle 	<ul style="list-style-type: none"> ● Intensive mixing process close to the wall allows effective heat transfer between the heat-controlled jacketed wall and the product; ● Optimal temperature control of the product and very accurate agglomeration with melt binders as well as rapid drying of wet agglomerates; ● High degree of dispersion and homogeneity and ultra-short cycle times. 	<ul style="list-style-type: none"> ● Hybridizer improved the flow of coated silica but Cyclomix reduced the flowability attributed mainly to breaking of silica particles [120].
MAIC	<ul style="list-style-type: none"> ● Magnetic particle size ● Magnet to powder mass ratio ● Processing time ● Frequency variations 	<ul style="list-style-type: none"> ● Agitated magnetic particles transfer their energy to the host and guest particles by collisions, these collisions promote deagglomeration; ● Magnetic particles are generally coated to prevent contamination; ● No substantial micronization and low particle attrition. 	<ul style="list-style-type: none"> ● Incomplete surface coverage compared with Cyclomix and hybridizer [117, 134].
Turbula Mixer	<ul style="list-style-type: none"> ● Rotation speed ● Processing time 	<ul style="list-style-type: none"> ● High mixing efficiency leads to very short mixing times and thus to an extremely gentle mixing process; ● The mixers are easy to operate and allow hygienic work; ● Flexibly choose different shapes and size of mixing containers and easily accessible container holder for fast exchange of containers; 	<ul style="list-style-type: none"> ● Most of them have just been used in laboratories study.
Picomix	<ul style="list-style-type: none"> ● Rotation speed ● Processing time ● Powder filling ratio 	<ul style="list-style-type: none"> ● Small volume mixer offers very fast mixing with full discharge without loss of material; ● Intensive but homogeneous and fast blending of the powder components takes place; ● Simple operate process; ● Process chamber can be cooled and easy to clean. 	<ul style="list-style-type: none"> ● Only 100 mL volume capability compares to Cyclomix.

As summarized in table 1.3, all of these devices can be used in dry coating process, the structure or working principle of them are quite different. Therefore, they are successfully used in different fields. The high-energy devices, such as mechanofusion, hybridizer, Cyclomix are more suitable for achieving stronger coating strength. Cyclomix is a very energy rich mechanism in which operating parameters are to be strictly controlled in order to achieve desired results. Increasing the operating parameters beyond optimum parameters does not cause such degradation in properties in devices like Co-Mill, MAIC and Mechanofusion.

Zhou et al. ^[135] tried to use Co-milling to develop coating parameters so as to improve the flowability and avoid reduction of tabletability. Silica loading was varied between 0 and 2% wt./wt. and co-milling cycles from 0 to 40 while not changing other parameters. The study demonstrated that increasing the silica loading and the number of co-milling cycles can improve flow properties, hence, they concluded that a certain number of cycles is necessary to break the agglomerates of guest particles and aid their proper spread on host particles.

Ghoroi et al. ^[136] applied MAIC and found that coated nanoparticles imparted nano scale roughness on the guest particles and host-host particle contacts, hence reducing cohesivity and agglomeration tendency thus increasing the dispersibility. Attrition of the particles was minimal. Surface coated fine particles and excipients generally showed improvement in flowability in comparison to uncoated ones. Powders which have good flow generally pack better because of the low cohesion.

Sato et al. ^[137] used sugar particles (Suglets) as host particles and magnesium stearate (MgSt) for guest particles to study dry particle coating in a high shear mixer. The Suglets particles were seen to have a mono-modal size distribution with a median diameter (D50) of about 250 μm , the MgSt has a wide particle size distribution ranging from 0.1 μm to 50 μm with a D50 of about 5 μm . To observe the effect of processing conditions on the coating and flowability, the rotation speed of the mixer varied from 250 to 1500 rpm and the processing time varied from 30 to 600 s. SEM was involved to know the coating consequence. The surface morphology of the coated particles indicated that at high rotational speeds, the coating phenomena proceed rapidly, even at short processing times. The flowability improved with longer processing times. Higher rotation speed was found beneficial to the flowability.

Zhou et al. ^[138] used mechanofusion technique to study the effects of mechanofusion technique on lactose monohydrate powder by coating it with MgSt and fumed silica. The results demonstrated that batch mechanofused with fumed silica showed rough surfaces similar to a batch mechanofused without fumed

silica. Mixing was unable to disperse MgSt particles on lactose, but mechanofused with MgSt showed a lower angle of repose indicating better flow.

Ouabbas et al. ^[139] studied the dry particle coating process by using different devices, MgSt was coated on silica gel of different weight ratio of 5 and 15% wt./wt., the results were compared with other one obtained with Turbula mixer. The study indicated that Cyclomix processing changed the shape of the particles whereas Hybridizer did not. Hybridizer improved the flowability of coated silica but Cyclomix reduced the flowability attributed mainly to breaking of silica particles (fine particles have larger cohesive force). Turbula mixer did not improve flowability. Processing silica with MgSt increased the hydrophobicity in all three machines. Interestingly after storage for a specific time under specific humidity conditions, the MgSt layer disappeared once again exposing the silica surface.

Lu et al. ^[101] investigated the preparation of Co/Al₂O₃ solid catalysts by dry coating technology. A high shearing mixer Picomix was carried out to synthesize the catalysts. Porous spherical γ -Al₂O₃ with a 278 mm mean particle diameter and 3 mm Co₃O₄ micro-powders were used as host and guest particles, respectively. Conventional impregnation catalysts preparation method was applied to compare the performance of catalysts. Co/Al₂O₃ catalysts containing 15 wt% of cobalt were synthesized using both impregnation and coating methods. For dry coating method, processing conditions include rotation speed 1500 rpm with 10 and 30 min respectively. The performance of the catalysts in Fischer Tropsch (FT) synthesis was evaluated in a milli fixed-bed reactor. The study illustrated that a uniform coating layer of a 1 mm and 3 mm thickness was observed, the Picomix was successfully used to synthesize the Co/Al₂O₃ solid catalysts. No formation of cobalt aluminate was found in the dry coating process, more importantly, the catalysts prepared by dry coating method in FT synthesis exhibited a high FT reaction rate comparable to that observed over most active state-of-the art catalysts.

1.4 Coating catalysts

Dry particle coating is applicable to a variety of industrially important problems because of its simplicity and environmental friendliness ^[103, 106]. Up to now, the dry particle coating technique has been used in pharmaceuticals, cosmetics, metal/ceramic composites, thermal spray materials, ceramic filters, solid lubricants, and electric contact materials ^[104, 132]. Nevertheless, very little research attempts to utilize the mechanical coating process in solid catalysts. Some efforts were made to towards the preparation of catalysts in literature and are listed in table 1.4.

Chapter 1: Literature Review

Table 1.4 Mechanical study of preparation of catalysts.

Devices (prepare catalysts)	Processing conditions	Size of host and guest	Mass fraction of guest (wt %)	Reactors and reactions	Results or application	Ref.
Hybridizer	8000 rpm; 12 min	Al ₂ O ₃ (3 μm); Platinum (10-40 nm)	0.4	A Micromeritics AutoChem 2910 instrument for determination of the catalyst metal Surface area per unit loading	Automotive vehicles have used catalytic converters to treat unburned hydrocarbons, carbon monoxide and Various nitrogen oxides produced from the combustion of hydrocarbon fuels in the engine	[140]
Hybridizer	2500 rpm; 30 min	Ceramic fiber (2-3 μm); Al ₂ O ₃ (50-150 nm)	3			
Hybridizer	8000 rpm; 3 min	Ceramic fiber (2-3 μm); Al ₂ O ₃ (50-150 nm)	6.5			
Ball-mill	8000 rpm; 0.5-12	CeO ₂ (2 cm); ZrO ₂ (10 mm)	18 g of balls to 1 g of powder	Oxygen storage capacity (OSC) was measured after reducing the catalyst (50 mg) at the appropriate temperature (650 K) under H ₂ flow (2 h, 35 ml/min)	The main purpose of this paper was to present a novel method for preparing ceria-zirconia mixed-oxide catalysts with a high oxygen storage capacity	[141]
Retsch PM100 Planetary Ball Mill	150 rpm; 1 h	Ag ₂ O (2-3.5 μm); Al ₂ O ₃ (not gave in the article)	2	A fixed-bed flow reactor was used to test the selective catalytic reduction (SCR) of NO _x . SCR is a means of converting nitrogen oxides, also refers to as NO _x with the aid of a catalyst into diatomic nitrogen (N ₂) and water (H ₂ O)	Catalyst made by ball milling: 99% NO _x conversion at 302 °C. Catalysts made by wet impregnation: 80% NO _x conversion at 478°C	[142]
Planetary Ball Mill	140rpm; 1h	WO ₃ and MoO ₃ (15-25g) TiO ₂	10% WO ₃ , 11% MoO ₃ .	A tubular quartz reactor was used to calcinate WO ₃ /TiO ₂ 893K for 7h; MoO ₃ /TiO ₂ were calcined at 823K for 4h	Monolayer's coating was observed by SEM, ball milling was regarded as a potential technique for the preparation of catalysts	[143]
Ball mill	Milled 8h at air atmosphere.	La ₂ O ₃ , Fe ₂ O ₃ , CuO or PdO	Not gave	The SCR of NO by C ₃ H ₆ was conducted in a tubular fixed bed reactor at atmospheric pressure	High SCR activity over LaFe _{0.97} Pd _{0.03} O ₃ is observed at T < 350 °C	[144]
Ball mill	340rpm; 0.5-24h	V ₂ O ₅ (20 mm, 10 mm, 5 mm) Ball to powder mass ratio was 50:1	2	The SCR activity was carried out in a fixed-bed quartz reactor	The activity of the mechanochemically prepared catalysts were found to be comparable and, in some cases, greater than the conventionally prepared catalyst	[145]
Planetary Ball Mill	500-1000 rpm; 5-300 min	ZnO; Ball to powder mass ratio was 10:1	Not gave	Photocatalytic degradation of malachite green	The catalyst milled at 1000 rpm for 30 min displayed the highest photocatalytic activity	[146]
Planetary Ball Mill	880 rpm; 3 min	TiO ₂ nanocrystals were prepared by milling Na ₂ CO ₃ and TiOSO ₄	0.1-0.5	Photocatalytic generation of hydroxyl radicals	Different milling materials were investigated. Catalyst prepared in corundum jars with a size of 37 nm doubly out performed that of standard TiO ₂	[147]
Planetary Ball Mill	250 rpm; 4 h	TiO ₂ and Fe ₂ O ₃ were milled	5-10	Oxidative degradation of dyes	TiO ₂ 5 mol% Fe ₂ O ₃ (calcined at 100 °C) displayed the best photocatalytic activity achieving activity 3-5 times higher than P25 TiO ₂	[148]

Chapter 1: Literature Review

Planetary Ball Mill	300 rpm; 120 h	TiO ₂ was ball milled, then NH ₃ • H ₂ O was added.	Not gave	Photocatalytic degradation of acetaldehyde and methylene blue	The mechanochemically prepared nitrogen doped catalyst was found to display greater activity than non-milled TiO ₂	[149]
High shear mixer Picomix	1500 rpm; 10-30 min.	γ-Al ₂ O ₃ : 278 μm; Co ₃ O ₄ 3 μm	10-30	A milli fixed-bed reactor was applied to test the performance of the catalysts in FT synthesis	The catalysts prepared by the mechanochemical method in FT synthesis exhibited a high FT reaction rate	[101]
Planetary Ball Mill 100	250 rpm	γ-Al ₂ O ₃ : 1860 μm and 71 μm; Co ₃ O ₄ 3 μm	15	The performance of the catalysts in FT synthesis was evaluated in a milli fixed-bed reactor	The performance of the catalysts prepared by mechanochemical method in FT reaction was found to relate the dispersion of Co	[102]
Ball milling Pulverisete 0; Planetary ball milling P100	250 rpm; 10-40 min	γ-Al ₂ O ₃ : 70-80 μm; Co ₃ O ₄ 3 μm	15	The catalytic performance of the catalysts in the FT synthesis was evaluated in a milli-fixed bed reactor	Both milling can be used to prepare the Co catalysts for FT synthesis, meanwhile, Co catalysts prepared by mechanochemical methods show better cobalt reducibility compared with the catalysts prepared by conventional impregnation	[131]
High shear mixer Picomix	5000 rpm; 5 min.	γ-Al ₂ O ₃ : 77 μm; Co ₃ O ₄ 0.1 μm	5-15	A milli-fixed bed reactor was conducted to evaluate the catalytic performance of the catalysts he catalytic performance of the catalysts	Co/Al ₂ O ₃ catalysts were prepared by particle coating can increase the catalytic activity and selectivity of C ₁ -C ₅ hydrocarbon and CO ₂ , accomplished by decreasing selectivity of when the FT reaction temperature between 220-280°C	[104]
Milling	20 min	Ni: 2.7-7.8 nm Al ₂ O ₃ : (not gave)	5-20	The catalytic activity measurements were performed at atmospheric pressure in a quartz fixed-bed microreactor at 200-500 °C	15 wt% Ni/Al ₂ O ₃ catalyst exhibits stable stability during 10 h. CO methanation was investigated on the 15 wt% Ni/Al ₂ O ₃ catalyst and the results showed that CO completely converted to CH ₄ at 300°C	[11]
Mechanochemical method (Mortar)	((NH ₄) ₂ CO ₃ to Al molar ratio of 3:2, (NH ₄) ₂ CO ₃ to Ni molar ratio of 1:1 and ((NH ₄) ₂ CO ₃ to Co molar ratio of 1:1). The mixed precursors were milled in a mortar for 20 min		10-15	The CO ₂ methanation was performed in a quartz microreactor atmospheric pressure in the temperature range of 200-500 °C	15 wt% Ni-12.5 wt% Co/Al ₂ O ₃ gave the highest catalytic performance in CO ₂ methanation (76.2% CO ₂ conversion and 96.39% CH ₄ selectivity at 400°C) and this catalyst presented high stability over 10 h	[10]
Ball mill (Retsch PM100)	250 rpm; 3-27 h	Ni: 3-7 μm; LaNi ₅ : 10 μm-1mm.0.125 g or 0.500 g of the powders were filled into the milling vial made of SUS304 steel, together with 10 balls of 10 mm-diameter		H ₂ and CO ₂ were separately leaked into the vial with using a 40 ml syringe until the total pressure reaches 1 atm. The volume ratio of the gases was H ₂ :CO ₂ = 2:1 milling was carried out for 21.3 h under the same atmosphere with 10 balls	The results show that finely dispersed carboxides of Fe and La could be intermediates to lead to mechanochemically activated CO ₂ methanation	[9]

The analysis of literature shows that the mechanical methods have been used to prepare catalysts for different reactions. Regarding the devices, the majority of the studies chose the ball milling (see table 1.4) to investigate their research. During the ball milling process, the collisions between the tiny rigid balls and particles will form catalysts. The degree of milling in the ball milling is influenced by the residence time of the materials in the mill chamber and the size, density, number of balls, and the rotation speed etc. ^[150].

The advantages of the mechanochemical synthesis method to prepare catalysts include as follows: simple and fast procedure; no high energy is consumed because of room temperature and atmospheric pressure operating conditions; no chemical solvent and associate problems of the catalyst recovery and subsequent reutilization or recycling of toxic and corrosive solutions. Given these advantages, this method in the

preparation of solid catalysts for methanation shows promising improvement. However, using the mechanical method to prepare catalysts for methanation is quite rare, very few articles can be found in the literature^[9-11]. High shearing mixer picomix has been used to prepare catalysts by researchers Lu et al.^[101, 102, 131, 132] and Liu et al.^[103, 104].

1.5 Nanomaterials/nanoparticles

In the dry particle coating process, it is necessary to know the number and mass of fine particles to coat one layer or multiple layers of host particles. The diameter of fine particles should be measured to obtain the number and mass of fine particles. However, the nanometric scale of the powders poses a major problem with the accuracy of size measurements. These powders are very cohesive and form agglomerates with uncontrollable sizes. The coating process requires knowledge of the size of the primary particles and not of the agglomerates! This will allow the best calculation of the powder layer with the primary particles disregarding the agglomerates.

1.5.1 Definition of Nanoparticles

A nanoparticle is usually defined as its diameter is between 1-100 nanometers (nm)^[151, 152], nanoparticle is usually distinguished from microparticles (1-1000 μm).

International Union of Pure and Applied Chemistry (IUPAC) defined a nanoparticle as a particle of any shape with dimensions in the 1×10^{-9} and 1×10^{-7} m range, in 2012, the IUPAC extends the term to include tubes and fibers with only two dimensions below 100 nm^[153].

Nanoparticles can have amorphous or crystalline forms, and their surfaces can act as carriers for liquid droplets or gases. To some degree, nanoparticulate matter should be considered a distinct state of matter, in addition to solid, liquid, gaseous, and plasma states, due to its distinct properties (large surface area and quantum size effects).

1.5.2. Nanoparticle classification and dimension

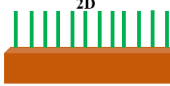
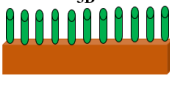
Nanoparticles are generally differentiated regarding their dimensionality, morphology, composition, uniformity, and agglomeration^[154].

1.5.2.1 Nanoparticle dimension

Nanoparticles have been divided into three parts (see Table 1.5). Table 1.5 shows the definition of different dimensional nanomaterials and their application fields. It can be seen that 1D materials are widely used in chemistry. Current applications of nanoscale materials include very thin coatings used, for example, in electronics and active surfaces (for example, self-cleaning windows).

For most applications the nanoscale components will be fixed or embedded but, in some cases, such as those used in cosmetics and in some pilot environmental remediation applications, free nanoparticles are used.

Table 1.5 Dimension of nanoparticles

Number of dimensions	Images of dimensions	Definition	Application field
One-dimensional (1D) nanomaterials	 <p>1D Thin films or surface coatings</p>	Thin films or surface coatings in the nanometer scale with one dimension are defined as one-dimensional(1D)	Electronics, chemistry, and engineering thin films have been already developed and used for decades. Thin films can be deposited by various methods, and can be grown controllably to be only one atom thick, a so-called monolayer [155].
Two-dimensional (2D) nanomaterials	 <p>2D Fixed long nanostructures</p>	Two-dimensional nanomaterials have a two-dimensional structure on the nanometer scale.	Asbestos fibers are an example of two-dimensional nanoparticles.
Three-dimensional (3D) nanomaterials	 <p>3D Fixed cylindrical nanostructures</p>	All three-dimensional nanomaterials are considered to be three-dimensional nanomaterials.	These include thin films deposited under conditions that form atomic-scale porosity, colloids, and free nanoparticles with various morphologies [156].

The ability to produce materials with very high precision and accuracy (better than 100 nm) is leading to considerable benefits in a wide range of industrial sectors, for example in the production of components for the information and communication technology, automotive and aerospace industries.

1.5.2.2 Nanoparticle morphology

Nanoparticles possess a variety of shapes, for example, there are spherical, nanoreefs, nanoboxes, nanoclusters, nanotubes etc. These shapes or morphologies sometimes arise spontaneously as an effect of

a templating or directing agent during synthesis. For example, during micellar emulsions or anodized alumina pores, or from the innate crystallographic growth patterns of the materials themselves. Controlling the morphology of nanoparticles is of key importance for exploiting their properties for their use in several emerging technologies. Optical filters and bio-sensors are among the many applications that use optical properties of gold nanoparticles and it requires anisotropy of the particle shape.

1.5.2.3 Nanoparticle composition, uniformity and agglomeration

The nanoparticles can be composed of a single constituent material or a composite of a plurality of materials. Nanoparticles found in nature are usually agglomerated (see figure 1.13) from materials of different compositions, and now it is easy to synthesize pure one-component materials by various methods.

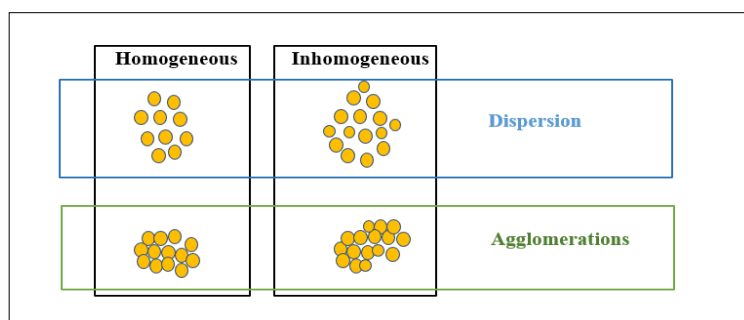


Fig.1.13 Uniformity and agglomeration of Nanoparticles

Depending on its chemical nature and electromagnetic properties, the nanoparticle may be present in a dispersed aerosol, suspension/colloid or condensed state. In an agglomerated state, the nanoparticle can behave like larger particles depending on the size of the agglomerates. It is therefore clear that agglomeration of nanoparticles, size and surface reactivity, as well as shape and size, must be taken into account when using nanoparticles.

1.5.3 Agglomeration of nanoparticles

Agglomeration is a size enlargement process in which primary particles stick together to form agglomerates ^[157]. The formation of agglomeration of nanoparticles can be explained by following reasons:

- 1) The distance between the nanoparticles is extremely short, and the mutual van der Waals force is much greater than their own gravity force, therefore, they tend to attract each other and form to agglomeration;
- 2) The surface hydrogen bonds and chemical bonds between nanoparticles lead to mutual attraction between nanoparticles and stick together to get agglomeration: the finer the particles, the stronger the agglomeration.

The agglomeration of nanoparticles can be divided into two types ^[158]: soft agglomeration and hard agglomeration. Soft agglomeration is mainly caused by the electrostatic force and van der Waals force between particles. Because the force is weak, it can be eliminated by some chemical action or mechanical energy. In terms of hard agglomeration, in addition to electrostatic force and van der Waals force, chemical bonding exists, which lead to the hard agglomerates cannot be easily disrupted.

There are some methods that have been used to separate agglomerations. Such as, adding dispersant (polymer organics, such as polyethylene glycol (PEG), ammonium polyacrylate, sucrose, etc.) to reduce the surface tension of the interface through absorption, and achieve the purpose of deagglomerations. Ultrasonic treatment is a common method to deagglomerate the aggregated nanoparticles. In mechanical mixing, the high shear mixer (such as Cyclomix, Picomix) has proved to have a deagglomeration effect.

1.5.4 Measurements of nanoparticles

Along with the rapid development of nanotechnology, some useful and powerful characterization techniques have been developed and/or identified for characterizing the size of nanoparticles. A wide range of advanced characterization techniques exists such as: transmission electron microscopy (TEM), small-angle X-ray scattering (SAXS), dynamic light scattering (DLS), specific surface area method, centrifugal liquid sedimentation (CLS), atomic force microscopy (AFM), tunable resistive pulse sensing (TRPS), nanoparticle tracking analysis (NAT), laser diffraction analysis (LD). In this section, we aim to introduce a number of typical characterization techniques that have been widely used to analyze the size of nanoparticles.

1.5.4.1 Transmission Electron Microscope (TEM)

TEM is a microscopy technique (see figure 1.14) in which a beam of electrons is transmitted through a sample and then form images. When high-energy electrons (usually is 50-200 KeV) penetrate the sample,

depending on the electron transmission intensity at different locations of the sample, different diffraction directions or electron through crystal sample, the image is displayed on the fluorescent screen. The TEM resolution is 0.3 nm and the lattice resolution is 0.1-0.2 nm. The samples can be tested on a copper network with a diameter of 2-3 mm. A TEM is composed of a vacuum system in which the electrons travel, an electron emission source for the generation of the electron stream, a series of electromagnetic lenses, as well as electrostatic plates.

The TEM is used for obtaining an image and chemical information about the nano and microstructure of all types of materials, ranging from metals and ceramics to soft biomaterials. 2D and 3D imaging of the structures is possible as well as the mapping of electric and magnetic fields.

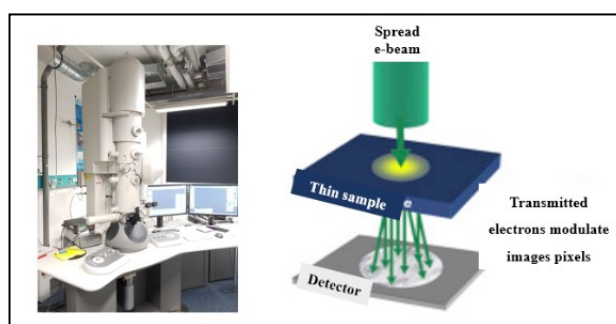


Fig.1.14 Photo and schematic of TEM ^[159].

In order to measure the particle size by electron microscopy, we should first take as many representative morphological images of nanoparticles as possible, and then measure the particle size by these electron microscopic photos under the help of Image software (ImageJ). ImageJ is a public java-based image processing software developed by the National Institutes of Health. It can do area and pixel statistics, spacing, can create histogram of size distribution. In the size analyzing process, in order to obtain the relatively accurate value, in the selecting process, different sizes, clearly visible areas should be chosen.

1.5.4.2 Small Angle X-Ray Scattering (SAXS)

SAXS is a small-angle scattering technique that is used to analyze nanoscale density differences in a sample. When an X-ray beam passes through a superfine powder layer, it scatters through the scattering of electrons in the particles at a very small angle (typically 0.1-10°). SAXS is capable of delivering structural information of dimensions between 1 and 100 nm, and of repeat distances in partially ordered systems of up to 150 nm. Each SAXS system consists of an X-ray source, a collimation system, a sample

stage, and a detector (see figure 1.15). Appropriate software is used to process and evaluate the measured scattering data.

SAXS is used for determining the microscale or nanoscale structure of particle systems in terms of average particle sizes, shapes, distribution etc. [160]. Whether the materials are solid or liquid, the SAXS is available to resolve size. Since it requires a minimum of sample preparation, it is widely used in the laboratory. In a typical experiment, a highly collimated beam of monochromatic x-rays is transmitted through a sample on the order of 1 mm in thickness. The scattered x-rays are collected on a 2-dimensional area detector azimuthally in 360 degrees at a continuous range of scattering angles which deviate from the direct, transmitted beam. The scattering angle, which is defined by convention as 2θ , the diameter of particle D can be expressed as [161] $D = 2\pi/q$, where $q = 4\pi\sin(\theta)/\lambda$, in which λ is the wavelength of the x-rays (typically 0.154 nm for the Cu x-ray source), q is the momentum transfer or scattering vector.

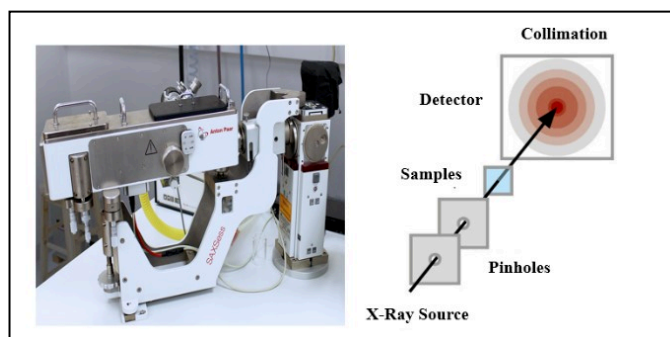


Fig.1.15 Photo and schematic of SAXS [162].

1.5.4.3 Dynamic Light Scattering (DLS)

DLS is a technique (see figure 1.16) that is used to determine the size distribution of small particles in suspension in solution. The basic principle of DLS is: the sample is illuminated by a laser beam, and the intensity of the scattered light (Brownian motion) can be measured. The fluctuations of the scattered light from Brownian motion are detected at a known scattering angle θ by a fast photon detector.

DLS instruments that measure at a fixed angle and can determine the mean particle size in a limited size range. The fluctuation of scattered light contains the dynamic information of size of particles and calculation equation can be expressed as follows [163-165]:

$$R = \frac{K_B T}{6\pi\eta C} \quad (\text{Eq. 1.3})$$

Where R is the radius of the particles, C is the translational diffusion coefficient of particles; K_B is the Boltzman constant, T is absolute temperature, η is viscosity.

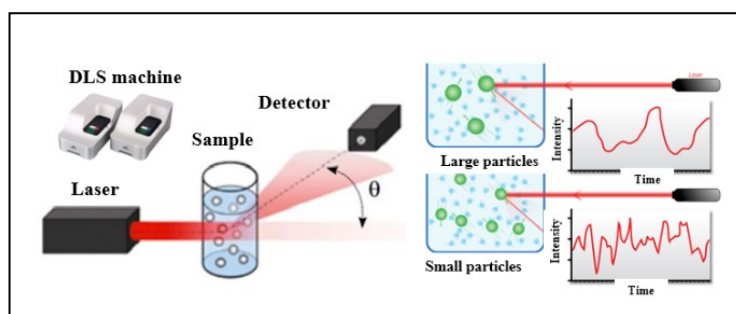


Fig.1.16 Work principle of DLS [166].

DLS is used to analyze size of various particles, such as nanoparticles: solids, proteins, polymers, micelles, vesicles, biological cells etc. [167].

1.5.4.4 Specific Surface Area Method

Surface area analysis (see figure 1.17) is an indirect method for measuring particle size. In surface area analysis, nitrogen is usually used because of its availability in high purity and its strong interaction with most solids. Because the interaction between gaseous and solid phases is usually weak, the surface is using liquid N_2 to obtain detectable amounts of adsorption. There is an inverse relationship between particle size and surface area. Nitrogen adsorption can be used to measure the specific surface area of a powder. Relative pressures less than atmospheric pressure are achieved by creating conditions of a partial vacuum. After the saturation pressure, no more adsorption occurs regardless of any further increase in pressure. Highly precise and accurate pressure transducers monitor the pressure changes due to the adsorption process. After the adsorption layers are formed, the sample is removed from the nitrogen atmosphere and heated to cause the adsorbed nitrogen to be released from the material and quantified. The data collected is displayed in the form of an isotherm curve, which plots the amount of gas adsorbed as a function of the relative pressure.

The method of Brunauer, Emmett, and Teller (BET) is commonly used to determine the total surface area. If the particles are assumed to be as spherical and in a narrow size distribution, BET calculation provides a precise specific surface area (S) evaluation of materials by nitrogen one layer adsorption measured as a

function of relative pressure using a fully automated analyzer. The technique encompasses external area and pore area evaluations to determine the total specific surface area in m²/g,

Determining the specific surface S (m²/g) and assuming that the particle is not porous, spherical and has a monomodal size distribution, we have [168-170].

$$S = \frac{\text{surface of sphere}}{\text{volume of sphere} \times \text{density of particles}} = \frac{6}{D \times \rho} \quad (\text{Eq. 1.4})$$

Where D is the diameter of particle and ρ is the density of materials.

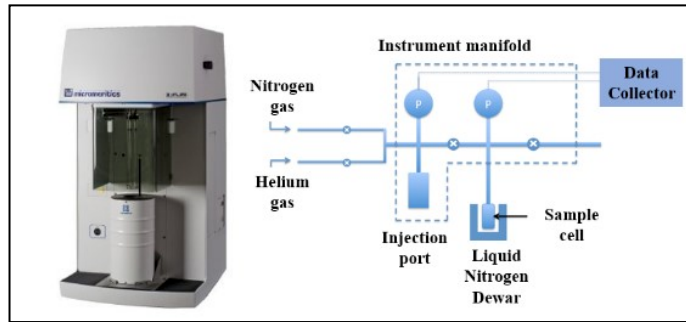


Fig.1.17 Photo of a 3Flex analyzer of surface area [171].

1.5.4.5 Centrifugal Liquid Sedimentation (CLS)

Centrifugal sedimentation method is an indirect method for measuring particle size distribution. Powder particles naturally settle in a stationary liquid medium depending on gravity to overcome the resistance and buoyancy of the medium, which results in the changes of suspension concentration, pressure, relative density, light transmittance, or sedimentation velocity. Measuring the variation of these parameters with time can reflect the particle size composition of the powder. Centrifugal sedimentation method is based on Stokes's law of particle sedimentation, which is proportional to particle concentration and shading. Stokes's law can be expressed by equation 1.5 in the settlement process under centrifugal inertial force [172].

$$D = \sqrt{\frac{18\eta \ln(D_2/D_1)}{(\rho - \rho_f)\omega^2 t}} \quad (\text{Eq. 1.5})$$

Where D is Stokes' diameter of particles; η is the viscosity; D_1 and D_2 are rotation center to the surface of settlement media and light point transmittance; ρ is the density of particles; ρ_f is the density of subsidence medium; ω is the angular velocity of settling; t is times.

A common CLS instrument is shown in fig. 1.18. The disc can be of virtually any size, typically the diameter of it is approximately 125-150 mm. The detector beam is usually a monochromatic light of relatively short wavelength (400-500 nm) or X-rays. Shorter wavelength light gives better detector sensitivity when particles smaller than 100 nm are measured. To prepare the analysis, the disc is set in motion at a constant speed, and then the disc chamber is filled with a fluid with contains a slight density gradient. Samples are prepared for analysis by dilution in a fluid of slightly lower density than the least dense fluid in the disc. The lower density fluid used for the sample reduces the initial mixing of the fluid inside the disc with the sample. When a sample is injected, it strikes the back inside the face of the disc, and forms a thin film, which spreads as it accelerates radially toward the surface of the fluid. When the sample dispersion reaches the fluid surface, it quickly spreads over the surface, because it is of lower density. Once a sample is on the fluid surface, sedimentation of individual particles begins.

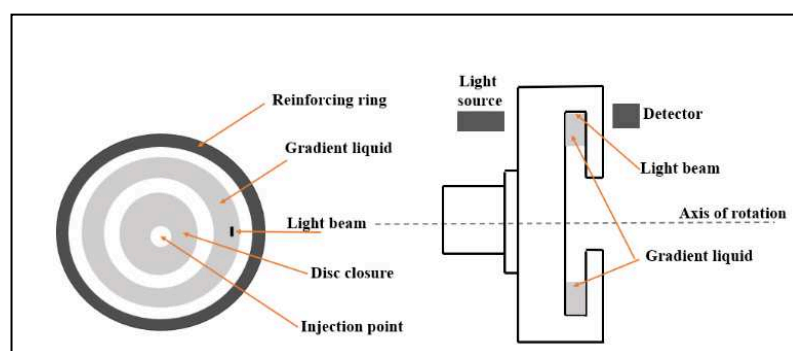


Fig.1.18 Schematic of a CLS ^[172].

Applications include analysis of polymer latexes and emulsions, fillers, ceramic oxides, pigments, microspheres, oil emulsions, and much more. Many materials - such as oil emulsions, adhesive latexes, and liposomes - that may have presented difficulties for measurement via differential sedimentation can be measured quickly and precisely ^[173, 174].

1.5.4.6 Atomic Force Microscopy (AFM)

AFM (figure 1.19) is a very high-resolution type of scanning probe microscopy with demonstrated resolution on the order of fractions of a nanometer.

It consists of a cantilever with a sharp probe and its end that is used to scan the specimen surface. Normally, the cantilever is made of silicon or silicon nitride, when the probe is brought to approach a sample surface,

the force will cause the cantilever to deform or change its motion state, these change distributions will be obtained by a 4-quadrant photo detector and then the surface structure information and surface roughness can be shown with nanometer resolution. Applications of AFM can be found in a wide range of disciplines of the natural sciences, molecular engineering, polymer chemistry, cell biology, and medicine [175].

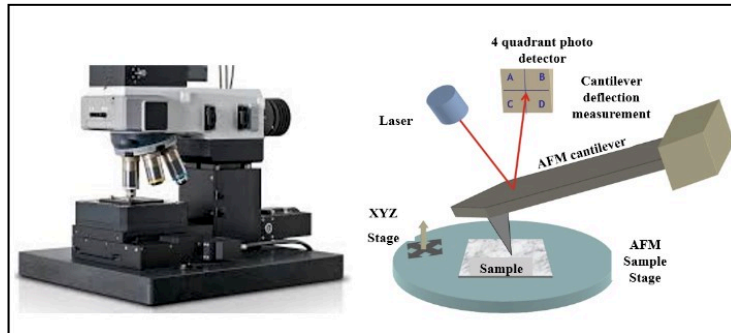


Fig.1.19 Photo and Schematic of an AFM (PI, Germany) [175].

1.5.4.7 Tunable Resistive Pulse Sensing (TRPS)

TRPS technology enables accurate measurements of nanoparticle properties suspended in solution [176]. The particles going through a pore are detected or blocked one by one as a transient change in the ionic current flow. Since the magnitude of the blockade is proportional to the particle size, it is possible to obtain an accurate particle size after calibration with a known standard. Figure 1.20 a) shows a TPRS technology (Izon Science Ltd.) and b) schematic illustration of the measurement principle.

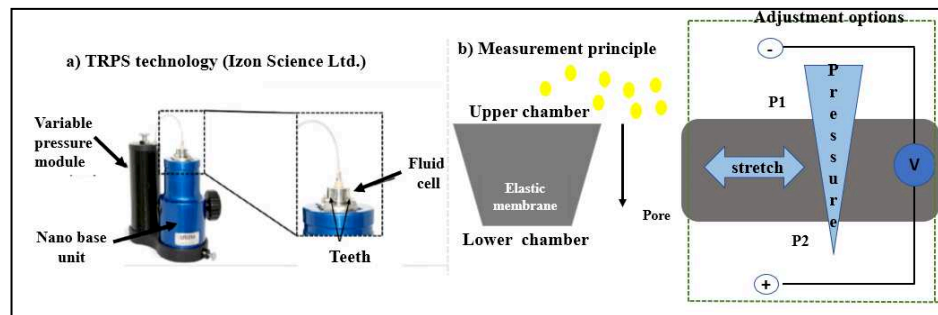


Fig.1.20 a) TRPS technology; b) schematic illustration of the measurement principle (The suspended particles in the upper compartment pass through the pore and cause the resistive pulse. There are three options to adjust the instrument for optimal settings for the specific sample: mechanical pore stretching, pressure difference adjustment, and the applied direct current voltage) [177].

The typical TRPS has 4 components, a variable pressure module, a nano base unit, teeth, and a fluid cell. b) Schematic illustration of the measurement principle of TRPS shows the suspended particles in the upper chamber pass through the pore and causes the resistive pulse. There are three options to adjust the instrument for optimal settings for the specific sample: mechanical pore stretching, pressure difference adjustment, and the applied direct current voltage.

TRPS is used to determine sample concentration and accurately obtain particle electrophoretic mobility and surface charge, in addition to particle size information ^[177].

1.5.4.8 Nanoparticle Tracking Analysis (NTA)

NTA is a technique that uses the characteristics of light scattering and Brownian motion to obtain the particle size distribution of the sample in the liquid. When a laser beam is passed through the sample chamber, the particles in suspension that fall in the laser beam path disperse light in such a way that they can be observed through a 20x magnification microscope. A camera mounted on this microscope records a video file of the movement of the particles under Brownian motion, within its field of view (see figure 1.21). The particles' movement is recorded on a frame-by-frame basis. At the same time, the NTA software detects and monitors the center of individual particles that were observed, and also measures the standard distance moved by individual particles in the direction of x and y planes. NTA allows the determination of a size distribution profile of small particles with a diameter of approximately 10-1000 nm in liquid suspension.

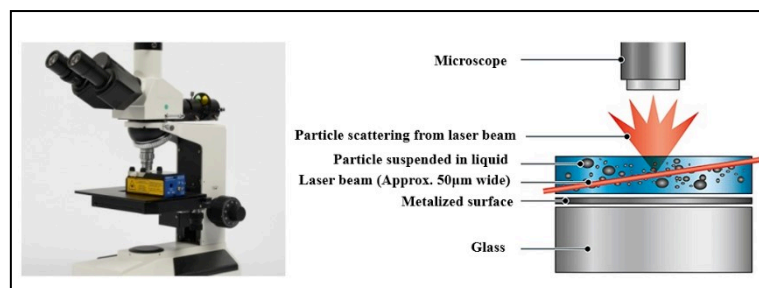


Fig.1.21 Photo of NTA (AZoNetwork UK Ltd.) and schematic of working principle ^[178].

NTA is used for commercial and academic work with nanoparticles, bacterial membrane, drug delivery, vaccine production, protein aggregation, etc. ^[177].

1.5.4.9 Laser Diffraction Analysis (LD)

LD is a technology that is widely used for analyzing particle size, it utilizes diffraction/diffusion patterns of a laser beam passed through any object ranging from nanometers to millimeters in size to quickly measure dimension of a particle. In a laser scattering measurement, a laser beam passes through scattered particle samples and angular light at angles inversely proportional to the particle size.

LD uses Mie's theory ^[177] (which describes the scattering of an electromagnetic plane wave by a homogeneous sphere) of light scattering to calculate the particle size distribution, assuming a volume equivalent to the sphere model. Mie's theory requires knowledge of the optical properties (refractive index and imaginary component) of both the sample being measured, along with the refractive index (describes how fast light travels through the material) of the dispersant. Usually, the optical properties of the dispersant are relatively easy to find in published data, and many modern instruments will have built-in databases that include common dispersants.

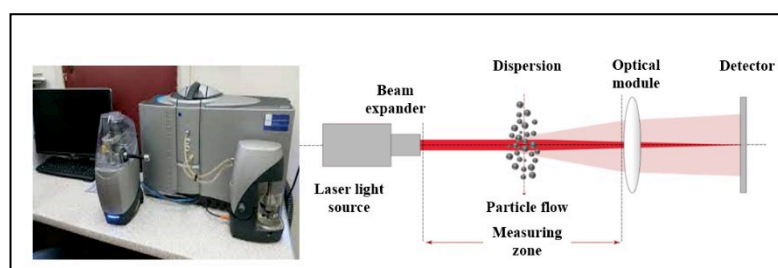


Fig.1.22 Photo of Master 3000 (Malvern UK Ltd.) and schematic of working principle ^[179].

Figure 1.22 present an example of a Master 3000 (Malvern UK Ltd.) and its working principle. The Mastersizer 3000 uses the technique of laser diffraction to measure the size of particles. It does this by measuring the intensity of light scattered as a laser beam passes through a dispersed particulate sample. This data is then analyzed to calculate the size of the particles that created the scattering pattern.

As mentioned above, a lot of methods can be used to analyze the nanoparticle size. Table 1.6 summarizes the advantages and limitations of different methods of nanoparticle measurement.

Souza et al. ^[180] compared TEM and DLS methods to analyze the size distribution of ceramic nanoparticles. TEM images (see figure 1.23) show a sample dispersion of the titanium oxide nanoparticles, and different size distribution using different methods for the same nanoparticles. It was found that mean and median values from DLS would be slightly higher than TEM due to the interference of the dispersant.

Chapter 1: Literature Review

Table 1.6 the advantages and drawbacks of different measurements.

Method	Analyze size range	Advantages	Drawbacks/Limitations
TEM	1-1000 nm	<ul style="list-style-type: none"> Powerful magnification; High quality and detailed; Information about surface features, shape, size etc.; Easy to operate; Wide applications, e.g., scientific, educational and industrial field. 	<ul style="list-style-type: none"> Few powders are used to observe, makes the analysis results lack of statistics; Potential artifacts from sample preparation; Samples are limited to those that are electron transparent, able to tolerate the vacuum chamber and small enough to fit in the chamber.
SAXS	1-100 nm	<ul style="list-style-type: none"> Samples need not be crystalline; Minimum of samples preparation required; Measurement is usually non-destructive; Able to measure various samples. 	<ul style="list-style-type: none"> Spatial averaging occurs due to random orientation of dissolved or partially ordered samples - leads to a loss of information; Radiation damage is possible for less robust samples e.g., proteins; Scattered intensity is weak for commonly used systems.
DLS	1 nm-10 μ m	<ul style="list-style-type: none"> No destroying and interfering with the original state of the system; It is fast, accurate and requires only a few samples to measure the dynamic properties of the medium; High resolution. 	<ul style="list-style-type: none"> Measuring process is slow; DLS must be used on highly dilute solutions.
Physical gas adsorption (BET measurement)	1-1000 nm	<ul style="list-style-type: none"> High accuracy and reliability of results for non-porous materials 	<ul style="list-style-type: none"> Complicated evaluation program; Since it measures pore size, which causes deviation with the real size of particle. Calculation just suitable for non-porous and spherical particle.
CLS	10-1000 nm	<ul style="list-style-type: none"> High size resolving power; Enabling populations of single particles to be distinguished from populations of dimension and multimers for the study of the agglomeration state of suspensions, as well as to separate distinct particle populations from each other. 	<ul style="list-style-type: none"> Settling medium and working speed will directly affect the measurement results. The types and usage of dispersants, sample concentration and sample amount will also affect the measurement results ^[181].
AFM	0.5 - 1000 nm	<ul style="list-style-type: none"> Easy to prepare samples for observation; It can be used in vacuums, air, and liquids. Measurement of sample sizes is accurate with a 3D imaging; It can be used to study living and nonliving elements; It can be used to quantify the roughness of surfaces; It is used in dynamic environments. 	<ul style="list-style-type: none"> It can only scan a single nanosized image at a time of about 150x150 nm. It has a low scanning time which might cause thermal drift on the sample. The tip and the sample can be damaged during detection. It has a limited magnification and vertical range.
TRPS	40 nm -10 μ m	<ul style="list-style-type: none"> High resolution and sensitivity, unique insights into size distribution and concentration of the nanomaterials, as well as particle behavior and morphology in complex media. 	<ul style="list-style-type: none"> TRPS requires optimization and standardization to establish sensitivity, specificity and reproducibility
NTA	10 nm-1 μ m	<ul style="list-style-type: none"> Highly precise, accurate, and reproducible concentration measurements on different types of nanoparticles; Considerably, repeatability and reproducibility of concentration measurements have been increased significantly. 	<ul style="list-style-type: none"> NTA can be time-consuming and requires some operational skills for the adjustment all software settings.
LD	30 nm-3.5 μ m	<ul style="list-style-type: none"> It has high information carrying capacity; It is free from electro-magnetic interference; It has very minimum signal leakage; Single laser beam can be focused in areas smaller than 1 micro diameter. 	<ul style="list-style-type: none"> It is expensive and hence more expenditure It increases complexity and duration of the treatment based on laser devices or equipment; It requires higher power during the cutting process.

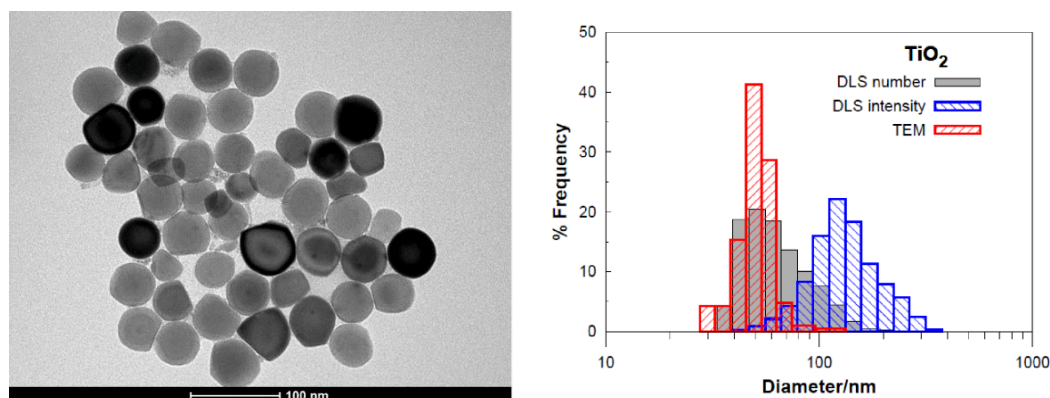


Fig.1.23 TEM images of TiO_2 and the correspondent TEM and DLS particle size distribution ^[180].

Braun et al. ^[182] analyzed the size of the silica nanoparticle by CLS methods. Fig.1.24 shows the sedimentation time as a function of the particle size as calculated from equation 1.5 for different values of the particle density. As the particle density and/or the particle size increase, the sedimentation time decreases. Nanoparticles under investigation will reach the detector in a time range roughly between 10 s and 20 min (see dotted lines in figure 1.24). The study has proved that the CLS method is robust and suitable for particle size in the range of about 35-50 nm.

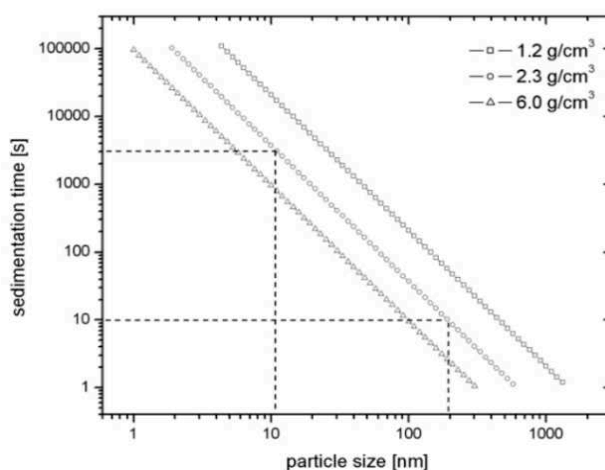


Fig.1.24 Sedimentation time as a function of particle size as calculated from equation 1.5 for three different particle density values (The horizontal dotted lines correspond to sedimentation times of 10 s and 20 min, resulting in a particle size range suitable to be characterized by CLS from roughly 10-200 nm, respectively.) ^[182].

Robert et al. ^[183] compared the AFM and NTA measurements with TEM for determining the mean diameter of nanoparticles. TEM images (see figure 1.25) provided two different size of latex 100 nm (a) and 200 nm (b).

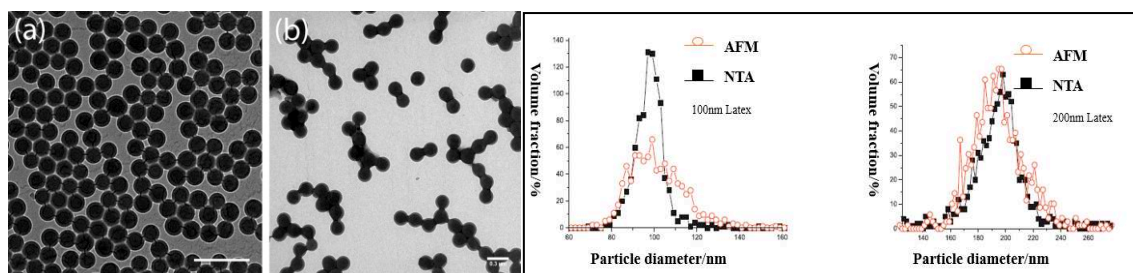


Fig. 1.25 TEM images of the nanoparticle samples (a) 100 nm latex and (b) 200 nm latex, size distribution that measured by AFM and NTA [183].

The results from three different particle measurement techniques have been compared. All techniques give standard deviation less than 1 nm. It has been demonstrated that these techniques give different results but these are all consistent considering the exact nature of each measurand and their physical conditions. This study leads the way for improvement in nanoparticle size measurement by allowing the results from different techniques to be compared directly.

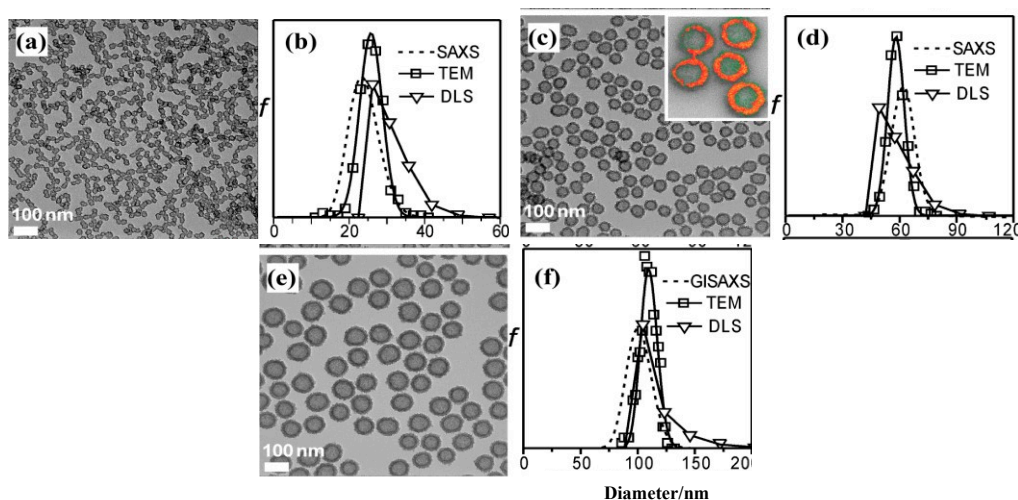


Fig. 1.26 TEM images of (a) HNP25, (c) HNP50, and (e) HNP100. Diameter distributions from TEM images, DLS, and SAXS fitting are shown in (b) for HNP25, (d) for HNP50, and (f) for HNP100. f is the number frequency. All distributions for a given HNP size are normalized to the same area [184].

Zhi et al. [184] measured the size of $\text{SiO}_2/\text{TiO}_2$ (different dispersion of SiO_2) hollow nanoparticles (HNPs, respectively, HNP25, HNP50, HNP100 mean different dispersion of SiO_2) by different measurements, respectively, SAXS, TEM and DLS. (See figure 1.26).

The study demonstrated that SAXS gives accurate information on diameter and size distribution, DLS measurements are quicker and perhaps cheaper than SAXS, but are less reliable in determining

polydispersity, giving higher values than SAXS. TEM may underestimate the polydispersity of the particles if sampling is not performed with great care.

Table 1.7 Summary of particle sizing techniques used for the commercial CsA nanoemulsion ^[185].

Technique	Measured value (nm)
DLS	117.9 ± 2.0 nm
LD	73.1 ± 1.5 nm
NTA	107.7 ± 1.3 nm
TEM	26.6 ± 14.3 nm

LD measurements has a wide measure range from 10 nm to 3.5 mm using a single optical measurement path, making it suitable for an extremely wide range of applications. Peter et al. ^[185] investigated the particle size and size distribution of Herein cyclosporine (CsA) ophthalmic emulsion. Assessment of particle size was performed using four fundamentally different particle sizing techniques, including DLS, LD, NTA and TEM. measured results are summarized in table 1.7.

The study illustrated that each technique has strengths and limitations depending on the type of sample, the state of dispersion, and the particle size range. Generally, each technique measures a different property that is used to infer size; therefore, direct inter-comparison of size values is less desirable as it may introduce errors due to conversion, different sample preparation, etc. In addition, the distribution range can vary drastically depending on the instrument configuration, sample type and preparation procedure, as well as measurement artifacts.

Given that each technique has its own advances and limitations, combining different characterization techniques is highly desirable to fully measure the size of nanoparticle. It is also important to understand the underlying working principles and optimized conditions to collect reliable data from each technique.

1.6 DEM modeling

1.6.1 Introduction

Discrete element modeling (DEM) is a method for computing the motion and effect of a large number of particles. With advances in computing power and numerical algorithms, it has become possible to

numerically simulate millions of particles on a single processor. DEM is an ideal model to track the particle motion, collision and to analyze the force (i.e. normal contact force), energy and velocity, etc. [104, 186].

DEM was developed by Cundall and Starck [187] in 1979 based on the molecular dynamics, it regards the entire medium as a series of discrete and independent particles. Particles can contact by angle and surface, particles can be translated, rotated, or deformed. The particle surface is available to be compressed, slipped, and separated. When the particle undergoes external force or boundary displacement, the position of particles is updated and the new contacts between bodies are taken place as the calculation based on Newton's second law.

In general, there are two types for contact of particle interactions in DEM: hard-sphere and soft sphere [188].

1.6.1.1 Hard Sphere

The hard spheres are widely used as model particles in the statistical mechanics' theory of fluids and solids [189]. They are defined simply as impenetrable spheres that cannot overlap in space. They mimic the extremely strong ("infinitely elastic bouncing") repulsion that atoms and spherical molecules experience at very close distances. As is shown in figure 1.27, this assumption suggests that the hard-sphere model is suitable for highly agitated or gravity-free conditions [190]. This model can be used to simulate the multiple contacts occurring at the same instant because the computational burden increases dramatically due to the update of information, such as particle velocity and trajectory whenever particle contact occurs [191].

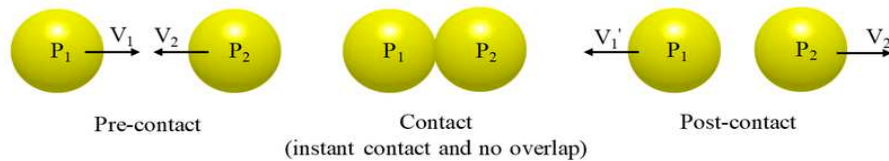


Fig. 1.27 Simple schematic diagram of hard-sphere model V_1 and V_2 : the velocity of each particle before contact; V_1' and V_2' : the velocity of each particle after contact [192].

1.6.1.2 Soft sphere

The soft sphere model is the most common and flexible model in DEM [193]. In this model, it is assumed that the particle contact is lasting, as is shown in Figure 1.28. Hence, the soft sphere model is desirable for

the investigation of long-lasting and multiple particle contact in a high dense system ^[194]. The soft-sphere model is referred to as a time-driven approach, as it sets a time step in which the contact force is calculated. Therefore, the time step should be carefully set for accurate simulation. The smaller time steps allow accurate integration of the resulting particle equations but can dramatically increase the computational time in the simulation.

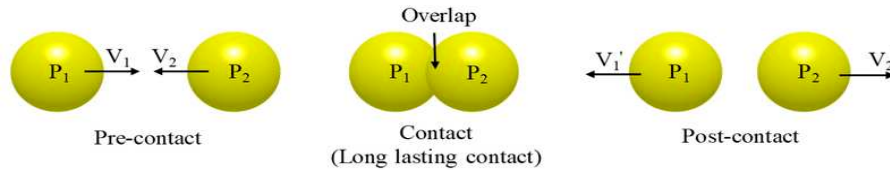


Fig.1.28 Simple schematic diagram of hard-sphere model V_1 and V_2 : the velocity of each particle before contact; V_1' and V_2' : the velocity of each particle after contact ^[192].

A number of studies have been performed using the soft-sphere model to simulate high shear granulation, coating, and milling processes ^[195, 196].

1.6.2 Studies of DEM modeling

DEM for particulate systems has been reported in the literature, it has been proved that these approaches are useful in developing a better understanding of particle motions and the mechanism of particulate processes. Some articles about DEM modeling on particle mixing and granulation are summarized in table 1.8.

Table 1.8 Summary of the work of the literature of DEM modeling on particle mixing and granulation.

Modeling information			Parameters	Objectives	Ref.
Materials	Diameter	Modeling number of particles			
Cluster	0.113-0.300 mm	500-3500	Size, number and shape of cluster	Determine the influence of particle shape and size on the particle behavior and the interface friction.	[196]
Steel ball	15 mm	230	Young's modulus of particles and velocity of rotation	Establish a general numerical way to check the performances of concrete	[197]
Not gave in the article	0.1-0.2 mm	1000-2000	Size and filling rate of particles	Study dissipation mechanisms of the non-obstructive particle damping (NOPD) based on a discrete element method (DEM).	[198]
Steel ball	29-54 mm	324	Size of ball and milling speed	Use DEM to simulate multiple interacting bodies undergoing relative motion and breakage and establish the interaction rules and the associated contact parameters.	[199]

Chapter 1: Literature Review

Sand	0.31-0.93 mm	250-1915	Size of sand, velocity and simulation time	Test the effect of material properties on flowability of particulate materials.	[200]
Steel balls	90 mm	48	Rotation speed	Study the dynamics of charge motion in tumbling mills both experimentally and theoretically.	[201]
Fabric	20-100 mm	1000	Size of grain and filling rate	Micromechanical studies of the granular material behavior at the grain scale level.	[202]
Steel balls	22.24 mm	120-216	Number of mills, filling rate, and critical speed	Study the effects of the mill speed on energy efficiency and capacity of mills and the behavior of the load in the mill.	[203]
Catalyst's particle (Fe/Al ₂ O ₃ -SiO ₂)	4.4 mm	40000	Simulation time	Combine DEM modeling and mass transfer was developed for investigating the local mass transfer throughout a catalytic gas-solid fluidized bed reactor.	[204]
Rock blocks	10 mm	30-1000	Chipping angle of rock blocks and orientation	Explore the effect of joint orientation on rock fragmentation by a tunnel boring machines cutter.	[205]
Tungsten steel	0.88 and 1.2 mm	1246, 386	Size of and number of particles, simulation time	Predict the damping characteristics and describe the motions of multi-bodies and determine the energy dissipation.	[206]
Sandstone	2.5-20 cm	2000	Size of particle and simulation time	Develop a robust numerical simulation capability for the exploration and prediction of near-wellbore mechanics.	[207]
Steel	2.36 - 9.52 mm	Total mass of milling balls: 5-50 g	Mill rotational speed, vibration frequency and amplitude, ball diameter, total mass of milling balls	Investigate the milling process of mechanical alloying in a SPEX 8000 series shaker mill by varying ball sizes and ball to powder mass ratios.	[19]
Polypropylene	10 and 16 mm	38878 and 9294	Size of particles and simulation time	Discuss the current state of the art in the modeling of granular flows in mixing processes.	[208]
CaCO ₃	1.7 mm	5000	Density of particles	Use DEM in parallel with a model for coalescence of deformable surface wet granule and predicted both collision rates and coalescence efficiencies.	[209]
Not gave in the article	2.0 mm	48000	Time step	Introduce a new modeling strategy for the simulation of the mixing of monodisperse particles.	[210]
Polyethylene	6 mm	3300	Time step, friction coefficient	Model the particle-particle interactions and studied the influence of the various assumptions and simplifications of particle processes.	[211]
Lactose primarily	0.19-0.99 mm	8000	Filling rate and size of particles	Present an appropriate multidimensional population balance equation model for high-shear granulation.	[212]
Granular catalyst	2-3 mm	18000 - 20000	Size and filling ratio of particles, time step, vessel speed	Use the DEM modeling to simulate flow, mixing, and heat transport in granular flow systems in rotary calciners and impregnators.	[213]
SiC	2.2-200 μm	5656 - 11313	Size of particles, speed	Develop a DEM model of polycrystalline SiC to simulate the ceramics machining process and quantitative description of the crack's initiation and propagation can be obtained and used for the assessment of the machining techniques.	[214]
Sand	1.5-2.7 mm	8791	Particle size and Friction coefficient	The sand particles were modeled by unbreakable 2-sphere clumps, so that interlocking between particles, which yielded more stable and efficient force chains, could take place.	[215]
γ-Al ₂ O ₃	2 mm	150000	Velocity	Develop a model of a fluidized bed granulator by combining the gas and particle dynamics with a simple model of particle wetting.	[216]
Placebo tablet	11.9 mm	875 - 1250	Loading mass of particles	Use DEM modeling to model the motion and orientation of several novel pharmaceutical tablet shapes in a film coating pan in order to predict coating uniformity.	[217]
Soybeans	5.4 mm	1000	Density and friction coefficient of particles	Develop and validate an appropriate particle model for one test seed, soybeans, based on these physical properties.	[218]

Nearly all of the related reports suggested changing the process parameters to understand the particle motions and mechanism of particulate processes, such as velocity and simulation time. More studies focused on the properties of the particles themselves, such as size, density, young's modulus etc., and found that these parameters play a critical role in particle motions. Therefore, these parameters should be properly considered for optimization as well as scale-up productions.

1.6.3 DEM modeling on dry particle coating

In recent decades, with the increased usage of high-speed mechanical mixing of large volume commercial applications, a better understanding of high-speed mixing especially in the dry coating field has become even more important. In dry particle coating, fine/guest particles are coated on the surface of large/host particles by using mechanical forces (i.e., shearing, impacting, compressing). Table 1.9 summaries the DEM modeling on coating.

Table 1.9 Summary of some articles of DEM modeling on coating.

Modeling information			Variation parameter	Model Devices	Objectives	Ref.
Materials	Diameter	Modeling number of particles				
Host: Polymethyl methacrylate Guest: Al ₂ O ₃	Host: 100-200 μm Guest: 100nm	Host: 1000 Guest: 56000	Rotation speed, host size and density	Magnetically-assisted impaction coating (MAIC)	Model and understand the processes happening at multiple length and time scales in magnetically assisted impaction coating process.	[219]
Host: Polymethyl methacrylate Guest: Al ₂ O ₃	Host: 400 μm	Host: 1000-4000	Rotation speed, loading number, simulation time	Mechanofusion, Hybridizer	Study the DEM modeling and see if it is a useful tool to model dry particle processes and can be used at various length scales to gain a certain understanding of mechanical devices.	[220]
Host: Pharmaceutical powders	1.0 mm	5000-20000	Particle number, speed, volume of vessel	Conical screen mill	Investigate the mechanical dry particle coating by DEM modeling and examine the influence of the operating parameters.	[221]
Host: Polymethyl methacrylate Guest: Al ₂ O ₃	Host: 200 μm	Host: 1000 Magnets: 10-80	Number of magnets	Magnetically-assisted impaction coating (MAIC)	Study the dry particle coating processes by DEM modeling and optimize its application in the commercial.	[13]
Host: Mannitol Guest: Lactose	Host: 100 μm Guest: 5 μm	Host: 200 Guest: 10000	Surface energy	Couette shear cell	Investigate the effect of particle interface energies and mixing energy input on the macroscopic behavior of the dry-coating process by using the discrete element method	[222]
Host: Potassiumchloride Guest: Aluminum silicate	Host: 125-250 μm Guest: 0.25-0.5 μm	Theoretical surface coverage: 100%	Size of host and guest particle	A high-intensity vibrational mixer	Investigate the effects of material stiffness, host and guest particle sizes, and mixing intensity on dry coating quality using a high-intensity vibrational mixer.	[110]
Host: Suglets Guest: MgSt	Host: 2 mm	40000	Rotation speed and simulation time	Cyclomix	Get a better understanding of dry particle coating process using experimental study and DEM modeling.	[223]

Chapter 1: Literature Review

Host: DPIs Guest: API	Host: 70 μm Guest: 5 μm	Host: 1 Guest: 200	Surface energy and velocity	Vibrated container	Understanding the adhesive interactions between active pharmaceutical ingredient (API) particles and carrier particles in dry powder inhalers (DPI) is critical for the development of formulations and process design.	[224]
Host: Mannitol Guest: lactose	Host: 100 μm Guest: 3 μm	Host: 2	Rotation speed, surface energy, collision frequency, surface coverage	Not gave in the article	Binary interaction between adhesive units formed from monodisperse spherical fines and carrier particles was studied with the discrete element method (DEM) in order to better understand phenomena such as lumping, bridging and flowability of adhesive units and mixtures.	[225]
Host: KCl Guest: PE	Host: 5 μm Guest: 1-5 μm	Host: 1000	Young's modulus and size of guest	Fluid energy mill (FEM)	Study the coating performance of polymeric materials and polyethylene (PE) effect on the breakage of the coarse particles.	[226]
Host: Glass bead Guest: Lactose	Host: 1.7 mm Guest: 1 mm	Host: 6000- 13000 Guest: 50000- 100000	Rotation speed and filling ratio of guest and host	Agitated filter dryer	Investigate the critical process parameters that affect the heat transfer in the filter dryer and compare the experimental temperature and solvent concentration profiles to the simulations under similar conditions.	[227]
Host: Glass bead Guest: MgSt	Host: 2-10 mm Guest: 5-100 μm	Host: 5000- 50000	Rotation speed and size of host and guest	Bladed mixers	Study the he kinematics of granular flow of cohesionless particles in a bladed mixer experimentally using particle image velocimetry and computationally using DEM modeling.	[228]
Host: Mannitol Guest: Lactose	Host: 200 μm Guest: 5 μm	Host: 1 Guest: 1000	Velocity, surface energy	Spherical shaped space	Examine the breakage and capturing behavior of loose fine-particle agglomerates on impact with target particle by DEM modeling.	[229]
Host: Mastic Guest: Bitumen	Host: 2-8mm Guest: 200 μm	Volume filling: 11-74%	Density and filling ratio of guest	Dynamic shear rheometer	Evaluate the rubber effects and the interaction among limestone filler, rubber by DEM modeling	[230]
Host: Ascorbic acid Guest: Cornstarch	Host: 315 μm Guest: 14 μm	Host: 80 Guest: 36864	Surface energy, mass ratio, velocity	Cylindrical polycarbonate jar	Understand the effect of fine particle amount and adhesion on the adhesive mixing process by DEM modeling via variation of surface energy.	[231]
Host: Mannitol Guest: Lactose	Host: 200 μm Guest: 5 μm	Host: 1 Guest: 1000	Velocity, surface energy	Spherical shaped space	Explore the effects of the interface energy between fines and host on agglomerate breakage by DEM modeling.	[232]
Host: Lactose Guest: MgSt	Host: 70 μm Guest: 2 μm	Host: 1 Guest: 2000	Surface energy, velocity	L-shaped cylindrical tube	Advance the use of the multi-scale simulation tool towards quantitative predication of the performance of dry powder for inhalation.	[233]
Host: Crystalline cellulose Guest: API	Host: 20-220 μm Guest: 10-93 μm	Mass ratio: 1-3.5%	Size of host and guest	Resonance acoustic mixer	Assess predictability of packing porosity as well as its bulk density reduction enhancements after dry coating for a wider variety of pharmaceutical powders.	[234]
Host: Drug particle Guest: Lactose	Host: 70 μm Guest: 2 μm	Host: 1 Guest: 2000	Surface energy velocity	Prototype inhaler	Develop a fundamental approach to simulate dose emptying and dispersion in a model dry powder inhaler that explicitly takes into account the interaction between carrier particles, that may be cohesive or adhesive, and their interaction with a possibly turbulent velocity field.	[235]
Guest: Glass bead	Host: 0.55-2 mm Guest: 100 μm	Host: 1 Guest: 1000	Size of host, velocity, surface energy	Spherical shaped space	Investigate the influence of interparticle cohesion on the energy propagated and dissipated in agglomerates during impact against a rigid target.	[236]

Through the analysis of the literature, it was found that in the DEM coating modeling, Hertz-Mindlin with JKR (Johnson-Kendall-Roberts) cohesion model was conducted. JKR cohesion model is a non-linear elastic contact model that allows us to represent the cohesive nature of fine and moist materials.

1.7 Different DEM model

Many papers concerning dry coating have been published [13, 101, 105, 131, 237-239], but this technique is not commercially used because a general rule governing the coating process is lacking and there is an inadequate understanding of the fundamental knowledge of coating mechanisms [104, 186]. Hence, it is imperative to simulate the dry coating behavior to understand the coating mechanism as well as to optimize the dry particle coating. In order to investigate the interactions between two particles or between the particle and the geometry, it is necessary to have a good understanding of contact models.

Contact models can be classified into contact and non-contact models (see figure 1.29). The contact model includes elastic contact and inelastic contact model. Elastic contact is the study of the deformation of solids that touch each other at one or more points [240], this contact moment is instantaneous and very short. Inelastic contact, in contrast to elastic contact, was suggested to model the dissipation of energy when plastic deformation between particles occurs [241]. The elastic contact model consists of two parts: linear model and a non-linear model.

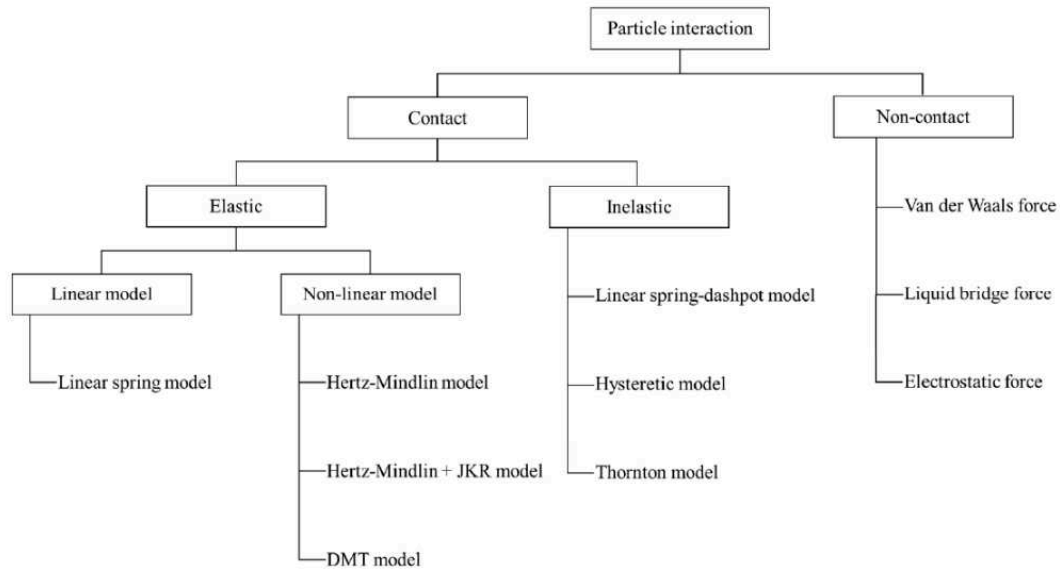


Fig. 1.29 Classification of particle interaction force models by contact force and non-contact force [192]. In addition, the non-contact forces such as van der Waals force, liquid bridge force and electrostatic force is described.

1.7.1 Elastic contact model

1.7.1.1 Linear spring model

The linear spring model is the contact model that represents the linear relationship between force and displacement (overlap), as shown in figure 1.30. The contact force increases with displacement. The contact forces in the normal and tangential direction respectively are given by ^[242]:

$$F_{n,ij} = -K_n \delta_n \quad (\text{Eq. 1.6})$$

$$F_{t,ij} = -K_t \delta_t \quad (\text{Eq. 1.7})$$

Where $F_{n,ij}$ and $F_{t,ij}$ are the normal contact force and the tangential contact force between particle i and j , δ_n and δ_t are the overlap in the normal and tangential direction, K_n and K_t are the spring constant of the particles involved in the normal contact and tangential contact direction, respectively. The spring constant is defined as the force required per unit of extension of the spring ^[243].

Because of the relationship between the contact force and the overlap, the linear spring model considers that two particles in contact are both normally and tangentially connected by a linear spring constant ^[244]. The linear spring model is not taking into account the dissipative energy that is produced when two particles collide. Practically, when particles collide and deform, some kinetic energy is dissipated by plastic deformation and the kinetic energy is converted to another energy ^[245]. It turns out that the linear spring model is hard to apply to particle contact modeling.

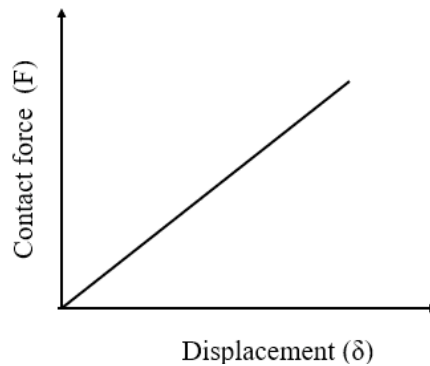


Fig. 1.30 Relationship between contact force and displacement.

1.7.1.2 Hertz-Mindlin Model

As is shown in Figure 1.31, when two particles collide, there is an area, or range, commonly described as “overlap” (δ), which can be calculated from equation 1.8.

$$\delta = R_1 + R_2 - d \quad (\text{Eq. 1.8})$$

Where R_1 and R_2 are the radius of particle 1 and 2, respectively; and d is the distance between the centers of particle 1 and 2 (C_1 and C_2).

The normal force is generally calculated by Hertz contact theory without considering particle surface adhesion. Hertz contact theoretical assumption is that the surface of the particles in contact with each other is smooth and homogeneous, the contact surface is very small compared with the particle surface, only elastic deformation occurs on the contact surface, and the normal contact force is perpendicular to the contact surface.

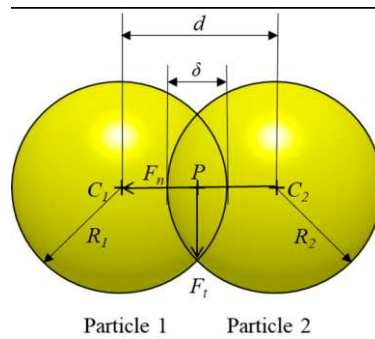


Fig. 1.31. Illustration of normal and tangential forces involved in the contact between particles. C_1 and C_2 : the center of particle 1 and particle 2; R_1 and R_2 : the radius of particle 1 and particle 2; d : the distance between the C_1 and C_2 ; δ the overlap between particle 1 and particle 2; P : the center point of overlap; F_n and F_t : the contact force in the normal direction and the contact force in the tangential direction, respectively [192].

Figure 1.31 shows two spherical particles in elastic contact, defining normal force between two particles $F_{n,ij}$.

$$F_{n,ij} = \frac{4}{3}E^*(R^*)^{1/2}\delta_n^{3/2} \quad (\text{Eq. 1.9})$$

Respectively, E^* and R^* are the equivalent Young's modulus and the equivalent radius, δ_n is the normal overlap between the contacting particle i and j ;

$$\frac{1}{E^*} = \frac{1-\nu_i^2}{E_i} + \frac{1-\nu_j^2}{E_j} \quad (\text{Eq. 1.10})$$

$$R^* = 1 / \left(\frac{1}{R_i} + \frac{1}{R_j} \right) \quad (\text{Eq. 1.11})$$

Where, E_i, ν_i and E_j, ν_j are the two sphere young's modulus and Poisson's ratio. A contact area is assumed to be circular ^[246], it can be calculated by equation 1.12.

$$a = \sqrt{\delta R^*} \quad (\text{Eq. 1.12})$$

Mindlin and Deresiewicz theory ^[247] stated that when two particles contact in the tangential direction, they start to slip along the circumference of the contact surface. The direction of the slip is consistent with the direction of the tangential force. Gradually, the slip develops into the interior of particles through the contact surface. Mindlin-Deresiewicz's contact theory describes this contact process and the relation between tangential displacement and tangential force.

The tangential contact force spring component ($F_{t,ij}$) between contacting two particle i and j can be given by:

$$F_{t,ij} = -K_t \delta_t \quad (\text{Eq. 1.13})$$

$F_{t,ij}$ is the tangential contact force between particle i and j ; δ_t is the tangential overlap between the contacting particle i and j ; K_t the tangential spring constant.

1.7.1.3 Hertz-Mindlin + JKR model

Hertz-Mindlin with JKR (Johnson-Kendall-Roberts) cohesion model is a non-linear elastic contact model that considers the cohesive nature of fine and moist materials. This contact theory is an extension of the Hertz contact theory that adhesion exists only on the contact surface ^[248]. The normal overlap (when two particles are compressed together, the deformation occurs, the overlap in the normal direction is defined as the normal overlap) between two particles can be calculated by equation 1.14.

$$\delta_n = \frac{a^2}{R^*} - \left(\frac{4\pi\gamma a}{E^*} \right)^{1/2} \quad (\text{Eq. 1.14})$$

Where δ_n : the normal overlap between the contacting particle i and j ; E^* : the equivalent Young's modulus; R^* the equivalent radius; a : the radius of the area of contact; γ : the surface energy (Surface energy quantifies the disruption of intermolecular bonds that occurs when a surface is created ^[249])

JKR normal force is based on the overlap δ , the interaction parameter and surface energy γ .

$$F_{n,ij} = -4\sqrt{\pi\gamma E^*} a^{\frac{3}{2}} + \frac{4E^*}{3R^*} a^3 \quad (Eq. 1.15)$$

When $\gamma = 0$, the normal force will be calculated by equation 1.9 (normal force Hertz-Mindlin model).

Figure 1.32 shows the variation of normal force with the normal overlap. The comparison between Hertz-Mindlin with JKR cohesion model results and Hertz Mindlin (no slip) model results is presented. The negative amount of overlap is the interval between two separate particles. When the Hertz-Mindlin model is applied, the relationship between the normal contact force and the normal overlap is presented as blue curve in figure 1.32. The adhesion is taken into account when two particles collide, the normal overlap and normal contact force can be seen in figure 1.32 as a pink color. As supposed, the normal force increases with the normal overlap, however Hertz-Mindlin normal force is bigger than the Hertz-Mindlin JKR normal force in the same overlap. δ_c is the maximum overlap between particles, which is calculated by Eq. 1.16

$$\delta_c = \frac{a_c^2}{R^*} - \sqrt{\frac{4\pi\gamma a_c}{E^*}} \quad (Eq. 1.16)$$

Where a_c is the corresponding maximum radius of contact area.

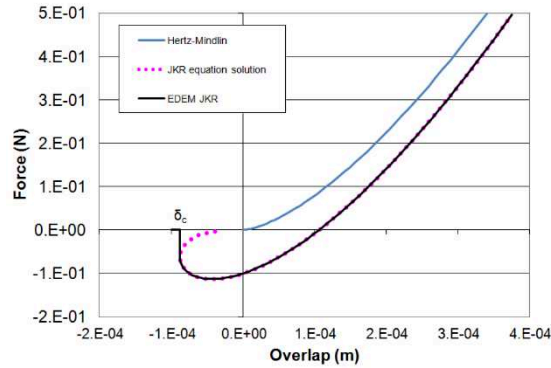


Fig. 1.32 The variation of normal force with the normal overlap ^[250] (Normal force as a function of normal overlap. Hertz-Mindlin with JKR cohesion model results are compared with Hertz-Mindlin model results. Negative overlap is the gap between two separated particles.)

The Hertz-Mindlin + JKR model also predicts larger contact areas than with conventional Hertz theory due to the cohesion ^[251]. The normal force will disappear when the overlap is less than 0, however, in the JKR contact model, the cohesive force still exists but is less than 0. The cohesive force is provided by JKR model as following equation:

$$F_{cohesive} = -\frac{3}{2}\pi\gamma R^* \quad (Eq. 1.17)$$

Eq.1.25 can explain why, when the overlap is less than 0, the normal force will become negative. If the force is bigger than this maximum cohesion force, the cohesive force between particles turn to zero, the particles will be completely separated.

1.7.1.4 DMT Model

The Derjaguin-Muller-Toporov (DMT) model is suitable for adhesive contact which assumes that the contact profile remains the same as in Hertzian contact. The difference with Hertz-Mindlin +JKR model is that the DMT model considers the attractive interactions outside the area of contact ^[252]. The contact force F_c in this model can be calculated with the following equation ^[253]:

$$F_C = \frac{4E^* a^3}{3R^*} - 2\pi \quad (Eq. 1.18)$$

The DMT model is used for very hard materials, or materials with a small tip radius and rigid spheres, and long range interactions ^[254]. However, the Hertz-Mindlin + JKR model is used for soft elastic material with a relative high surface energy ^[253].

1.7.2 Inelastic contact model

1.7.2.1 Linear spring-dashpot model

Unlike the elastic contact model, the inelastic contact model was suggested to simulate the dissipation energy when plastic deformation between particle collide ^[241]. The linear spring-dashpot is the most common model for inelastic contact model, it was proposed by Walton ^[255] based on a study by Cundall and Strack ^[187]. In this model, the normal contact force is calculated with the following equation ^[256]:

$$F_{n,ij} = -K_n \delta_n + \eta_n V_n \quad (Eq. 1.19)$$

Where η_n is the normal damping coefficient; V_n is the relative velocity on the normal direction.

The tangential contact force is calculated by applying the linear spring but is also limited by Coulomb's law of friction using the following equation ^[257, 258]

$$F_{t,ij} = \min\{\mu_f F_{n,ij}, K_t \int V_t dt + \eta_t V_t\} \quad (Eq. 1.20)$$

Where μ_f is the coefficient of friction; η_t is the tangential damping coefficient; V_t is the relative velocity on the tangential direction; K_t is the tangential spring constant; d_t is the distance moved at time t . The tangential force equals the smallest of these two forces. Due to its simplicity and robustness ^[259], the application of this model can be found in various pharmaceutical manufacturing process, such as blending, and high shear wet granulation ^[260, 261].

1.7.2.2 Hysteretic Model

The hysteretic model uses various spring constants during the loading, unloading, and reloading stages ^[262]. In this model, a partially latched spring force-overlap model is applied in the normal direction. The approximation of Mindlin and Deresiewicz theory issued for the case of the constant normal force in the tangential direction ^[259]. Hence, this model is limited as it only considers the plastic deformation and the normal direction. This model has been studied by Chushuri et al. ^[263] they investigated the effect of cohesion in the blending and size segregation of binary mixture in blending process simulation. Sahni et al. ^[264] used the hysteretic model in coating process simulation to obtain the optimal blending conditions in a pan coater.

1.7.2.3 Thornton Model

The Thornton model is based on Thornton's theory ^[265]. This model proposed to study the normal contact between two elastic, perfectly spherical plastic particles. This model is based on the Hertz theory for normal force-displacement relationship during the initial elastic loading but it suggests that plastic deformation occurs if the limiting contact pressure is reached at the center of the contact area. Kluth et al. ^[266] used this model to study the correlation between sputter parameters, film growth and structural properties of zinc oxide.

1.7.3 Non-contact model

Non-contact model comprises van der Waals' force, liquid bridge force and electrostatic force. These forces can act simultaneously or successively between the particles to influence their micro- or macroscopic dynamics of powders.

In terms of van der Waals' force, it is a very weak force but denotes the attractive intermolecular forces, such as dipole-dipole [267]. In DEM modeling, van der Waals force F_{vdw} is calculated by the following equation [268]:

$$F_{vdw} = -\frac{AR_iR_j}{6(R_i+R_j)z^2} \quad (Eq. 1.21)$$

Where z is the surfaces distance of the 2 particles. z is assumed to be 0.4 nm [269]. R_i and R_j are the radius of spherical particle i and particle j , A is the Hamaker constant.

Therefore, in DEM simulation, the minimum separation distance is taken into account in the calculation of van der Waals' force. This minimum separation distance is named by cut-off distance [270]. In several DEM modeling studied [270-273] the cut-off distance is determined within the range of 0.1-1.0 nm.

The liquid bridge force is the cohesive force generated by the formation of the liquid bridge between two wet particles [274]. It is very hard to get the accurate information on the wet particles and calculate this force [274, 275]. Therefore, in DEM modeling, some simplified solutions have been used to easily calculate the capillary force (the capillary force is mainly raised by the surface tension at solid/liquid/air interfaces) instead of liquid force [270, 276, 277], otherwise, this force is ignored in the dry coating process [270, 275].

The electrostatic force exists between charged particles, which is often approximately evaluated by the classical Coulomb's law [278-280].

$$F_{12}^e = -\frac{1}{4\pi\epsilon_0 R_{12}^2} \frac{q_1 q_2}{q_1 + q_2} \quad (Eq. 1.22)$$

F_{12}^e is the electrostatic Coulomb force between the charged particles 1 and 2 ; q_1, q_2 are the signed magnitudes of the charges of particles 1 and 2 ; ϵ_0 is permittivity of vacuum, constant as 8.854e-12 F/m [281].

Non-contact forces in DEM modeling were mainly studied for the pharmaceutical manufacturing process. Yang et al. [282] investigated the effect of van der Waals' force and liquid bridge force on the packing behavior of cohesive particles by DEM modeling. Rhodes et al. [283] studied the impact of van der Waals' force and liquid bridge force on fluidization characteristics using DEM modeling. Additionally, Peng et al. [284] took into account van der Waals' force and electrostatic force to study the aggregation in suspensions using DEM modeling.

1.7.4 Contact model used in this study

In this study, the Hertz-Mindlin (no slip) model and Hertz-Mindlin + JKR model were used for the dry particle coating process. The Hertz-Mindlin (no slip) model is accurate and efficient for force calculation, in this model both normal and tangential forces have been considered to relate to the coefficient of restitution and the rolling friction. The Hertz-Mindlin + JKR model only considers the attractive interactions on the contact area.

1.7.4.1 Governing equations

The particle in granular flows is involved with two types of motion: translational and rotational. In DEM modeling, the first step for getting the evolution in time of the (translational and rotational) velocity and position of the particles is to calculate the particle translation and rotational motions according to Newton's second law^[285]. The total force and torque acting on a solid particle can be expressed by equation 1.23^[286].

$$\sum \mathbf{F}_i = \sum_j \mathbf{F}_{ij}^c + \sum_k \mathbf{F}_{ik}^{nc} + \mathbf{F}_i^f + \mathbf{F}_i^g \quad (\text{Eq. 1.23})$$

Where \mathbf{F}_i is the total force acting on particle i ; \mathbf{F}_{ij}^c is the contact force acting on particle i by its contacting particle j or walls; \mathbf{F}_{ik}^{nc} is the non-contact force (including van der Waals force, liquid bridge force and electrostatic force) acting on particle i by its neighbor non-contacting particle k or other sources; \mathbf{F}_i^f is the particle fluid interaction force acting on particle i ; \mathbf{F}_i^g is the gravity(g) force acting on particle i ($\mathbf{F}_i^g = m_i \mathbf{g}$, m_i is the mass of particle i , \mathbf{g} is the gravitational acceleration, which equal to 9.81 m/s²). Figure 1.33 shows the forces and torque acting on the particle i in the DEM modeling.

The total force acting on each particle are calculated based on the Newton's second law, the equations for the translational and rotational motions of particle i can be given:

$$m_i \frac{dV_i}{dt} = \sum F_i \quad (\text{Eq. 1.24})$$

$$I_i \frac{d\omega_i}{dt} = \sum M_i \quad (\text{Eq. 1.25})$$

Where \mathbf{F}_i is the total force acting on particle i ; \mathbf{M}_i is the total torque acting on particle i ; m_i is the mass of particle i ; \mathbf{I}_i is the moment of inertial of particle i ; for a radius R_i of spherical particle, $I_i = \frac{2}{5} m_i R_i^2$; V_i is

the translational velocity of particle i ; ω_i is the angular velocity of particle i ; t is the motion time, $\frac{dV_i}{dt}$ and $\frac{d\omega_i}{dt}$ are acceleration of translational and angular velocities of particle i .

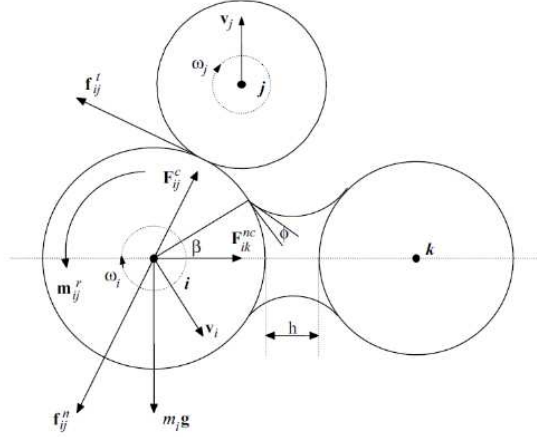


Fig. 1.33 Schematic structure of the forces and torque acting on particle i and non-contacting particle k [286]. (f_{ij}^t is the contact tangential force on particle i by particle j ; f_{ij}^n is the contact normal force on particle i by particle j ; $m_i g$ is the gravity force of particle i ; V_i and V_j are the translational velocity of particle i , j ; ω_i and ω_j are the angular velocity of particle i , j ; M_{ij} is the torque acting on particle i by particle j)

The updated velocities of particle after a single time-step (Δt) can be expressed by equation 1.26 and 1.27:

$$V_{it+\Delta t} = V_{it} + \left(\frac{dV_i}{dt} \Delta t \right) \quad (\text{Eq. 1.26})$$

$$\omega_{it+\Delta t} = \omega_{it} + \left(\frac{d\omega_i}{dt} \Delta t \right) \quad (\text{Eq. 1.27})$$

Where $V_{it+\Delta t}$ and V_{it} are the translational velocities of particle i at time $t + \Delta t$ and t ; $\omega_{it+\Delta t}$ and ω_{it} are the angular velocities of particle i at time $t + \Delta t$. The displacements of all single particles are evaluated and updated as follows:

$$u_{it+\Delta t} = u_{it} + u_{it} \Delta t \quad (\text{Eq. 1.28})$$

$$\varphi_{it+\Delta t} = \varphi_{it} + \varphi_{it} \Delta t \quad (\text{Eq. 1.29})$$

Where $u_{it+\Delta t}$ and u_{it} are the translational displacement of particle i at time $t + \Delta t$ and t ; $\varphi_{it+\Delta t}$ and φ_{it} are the angular displacement of particle i at time $t + \Delta t$. As we can see, the velocity, acceleration and displacement are combined with time step (Δt). DEM modeling assumes that, in a calculated time step, the force received by the particle is constant, i.e., the acceleration is constant. The time step is fixed and remains constant throughout the simulation.

Chapter 1: Literature Review

When using a simulation with a range of particle sizes, the Rayleigh time step is calculated based on the smallest particle size. The Rayleigh time step (ΔT) can be calculated [287, 288]:

$$\Delta T = \pi \left(\frac{R}{0.163\nu + 0.877} \sqrt{\frac{G}{\rho}} \right) \quad (\text{Eq. 1.30})$$

Where R is the particle radius; G is shear modulus of particle; ρ is solid density of particle; ν is Poisson ratio of particle.

1.7.4.2 Summary of equations involved in these two models

As analyzed above, the particle motions and interaction will be calculated by forces, energies, velocities etc., the equations get involved in this study are summarized in table 1.10.

Table 1.10 Summary of equations get involved in these two models

Parameters	Definitions	Equations
Rayleigh time-step (ΔT)	The Rayleigh time step is the time taken for a shear wave to propagate through a solid particle Rayleigh wave method is using for calculation.	$\Delta T \approx (0.1 \sim 0.5)t_{\text{rayleigh}} = \pi \left(\frac{R}{0.163\nu + 0.877} \sqrt{\frac{\rho}{G}} \right)$ R is radius of particle; ν is Poisson's ratio of particle ; ρ is the solid density of particle; G is the shear modulus of particle.
Overlap (δ)	When two particles collide in physical, there is an area or range in common for, which is named by overlap.	$\delta = R_i + R_j - d$ R_i and R_j are the radius of particle i and j , respectively; and d is the distance between the centers of particle i and j .
Normal contact force ($F_{n,ij}$)	The normal contact force describes the interparticle force acting at the contact point. The normal contact force is supposed to contribute to the translational motions of particles.	$F_{n,ij} = \frac{4}{3}E^*(R^*)^{1/2}\delta_n^{3/2}$ (Hertz-Mindlin (no slip) model); $F_{n,ij} = -4\sqrt{\pi\gamma E^*}a^{3/2} + \frac{4E^*}{3R^*}a^3$ (when the Hertz-Mindlin + JKR contact model is applied.
Equivalent Young's modulus (E^*)	When two particles are in contact and deformation occurs, a new area will be formed, the young's modulus of this new area is named by equivalent young's modulus.	$\frac{1}{E^*} = \frac{1 - \nu_i^2}{E_i} + \frac{1 - \nu_j^2}{E_j}$ E_i, ν_i and E_j, ν_j are the two sphere young's modulus and Poisson's ratio.
Equivalent radius (R^*)	When two particles are in contact and deformation occurs, a new area will be formed, the radius of this new area is named by equivalent radius.	$R^* = \frac{1}{\left(\frac{1}{R_i} + \frac{1}{R_j}\right)}$
Contact area (a)	When two particles are in contact and deform, this contact and deformed area is called contact area, it is assumed to be circular.	$a = \sqrt{\delta R^*}$
Tangential contact force	The tangential colliding force facilitate the rotational motions of particles.	$F_{t,ij} = -K_t \delta_t$

Chapter 1: Literature Review

$(F_{i,j})$		δ_t is the tangential overlap between the contacting particle i and j ; K_t is the tangential spring constant.
Normal overlap (δ_n)	The overlap in the normal direction is defined as the normal overlap	$\delta_n = \frac{a^2}{R^*} - \left(\frac{4\pi\gamma a}{E^*}\right)^{1/2}$ when the Hertz-Mindlin + JKR contact model is applied.
Number of collisions ($N_{collision}$)	When two particles collide, it will count as one collision, no matter how long the particles stay in contact, only the completed collisions are counted.	
Number of contacts ($N_{contact}$)	The total number of contacts of particle-particle are the impacts occurring between all particles at data write-out points. In other words, the contact is in progress when the write-out takes place.	
Translational velocity (v)	The translational velocity is defined as the rate of change in displacement.	$v_{it+\Delta t} = v_{it} + \left(\frac{dv_i}{dt}\Delta t\right)$ $v_{it+\Delta t}$ and v_{it} are the translational velocities of particle i at time $t + \Delta t$ and t
Angular velocity (ω)	Angular velocity refers to how fast an object rotates or revolves relative to another point,	$\omega_{it+\Delta t} = \omega_{it} + \left(\frac{d\omega_i}{dt}\Delta t\right)$ $\omega_{it+\Delta t}$ and ω_{it} are the angular velocities of particle i at time $t + \Delta t$
Collision frequency (f_n)	Collision numbers per particle per second is defined as the collision frequency	It is given by $f_n = \frac{N_{collision}}{N_0 T}$, Where the $N_{collision}$ is the accumulative collision numbers during the simulation period time T , N_0 is the total simulated number.
Total force (F_i)	The total force and torque acting on a solid particle mainly includes: F_{ij}^c is the contact force acting on particle i by its contacting particle j or walls; F_{ik}^{nc} is the non- contact force (including van der Waals force, liquid bridge force and electrostatic force) acting on particle i .	$\sum F_i = \sum_j F_{ij}^c + \sum_k F_{ik}^{nc} + F_i^f + F_i^g$ F_i^f is the particle fluid interaction force acting on particle i ; F_i^g is the gravity(g) force acting on particle i ($F_i^g = m_i g$, m_i is the mass of particle i , g is the gravitational acceleration, which equal to 9.81m/s^2)
Cohesive force ($F_{cohesive}$)	Cohesive force is the behavior or nature of molecules that exert intermolecular forces on each other, it belongs to non-contact force.	$F_{cohesive} = -\frac{3}{2}\pi\gamma R^*$ γ is the surface energy

As it can be seen, when the Hertz-Mindlin + JKR cohesive model is applied, the surface energy is necessary to calculate the normal force and cohesive force.

1.7.4.3 Surface energy

Surface energy of particles is important in many application areas ^[289]. The surface energy of a solid predicts how a coating formulation spreads on it. Interactions between solid is important as they determine the adhesion between the two phases. Johnson ^[290] concluded that mechanical work must be expended to overcome the adhesive forces to separate bodies in intimate contact. The surface energy of a solid is defined as the change of the total surface energy (γ) per surface area (S) at constant temperature (T), pressure (P) and moles (n) ^[291, 292].

$$\gamma_s = (\delta\gamma/\delta S)_{T,P,n} \quad (Eq. 1.31)$$

In term of liquids, the surface area will be different under the above conditions. However, for solids, the surface area cannot be changed, generally, because changing the surface area needs to against the elastic forces [291].

Wetting has traditionally been the standard approach for studying the energy of a solid surface. It is agreed that the measurement of contact angle on a given solid is the most practical way to get the surface energy of the solid [293-297]. It was proposed nearly 200 year ago. The theory of the contact angle of pure liquids on a solid is expressed by young's equation [290, 292, 293, 298, 299]:

$$\gamma_s = \gamma_{sl} + \gamma_l \cos \theta_1 \quad (Eq. 1.32)$$

Where γ_l is the experimentally determined surface tension of the liquid, θ_1 is the contact angle, γ_s is the surface energy of the solid, γ_{sl} is the interfacial surface between the liquid and solid.

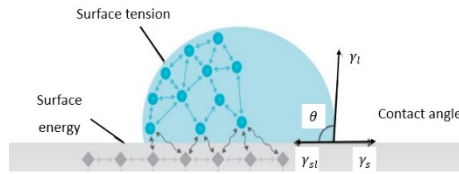


Fig.1.34 Schematic depicting the interfaces of a liquid droplet on a solid surface [300].

As Eq.1.32 indicates that the surface energy of a solid depends on the interfacial surface γ_{sl} and γ_l and contact angle θ . The interfacial surface relationship is given by Girifalco and Good [301] by follows:

$$\gamma_{sl} = \gamma_s + \gamma_l - 2(\gamma_s\gamma_l)^{0.5} \quad (Eq. 1.33)$$

Where γ_s is the solid surface energy, γ_l is the liquid surface energy.

Fowkes et al. [302, 303] proposed an approach to estimate the solid or liquid surface energy. In his proposal, the surface energy is separated into different component's energy:

$$\gamma_s = \gamma^d + \gamma^p + \gamma^i \quad (Eq. 1.34)$$

Where γ^d is the dispersion component, γ^p is the polar, γ^i is the dipole. The polar γ^p also is called (acid/base). Kaeble et al. [304] treated polar interactions as one type of force also defined by a geometric mean relationship. The interfacial surface γ_{sl} must be lower than the sum of two individual surface tensions.

$$\gamma_{sl} = \gamma_s + \gamma_l - 2(\gamma_s^d \gamma_l^d)^{0.5} - 2(\gamma_s^p \gamma_l^p)^{0.5} \quad (Eq.1.35)$$

Where γ_s^d is the polar energy of solid, γ_l^d is the polar energy of liquid, γ_s^p is the dipole energy of solid, γ_l^p is the dipole energy of liquid.

In DEM modeling, the interfacial energy of particles originally proposed by Johnson et al.^[290]. As they proved that it is possible to correlate the interfacial surface energy with surface wettability by using young's equation. Therefore, in the JKR cohesion contact model, the surface energy is the work that has to be done to separate two contact particles i and j . This energy is referred to as the work of adhesion W_{ij} ^[305]. For the same particles ($i = j$), W_{ij} becomes the work of adhesion W_{ii} , that is

$$\gamma_i = \frac{1}{2} W_{ii} \quad (Eq.1.36)$$

For different particles, especially solid particles, the interfacial energy is evaluated by combining two particles work of adhesion,^[222, 305] as follows:

$$W_{ij} \approx \sqrt{W_{ii}^d W_{jj}^d} \approx 2 \sqrt{\gamma_{s,i}^d \gamma_{s,j}^d} \quad (Eq.1.37)$$

Then the interfacial energy of two different solid particles can be expressed :

$$\gamma_{s,i,j} = \gamma_{s,i} + \gamma_{s,j} - 2(\gamma_{s,i}^d \gamma_{s,j}^d)^{0.5} \quad (Eq.1.38)$$

This approach is consistent with the general method of calculating the Hamaker coefficient of dissimilar interacting bodies^[306]

$$W_a = 2\gamma = \frac{A}{12\pi D_{min}^2} \quad (Eq. 1.39)$$

W_a is the work to need to separate two adhered surfaces, D_{min} is the minimum separation distance. This equation indicates that the surface energy is related to Hamaker constant and minimum separation distance. In DEM simulation, the minimum separation distance is taken into account in the calculation of van der Waals force. This minimum separation distance is named by cut-off distance^[188]. In several DEM modeling studied^[267, 271, 272, 307] the cut-off distance is determined within the range of 0.1-1.0 nm.

Tamadondar et al.^[222] investigated the effect of particle interface energies and mixing energy on the macroscopic behavior of the dry-coating process by using the JKR model in a Couette shear cell. The cell was first filled with 200 host particles (D-Mannitol) with a 100 μm diameter, and 10000 of 100 fine particles (lactose monohydrate) with a 5 μm diameter. Different cases were devised and simulated to study

the effect of particle interfacial energies as well as impeller speed. The interfacial energy was calculated by equations 1.37-1.39. The study demonstrated that interfacial energy plays a key role in the formation and breakage of agglomerates and in controlling the adhesion of fines to a carrier's surface.

Duy et al. [229] used the JKR model to examine the breakage and capturing behavior of loose fine-particle agglomerates on impact with a target particle. The loose agglomerate was made of 10000 spherical elastic particles of 5 μm diameter with physical properties corresponding to lactose monohydrate. Host particle was a spherical particle with physical properties corresponding to D-Mannitol with a diameter 200 μm . The interfacial energy was given by equation 1.39. To study the effects of the impact parameters, the agglomerate was guided to collide with the mannitol particle at different velocities. The study indicated that velocity is a significant parameter for adhesion, because velocity of particle governs the collision.

Roberto et al. [236] studied the influence of interparticle cohesion on the energy propagated and dissipated in agglomerates during impact against a rigid target. The agglomerate impact was simulated using the JKR model. Four spherical agglomerates are made of 3000 spherical elastic particles, every 100 μm in diameter and with physical properties that approximately correspond to glass beads. The only differences between the agglomerates arise from the differences in values of surface energy that have been used. These values are 0.5, 3.5, 20 and 35 J/m^2 . Briefly, the 3000 particles that form the final agglomerates were randomly positioned within a prescribed spherical space. Particle motion was initiated by a centripetal force that brought all the particles together. The study indicated that the energy required to break the interparticle contacts is less than 10% of the total energy dissipated by the agglomerates during impact.

Sohan et al. [225] used the JKR model to probe the stability and mechanical properties of adhesive units during binary head on collisions as a function of the number of adhered fine particles, the initial collision velocity, and the surface energy between the particles. Fines and hosts were modeled as elastic spheres of 3 and 100 μm . Various combinations of surface energies ranging between 0.01 and 0.05 J/m^2 were investigated. Fifteen different velocities ranging from 0.04 m/s to 1.7 m/s were studied. The study revealed that the integrity of adhesive units following binary impacts was most strongly influenced by the surface energy.

Yang et al. [224] reported DEM analysis to provide insights into the attachment process during mixing. The impact between two spheres is analyzed to establish a criterion for determining whether two particles will attach or rebound during an impact. Besides, the adhesive interaction between active pharmaceutical ingredient (API) particles and a large carrier particle in a vibrating container is analyzed and the effects of vibration conditions are examined. All the carrier and API particles are spherical particles. The diameter

of the carrier particle and API particles are 70 and 5 μm , respectively. The interfacial surface energy between two particles was studied between 0.044–4.4 J/m^2 . The study demonstrated that the velocity is very important for understanding the macroscopic behavior of dry powder inhalers (DPI) formulations and provides science-based guidance for DPI formulation design. Moreover, it shows that the velocity increases with increasing work of adhesion and decreasing particle radius.

It is found that the JKR model is generally considered to be an appropriate model for modeling adhesive mixtures. Accordingly, velocity and surface energy are two critical parameters for studying the coating process. However, the effect of material properties, e.g. material hardness and plasticity, size of guest and host, on adhesion behavior should be investigated to obtain a better understanding of dry particle coating [229].

1.8 Objectives of the thesis

The goal of this study is to propose a new methodology to prepare catalyst supports for the methanation reaction. In particular, a mechanical method – dry particle coating – was used to prepare the new supports. Dry particle coating is considered to be an environmentally-friendly and low-cost technique. Meanwhile, it's crucial to understand the mechanism of the dry coating process, the factors that affect coating performance, the evaluation of coating quality, the scale-up production as well as the exploration of novel application fields.

This work consists of 3 main parts:

1. Study and Analysis of nanopowder

In this work, the method for the preparation of new catalyst supports consists in coating large $\gamma\text{-Al}_2\text{O}_3$ and S.S316L particles with nanoparticles of TiO_2 , SiO_2 , and Zeolite. However, these powders (TiO_2 , SiO_2 , and Zeolite) are very cohesive and form agglomerates with uncontrollable sizes, the nanometric scale of the powders poses a major problem in the accuracy of size measurements. The coating process requires knowledge of the size of the primary particles and not of the agglomerates! This will allow the best calculation of the powder layer with the primary particles and not of the agglomerates. Therefore, analyze the size of nanoparticles is the most important task.

2. Preparation of new supports

When the analysis of nanopowder is done, preparation of new supports by mechanical energy or solvent-free is arranged. The basic principle of dry particle coating process is mixing particles under the mechanical force (impact/compression/shearing force). Host particle: γ -Al₂O₃ and S.S316L have an average diameter of around 67 μ m and 98.3 μ m will be used as host particles to prepare new supports.

Guest particles: TiO₂, SiO₂, and Zeolite with nanosize will be used to coat on the surface of γ -Al₂O₃ and S.S316L to prepare the new supports (such as TiO₂/ γ -Al₂O₃, SiO₂/ γ -Al₂O₃, zeolite/ γ -Al₂O₃, TiO₂/S.S316L, SiO₂/S.S316L, and zeolite/S.S316L).

3. DEM modeling

Considering that dry particle coating is driven by mechanical forces, it depends on particle motions and particle-geometry interactions ^[223]. Directly observing the interactions between particles and geometry is very difficult so far. As a result of the experimental work on dry coating and the preparation of supports and catalysts, many questions have arisen about the phenomena of collision and adhesion of the particles in the picomix, as well as the variation of the different forces applied to the particle surfaces and the particle velocities. Similarly, the impact of operating conditions plays a very important role, such as the physical and mechanical properties of the particles, the speed of rotation and coating time in the picomix. Work and analysis by numerical modeling (Discrete element method: DEM) seem indispensable in this work. This numerical modeling work will allow us to answer and explain the phenomena and coating mode.

Chapter 2: Experiments and Materials

2.1 Introduction

This study aims to prepare new solvent-free (dry process), or by mechanochemistry, catalysts for the methanation reaction. Five supports have been classified for the preparation of catalysts, γ -Al₂O₃, S.S316L (Stainless steel), SiO₂, TiO₂ (Anatase titania), and Zeolite (Beta-zeolite) (see table 2.1). S.S316L and γ -Al₂O₃ have an average diameter of around 98 μ m and 67 μ m, ideal size for supports and the preparation of catalysts. However, the other three supports (Zeolite, TiO₂, and SiO₂) have extremely small diameters. Thus, several processes (granulation, pelletizing, and atomization) were applied to obtain larger diameters around 80 μ m. But the agglomerates obtained were very brittle and break quickly. In such cases, a solution had to be found to obtain SiO₂, TiO₂ and Zeolite supports with a diameter around 80 μ m and with high stability and hardness. To solve this problem, a new approach to the preparation of the supports for SiO₂, TiO₂ and Zeolite has been implemented. The new preparation consists of using S.S316L and γ -Al₂O₃ as the support core and coating the fine particles of SiO₂, TiO₂, and Zeolite to form new support as shown in figure 2.1: SiO₂/ γ -Al₂O₃, TiO₂/ γ -Al₂O₃, Zeolite/ γ -Al₂O₃, SiO₂/S.S316L, TiO₂/S.S316L and Zeolite/S.S316L.

The Picomix was used in the coating process. It is a solvent-free process and the adhesion of fine particles to the coarse particles is achieved by adhesion (roughness) and interactions of van der Waals' forces. The coating operations are conducted in the picomix process and the operating conditions including rotation speed 3500 rpm, processing time 5 min, and filling ratio 40% (total powder is 40% of volume of the 100 mL vessel of picomix). The density of all materials (γ -Al₂O₃, S.S316L, SiO₂, TiO₂, and Zeolite) was measured via a density test (see paragraph 2.3.2), because the density is one of the important parameters, it was used to calculate the mass of guest and host particles (see equation 2.2). All of the materials and prepared new supports were characterized by particle size (Mastersizer 3000, paragraph 2.3.1.1) and morphological properties (SEM, paragraph 2.3.3). The size of three nanoparticles TiO₂, SiO₂, and Zeolite were analyzed by five different methods, LD (laser diffraction, paragraph 2.3.1.1), TEM (Transmission electron microscope, paragraph 2.3.1.2), DLS (dynamic light scattering, paragraph 2.3.1.3), SAXS (small-angle X-ray scattering, paragraph 2.3.1.4), and BET specific surface area (paragraph 2.3.1.5).

2.2 Materials and methodology

2.2.1 Materials

All used commercially available materials (γ -Al₂O₃, S.S316L, SiO₂, TiO₂, and Zeolite) are summarized and listed in table 2.1. In order to avoid the influence of small particles of the host particles on the experimental results, the host particle of γ -Al₂O₃ was sieved at 63-90 μ m and S.S316L was sieved above 63 μ m to prepare the new support.

Table 2.1 The list of commercially available materials used in this study

Power	Component	Purity	Supplier
Alumina (Scca-5/170)	γ -Al ₂ O ₃	$\geq 99\%$	Sasol-Germany
Anatase titania	TiO ₂	$\geq 99.5\%$	Sigma-Aldrich
Silica	SiO ₂	$\geq 99\%$	Fuji Silysia Chemical Ltd. Japan
Zeolite (CP814E*)	Beta-zeolite		Zeolyst
Stainless steel 316L	Fe, Cr (main component, others are C, Ni, Si, O, N etc.)		Höganäs

2.2.2 Supports preparation

The news supports SiO₂/ γ -Al₂O₃, TiO₂/ γ -Al₂O₃, Zeolite/ γ -Al₂O₃, SiO₂/S.S316L, TiO₂/S.S316L, and Zeolite/S.S316L were prepared via dry particle coating process. The detailed preparation procedures and relevant involved device and relevant information will be displayed in this section.

2.2.2.1 New supports preparation

γ -Al₂O₃ and S.S316L have an average diameter of around 67 μ m and 98 μ m, the size of three nanopowder TiO₂, SiO₂, and Zeolite will be listed in Chapter 3.

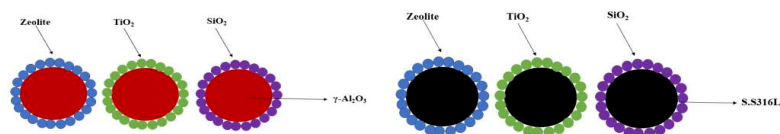


Fig. 2.1. Images of new supports: left (γ -Al₂O₃ as a core shell, Zeolite, TiO₂, and SiO₂ are coated), and right (S.S316L as a core shell, Zeolite, TiO₂, and SiO₂ are coated).

Chapter 2: Experiments and Materials

γ -Al₂O₃ and S.S316L were used as host particles to coat with the fine particles of SiO₂, TiO₂, and Zeolite to form the new supports under 3500 rpm and 5 mins, filling ratio was set at 40% of vessel volume (40 mL of powders were added into the 100 mL vessel, which means total powders of host and guest are 40 mL). The exact grams of host and guest were determined by the calculation (see table 2.2). As shown in figure 2.1: SiO₂/ γ -Al₂O₃, TiO₂/ γ -Al₂O₃, Zeolite/ γ -Al₂O₃, SiO₂/S.S316L, TiO₂/S.S316L, and Zeolite/S.S316L.

Table 2.2 List of particles new supports prepared in this work by dry particle coating.

New supports	Host particles	Guest particles	Mass of particles (g) in Picomix		Preparation conditions
			Host particles	Guest particle	
TiO ₂ ^{LD} / γ -Al ₂ O ₃	γ -Al ₂ O ₃	TiO ₂ ^{LD}	24.56	5.09	Rotation speed: 3500 rpm; Processing time: 5 min; Filling ratio: 40%.
TiO ₂ ^{DLS} / γ -Al ₂ O ₃		TiO ₂ ^{DLS}		0.19	
TiO ₂ ^{TEM} / γ -Al ₂ O ₃		TiO ₂ ^{TEM}		0.05	
SiO ₂ ^{LD} / γ -Al ₂ O ₃		SiO ₂ ^{LD}		0.45	
SiO ₂ ^{DLS} / γ -Al ₂ O ₃		SiO ₂ ^{DLS}		0.11	
SiO ₂ ^{TEM} / γ -Al ₂ O ₃		SiO ₂ ^{TEM}		0.09	
Zeolite ^{LD} / γ -Al ₂ O ₃		Zeolite ^{LD}		6.32	
Zeolite ^{DLS} / γ -Al ₂ O ₃		Zeolite ^{DLS}		0.19	
Zeolite ^{TEM} / γ -Al ₂ O ₃		Zeolite ^{TEM}		0.01	
TiO ₂ ^{LD} /S.S316L	S.S316L	TiO ₂ ^{LD}	136.46	9.14	Rotation speed: 3500 rpm; Processing time: 5 min; Filling ratio: 40%.
TiO ₂ ^{DLS} /S.S316L		TiO ₂ ^{DLS}		0.35	
TiO ₂ ^{TEM} /S.S316L		TiO ₂ ^{TEM}		0.09	
SiO ₂ ^{LD} /S.S316L		SiO ₂ ^{LD}		0.82	
SiO ₂ ^{DLS} /S.S316L		SiO ₂ ^{DLS}		0.20	
SiO ₂ ^{TEM} /S.S316L		SiO ₂ ^{TEM}		0.02	
Zeolite ^{LD} /S.S316L		Zeolite ^{LD}		11.02	
Zeolite ^{DLS} /S.S316L		Zeolite ^{DLS}		0.35	
Zeolite ^{TEM} /S.S316L		Zeolite ^{TEM}		0.02	

The mass of guest particles of TiO₂, SiO₂, and Zeolite were mixed with host particles of γ -Al₂O₃ or S.S316L under 3500 rpm, 5 min, and filling ratio 40% in picomix to prepare new supports. Table 2.2

summarizes the mass of host and guest that have been used in this study. The size of three nanoparticles TiO_2 , SiO_2 , and Zeolite were analyzed by three different methods, LD (Laser Diffraction), TEM (Transmission Electron Microscope), DLS (Dynamic Light Scattering). The materials with size analyzed by the 3 methods were labeled respectively: Zeolite^{LD}, Zeolite^{DLS}, Zeolite^{TEM}, TiO_2^{LD} , $\text{TiO}_2^{\text{DLS}}$, $\text{TiO}_2^{\text{TEM}}$, SiO_2^{LD} , $\text{SiO}_2^{\text{DLS}}$, and $\text{SiO}_2^{\text{TEM}}$ (the details of the analyses are presented in the paragraph 2.3 and results in chapter 3).

2.2.2.2 Picomix (high shearing mixer)

During the preparation of the supports a small capacity, 100 mL, high shearing mixer Picomix (Hosokawa Micron B.V, see Figure 2.2) was applied to study the dry particle coating process. The Picomix offers very fast mixing with a full discharge without loss of material. The Picomix consists of an LCD touch screen, a stainless-steel conical agitator vessel, and a rotor that has three pairs of angled paddles. The angle between the paddles and the horizontal plane is 60° , clearance gap between the wall of the vessel and paddles is 1.3 ± 0.3 mm (more dimensions can be seen from the figure 2.2). These three pairs of paddles play different roles in the mixing process. The paddle in the bottom of the vessel is mainly responsible for the act of mixing (the distance between the bottom to this paddle is 1 mm); the middle paddle gives shearing/impacting force to advance adhesion of the guest particles onto the host particles; the main job of the top paddle is to break up the agglomerated particles and turn them into individual particles. High-speed rotation of the paddles creates a centrifugal force and moves the particles from the bottom to the wall of the vessel.

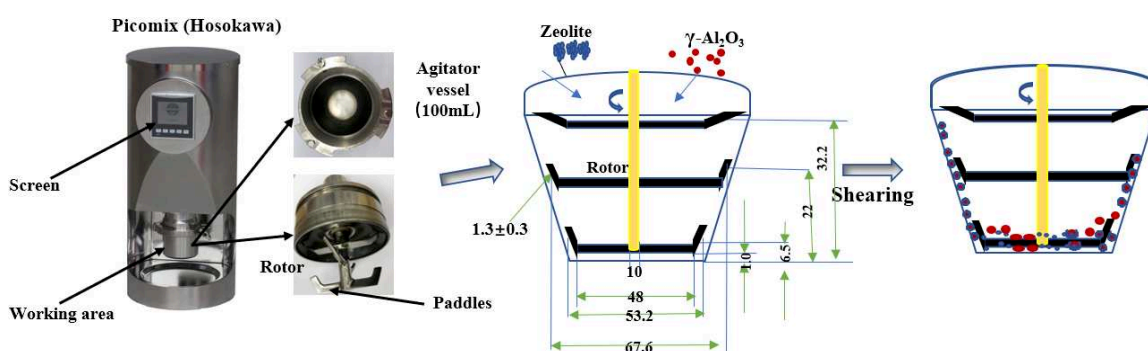


Fig. 2.2 High shearing mixer-Picomix ^[101, 104] (*The unit of the dimension in this figure is mm).

During the mixing process, fine particles and host particles interact and collide under the high shearing/impacting force between the particles and the wall. The working volume of the picomix is from

25 mL to 100 mL, the rotation speed can reach up to 6000 rpm. The working time and rotation speed can be controlled by the LCD touch screen.

The rotating mixing element is arranged in a conical agitator vessel. As a result of the special geometry of the mixing element and the high shear speed, an intensive but homogeneous and fast blending of the powder components takes place. After filling the powder components into the agitator vessel, the machine is then closed. Once the mixing process is completed, the vessel is removed from the machine and the mixture is emptied out. The mixing efficiency is regulated by the rotor speed, the mixing time, and the degree of filling.

2.2.2.3 Coating layer calculation

In this study, calculating the coating layer, i.e. the number of particles needed to coat the host particle to form a monolayer is very important. The percentage by mass of guest particles used in the coating experiment was calculated based on the assumption of 100% surface coverage of the host particles with a monolayer of guest particles. It was assumed that all guest particles are of the same size, both host and guest particles are spherical, and that the host and guest particles do not deform during the coating process. Based on these assumptions, the number of guest particles for monolayer coating can be seen as the following equations: ^[101, 105, 308]

$$N = \frac{4(D_{host} + D_{guest})^2}{D_{guest}^2} \quad (Eq. 2.1)$$

Respective D_{host} , D_{guest} (in this work we used the mean diameter $dp_{(3,2)}$) are the diameter of host and guest particles; N is the number of guest particles per host particle.

After obtaining how many guest particles are needed to coat one host particle, in the experiment, it requires the mass of the guest, equation 2.2 is used to calculate the mass fraction of the guest particles, $w\%$.

$$w\% = \frac{ND_{guest}^3 \rho_{guest}}{(D_{host}^3 \rho_{host}) + (ND_{guest}^3 \rho_{guest})} \times 100\% \quad (Eq. 2.2)$$

Respective densities of host particles and guest particles ρ_{host} , ρ_{guest} ; Equation 2.1 and 2.2 were used to calculate the mass of guest in this study, the calculated results have been shown in table 2.2.

2.3 Characterization methods

The prepared new supports $\text{SiO}_2/\gamma\text{-Al}_2\text{O}_3$, $\text{TiO}_2/\gamma\text{-Al}_2\text{O}_3$, Zeolite/ $\gamma\text{-Al}_2\text{O}_3$, $\text{SiO}_2/\text{S.S316L}$, $\text{TiO}_2/\text{S.S316L}$, and Zeolite/ S.S316L were analyzed by a physical way via size distribution, and the surface morphologies were measured with a scanning electron microscope. For three (TiO_2 , SiO_2 , and Zeolite) nanopowder, different devices/measurements were used to analyze their size and will be described in the following sections.

2.3.1. The characterization methods for nanopowder

In this study, TiO_2 , SiO_2 , and Zeolite are nanoparticles, which means always accompanied by agglomeration. Agglomeration is a size enlargement process in which primary particles stick together to form agglomerates because of adhesion force, such as electrostatic force and van der Waals' force. Uncontrollable agglomeration makes it very difficult to analyze the size of nanoparticles because the ideal analysis method is to analyze the size of particles one by one.

As described in Chapter 1, paragraph 1.5.4, each technique has strengths and limitations depending on the type of sample, the state of dispersion, and the particle size range. Generally, each technique measures a different property that is used to infer size; therefore, direct inter-comparison of size values is less desirable as it may introduce errors due to conversion, different sample preparation, etc. In addition, the distribution range can vary drastically depending on the instrument configuration, sample type, and preparation procedure, as well as measurement artifacts. Five techniques were used in this experiment to measure the size of nanomaterials, and they are respectively: LD, TEM, DLS, SAXS, BET surface area.

2.3.1.1 Laser Diffraction analysis (LD)

$\gamma\text{-Al}_2\text{O}_3$, S.S316L , SiO_2 , TiO_2 , and Zeolite used in this study have had their sizes measured by using Mastersizer 3000 (Malvern Ltd., UK) equipped with Hydro LV (600 mL volume) (see figure 2.3). It provides 0-3500 rpm and ultrasonic energy to ensure the uniformity of particle dispersion. The Mastersizer 3000 uses the technique of laser diffraction/diffusion to measure particle size distributions from 10 nm up to 3.5 mm.

In a laser diffraction/diffusion measurement, a laser beam passes through a dispersed particulate sample and the angular variation in the intensity of the scattered light is measured. Large particles scatter light at

small angles relative to the laser beam and small particles scatter light at large angles. The angular scattering intensity data is then analyzed to calculate the size of the particles that created the scattering pattern using the Mie theory of light scattering. The particle size is reported as a volume equivalent sphere diameter. The Mastersizer 3000 uses a sequential combination of measurements with red and blue light sources to measure across the entire particle size range. Measurement of large particulates is provided by an advanced focal plane detector design able to resolve very small diffraction angles. Sensitivity to sub 100 nm particles, scattering light at wide angles is achieved using advanced optics and a powerful 10 mW solid-state blue light source.

The measurement procedure is as follows: Firstly, dispersed the samples in the water, for this, a volumetric flask with the capability of 50 mL was used. Secondly, manually shook the volumetric flask until the powder dispersed uniformly. Thirdly, the samples were poured into the Hydro LV and started to test. For each measurement, 2500 rpm rotation speed with demineralized water (DW) was conducted. In order to check the stability of the results, each sample was tested 6 times, 3 times without ultrasonic and 3 times with 10 s and 30% ultrasonic.

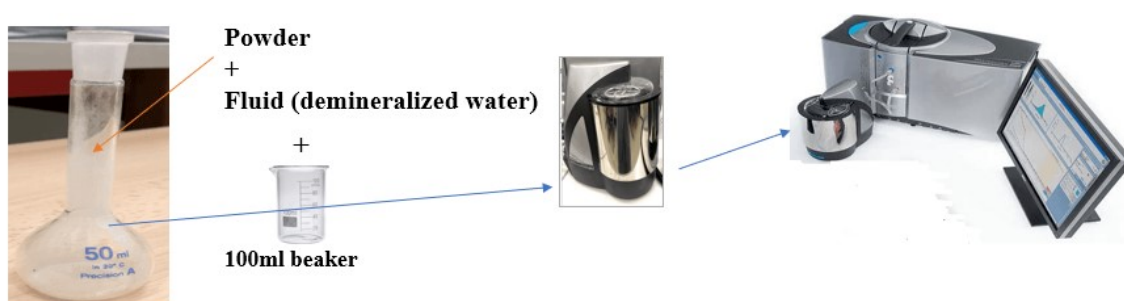


Fig.2.3 Mastersizer 3000 particle size analyzer (Malvern Ltd., UK) and analyzing process.

The particle refractive index (RI) and particle absorption index (AI) got involved for measuring (selected from the system database) are listed in table 2.3. The absorption indexes were selected to take into account materials that were completely transparent (absorption index equal to 0), completely absorbing (absorption index equal to 1), and intermediate values of 0.01 and 0.1. For the prepared new supports, theoretically, we should choose RI and AI of the guest material in the measurement. However, since the coating is very thin, its mass is very small, therefore during the measurement, the RI and AI of the host particles were chosen to complete the analysis.

The LD measurement, the size of the particle that has the same energy diffracted or scattered by the laser.

Chapter 2: Experiments and Materials

The LD measurements obtained is the size distribution volume% with d_i , what we need is the mean diameter ($dp_{(3,2)}$). According to the definition of “volume-surface” can obtain the mean diameter ($dp_{(3,2)}$) of the powders [309]:

$$dp_{(3,2)} = \frac{\sum N_i d_i^3}{\sum N_i d_i^2} \quad (Eq.2.3)$$

Here N_i is the number of particles in class i , and d_i is the average dimension of the particle in this class.

Table 2.3 The RI and AI of different materials.

Materials	Refractive index	Absorption index	Operation conditions
γ -Al ₂ O ₃	1.766	0.01	Shaking + a 2500 rpm in rotation speed with demineralized H ₂ O was used to provide the calibration and baseline determination; 3 times without ultrasonic; 3 times with 10s and 30% ultrasonic.
S.S316L	2.757	1	
TiO ₂	2.7	0.01	
SiO ₂	1.45	0.01	
Zeolite	1.446	0.01	
SiO ₂ / γ -Al ₂ O ₃ , TiO ₂ / γ -Al ₂ O ₃ , and Zeolite/ γ -Al ₂ O ₃	1.766	0.01	
SiO ₂ /S.S316L, TiO ₂ /S.S316L, and Zeolite/S.S316L	2.757	1	

Note: Refractive index of water: 1.33.

Three nanopowder (TiO₂, SiO₂, and Zeolite) were dispersed in a flask with demineralized water to which was added 0.5% of sodium pyrophosphate decahydrate (99% purity) as dispersant.

2.3.1.2 Transmission electron microscope (TEM)

Transmission electron microscope (TEM, see Figure 2.4) was used to get the images of three nanopowder (SiO₂, TiO₂ and Zeolite) and then ImageJ was used to calculate the mean diameter ($dp_{(3,2)}$) of nanopowder. The principle of TEM is: high-energy electrons (usually is 50-200 KeV) penetrating the sample, depending on the electron transmission intensity at different locations of the sample, different diffraction direction of electron through crystal sample is different. After enlarging the rear electromagnetic lens, the image is displayed on the fluorescent screen. The TEM resolution is 0.3 nm and the lattice resolution is 0.1-0.2 nm. The samples can be tested on a copper network with a diameter of 2-3 mm. To measure the particle size by transmission electron microscopy, we should first take as many representative morphological images of nanoparticles as possible, and then measure the particle size by software ImageJ.

The procedure of sample preparation is as follows:

Put the powders and ethanol in a small beaker, stirring by ultrasound for 10~30 min; then, suck the mixture of powder and ethanol with a glass capillary, put 2~3 drops of the mixture on a micro grid; finally wait more than 15 min to allow the ethanol to evaporate; load the sample on the stage and insert it into the TEM to perform the measurement.

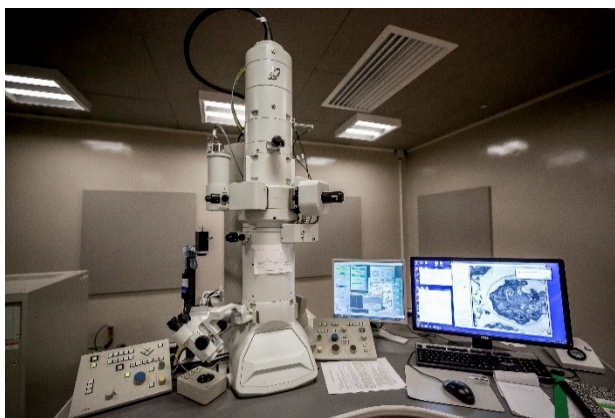


Fig. 2.4 Transmission electron microscope (TEM).

To determine the size distribution and the mean diameter ($dp_{(3,2)}$), the Image J software was carried out in this investigation. For each particle, 20 images were used to select the clear and visible surface area. the number of selected surface areas respectively, are SiO₂ - 192, Zeolite - 237, and TiO₂ - 296. For each particle, the diameter of the surface area was calculated by $S = \pi * (d_i/2)^2$, then $d_i = (4S/\pi)^{0.5}$, where S is the surface area, d_i is the diameter of the selected surface area. By the TEM images can obtain the number of the particle (N_i) and the number of fractions ($N_i\%$), but we need the volume fraction ($V_{fi}\%$) for drawing size distribution graph. For this then divide the size into different classifications, count the number belongs to the different classifications. The total volume (V_{total}) of particle $V_{total} = \sum_{i=0}^N N_i * V_{fi}$ that is $V_{total} = \sum_{i=0}^N N_i * (\pi d_i^3)/6$. Therefore, the volume fraction ($V_{fi}\%$) can be expressed $V_{fi}\% = V_{fi}/V_{total}$.

In this calculation, we assumed that the surface area of the selected two-dimensional equals the three-dimensional area of this particle. The mean diameter ($dp_{(3,2)}$) of particles was calculated by equation 2.3. The information on this method is summarized in table 2.4.

Chapter 2: Experiments and Materials

Table 2.4 Detailed information about this method

Powders	Number: Selected surface areas	Diameter (d_i) of selected surface area	The mean diameter ($dp_{(3,2)}$) of particles	For each particle, 20 images were used to select the clear and visible surface area
SiO ₂	192	$d_i = (4S/\pi)^{0.5}$ S is the surface area	$dp_{(3,2)} = \frac{\sum N_i d_i^3}{\sum N_i d_i^2}$	
Zeolite	237		N_i is the number of particles in class i , and d_i is the average dimension of the particle in this class.	
TiO ₂	296			

Therefore, the clear and visible particles were selected and used ImageJ to calculate the size of the selected surface area to obtain a relatively accurate value.

Basic operating steps are as follows (an example as shown in figure 2.5): firstly, open the TEM image, secondly, set known distance which is in the left bottom of the image (e.g., 20 nm), select surface area (see figure 2.5a) to analyze. The results show in figure 2.5b (selected 4 surface areas). The area is the surface area that was selected, here the mean stands for average diameter, as it can be seen, here it displays the minimum and maximum of the diameter because the area shown in figure 2.5a is not the complete circle area. Feret's diameter is the longest distance between any two points along the selection boundary.

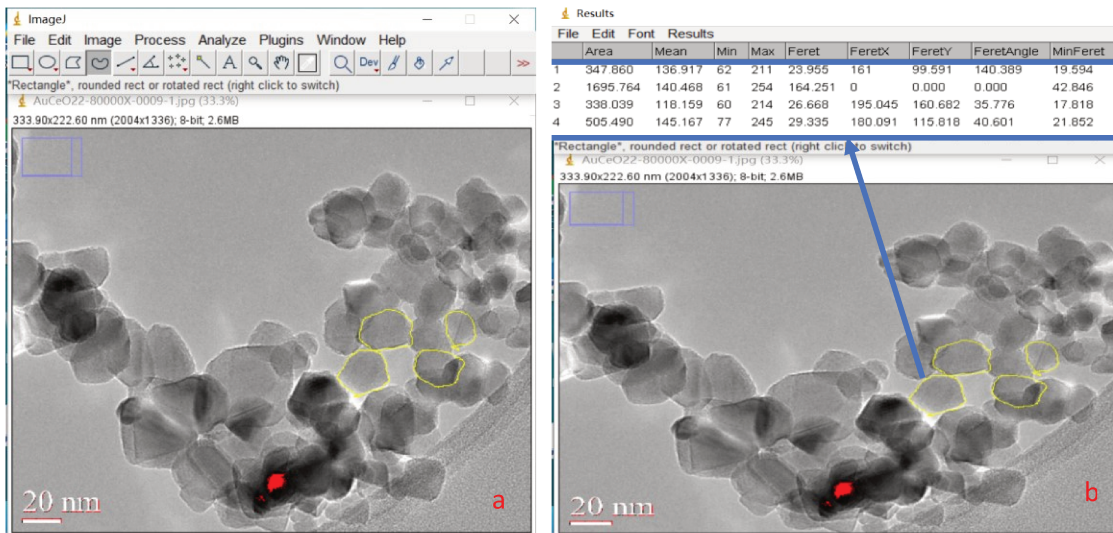


Fig.2.5 The calculation process of ImageJ.

2.3.1.3 Dynamic Light Scattering (DLS)

The Zetasizer Nano S (see Figure 2.6) is a research grade dynamic light scattering system for 0.3 nm to 10 μm . The basic principle of DLS is when illumination reaches the medium, the alternating electromagnetic field causes the electrons in the molecule of the medium to move faster, and the vibrating electric dipole acts as a secondary source to radiate electromagnetic waves in all directions. These secondary waves emitted from different scatters superimpose each other to form scattering light. The phase and polarization of light depend on the position and orientation of the scatters. Because of Brownian motion, when the position and orientation of the scatters change with time, the phase and polarization of the scattered light also change (that is, fluctuation). The following equation is used to calculate the radius of the particle ^[310-312].

$$R = \frac{K_B T}{3\pi\eta C} \quad (\text{Eq. 2.4})$$

Where R is the radius of the particles, C is the translational diffusion coefficient of particles; K_B is the Boltzman constant, T is absolute temperature, η is viscosity.

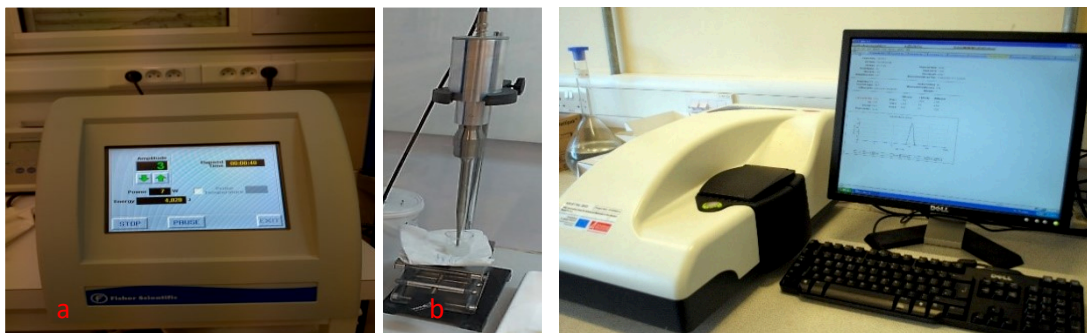


Fig. 2.6 Photo of Fisher Scientific Ultrasonic Probe(a) and Nano Sizer(c).

The sample preparation process is as follows:

1. Water/ethanol solution + dispersant (sodium pyrophosphate decahydrate);
2. Magnetic stirring the solution + Ultrasonic probe power (see figure 2.6a) + sample (see figure 2.6b);
3. Ultrasonic probe power (5 W) + sample string (10 min) + analyze.

The purpose of adding dispersant and an ultrasonic probe is to break the agglomeration between particles and acquire a more accurate particle size of nanopowder. During the measurement process, different ultrasonic probe power (7-13 W), concretion of dispersants (0.5-6 g/L), solvents (water/ethanol), process

times (1-30 min) were utilized to avoid the influence of agglomerated particles on the results (see table 2.5). Each sample was measured more than 20 times under different conditions.

Table 2.5 DLS analysis of nanoparticle.

Samples	Refractive index	Absorption index	Number of sample tests	Solution of dispersant (g/L)	Ultrasonic probe power (w)	Process time (min)
TiO ₂	2.7	0.01	41	0.5-5	7-13	1-30
SiO ₂	1.45	0.01	21	0.5-2	7-13	1-10
Zeolite	1.446	0.01	37	0.5-6	7-13	1-30

*Note: Dispersant = sodium pyrophosphate decahydrate;
Refractive index of solvents: water: 1.33; ethanol: 1.36.

2.3.1.4 Small Angle X-Ray Scattering (SAXS)

Small-angle X-ray scattering (SAXS) is an analytical technique that measures the intensities of X-rays scattered by a sample as a function of the scattering angle. A SAXS signal is observed whenever a material contains structural features on the length scale of nanometers, typically in the range of 1-100 nm.

A typical scattering experiment aims at measuring the scattering intensity produced by a sample illuminated by a monochromatic beam (λ) of X-ray or neutron (see figure 2.7).

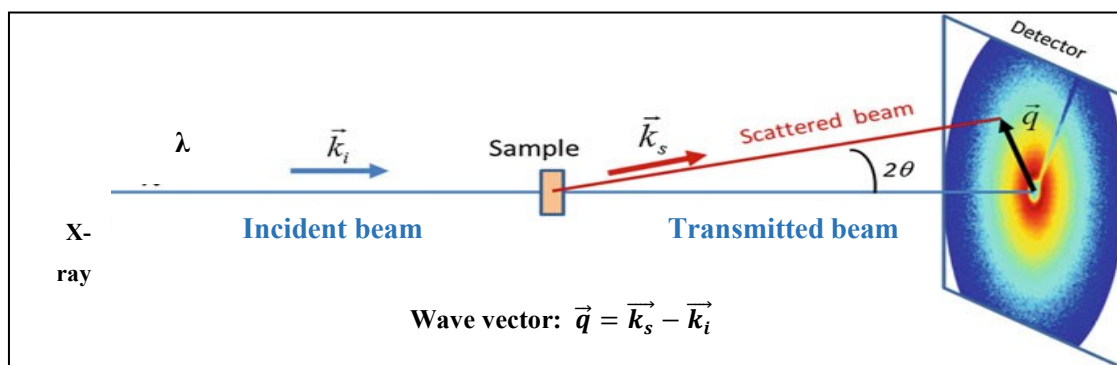


Fig. 2.7 Schematic of SAXS ^[313].

In a SAXS experiment, the intensity is expressed as a function of the scattering vector q resulting from a photon of wavelength λ scattering off the sample at an angle 2θ , $q = 4\pi \sin(\theta)/\lambda$.

The diameter of particle D is given by ^[161]

$$D = 2\pi/\lambda q \quad (\text{Eq.2.5})$$

in which λ is the wavelength of the x-rays (0.154 nm with Cu x-ray source).

A Xeuss 2.0 (Xenocs - France) (see figure 2.8) was applied in this study, it with Cu $k\alpha$ ($\lambda=0.154$ nm) radiation at a tube voltage of 8 Kev, the working distance was utilized 250 cm (see figure 2.8b) and 2θ angles ranged from 0.1° to 61.6° , 1g sample was put in the measuring vessel (see figure 2.8b).



Fig. 2.8 Xeuss 2.0 SAXS instrument: a. the whole device; b. put sample part; c. detector.

2.3.1.5 Specific surface area (BET)

The textural structure properties including specific surface area (S_{BET}) and porosity of materials were measured by low temperature (77K) N_2 adsorption-desorption isotherms performed on the 3Flex analyzer (Micromeritics Instrument Corp.) (see Figure 2.9).

Before the measurement, a separated device (VacPrep061, Micromeritics Instrument Corp.) was applied to degas the sample under vacuum at 423 K around 5 h. When the degassed procedure was done, the sample tube was filled with N_2 and fixed on the analytical platform of 3Flex for measurements.

The method of Brunauer, Emmett, and Teller (BET) is commonly used to determine the total surface area. Common equation is used for determination BET as follows ^[314, 315]:

$$\frac{1}{X\left[\left(\frac{P}{P_0}\right)-1\right]} = \frac{1}{X_m C} + \frac{C-1}{X_m C} \left(\frac{P}{P_0}\right) \quad (\text{Eq.2.6})$$

X is the weight of nitrogen adsorbed at a given relative pressure (P/P_0), X_m is monolayer of N_2 , which is the volume of gas adsorbed at standard temperature (273 K) and pressure (1 atm), and C_s is constant. 0.025

$\leq P/P_o \leq 0.30$ should be used to determine the surface area using the BET equation. At relative pressures higher than 0.5, there is the onset of capillary condensation, and at relative pressures that are too low, only monolayer formation is occurring.



Fig. 2.9 The 3Flex analyzer (Micromeritics Instrument Corp.)

When the BET equation is plotted, the graph should be linear with a positive slope.

The monolayer capacity X_m can be calculated with equation 2.7^[316, 317]:

$$X_m = \frac{1}{S_l + i} \quad (\text{Eq. 2.7})$$

Where S_l is the slope of the linear BET plot and i is the intercept. Once X_m is determined, the total surface area S_{BET} can be calculated with the following equation.

$$S_{BET} = \frac{X_m L_{av} A_m}{M_v} \quad (\text{Eq. 2.8})$$

Where L_{av} is Avogadro's number, which equals to $6.022 \times 10^{23} \text{ mol}^{-1}$; A_m is the cross-sectional area of the adsorbate and equals 0.162 nm^2 for an adsorbed nitrogen molecule, and M_v is the molar volume and equals 22.4 L/mol .

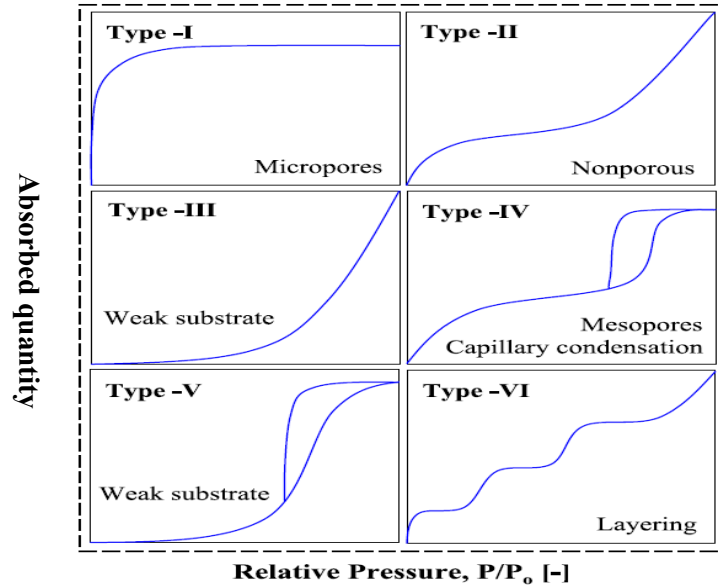


Fig.2.10 The six types of adsorption isotherm, in the classification of BET isotherms ^[318] (Capillary condensation is the "process by which multilayer adsorption from the vapor phase into a porous medium proceeds to the point at which pore spaces become filled with condensed liquid from the vapor phase).

Barrett-Joyner-Halenda (BJH) is a method to determine pore size distribution of a mesoporous solid ^[319] using the desorption branch of N_2 isotherm (see figure 2.10). According to the International Union of Pure and Applied Chemistry (IUPAC) classification, there are three types of pores: those smaller than 2 nm are called micropores (see Type-I in the figure 2.10); those larger than 50 nm are called macropores; and those between 2 nm and 50 nm are called mesopores (see Type-IV in the figure 2.10) ^[320].

Type-VI isotherms are a special type of isotherm reflecting the result of multilayer adsorption on a non-porous homogeneous solid surface (e.g., a clean metal or graphite surface). Actual solid surfaces are mostly inhomogeneous; hence it is difficult to encounter this situation. The type-V isotherm is similar to the type-III isotherm, but the number of adsorption layers is limited when the saturation vapor pressure is reached and the adsorption volume tends to a limiting value. At the same time, due to the occurrence of capillary coalescence, the isotherm rises faster at moderate relative pressures and is accompanied by a hysteresis loop.

The literature ^[168-171, 321] show that from the measurement of the BET specific surface one can estimate a particle size but this under conditions that the particle is not porous, spherical, smooth and has a monomodal size distribution. If a powder is not porous, spherical, and smooth, the following equation can be used to calculate the size of particle ^[168-170].

Chapter 2: Experiments and Materials

$$D = \frac{\text{surface of sphere}}{\text{volume of sphere} * \text{density of particles}} = \frac{6}{S * \rho} \quad (\text{Eq.2.9})$$

Where D is the diameter of particle and ρ is the density of materials. This equation was carried out to estimate the diameter of particle in this study.

Five measurements were utilized to analyze the size of nanoparticles in this study and were summarized in table 2.6.

Table 2.6 Summary of five techniques were used in this study.

Analysis methods	Devices	Diameter calculation equations	
LD	Master 3000 (Malvern Ltd., UK)	$dp_{(3,2)} = \frac{\sum N_i d_i^3}{\sum N_i d_i^2}$	3D
TEM	FEI Tecnai G2-20 (European fund)	$D = (4S/\pi)^{0.5}$ and $dp = \frac{\sum N_i d_i^3}{\sum N_i d_i^2}$	2D
DLS	Nanosizer (Malvern Ltd., UK)	$R = \frac{k_B T}{3\pi\eta c}$	3D
SAXS	Xeuss 2.0 (Xenocs, France)	$D = 2\pi/q$	2D
BET	3Flex analyzer (Micrometric instrument Crop.)	$D = \frac{6}{S * \rho}$	-

Note: In TEM analysis, for each powder, 20 images were used in Image J, the number of selected surface areas respectively, are SiO₂ - 192, Zeolite - 237, and TiO₂ - 296.

For all particles, the mean diameter ($dp_{(3,2)}$) is calculated by equation 2.3.

2.3.2 Particle solid density

The density (ρ) measurements were performed using a Helium pycnometer (AccuPyc1330, micromeritics Instrument Corp, see Figure 2.11). The AccuPyc 1330 Pycnometer is an easy-to-use, fully-automatic gas displacement pycnometer. Analyses are initiated with a keystroke. Once an analysis is initiated, data are collected, calculations are performed, and results displayed without further operator intervention. The AccuPyc 1330 Pycnometer's unique run precision feature increases the precision of analysis results by reporting data from five consecutive runs that are within a user-specified tolerance. This feature allows early termination of analyses, thereby decreasing the number of runs needed for accurate results. The AccuPyc 1330 Pycnometer determines density and volume by measuring the pressure change of helium in a calibrated volume.



Fig. 2.11 The AccuPyc1330 Pycnometer (Micromeritics Instrument Corp.).

2.3.3 Scanning Electron Microscope (SEM)

Scanning electron microscope is an electron microscope that produces an image of the surface of a sample. The electrons interact with the atoms in the sample to produce various signals containing information about the surface topography and composition of the sample. The electron beam is usually scanned with a grating scan pattern, and the position of the beam is combined with the detected signal to produce an image. Scanning electron microscopy can achieve resolution greater than 1 nanometer. Samples can be observed under high vacuum, low vacuum, wet conditions (using an environmental scanning electron microscope) and a wide range of low or high temperatures.



Fig. 2.12 Scanning electron microscope (Hitachi Ltd.).

The most common scanning electron microscope mode is the detection of secondary electrons (SE) emitted by atoms excited by the electron beam. The number of secondary electrons that can be detected depends on the sample topography and other factors. An image showing the morphology of the surface

was created by scanning the sample and collecting the emitted secondary electrons using a special detector. A S-3400N SEM (see figure 2.12) was used in this study. The voltage was set between 7.0 to 15 kV.

2.3.4 Flowability tester

Powder flow, also known as flowability, is defined as the relative movement of a bulk of particles among neighboring particles or along the container wall surface [322]. A change in the cohesive properties of a powder may have an important effect on dry coating and coating quality. ICarr's index (IC) and Hauser ratio (HR) are two parameters that always [323] are used to estimate the flowability of powders. The IC and HR values have been calculated by the bulk density (ρ_{bulk}) and tapped density (ρ_{tap}) of powders, the equation as follows [101, 104, 323]:

$$IC = \frac{\rho_{bulk} - \rho_{tap}}{\rho_{bulk}} \times 100\% = \left(1 - \frac{\rho_{tap}}{\rho_{bulk}}\right) \times 100\% \quad (Eq.2.10)$$

$$Hr = \frac{\rho_{tap}}{\rho_{bulk}} \quad (Eq.2.11)$$

The IC and HR calculate the flowability index of powder. It is divided into 4 ranges, 5 - 10%, 12 - 16%, 18 - 21%, and 23 - 28%, respectively, excellent, good, fair and poor flow properties of the materials [324]. Indicating good flowability of materials if $HR < 1.2$, and poor flowability of the materials if $HR \geq 1.4$ [324, 325]. A HR greater than 1.20 - 1.4 is considered to be an indication of poor flowability [326].



Fig. 2.13 Picture of the tapped density tester (SVM22, Erweka GmbH, Germany).

The bulk and tapped density were measured by a tapped density tester (SVM22, Erweka GmbH, Germany) and is shown in Figure 2.13. Each sample was measured three times to reduce error in this study.

2.4 Conclusions

In this chapter, a solvent-free method - dry particle coating was introduced to prepare new supports (see figure 2.2) via a high shear mixing - Picomix under 3500 rpm, 5 min, filling ratio 40%. γ -Al₂O₃ and S.S316L were using as the support core and coating the fine particles of SiO₂, TiO₂, and Zeolite to form new supports SiO₂/ γ -Al₂O₃, TiO₂/ γ -Al₂O₃, Zeolite/ γ -Al₂O₃, SiO₂/S.S316L, TiO₂/S.S316L, and Zeolite/S.S316L. In order to know the amount of guest used in the experiment, the mass of the coating layer of the guest was calculated based on the assumption of 100% surface coverage of the host particles with a monolayer of guest particles.

To understand the property of the raw materials γ -Al₂O₃, S.S316L, SiO₂, TiO₂, and Zeolite, the various characterization techniques (such as solid density, BET surface area, flowability, surface morphology) were described in this chapter. According to the characterization results and statistics, the mechanism of dry particle coating not only could be described but also possibly could be explained.

Moreover, five different devices/methods, LD (Laser Diffraction), TEM (Transmission Electron Microscope), DLS (Dynamic Light Scattering), SAXS (Small Angle X-ray Scattering), and BET specific surface area were used to analyze the three nanopowder: SiO₂, TiO₂, and Zeolite. The results of the three analyses were labeled as Zeolite^{LD}, Zeolite^{DLS}, Zeolite^{TEM}, TiO₂^{LD}, TiO₂^{DLS}, TiO₂^{TEM}, SiO₂^{LD}, SiO₂^{DLS}, and SiO₂^{TEM}, and these three sizes were used to investigate the preparation of new supports.

Chapter 3: Results and Discussion of Characterization of Host and Guest particles

3.1 Introduction

In order to understand the property of the host and guest particles, different characterization was used to analyze the host and guest particles, such as density, size, BET, and flowability. In this chapter, the results of these different characterizations were presented in details as follows:

- The density of all materials (γ -Al₂O₃, S.S316L, SiO₂, TiO₂, and Zeolite) was measured via a density test (see Chapter 2, paragraph 2.3.2), because the density is one of the important parameters, it was used to calculate the mass of guest and host particles (see Chapter 2, equation 2.2).
- All of the raw materials (host/guest) were characterized by particle size (Mastersizer 3000, see Chapter 2, paragraph 2.3.1.1) and morphological properties (SEM, see Chapter 2, paragraph 2.3.3) to know the size and surface morphology of the host and guest particles.- Different size measurements LD (laser diffraction), DLS (dynamic light scattering), TEM (transmission electron microscope), SAXS (small-angle X-ray scattering), and BET (specific surface area were conducted to analyze the size of three types of guests nanopowder TiO₂, SiO₂, and Zeolite to compare the effect of different testing methods on the size of guest particles.
- BET specific surface area (S_{BET}) was measured by low temperature (77 K) N₂ adsorption-desorption isotherms performed on the 3Flex analyzer (see Chapter 2, paragraph 2.3.1.5) to know the porosity of materials.
- The results of particle flowability (see Chapter 2, paragraph 2.3.4) were presented to see if the guest particles have a good fluid and how the flowability will affect the coating process.

3.2 Density of powders

The densities of all five particles were measured by the Helium pycnometer (AccuPyc 1330, Micrometrics Instrument Crop. As has been showed in Chapter 2, figure 2.11) and the results are summarized in table 3.1.

Table 3.1 The density of materials.

Samples	Density (g/cm ³)
γ -Al ₂ O ₃	3.258
S.S316L	8.102
TiO ₂	3.955
SiO ₂	2.043
Zeolite	2.04

Regarding the two host particles S.S316L and γ -Al₂O₃, it is noted that S.S316L has a higher density than γ -Al₂O₃. The latter is a mesoporous material (see figure 3.1). These 2 host materials not only are different by their densities but also by their surface state and morphology. For the three guest particles, we can note that the density of SiO₂ and zeolite are two times less dense than TiO₂. The density of the powders has an important effect especially on the mass of the guest particles, the more the mass is important the more the number of particles increases and the coating can be complex.

3.3 BET analysis

The BET specific surface area and porous structure of raw γ -Al₂O₃, S.S316L, SiO₂, TiO₂, and Zeolite were analyzed by low temperature (77 K) N₂ adsorption-desorption isotherms performed on the 3Flex analyzer (see Chapter 2, paragraph 2.3.1.5). Figure 3.1 shows the N₂ adsorption-desorption isotherms of five samples.

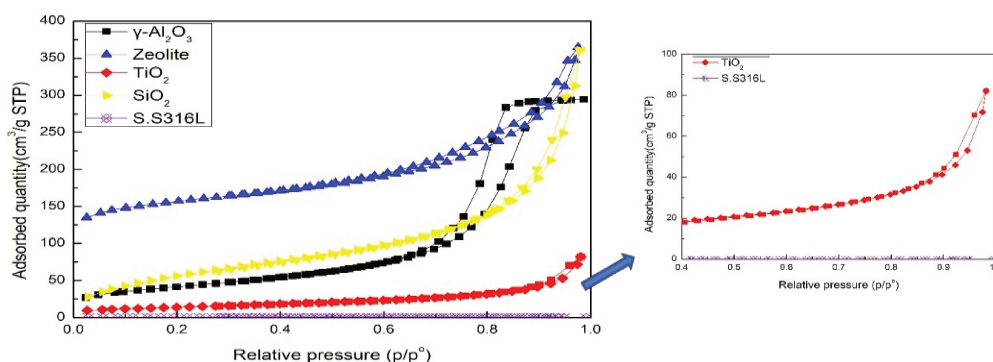


Fig.3.1 N₂ adsorption-desorption isotherms of γ -Al₂O₃, S.S316L, SiO₂, TiO₂, and Zeolite

γ -Al₂O₃ and SiO₂ exhibited type IV-isotherms^[320], indicating the mesoporous texture, Zeolite exhibited type I-isotherms, indicating the microporous texture, TiO₂ exhibited type II-isotherms, indicating non-porous, S.S316 had no isotherms, indicating non-porous as well. As displayed in table 3.2, the specific surface area (S_{BET}) of γ -Al₂O₃, S.S316L, SiO₂, TiO₂, and Zeolite respectively are 148.96, 1.79, 220.59, 50.55, and 506.60m²/g (see table 3.2).

Table 3.2 The BET specific surface method measured results.

Powders	BET specific surface area (m ² /g)
γ -Al ₂ O ₃	148.96
S.S316L	1.79
SiO ₂	220.59
TiO ₂	50.55
Zeolite	506.60

3.4. Size analysis for γ -Al₂O₃ and S.S 316L

The size distribution of two host particles γ -Al₂O₃ and S.S316L was presented in figure 3.2. The results showed that both γ -Al₂O₃ and S.S316L possessed one main mode, which located around 67 μ m and 98 μ m, the mean diameter ($dp_{(3,2)}$) was given that for γ -Al₂O₃: 67.7 μ m, S.S316L: 98.3 μ m.

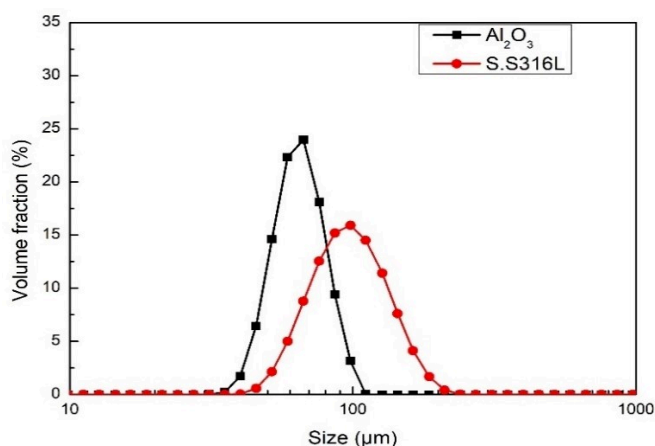


Fig.3.2 Size distribution of raw γ -Al₂O₃ and S.S316L

3.5 Analysis and results of nanoparticle size: SiO₂, TiO₂, and Zeolite

In this study, five devices/measurements LD (laser diffraction, see Chapter 2, paragraph 2.3.1.1), TEM (Transmission electron microscope, see Chapter 2, paragraph 2.3.1.2), DLS (dynamic light scattering, see Chapter 2, paragraph 2.3.1.3), SAXS (small angle X-ray scattering, see Chapter 2, paragraph 2.3.1.4), and BET specific surface area (see Chapter 2, paragraph 2.3.1.5) were involved to measure the nanosize of the 3 powders (TiO₂, SiO₂, and Zeolite).

The five analytical techniques were presented (LD, DLS, TEM, BET, SAXS) in Chapter 2. At first, we can say that the physical absorption analysis technique (BET method) is rather applied to measure the specific surface (developed surface) and the pore distribution. The literature cites this technique as being applicable for the measurement of nanoparticle size from the equation (see Chapter 2, equation 2.9). However, this method is only valid for spherical, non-porous, monodisperse powders with a smooth surface. This is not the case for our three powders TiO₂, SiO₂, and Zeolite. Thus, we decided not to present the results (the size calculated by BET can be found in Appendix).

SAXS theoretically gives very accurate measurements of nanopowder, since we do not have this instrument in our group, the results (see Appendix) got from other analyzing place were late and additional software was needed to analyze the results of size distribution, it will not be introduced here as well.

3.5.1 TEM (*Transmission electron microscope*)

First of all, in this work, we will start with the analysis of nanoparticles with TEM. This technique will allow us to obtain images that visualize the distribution of nanoparticles in each sample of powders. TEM images (see figure 3.3) of sample TiO₂, sample SiO₂, and sample Zeolite were recorded to analyze the size of particles. This technique directly reflects the morphology and size of nanoparticles through the projection of nanoparticle images. TiO₂ can be seen more clearer than SiO₂ and Zeolite in the same scale bar. This shows a larger size of TiO₂. SiO₂ and Zeolite present a large agglomeration phenomenon. In this case, the agglomeration of a large number of particles makes it much more difficult to analyze the diameter of the particles. Therefore, in the analysis of this technique, we can only obtain more accurate results by obtaining as many clear pictures as possible. For each particle, 20 images were taken of the visible particles. The procedure of image processing and determination of the size and the average diameter was described in Chapter 2, paragraph 2.3.1.2.

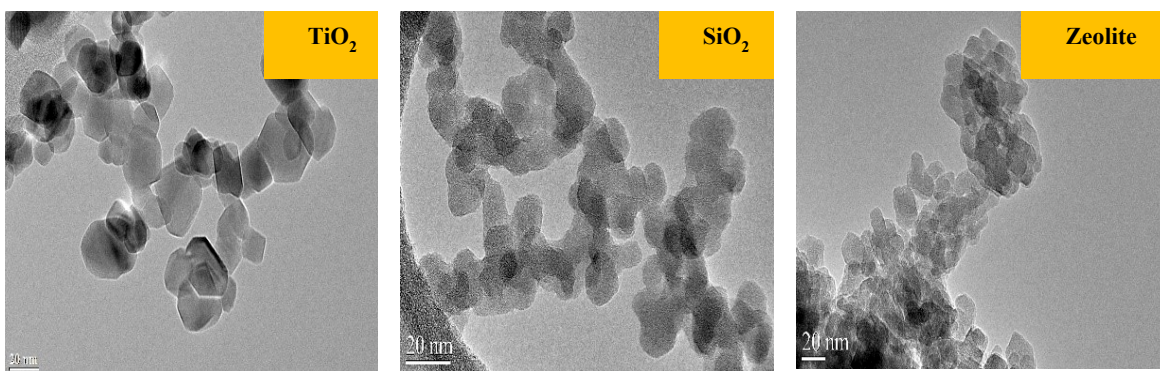


Fig. 3.3 TEM images of TiO₂, SiO₂, and Zeolite.

In this study, different images were selected around 200 number of particles (192 for SiO₂, 237 for zeolite, 296 for TiO₂) to analyze the size of nanoparticles. The size distribution i.e., the variation of the volume fraction as a function of the size of TiO₂, SiO₂, and Zeolite is shown in Figure 3.4.

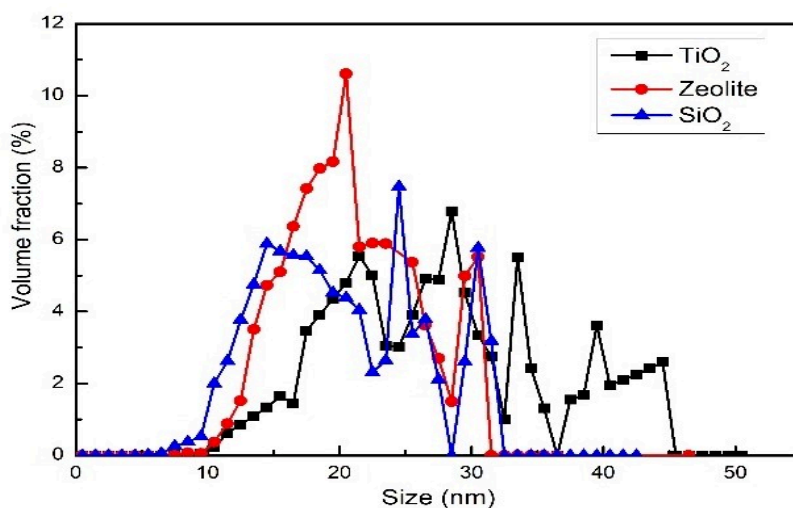


Fig. 3.4 Size distribution of TiO₂, SiO₂, and Zeolite are measured by TEM.

TiO₂ has the biggest agglomerates and mean diameter $dp_{(3,2)} = 25.16$ nm (see table 3.5) between the three of them. The mean diameter $dp_{(3,2)}$ of SiO₂ and Zeolite respectively are 17.39 nm, 19.78 nm (see table 3.5). Similarly, SiO₂ appears to have the smallest size and the most deviated particle size distribution towards the smaller sizes. The three powders show a very small particle size and at the nanometer scale. Thus, the powders were characterized by very cohesive powders and spontaneously form agglomerates of variable sizes under the action of the van der Waals' forces.

3.5.2 LD (laser diffraction)

In this study, for each measurement, a 2500 rpm rotation speed with demineralized water (DW) was conducted. In order to check the stability of the results, each sample was tested 6 times, 3 times without ultrasonic and 3 times with 10 s and 30% ultrasonic.

Figure 3.5 displays the size distribution of TiO_2 , SiO_2 , and Zeolite particles measured by Mastersizer 3000 (see Chapter 2, paragraph 2.3.1.1). As it can be seen that the blue curve (SiO_2) with two main modes, one is narrow around 20 μm , and another one is around 0.7 μm , respectively, which implies the agglomeration phenomena of the SiO_2 nanoparticles. On the contrary, the Zeolite particles (red color) present a narrow size distribution with one main model locating at 7.8 μm . TiO_2 (black color) particles show the main model locating at 2.7 μm and two small models after 50 μm , which indicates slight agglomeration of the TiO_2 nanoparticles.

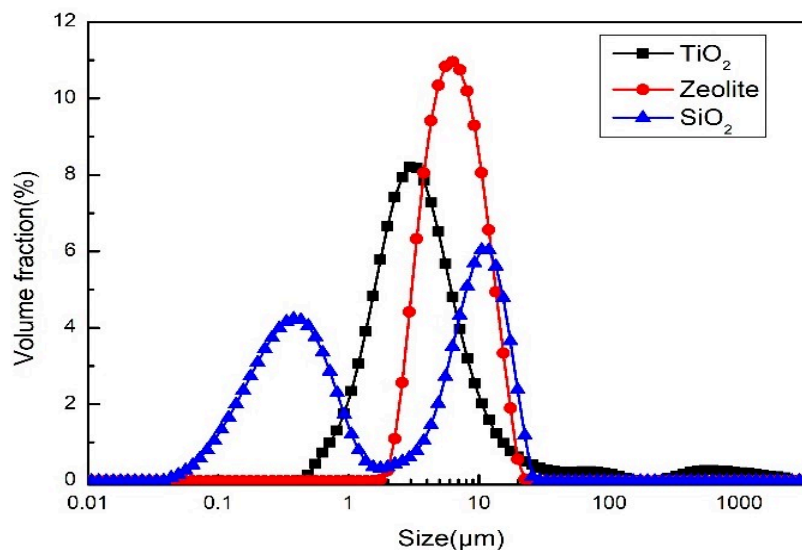


Fig.3.5 Size distribution of TiO_2 , SiO_2 , and Zeolite are measured by LD.

The results were grouped in table 3.3. We noted that these results highlight the analysis of the agglomerates and not the primary particles, especially, Zeolite, the standard deviation between the results with and without ultrasonic was relatively large, which indicated that there was a large amount of agglomeration of Zeolite particles when analyzed without ultrasonic. With this analysis, we noted that the mean diameter $dp_{(3,2)}$ of SiO_2 , TiO_2 , and Zeolite respectively are 0.48, 2.67, and 7.79 μm , which are corresponding with the results of the first test (operating conditions DW+2500 rpm).

Chapter 3: Results and Discussion of Characterization of host and guest particles

Table 3.3 Size of different particles with 6 times test results by LD.

Samples	Operating conditions		Mean diameter $dp_{(3,2)}$ (μm)	Average mean diameter $dp_{(3,2)}$ (μm) \pm standard deviation
Zeolite	DW	1	7.79	6.83 ± 0.814
	(Demineralized water) +2500 rpm	2	7.8	
		3	7.73	
	DW	1	5.94	
	+10s	2	5.89	
	+ultrasonic+2500 rpm	3	5.96	
TiO ₂	DW	1	2.67	2.49 ± 0.024
	(Demineralized water) +2500 rpm	2	2.73	
		3	2.71	
	DW	1	2.33	
	+10s	2	2.35	
	+ultrasonic+2500 rpm	3	2.39	
SiO ₂	DW	1	0.484	0.469 ± 0.0003
	(Demineralized water) +2500 rpm	2	0.492	
		3	0.487	
	DW	1	0.451	
	+10s	2	0.449	
	+ultrasonic+2500 rpm	3	0.452	

3.5.3 DLS (dynamic light scattering)

The particle size analysis protocol was detailed in Chapter 2, paragraph 2.3.1.3, as was mentioned, for each type of particle, more than 20 times were used to measure the particle size of the nanoparticles. Different ultrasonic probe power (7-13 W), the concentration of dispersants (0.5-6 g/L), and process times (1-30 min) were utilized to break up the agglomerates and measure the primary particles. Under these 20 different sets of conditions of measurement, the operating conditions with smaller amount of dispersant, lower power of ultrasonic probe, shorter ultrasonic probe time and smaller particle size obtained are called the optimal operating conditions, the obtained results are under the conditions of Table 3.4.

Chapter 3: Results and Discussion of Characterization of host and guest particles

Table 3.4 Optimal of operating conditions.

Samples	Mean diameter $dp_{(3.2)}$ (nm)	Optimal conditions dispersant (g/L)	Optimal conditions ultrasonic probe power (W)	Optimal conditions time under ultrasonic probe power (min)
TiO ₂	107	1	7	10
Zeolite	206	5	7	10
SiO ₂	119	1	7	5

*Note: the dispersant is sodium pyrophosphate decahydrate.

Figure 3.6 presents the size distribution of TiO₂, SiO₂, and Zeolite that obtained by DLS measurement (under the conditions of table 3.4). The mean diameter $dp_{(3.2)}$ of SiO₂, TiO₂, and Zeolite respectively are 119 nm, 107 nm, and 206 nm. In this method, TiO₂ has the smallest size. For Zeolite, there are two peaks. This occurrence of the two peaks because of the agglomeration of Zeolite particles.

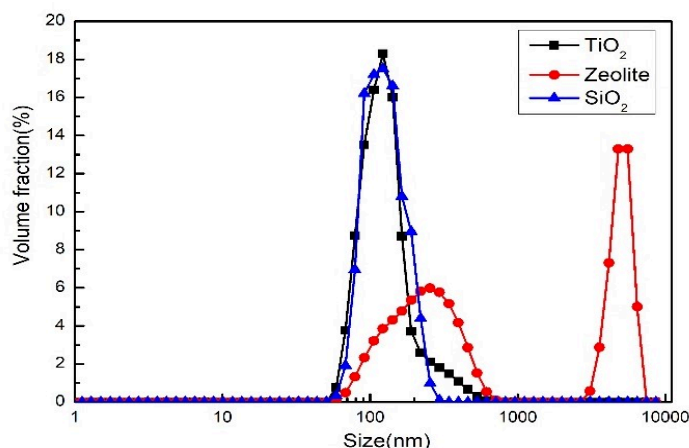


Fig.3.6 Size distribution of TiO₂, SiO₂, and Zeolite are measured by DLS.

In conclusion of this paragraph, the size of TiO₂, SiO₂, and Zeolite has been measured by 3 different methods and the results are shown in table 3.5. It demonstrates using different methods will obtain the different diameters, using LD measurement gets the biggest diameter (agglomerates) and TEM gets the smaller diameter (primary particle).

Table 3.5 Diameter of three guest particles measured by three different methods.

Samples	Mean diameter $dp_{(3.2)}$		
	LD (μ m)	DLS (nm)	TEM (nm)
TiO ₂	2.67	107	25.16
SiO ₂	0.48	119	17.39
Zeolite	7.79	206.84	19.79

It can be seen that the LD analysis has the largest diameter, which means the measurement of agglomerates. The DLS has a smaller size but it always remains agglomerates. Finally, the TEM indicates the smallest diameter because the technique allows us to see the particle and measure them by image processing.

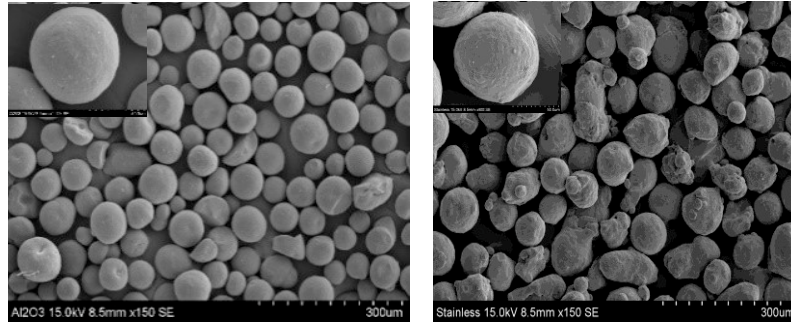
It should be noted that differences in the size of nanoparticles were determined by the use of different techniques. This is not caused by measurement error, but in fact by the specificity of each technique. TEM measures the geometric size of the nanoparticles deposited on the surface; therefore, the advantage of TEM is that it can directly observe the morphology and determine the size of particle size, which has certain intuitiveness and credibility. However, this method is the result of observation of local areas, thus, it has certain contingency and statistical errors. The average particle size of nanoparticles can be obtained by measuring and statistical analysis of particle size with a certain number of photos. As a result, the size of measured nanoparticles can be different by the different techniques.

However, the difference between nanoparticle size for the same particle due to the agglomerates as discussed earlier. Moreover, it is important to be aware that each particle size characterization technique will measure a different property of a particle and therefore will give a different value from another technique that measures an alternative dimension. This leads to many approaches to data analysis which can affect the particle size information obtained. As a result, each technique is not wrong, they all are correct; it is simply that a different property of nanoparticles is being measured.

3.6 Morphology of powders

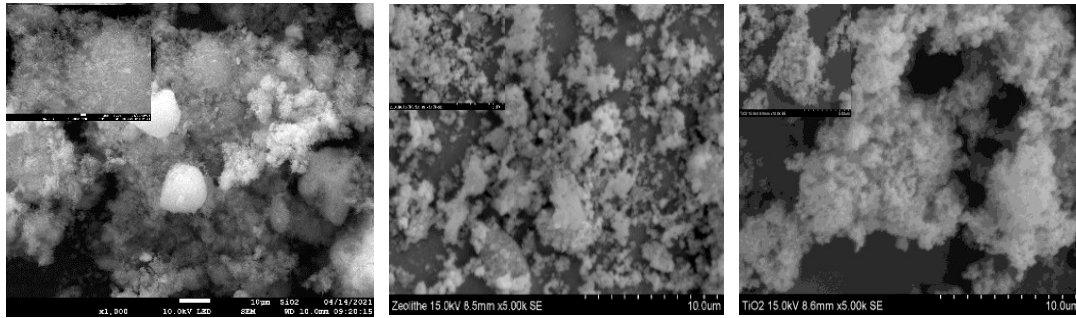
The surface morphologies of five powder γ -Al₂O₃, S.S316L, SiO₂, TiO₂, and Zeolite were characterized by SEM, as shown in Figure 3.7. Two host particles γ -Al₂O₃ (see figure 3.7a) and S.S316L (see figure 3.7b) presented a relatively smooth surface and uniform spherical shape. It is important to note that not every S.S316L particle is spherical, some S.S316L particles have a very small part of the surface linked, generally, these small parts are difficult to occur the coating.

Apparently, all three guest particles SiO₂ (see figure 3.7c), TiO₂ (see figure 3.7e), and Zeolite (see figure 3.7d) showed different degrees of agglomeration because of the strong cohesive force (van der Waals's force). This agglomeration can be broken during the coating process at high rotational speeds, and perhaps it is possible that the coating will continue to form as an agglomeration, adhering to the surface of the host particles.



(a) $\gamma\text{-Al}_2\text{O}_3$

(b) S.S316L



(c) SiO_2

(d) Zeolite

(e) TiO_2

Fig.3.7 SEM images of $\gamma\text{-Al}_2\text{O}_3$, S.S316L, SiO_2 , TiO_2 , and Zeolite.

3.7 Flowability of powders

The flowability of the raw materials Zeolite, TiO_2 , SiO_2 , and $\gamma\text{-Al}_2\text{O}_3$ were measured with the tapped density tester (SVM22, Erweka GmbH, Germany) (see chapter 2, paragraph 2.3.4, figure 2.13). The *IC* and *HR* values have been calculated by the bulk density (ρ_{bulk}) and tapped density (ρ_{tap}) of powders, the equations can be seen in Chapter 2 (equations 2.10 and 2.11). The analyzed results are summarized in table 3.6.

Table 3.6 The flowability of materials.

Samples	Flowability	
	<i>IC</i>	<i>Hr</i>
$\gamma\text{-Al}_2\text{O}_3$	$5.7\% \pm 0.7\%$	1.07 ± 0.02
SiO_2	$44\% \pm 0.5\%$	1.74 ± 0.03
TiO_2	$43\% \pm 2\%$	1.77 ± 0.08
Zeolite	$41\% \pm 2\%$	1.69 ± 0.08

IC and *HR* are two the most important and significant values to describe the flowability of powder as introduced in Chapter 2, paragraph 2.3.4. A higher value of *IC* corresponds to the cohesive powder, the *IC* of host particle $\gamma\text{-Al}_2\text{O}_3$ ($5.7\% \pm 0.7\%$) is much smaller than that of three guest particles, the *IC* of Zeolite, TiO_2 , and SiO_2 are respectively, $41\% \pm 2\%$, $43\% \pm 2\%$, and $44\% \pm 2\%$. This result is logical because the previous size analysis and SEM images of three guest particles also showed a large amount of agglomeration. In Chapter 2, paragraph 2.3.4, it was indicating good flowability of materials if $HR < 1.2$, and poor flowability of the materials if $HR \geq 1.4$. Obviously, $\gamma\text{-Al}_2\text{O}_3$ presents a good flowability because the value of *HR* is 1.07 ± 0.02 . S.S316L has a size of $98.3 \mu\text{m}$, which is larger than that of $\gamma\text{-Al}_2\text{O}_3$ ($67.7 \mu\text{m}$). Since $\gamma\text{-Al}_2\text{O}_3$ has a good flowability, S.S316L has good flowability because the larger the particle size, the better the flowability. Therefore, in this study, the flowability of S.S316L was not measured. For three guest particles, the values of *HR* demonstrated that they have poor flowability.

3.8 Conclusion

In this chapter, the results of different characterizations were summarized and showed as below:

- 1 - The density of $\gamma\text{-Al}_2\text{O}_3$, S.S316L, TiO_2 , SiO_2 , and Zeolite were analyzed and respectively, are 3.258, 8.102, 3.955, 2.043, and 2.04 g/cm³.
- 2 - The BET analysis of isotherms showed that $\gamma\text{-Al}_2\text{O}_3$ and SiO_2 are the mesoporous texture, Zeolite is the microporous texture, TiO_2 and S.S316L are non-porous materials. The specific surface area (S_{BET}) of $\gamma\text{-Al}_2\text{O}_3$, S.S316L, SiO_2 , TiO_2 , and Zeolite respectively are 148.96, 1.79, 220.59, 50.55, and 506.60 m²/g.
- 3 - The size analysis gave the mean diameter ($dp_{(3,2)}$) of two host particles, which are $\gamma\text{-Al}_2\text{O}_3$: $67.7 \mu\text{m}$, S.S316L: $98.3 \mu\text{m}$.
- 4 - Three different results for measuring nanoparticles were presented. The analysis of nanopowder demonstrated that the LD gave the largest diameter because of the measurement of agglomerates. The DLS provided a smaller size but it always remains agglomerates. The TEM indicated the smallest diameter because the technique allows us to see the particle and measure them by image processing.
- 5 - SEM images of two host particles $\gamma\text{-Al}_2\text{O}_3$ and S.S316L presented a relatively smooth surface and uniform spherical shape. The SEM images of three guest particles SiO_2 , TiO_2 , and Zeolite showed different degrees of agglomeration.

6 - The flowability of powder proved that three guest particles Zeolite, TiO₂, and SiO₂ are cohesive powder and have poor flowability.

Chapter 4: Dry Coating Results and Discussions

4.1 Introduction

As discussed in Chapter 2, the main objective of this study is to prepare catalysts for methanation reactions by dry coating. After an extensive literature analysis, 5 supports (γ -Al₂O₃, S.S316L, SiO₂, TiO₂, and Zeolite) were selected to prepare the catalysts. However, except for γ -Al₂O₃ and S.S316L, which have large sizes and can be used directly to prepare catalysts in picomix, the other three particles (SiO₂, TiO₂, and Zeolite) are nanoparticles and cannot be used directly as the host particles to prepare catalysts.

Thus, three ways (granulation, pelletizing, and atomization) were used to go increasing the size of nanoparticles to around 80 μ m. 80 μ m. However, the results obtained were very disappointing, and the obtained large diameters of Zeolite, TiO₂, and SiO₂ were very fragile and easily break.

In this case, we considered preparing new supports, using γ -Al₂O₃ and S.S316L as hosts, the fine particles of SiO₂, TiO₂, and Zeolite were coated to form new supports as shown in figure 4.1: SiO₂/S.S316L, TiO₂/S.S316L, Zeolite/S.S316L, SiO₂/ γ -Al₂O₃, TiO₂/ γ -Al₂O₃, and Zeolite/ γ -Al₂O₃.

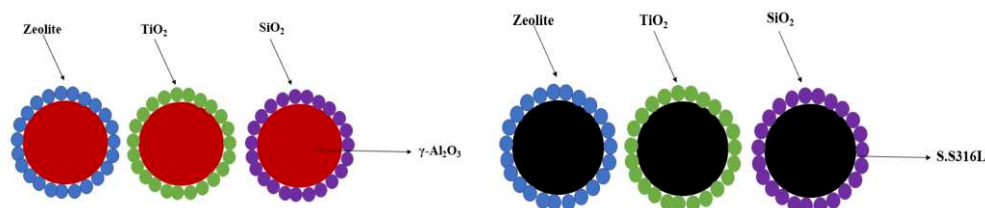


Fig. 4.1. Images of new supports: left (γ -Al₂O₃ as a core shell, Zeolite, TiO₂, and SiO₂ are coated), and right (S.S316L as a core shell, Zeolite, TiO₂, and SiO₂ are coated).

Therefore, this program has been implemented and the results of these dry coatings will be presented in detail in this chapter.

The operating conditions of picomix were as follows: 3500 rpm and 5 mins, the filling ratio was set at 40% of the vessel volume (40 mL of powders were added into the 100 mL vessel, which means total powders of host and guest are 40 mL). The exact mass of host and guest particles were determined by calculation (see Chapter 2, paragraph 2.2.2.3 and table 2.2).

The size of three nanoparticles TiO₂, SiO₂, and Zeolite were analyzed by three different methods, LD (laser diffraction), DLS (dynamic light scattering), TEM (transmission electron microscope). The

materials with size analyzed by the three methods were labeled respectively: Zeolite^{LD}, Zeolite^{DLS}, Zeolite^{TEM}, TiO₂^{LD}, TiO₂^{DLS}, TiO₂^{TEM}, SiO₂^{LD}, SiO₂^{DLS}, and SiO₂^{TEM}.

4.2 Adhesion effects phenomena

Dry particle coating is a solvent free method where guest particles adhere uniformly to the surface of a host particle by strong adhesion forces. Since the guest particles (Zeolite, TiO₂, and SiO₂) were conducted in this study are nanopowder and very cohesive and always show agglomeration and poor flowability (see Chapter 3, paragraph 3.7). The goal of this study is to know the effect of adhesion on the dry coating process by calculating the van der Waals' forces between different materials.

Figure 4.2 shows a schematic of the formation of agglomerates. As it can be seen, when the size of particles is less than 50 μm, the particles can easily form agglomerates, and the smaller the particles, the easier they can agglomerate together^[156]. Once the particles are agglomerated together, the interparticle forces (van der Waals' forces) will be larger than the gravity of the particles themselves and have poor flowability^[308]. The behavior of cohesive powders is mainly observed through the external contact forces acting on the particle surface and the adhesion caused by the interparticle forces (van der Waals' forces)^[327, 328].

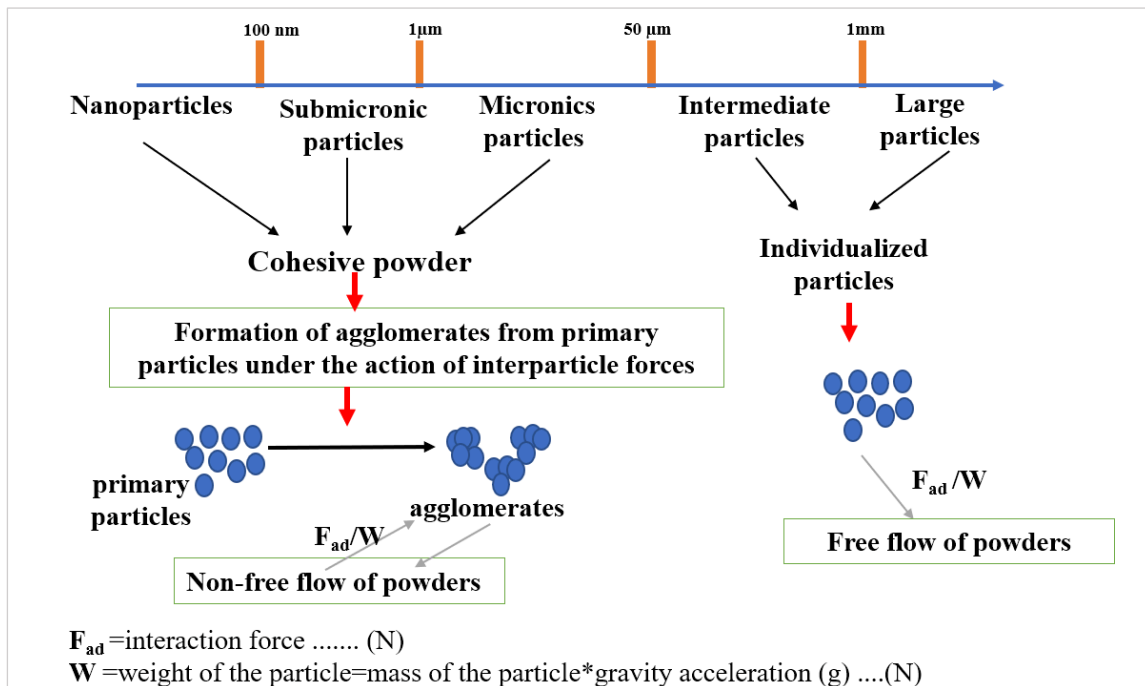


Fig. 4.2 The formation process of agglomerates.

Adhesion may occur between the surface of the particles ^[296], the adhesion forces are the attractive forces between unlike molecules ^[296, 329], they are caused by forces acting between two surfaces. Adhesion between powder particles or particles and surface plays a very important role in the understanding of powder flow and powder mixing ^[328, 330]. In the most general cases ^[296, 329-332] the adhesion force, F_{ad} , is a combination of:

- F_{vdw} is the van der Waals' force;
- F_{12}^e is the electrostatic Coulomb force between the charged particles 1 and 2;
- F_{cap} is the capillary force;
- F_{che} is the force because of chemical bonds or acid-base interactions ^[333]:

$$F_{ad} = F_{vdw} + F_{cap} + F_{12}^e + F_{che} \quad (Eq. 4.1)$$

In the dry media, the adhesion force is mainly assessed by the magnitude of van der Waals' forces, calculated by the following equation ^[229, 268, 305]:

$$F_{vdw} = -\frac{AR_iR_j}{6(R_i+R_j)z^2} \quad (Eq. 4.2)$$

Where z is the distance between two particles. z is assumed to be 0.4 nm ^[269]. R_i and R_j are the radius of spherical particle i and particle j , A is the Hamaker constant.

The expression for the Hamaker constant is based on Lifshitz theory ^[305, 334]. This theory deals with van der Waals' forces between bodies, it does not assume to order pairwise addition of the individual intermolecular forces; that is, the theory takes into account the influence of neighboring molecules on the interaction between each pair of molecules located in two bodies, rather than treating each pair individually ^[305, 335]. The equation for calculating the Hamaker constant can be seen as follows ^[305, 334-337]:

$$A = \frac{3BT}{4} \left(\frac{\epsilon_1 - 1}{\epsilon_1 + 1} \right)^2 + \frac{3hv_e}{16\sqrt{2}} \frac{(n_1^2 - 1)^2}{(n_1^2 + 1)^{3/2}} \quad (Eq. 4.3)$$

Where B is the Boltzmann's constant ($1.38 \times 10^{-23} \text{ J} \cdot \text{K}^{-1}$ ^[305]), T is the temperature, ϵ_1 is the dielectric constant, h is the Planck's constant ($6.63 \times 10^{-34} \text{ (J} \cdot \text{s)}$ ^[305, 338]), v_e is the UV adsorptive frequency, n_1 is the refraction index. In this calculation, we assumed that the agglomerated cohesive powder has the same Hamaker constant as the individual particle. Based on this assumption, the Hamaker constant of all of the materials are listed in table 4.1.

Chapter 4: Dry Coating Results and Discussions

The Hamaker constant, in table 4.1, is calculated at room temperature ($T = 298$ K), the dielectric constant, the UV adsorptive frequency, and the refraction index were cited from the literature. The calculated values deviate somewhat from references, which is acceptable.

Table 4.1 Parameters of the materials in this study

Materials	Dielectric constant (ϵ_1)	Refraction index (n)	Adsorptive frequency (ν_e) (10^{15}s^{-1})	Hamaker constant (A) (10^{-20}J)	
				Calculated	From references
$\gamma\text{-Al}_2\text{O}_3$	10.1 [337]	1.806 [339]	3.0 [340]	20.7	14-15 [305, 337]
S.S316L	15.6 [341]	2.3 [342]	3.0 [305]	23.9	22 [343]
Zeolite	2.7 [344]	1.47 [345]	3.0 [305]	6.51	4.4 [346]
TiO ₂	17.0 [347]	2.61 [305]	3.0 [305]	24.4	43 [305]
SiO ₂	3.5 [348]	1.457 [349]	1.71 [340]	0.09	0.05 [350]

For the same size and spherical particle, that is to say, $R_i = R_j$, van der Waals' force can be calculated by $F_{vdw} = -\frac{AR_i}{12z^2}$. It is only necessary to calculate the Hamaker constant (or find it from literature) to know the magnitude of the van der Waals' forces. However, in this study, the guest particles and host particles are spherical particles of different sizes ($R_i \neq R_j$), which involves the calculation of the Hamaker constant (A_{ij}), it was approximately evaluated by the following equation [305, 336, 337, 351, 352]:

$$A_{ij} = (A_i A_j)^{\frac{1}{2}} \quad (\text{Eq. 4.4})$$

Where A_i and A_j respectively, are the Hamaker constant of particle i and j .

Table 4.2 The Hamaker constant of different materials in this study

Materials			Hamaker constant (A) (10^{-20}J)		
Host particles	Guest particles	New supports	Host particles (A_i)	Guest particles (A_j)	New supports (A_{ij})
$\gamma\text{-Al}_2\text{O}_3$	Zeolite	Zeolite/ $\gamma\text{-Al}_2\text{O}_3$	20.7	6.51	11.61
	TiO ₂	TiO ₂ / $\gamma\text{-Al}_2\text{O}_3$		24.4	22.47
	SiO ₂	SiO ₂ / $\gamma\text{-Al}_2\text{O}_3$		0.09	1.36
S.S316L	Zeolite	Zeolite/S.S316L	23.9	6.51	12.47
	TiO ₂	TiO ₂ /S.S316L		24.4	24.15
	SiO ₂	SiO ₂ /S.S316L		0.09	1.47

Chapter 4: Dry Coating Results and Discussions

According to the equation 4.4, the Hamaker constant of different particles were calculated and shown in table 4.2.

After obtaining the Hamaker constant of the different materials, the van der Waals' forces were calculated via equation 4.2 and listed in the table 4.3.

Table 4.3 van der Waals forces between host-guest particles

Materials			Radius of particle (nm)		Hamaker constant (A_{ij}) (10^{-20}J)	van der Waals force F_{vdw} (N)
Host particles	Guest particles	New supports	Host particles	Guest particles		
$\gamma\text{-Al}_2\text{O}_3$	Zeolite ^{LD}	Zeolite ^{LD} / $\gamma\text{-Al}_2\text{O}_3$		3895		4.21E-07
	Zeolite ^{DLS}	Zeolite ^{DLS} / $\gamma\text{-Al}_2\text{O}_3$		103.42	11.61	1.25E-08
	Zeolite ^{TEM}	Zeolite ^{TEM} / $\gamma\text{-Al}_2\text{O}_3$		9.895		1.20E-09
	TiO ₂ ^{LD}	TiO ₂ ^{LD} / $\gamma\text{-Al}_2\text{O}_3$		1335		3.00E-07
	TiO ₂ ^{DLS}	TiO ₂ ^{DLS} / $\gamma\text{-Al}_2\text{O}_3$	32500	53.5	22.47	1.25E-08
	TiO ₂ ^{TEM}	TiO ₂ ^{TEM} / $\gamma\text{-Al}_2\text{O}_3$		12.58		2.94E-09
	SiO ₂ ^{LD}	SiO ₂ ^{LD} / $\gamma\text{-Al}_2\text{O}_3$		225		3.17E-09
	SiO ₂ ^{DLS}	SiO ₂ ^{DLS} / $\gamma\text{-Al}_2\text{O}_3$		59.5	1.36	8.41E-10
	SiO ₂ ^{TEM}	SiO ₂ ^{TEM} / $\gamma\text{-Al}_2\text{O}_3$		8.695		1.23E-10
S.S316L	Zeolite ^{LD}	Zeolite ^{LD} /S.S316L		3895		5.02E-07
	Zeolite ^{DLS}	Zeolite ^{DLS} /S.S316L		103.42	12.47	1.34E-08
	Zeolite ^{TEM}	Zeolite ^{TEM} /S.S316L		9.895		1.29E-09
	TiO ₂ ^{LD}	TiO ₂ ^{LD} /S.S316L		1335		3.35E-07
	TiO ₂ ^{DLS}	TiO ₂ ^{DLS} /S.S316L	49150	53.5	24.15	1.35E-08
	TiO ₂ ^{TEM}	TiO ₂ ^{TEM} /S.S316L		12.58		3.16E-09
	SiO ₂ ^{LD}	SiO ₂ ^{LD} /S.S316L		225		3.44E-09
	SiO ₂ ^{DLS}	SiO ₂ ^{DLS} /S.S316L		59.5	1.47	9.11E-10
	SiO ₂ ^{TEM}	SiO ₂ ^{TEM} /S.S316L		8.695		1.33E-10

As already stated in figure 4.2, particles will clump together when the van der Waals force is greater than their gravity, and the greater the ratio of van der Waals' force to gravity between particles, the more likely the particles will clump together. In the coating process, the host particles used are $\gamma\text{-Al}_2\text{O}_3$ and S.S316L (both with particle size greater than 50 μm), and the gravity force is greater than the van der Waals' force itself.

Chapter 4: Dry Coating Results and Discussions

Equation 4.2 shows that, with the same Hamaker constants, the van der Waals' force is mainly determined by the radius of particle. Since Zeolite^{LD}/γ-Al₂O₃, Zeolite^{DLS}/γ-Al₂O₃, and Zeolite^{TEM}/γ-Al₂O₃, are formed by the same guest and host particle, the hypothesis in this study is the agglomerated particles have the same Hamaker constant as the individual particle. Therefore, the Zeolite^{LD}, Zeolite^{DLS}, and Zeolite^{TEM} have the same Hamaker constant in this study, same as other particles. The only difference is that Zeolite^{LD}, Zeolite^{DLS}, and Zeolite^{TEM} represent three different measurements, the van der Waals' force between the different particles is presented in Figure 4.3.

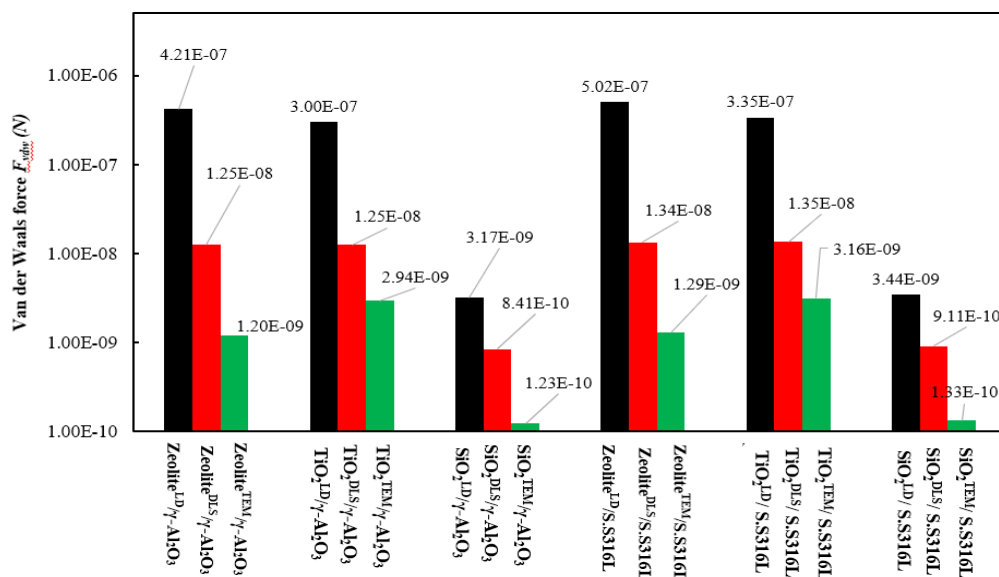


Fig 4.3 van der Waals forces between host-guest particles.

As it can be seen in Figure 4.3, when the host is the same, for the same guest particle, the van der Waals force of the particle represented by LD is also the largest because of the large particle size (large agglomeration) provided by the way LD was analyzed. E.g., the van der Waals force follows this order: TiO₂^{LD}/γ-Al₂O₃ > TiO₂^{DLS}/γ-Al₂O₃ > TiO₂^{TEM}/γ-Al₂O₃. The results of this van der Waals' force data unexpectedly indicated that the coating of TiO₂^{LD}/γ-Al₂O₃ will be accompanied by a large amount of agglomeration during the coating process, forming a large number of layers.

4.3 Calculation of uncoated guest particle in picomix

During the coating technique a significant mass of the guest particles adheres to the walls of the picomix. Thus, it is important to quantify this mass of powder to be able to evaluate the real quantity of powder that adheres to the surface of the host particles. There are some particles that were found staying on the wall of the vessel and the rotor (includes three paddles), by measuring the mass of the particles adhered on the wall and the rotor of the picomix, an uncoated particle fraction can be obtained to estimate the coating degree. Figure 4.4 shows one of the mixing examples, it can be seen that a quantity of Zeolite^{LD} particle powder was adhered to the surface of the wall of the vessel and the rotor after mixing. This was because of severe particle-wall collisions under high-shearing/impacting forces.

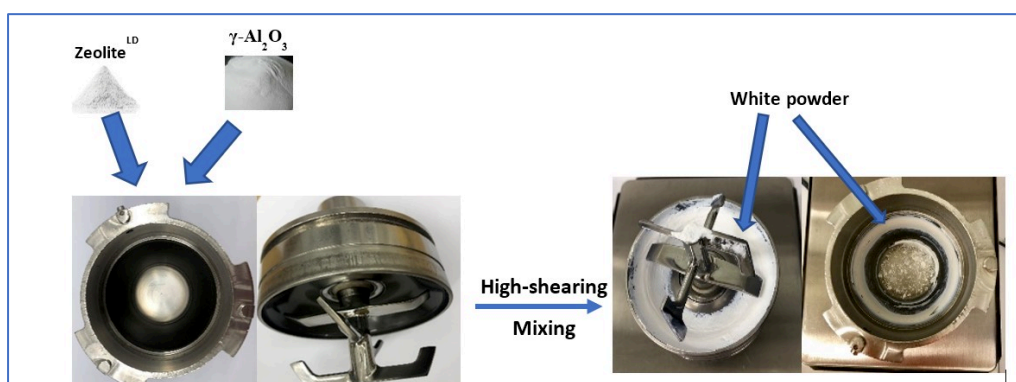


Fig. 4.4 Photos of the vessel and the rotor before (left) and after (right) high-shear mixing of $\gamma\text{-Al}_2\text{O}_3$ and Zeolite^{LD} particles in Picomix.

All the powders sticking to the walls and rotor of the picomix were analyzed. This work was done in the following way:

- 1) Weighted the mass of rotor and vessel before the coating (see figure 4.4 (left), the cleaned vessel and rotor), was named as $m_{\text{vessel before mixing}}$ and $m_{\text{rotor before mixing}}$;
- 2) Weighted the mass of the coated rotor and vessel, this mass is the mass of the rotor and vessel with the powder adhered on the rotor and vessel (see figure 4.4 (right), the vessel and rotor with powders), and was named as $m_{\text{vessel after mixing}}$ and $m_{\text{rotor after mixing}}$.
- 3) The mass of particles that stayed on the vessel and the rotor after mixing were obtained from equations 4.5 and 4.6.

Chapter 4: Dry Coating Results and Discussions

The mass of particles that adhered on the wall of the vessel ($m_{particle's\ mass\ on\ the\ wall}$) and the rotor ($m_{particle's\ mass\ on\ the\ rotor}$) was estimated by:

$$m_{particle's\ mass\ on\ the\ wall} = m_{vessel\ after\ mixing} - m_{vessel\ before\ mixing} \quad (Eq. 4.5)$$

$$m_{particle's\ mass\ on\ the\ rotor} = m_{rotor\ after\ mixing} - m_{rotor\ before\ mixing} \quad (Eq. 4.6)$$

Since some particles stayed on the surface of the mixer, the actual coated mass of guest particles was less than the value that was calculated for coating (see Chapter 2, table 2.2). In this study, the mass percentage of particles adhered on the wall of vessel and rotor ($\varphi_{1\%}$) was calculated by:

$$\varphi_{1\%} = \frac{m_{particle's\ mass\ on\ the\ wall} + m_{particle's\ mass\ on\ the\ rotor}}{m_{guest} + m_{host}} \times 100\% \quad (Eq. 4.7)$$

Where $\varphi_{1\%}$ is the percentage of guest particles that adhered on the wall of the vessel and on the surface of the rotor, m_{guest} and m_{host} are mass of initial mass of guest and host powder before mixing.



Fig. 4.5 The photo of sieve shaker (Retsch, France)

Besides, after mixing, mixed particles were sieved by a sieve shaker (Retsch, France, see figure 4.5), because before the mixing, $\gamma\text{-Al}_2\text{O}_3$ was sieved at 63-90 μm before applying for coating and S.S316L was sieved more than 63 μm to prepare the new support in order to eliminate their difference in particle size distribution. After mixing, by sieving mixed particles (such as Zeolite^{LD}/ $\gamma\text{-Al}_2\text{O}_3$) it is possible to know how many guest particles have not been coated with the host particles. In this study, a 63 μm sieve was used to estimate the uncoated guest particles, that is to say, particles with particle size less than 63 μm are considered as uncoated guest particles.

Chapter 4: Dry Coating Results and Discussions

Therefore, uncoated particles include two sections: the particles adhered to the mixer (the vessel and rotor) and the particles that the size is less than 63 μm . Here mass fraction of uncoated particles ($\varphi\%$) was calculated by:

$$\varphi\% = \varphi_{1\%} + \varphi_{2\%} \quad (\text{Eq. 4.8})$$

Where $\varphi_{1\%}$ is the mass fraction of uncoated particles, $\varphi_{2\%}$ is the mass fraction of the particles that the size less than 63 μm after sieving ($m_{\text{size less than } 63 \mu\text{m after sieving}}$), which is given as follows:

$$\varphi_{2\%} = \frac{m_{\text{size less than } 63 \mu\text{m after sieving}}}{m_{\text{guest}} + m_{\text{host}}} \times 100\% \quad (\text{Eq. 4.9})$$

The mass fraction of uncoated guest particles ($\varphi\%$) can be used to evaluate the quality of coating, the smaller the mass fraction of uncoated guest particles, the better the result of the coating. The mass fraction of uncoated guest particles ($\varphi\%$) of 18 samples is shown in figure 4.6.

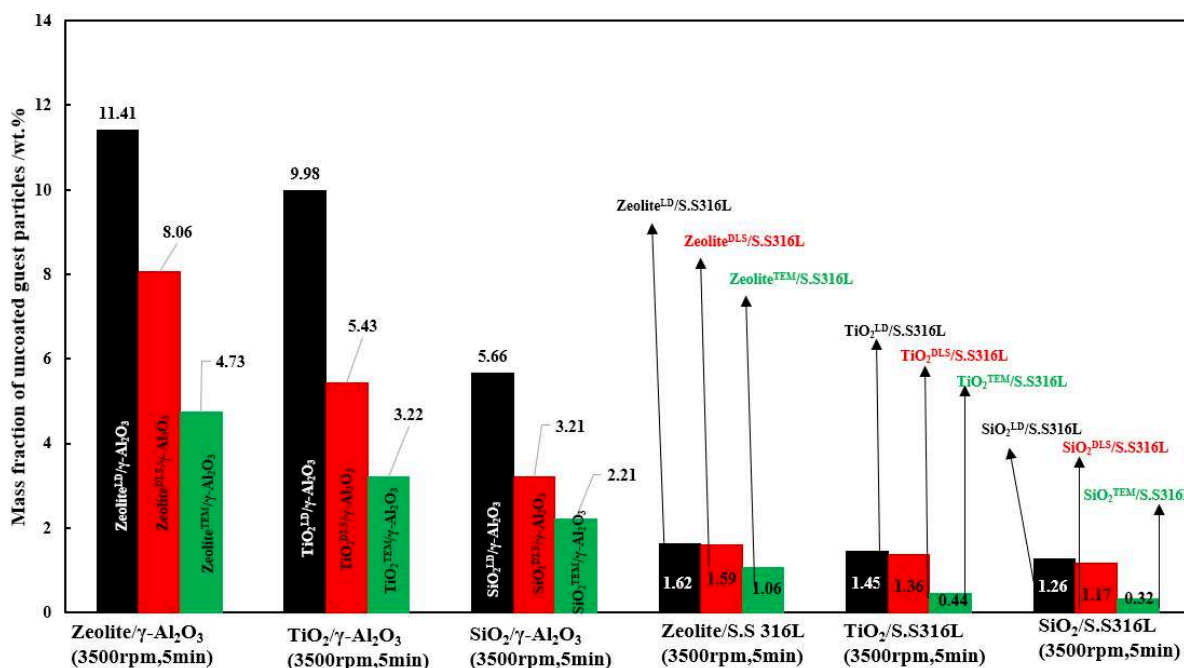


Fig. 4.6 Mass fractions of uncoated guest particles in the preparation of new supports under 3500rpm, 5min.

*LD (laser diffraction), DLS (dynamic light scattering), TEM (transmission electron microscope).

It was found that among all the new supports, Zeolite^{LD}/γ-Al₂O₃, Zeolite^{DLS}/γ-Al₂O₃, and TiO₂^{LD}/γ-Al₂O₃ these three supports have the largest number of guest particles uncoated on the host particles in the process of preparation, the mass fraction of uncoated guest particles respectively is 11.41%,

8.06%, and 9.98%. It is worth noting that for the same host particles, e.g., for γ -Al₂O₃ particles, uncoated guest particles of Zeolite^{LD} are more than Zeolite^{DLS} and Zeolite^{TEM}. This is possible because a large amount of agglomerated Zeolite^{LD} particles was broken under high shearing mixing (3500 rpm) in the process of preparation of Zeolite^{LD}/ γ -Al₂O₃, which resulted in the actual preparation of Zeolite^{LD}/ γ -Al₂O₃ requiring less mass than the theoretically calculated one. The percentage by mass of guest particles used in the coating experiment was calculated based on the assumption of 100% surface coverage of the host particles with a monolayer of guest particles (see Chapter 2, paragraph 2.2.2.3). Excess Zeolite^{LD} particles stayed on the walls of the vessel and the surface of the rotor. Besides, because high rotation speed produced high energy to particles and created drastic collisions for particle-particle and particle-wall. Therefore, high rotation caused an increase of local temperature of the powder. If this is the case, it is not only beneficial for the guest particles to coat on the host particles, but also promoted adhesion of the guest particles to adhere to the steel vessel and rotor of Picomix.

Additionally, unlike host particle γ -Al₂O₃, Zeolite, TiO₂, and SiO₂ particles in the process of coating with S.S316L (Zeolite/S.S316L, SiO₂/S.S316L, and TiO₂/S.S316L), much fewer mass fraction of uncoated guest particles were observed. Furthermore, the amount of uncoated guest particles is not very different, the mass fraction of uncoated guest particles is 0.33-1.62 wt.%. This phenomenon could be explained by following four reasons:

1) Both host particle and the material of Picomix are steel, which means both are equally attractive to particles (adhesion force will be the same), this could be the reason that why for the same guest particles (such as Zeolite), different host particles of γ -Al₂O₃ and S.S316L, the Zeolite particles not coated to the γ -Al₂O₃ are more than S.S316L.

2) S.S316L is harder than γ -Al₂O₃, there may be no deformation between guest particles and S.S316L in the process of coating.

3) It could be related to the sieving process, although the same parameters were set during the sieving process, the quality of the sieving was also confirmed after the sieving was completed, there may still be a small amount of small γ -Al₂O₃ particles (the size is less than 63 μ m) adhering to the surface of larger γ -Al₂O₃ particles, which will cause the sieving to fail to separate them. However, these small γ -Al₂O₃ particles will fall off during the high-speed mixing process. Then at the end of the mixing, it is re-sieved out during the sieving process, these amounts of small γ -Al₂O₃ particles are also counted in the uncoated particles, making the number of uncoated particles increase.

4) The surface morphology of the γ -Al₂O₃ particles (see Chapter 3, figure 3.7a) shows that some γ -Al₂O₃ shapes are not spherical, and these γ -Al₂O₃ may be damaged by the high-speed rotation at 3500 rpm and then sieved out during the sieving process. Since $\phi_{2\%}$ is the mass fraction of the particles that the size less than 63 μm after sieving of coatings, thus, as long as the particles smaller than 63 μm were regarded as uncoated guest particles, this could be one of the reasons that the mass fraction of uncoated guest particles is high in γ -Al₂O₃.

4.4 The effect of guest and host particles on coating process

Two host particles S.S316L and γ -Al₂O₃ were used in this work, these two powders are different by their density and their size distribution (see Chapter 3, table 3.1 and figure 3.2). The γ -Al₂O₃ powder is porous with a specific surface of 148.96 m²/g, however, S.S316L is non-porous. Also, from Chapter 3, figure 3.7, we note a rather smooth surface for S.S316L and rougher for γ -Al₂O₃.

The effect of guest and host particles has been investigated in this section. Host particle of S.S316L (mean diameter $dp_{(3,2)} = 98.3 \mu\text{m}$) and γ -Al₂O₃ (mean diameter $dp_{(3,2)} = 67 \mu\text{m}$), three guest particles Zeolite, TiO₂, and SiO₂ (mean diameter $dp_{(3,2)}$ see Chapter 3, table 3.5). The operating conditions were summarized in table 4.4.

Table 4.4 Operating conditions

Device	Rotation speed (rpm)	Operating time (min)	Filling ratio (%)	Mass of host and guest (g)
Picomix	3500	5	40	See table 2.2

4.4.1 Size distribution analysis

Figure 4.7 displays the size distribution of coated particles with different guest particles. The size of three nanoparticles TiO₂, SiO₂, and Zeolite were analyzed by three different methods, LD (laser diffraction), DLS (dynamic light scattering), and TEM (transmission electron microscope). The materials with size analyzed by the three methods were labeled respectively: Zeolite^{LD}, Zeolite^{DLS}, Zeolite^{TEM}, TiO₂^{LD}, TiO₂^{DLS}, TiO₂^{TEM}, SiO₂^{LD}, SiO₂^{DLS}, and SiO₂^{TEM}. Therefore, after coating, the uncoated powder was named Zeolite^{LD}/ γ -Al₂O₃, Zeolite^{DLS}/ γ -Al₂O₃, Zeolite^{TEM}/ γ -Al₂O₃, etc.

As is shown in figure 4.7, the prepared new supports Zeolite^{LD}/ γ -Al₂O₃, Zeolite^{DLS}/ γ -Al₂O₃, and Zeolite^{TEM}/ γ -Al₂O₃ (see figure 4.7a); TiO₂^{LD}/ γ -Al₂O₃, TiO₂^{DLS}/ γ -Al₂O₃, and TiO₂^{TEM}/ γ -Al₂O₃ (see figure 4.7b); SiO₂^{LD}/ γ -Al₂O₃, SiO₂^{DLS}/ γ -Al₂O₃, and SiO₂^{TEM}/ γ -Al₂O₃ (see figure 4.7c) display similar size distribution as γ -Al₂O₃ particles (the original γ -Al₂O₃ particles present a narrow size distribution with one mode locating at 67.7 μ m). There are no small peaks that have been observed, which indicates good coating, it is also possible that all coated particles were sieved before measurement to evaluate the uncoated guest particles, the mass fraction of uncoated guest particles has been described in the above section 4.2.

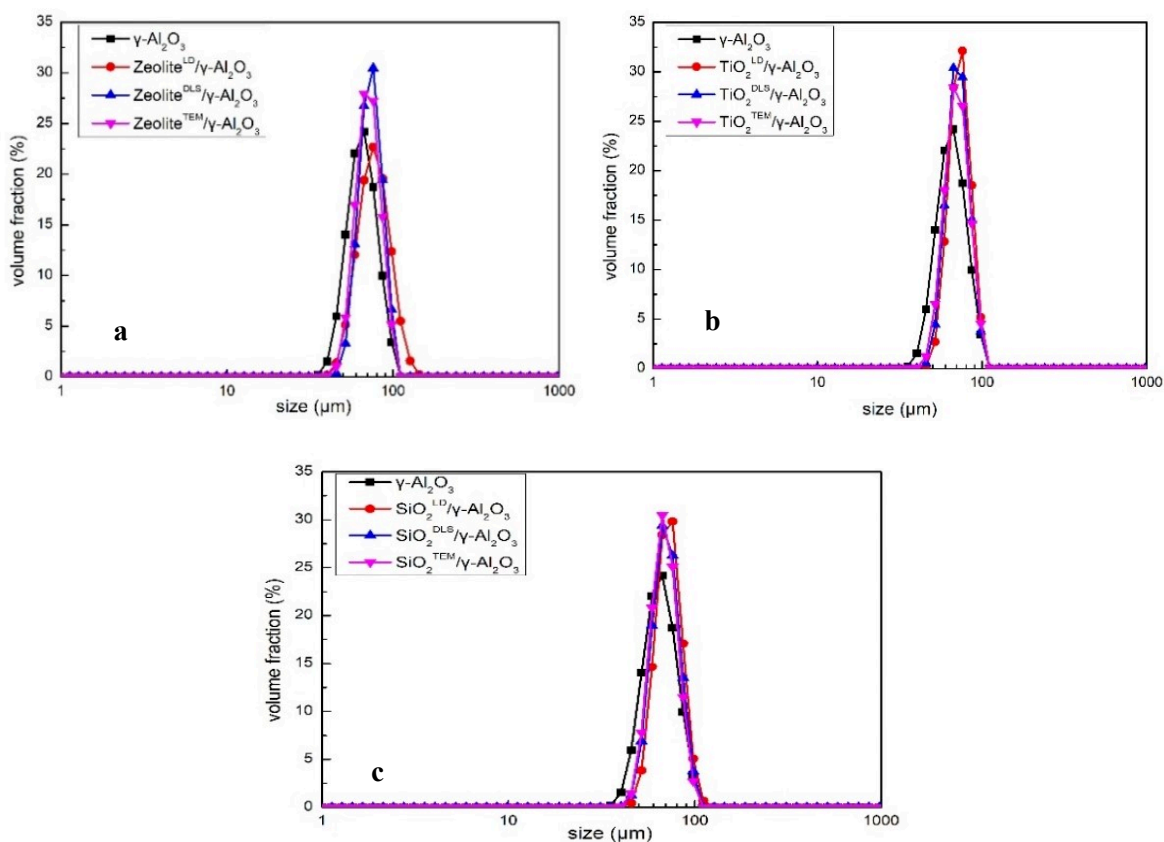


Fig.4.7 Particle size distribution of coated particle (a) Zeolite/ γ -Al₂O₃; (b) TiO₂/ γ -Al₂O₃; (c) SiO₂/ γ -Al₂O₃.

Fig.4.8 presents the size distribution of coated particles of Zeolite^{LD}/S.S316L, Zeolite^{DLS}/S.S316L, and Zeolite^{TEM}/S.S316L (see figure 4.8a); TiO₂^{LD}/S.S316L, TiO₂^{DLS}/S.S316L, and TiO₂^{TEM}/S.S316L (see figure 4.8b); SiO₂^{LD}/S.S316L, SiO₂^{DLS}/S.S316L, and SiO₂^{TEM}/S.S316L (see figure 4.8c). It can be seen that all peaks are located around 100 μ m. More specifically, TiO₂/S.S316L and SiO₂/S.S316L particle provide almost the same peak as the original S.S316L particles, nevertheless, the peak of Zeolite/S.S316L

has a bit different from the original S.S316L. This is because Zeolite has a big size compared with TiO_2 and SiO_2 .

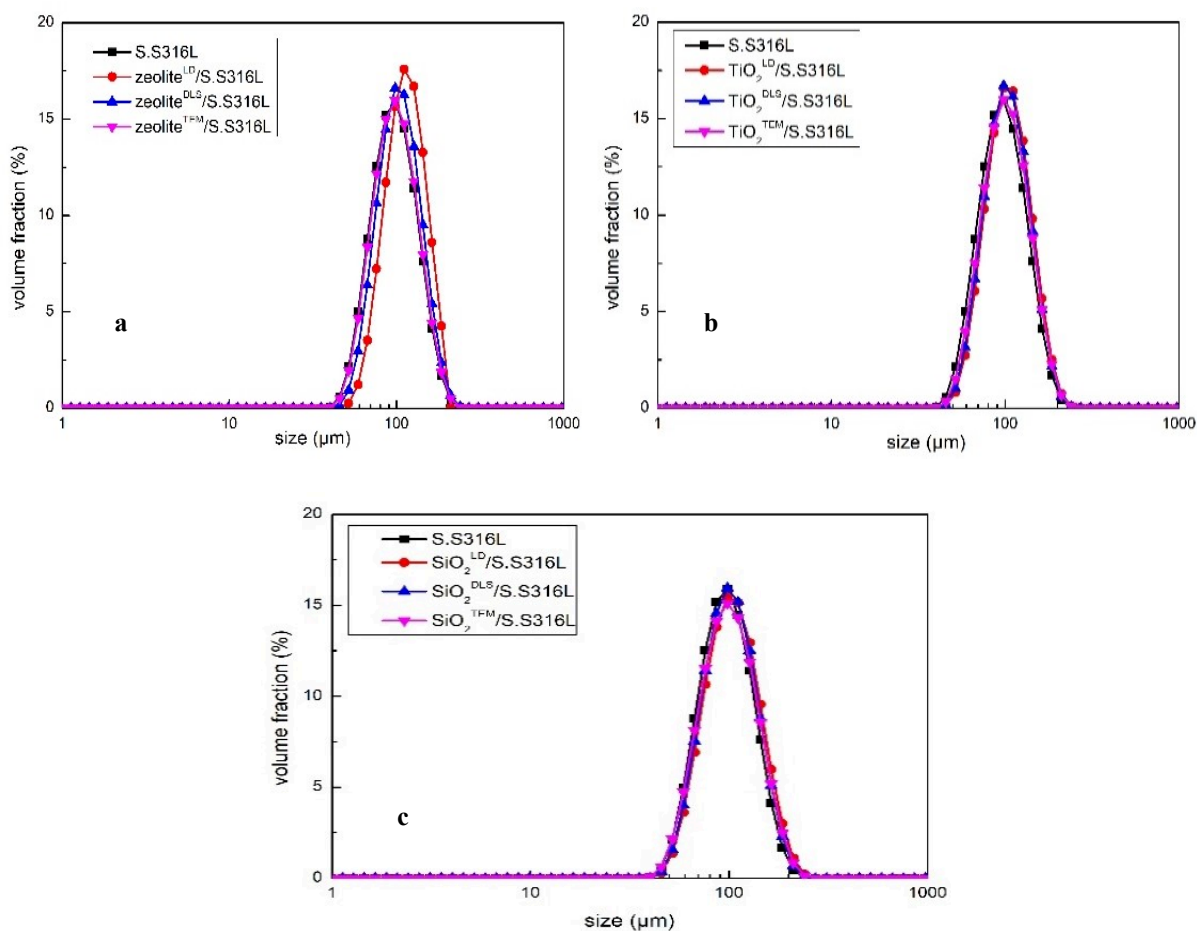


Fig.4.8 Particle size distribution of coated particle **(a)** Zeolite/S.S316L; **(b)** TiO_2 /S.S316L; **(c)** SiO_2 /S.S316L.

Table 4.5 summarizes the mean diameter ($dp_{(3,2)}$) of all coated particle, and the mass fraction of uncoated guest particles (φ_0).

Particle size distribution indicated that both S.S316L and $\gamma\text{-Al}_2\text{O}_3$ provided a good coating because the size of coated particles has all increased. Zeolite^{LD}/S.S316L gave a bigger size compared with Zeolite^{DLS}/S.S316L and Zeolite^{TEM}/S.S316L. TEM images (see Chapter 3, figure 3.3) have demonstrated that Zeolite has a lot of agglomeration, although, after 3500rpm, 5min, on the surface of Zeolite^{LD}/S.S316L might still have aggerated Zeolite^{LD} particle. This may be the reason that why Zeolite^{LD}/S.S316L presented

Chapter 4: Dry Coating Results and Discussions

the largest size compared with all coated particles. Meanwhile, the mass fraction of uncoated guest particles proved that only 1.62% of Zeolite^{LD} stayed on the surface of mixer (the vessel and rotor).

Table 4.5 Mean diameter ($dp_{(3,2)}$) of all coated particle, and the mass fraction of uncoated guest particles ($\varphi\%$)

Samples	Mean diameter $dp_{(3,2)}$ (μm)	Mass fraction of uncoated guest particles (%)	Samples	Mean diameter $dp_{(3,2)}$ (μm)	Mass fraction of uncoated guest particles (%)
$\gamma\text{-Al}_2\text{O}_3$	67.7		S.S316L	98.3	
Zeolite ^{LD} / $\gamma\text{-Al}_2\text{O}_3$	79.4	11.41	Zeolite ^{LD} /S.S316L	115	1.62
Zeolite ^{DLS} / $\gamma\text{-Al}_2\text{O}_3$	76.9	8.06	Zeolite ^{DLS} /S.S316L	105	1.59
Zeolite ^{TEM} / $\gamma\text{-Al}_2\text{O}_3$	74.2	4.73	Zeolite ^{TEM} /S.S316L	99.9	1.06
TiO ₂ ^{LD} / $\gamma\text{-Al}_2\text{O}_3$	76.5	9.98	TiO ₂ ^{LD} /S.S316L	106	1.45
TiO ₂ ^{DLS} / $\gamma\text{-Al}_2\text{O}_3$	74.4	5.43	TiO ₂ ^{DLS} /S.S316L	104	1.36
TiO ₂ ^{TEM} / $\gamma\text{-Al}_2\text{O}_3$	73.9	3.22	TiO ₂ ^{TEM} /S.S316L	103	0.44
SiO ₂ ^{LD} / $\gamma\text{-Al}_2\text{O}_3$	75.9	5.66	SiO ₂ ^{LD} /S.S316L	103	1.26
SiO ₂ ^{DLS} / $\gamma\text{-Al}_2\text{O}_3$	71.8	3.21	SiO ₂ ^{DLS} /S.S316L	102	1.17
SiO ₂ ^{TEM} / $\gamma\text{-Al}_2\text{O}_3$	72.8	2.21	SiO ₂ ^{TEM} /S.S316L	100	0.32

4.4.2 Characterization of the coating of the particles

From the size distribution, we can see that there are guest particles coated on the surface of S.S316L and $\gamma\text{-Al}_2\text{O}_3$ because the particle size of the coated particles is larger than that of the original host particles.

Since the coated particles were firstly sieved with a sieve larger than 63 μm , thus, only one main peak was observed in the particle size analysis. In this section, we will analyze each coated powder individually by SEM (all of the coated particles were sieved before the SEM analysis) for obtaining a better understanding of coating.

4.4.2.1 Analysis of the quality of the coating of Zeolite/ $\gamma\text{-Al}_2\text{O}_3$, TiO₂/ $\gamma\text{-Al}_2\text{O}_3$ and SiO₂/ $\gamma\text{-Al}_2\text{O}_3$

First of all, the surface morphologies of Zeolite, $\gamma\text{-Al}_2\text{O}_3$, and Zeolite/ $\gamma\text{-Al}_2\text{O}_3$ (Zeolite^{LD}/ $\gamma\text{-Al}_2\text{O}_3$, Zeolite^{DLS}/ $\gamma\text{-Al}_2\text{O}_3$, and Zeolite^{TEM}/ $\gamma\text{-Al}_2\text{O}_3$) are shown in figure 4.9. Apparently, the guest particle Zeolite

agglomerated together because of the strong cohesive force. The γ -Al₂O₃ particles exhibit a relatively uniform spherical shape and smooth surface.

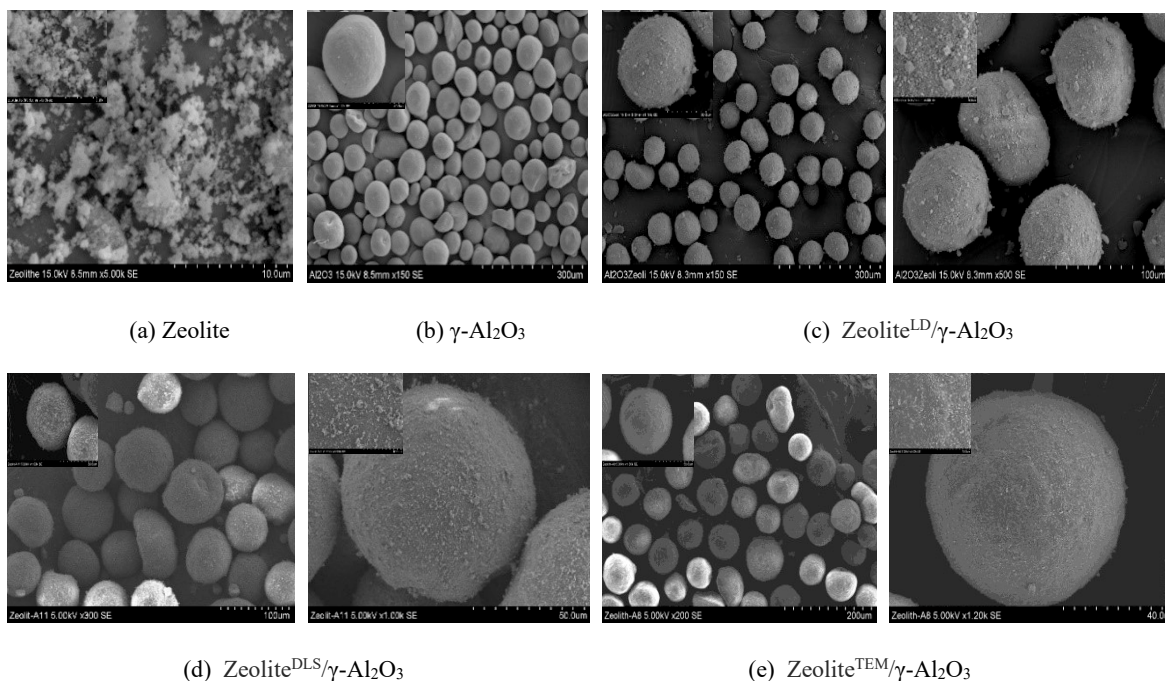


Fig. 4.9 SEM images of original Zeolite powder (a), γ -Al₂O₃ powder (b), Zeolite^{LD}/ γ -Al₂O₃ (c), Zeolite^{DLS}/ γ -Al₂O₃ (d), Zeolite^{TEM}/ γ -Al₂O₃ (e) coating under 3500rpm, 5min in Picomix.

It was found that Zeolite^{LD}/ γ -Al₂O₃, Zeolite^{DLS}/ γ -Al₂O₃, and Zeolite^{TEM}/ γ -Al₂O₃ present the same shape as host particle γ -Al₂O₃ but no smooth surface (see figure 4.9c-e). In terms of Zeolite^{LD}/ γ -Al₂O₃, there are lots of small debris (see figure 4.9c) which can be seen on the surface and cannot be easily removed by sieving because of the large number of Zeolite agglomerations. Compared with Zeolite^{LD}/ γ -Al₂O₃ and Zeolite^{DLS}/ γ -Al₂O₃ (see figure 4.9d), almost no debris can be seen on the surface of Zeolite^{TEM}/ γ -Al₂O₃ (see figure 4.9e). A conclusion can be made here that γ -Al₂O₃ coating with Zeolite in the TEM size has the ideal coating effect.

Figure 4.10 presents the images from SEM analysis of TiO₂, γ -Al₂O₃, and TiO₂/ γ -Al₂O₃ (TiO₂^{LD}/ γ -Al₂O₃, TiO₂^{DLS}/ γ -Al₂O₃, and TiO₂^{TEM}/ γ -Al₂O₃). Guest particle TiO₂ gives a severe agglomeration phenomenon because of its strong interparticle force (van der Waals' force). It can be seen that TiO₂^{LD}/ γ -Al₂O₃ particles (see figure 4.10c) show a rough surface, maybe because too many TiO₂ particles bonded with γ -Al₂O₃. The surface morphologies of TiO₂^{DLS}/ γ -Al₂O₃ (see figure 4.10d) show a relatively smooth surface though there are agglomeration phenomena that can be observed. Unlike TiO₂^{LD}/ γ -Al₂O₃ and TiO₂^{DLS}/ γ -Al₂O₃,

the surface morphologies of $\text{TiO}_2^{\text{TEM}}/\gamma\text{-Al}_2\text{O}_3$ (see figure 4.10e) present a quite smooth surface, however, a little bit agglomerated of TiO_2 particles were captured. Comparing the coating results of the three, we can conclude that $\text{TiO}_2^{\text{TEM}}/\gamma\text{-Al}_2\text{O}_3$ gives the best coating.

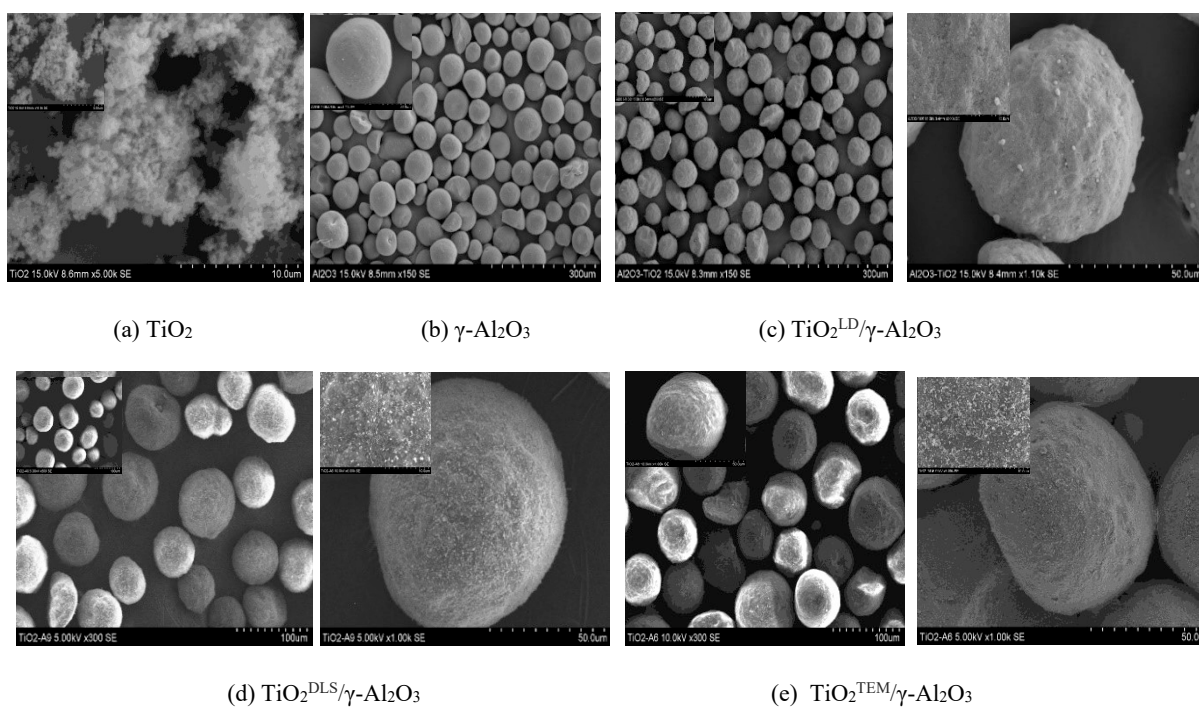


Fig. 4.10 SEM images of TiO_2 (a), $\gamma\text{-Al}_2\text{O}_3$ (b), and new supports $\text{TiO}_2^{\text{LD}}/\gamma\text{-Al}_2\text{O}_3$ (c), $\text{TiO}_2^{\text{DLS}}/\gamma\text{-Al}_2\text{O}_3$ (d), $\text{TiO}_2^{\text{TEM}}/\gamma\text{-Al}_2\text{O}_3$ (e) coating under 3500rpm, 5min in Picomix.

Figure 4.11 shows the surface morphologies of SiO_2 , $\gamma\text{-Al}_2\text{O}_3$, and $\text{SiO}_2/\gamma\text{-Al}_2\text{O}_3$ ($\text{SiO}_2^{\text{LD}}/\gamma\text{-Al}_2\text{O}_3$, $\text{SiO}_2^{\text{DLS}}/\gamma\text{-Al}_2\text{O}_3$, and $\text{SiO}_2^{\text{TEM}}/\gamma\text{-Al}_2\text{O}_3$). A large number of agglomerated SiO_2 particles were observed (see figure 4.11a). After coating with $\gamma\text{-Al}_2\text{O}_3$, the agglomerated SiO_2 particles were found to adhere onto the surface of $\gamma\text{-Al}_2\text{O}_3$ particles and form relatively uniform coatings (see figure 4.11c-e). No visible chips were seen on the surface of $\text{SiO}_2^{\text{LD}}/\gamma\text{-Al}_2\text{O}_3$, $\text{SiO}_2^{\text{DLS}}/\gamma\text{-Al}_2\text{O}_3$, and $\text{SiO}_2^{\text{TEM}}/\gamma\text{-Al}_2\text{O}_3$. But more specifically, $\text{SiO}_2^{\text{LD}}/\gamma\text{-Al}_2\text{O}_3$ (see figure 4.11c) gives multiple layers, which means agglomerated SiO_2^{LD} particles. The surface of $\text{SiO}_2^{\text{DLS}}/\gamma\text{-Al}_2\text{O}_3$ (see figure 4.11d) shows a relatively smooth surface. Nevertheless, when the magnification of the measurement is increased, the agglomerated $\text{SiO}_2^{\text{DLS}}$ particles can be found (see figure 4.11d). It was noted that $\text{SiO}_2^{\text{TEM}}$ particles (see figure 4.11e) look uniformly dispersed on the surface of $\gamma\text{-Al}_2\text{O}_3$ particles. No agglomerated particles were captured even at high magnification (5000). This is because during the calculation of the coating (see Chapter 2, table 2.2), because $\text{SiO}_2^{\text{TEM}}$ has a small

particle size, very little mass was used in the experiment and each $\text{SiO}_2^{\text{TEM}}$ particle had the opportunity to go into a collision with the $\gamma\text{-Al}_2\text{O}_3$ particles, which then formed the coating.

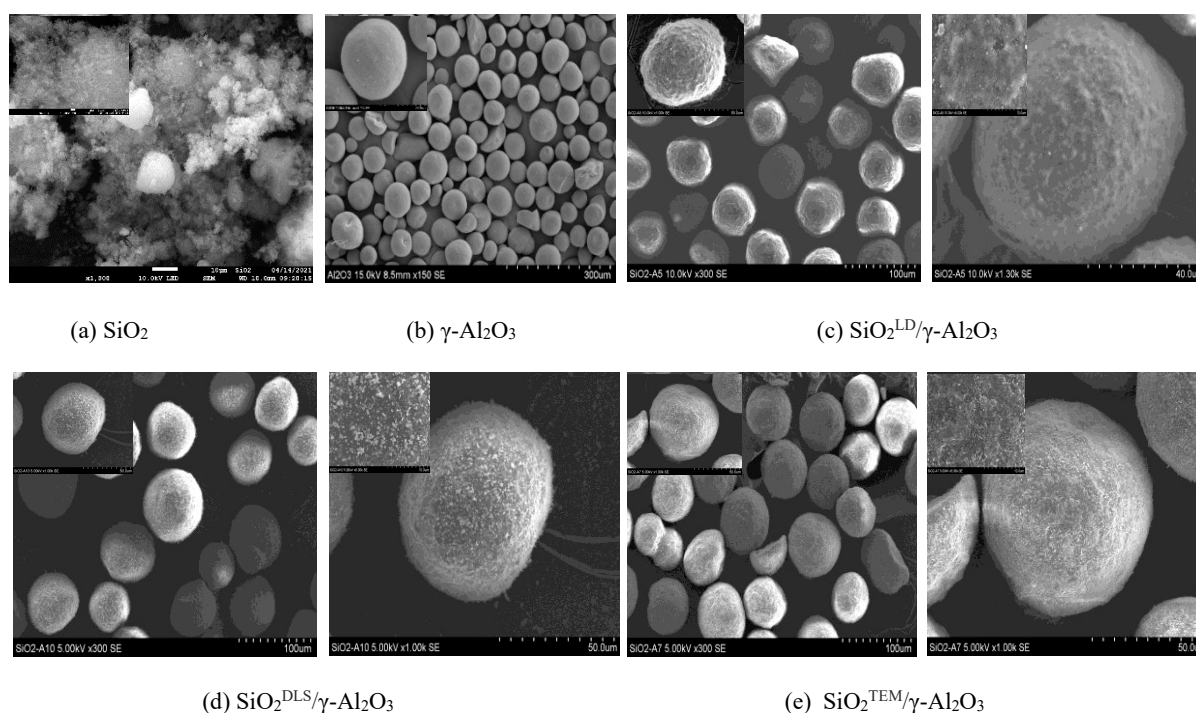


Fig. 4.11 SEM images of SiO_2 (a), $\gamma\text{-Al}_2\text{O}_3$ (b), and new supports $\text{SiO}_2^{\text{LD}}/\gamma\text{-Al}_2\text{O}_3$ (c), $\text{SiO}_2^{\text{DLS}}/\gamma\text{-Al}_2\text{O}_3$ (d), $\text{SiO}_2^{\text{TEM}}/\gamma\text{-Al}_2\text{O}_3$ (e) under 3500rpm, 5min in Picomix.

4.4.2.2 Analysis of the quality of the coating of Zeolite/S.S316L, $\text{TiO}_2/\text{S.S316L}$, and $\text{SiO}_2/\text{S.S316L}$

In this part, we will examine the quality of the coating for the host S.S316L particles and the three powders (Zeolite, SiO_2 , and TiO_2) invited for the three analysis methods (LD (laser diffraction), DLS (dynamic light scattering), and TEM (transmission electron microscope)).

The surface morphologies of original Zeolite particles, original S.S316L particles, and the coated particles Zeolite/S.S316L ($\text{Zeolite}^{\text{LD}}/\text{S.S316L}$, $\text{Zeolite}^{\text{DLS}}/\text{S.S316L}$, and $\text{Zeolite}^{\text{TEM}}/\text{S.S316L}$) are shown in figure 4.12. It is obvious that guest Zeolite particles are agglomerated together (see figure 4.12a) because it is a nanoparticle, and the adhesion between the particles is greater than its gravity, making it less fluidity/poor flowability (see Chapter 3, table 3.6) and thus agglomerates in large quantities. The S.S316L particles (see figure 4.12b) exhibits a relatively smooth surface and spherical shape. It is very important to note that not every S.S316L particle is spherical, some S.S316L particles have a very small part of the surface linked,

generally, the coatings are very difficult to occur in these small parts. Zeolite^{LD}/S.S316L particles (see figure 4.12c) present discontinuous coating (occurred on the small part of the surface linked with S.S316L) and a great quantity of agglomerated Zeolite^{LD} particles, which is because the mass of zeolite particles needed to coat 136.46 g S.S316L particles is less than the calculated mass (11.02g of Zeolite particles). Which resulted in many Zeolite particles had no place to stick except on the surface of Zeolite^{LD}/S.S316L to form a multi-layer coating or to stick on the surface of the mixer.

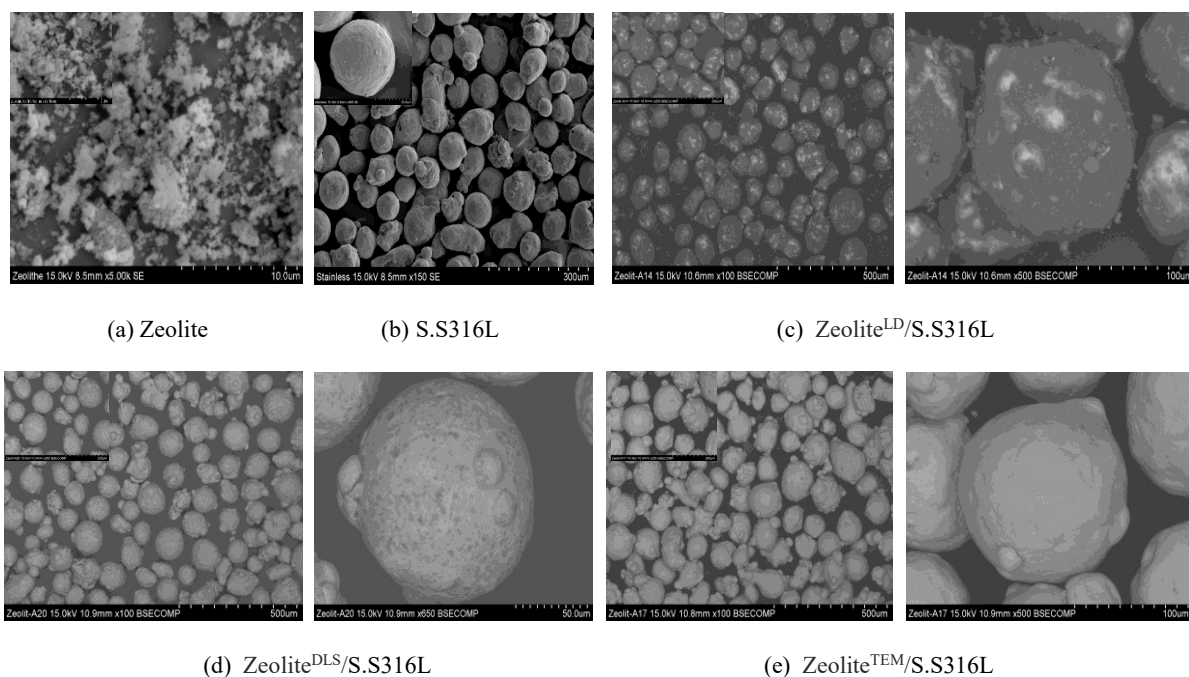


Fig. 4.12 SEM images of Zeolite (a), S.S316L (b), and coated particles Zeolite^{LD}/S.S316L (c), Zeolite^{DLS}/S.S316L (d), Zeolite^{TEM}/S.S316L (e) under 3500rpm, 5min in Picomix.

Compared to Zeolite^{LD}/S.S316L particles and Zeolite^{DLS}/S.S316L particles (see figure 4.12d) show a better coating results because Zeolite^{DLS}/S.S316L particles do not show agglomeration of large particles. In the case of Zeolite^{TEM}/S.S316L particles (see figure 4.12e), different from both of Zeolite^{LD}/S.S316L and Zeolite^{LD}/S.S316L coatings, Zeolite^{TEM}/S.S316L clearly gives the best coating with uniform dispersion and smooth surface.

Figure 4.13 shows the surface morphologies of TiO₂, S.S316L, and TiO₂/S.S316L particles (TiO₂^{LD}/S.S316L, TiO₂^{DLS}/S.S316L, and TiO₂^{TEM}/S.S316L). TiO₂^{LD}/S.S316L particles (see figure 4.13c) exhibited a good uniform coating but a multiple layer of TiO₂^{LD} particles. The morphologies of TiO₂^{DLS}/S.S316L (see figure 4.13d) and TiO₂^{TEM}/S.S316L (see figure 4.13e) present a very smooth surface,

Chapter 4: Dry Coating Results and Discussions

which implies a very good coating. In the results of particle size analysis in Chapter 3, we know that DLS and TEM provided the small size of guest particles. During the coating process, a small number of masses of guest particles $\text{TiO}_2^{\text{DLS}}$ and $\text{TiO}_2^{\text{TEM}}$ are needed (see Chapter 2, table 2.2), which may be just enough mass to coat $\text{TiO}_2^{\text{DLS}}$ and $\text{TiO}_2^{\text{TEM}}$ the surface of the host S.S316L particles, leaving no excess mass $\text{TiO}_2^{\text{DLS}}$ and $\text{TiO}_2^{\text{TEM}}$ to form multiple layers of coatings.

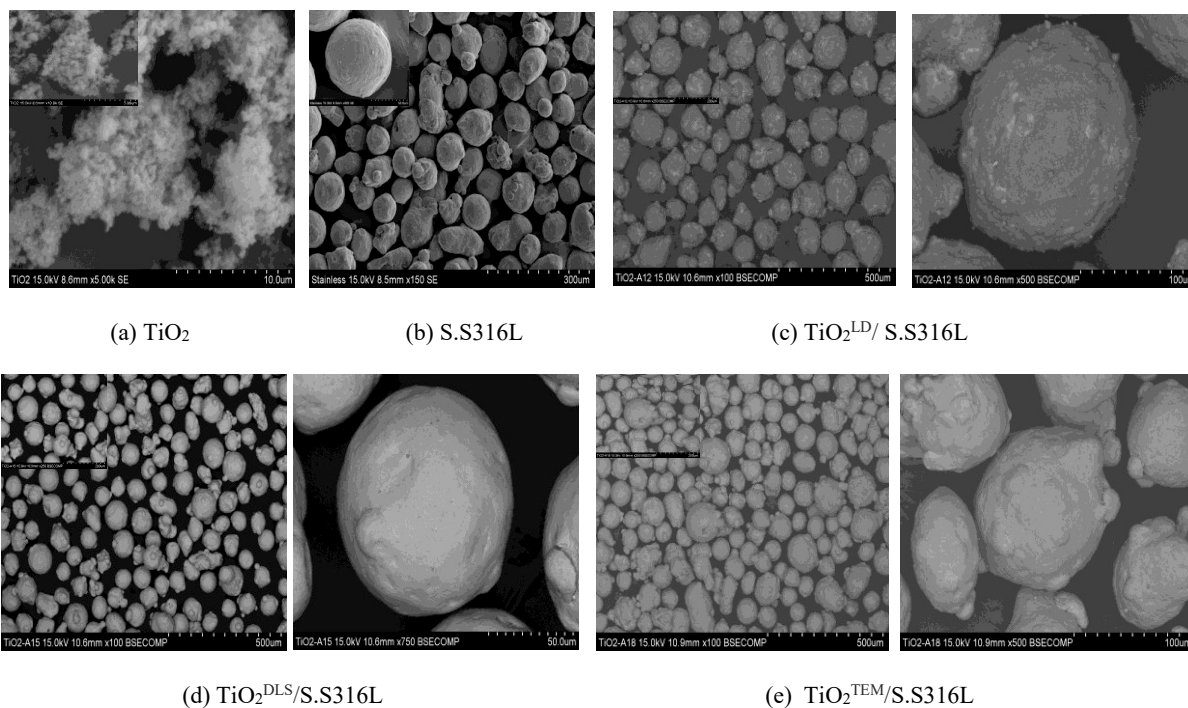


Fig. 4.13 SEM images of TiO_2 (a), S.S316L (b), and coated particles $\text{TiO}_2^{\text{LD}}/\text{S.S316L}$ (c), $\text{TiO}_2^{\text{DLS}}/\text{S.S316L}$ (d), $\text{TiO}_2^{\text{TEM}}/\text{S.S316L}$ (e) under 3500rpm, 5min in Picomix.

The surface morphologies of SiO_2 , S.S316L, and $\text{SiO}_2/\text{S.S316L}$ ($\text{SiO}_2^{\text{LD}}/\text{S.S316L}$, $\text{SiO}_2^{\text{DLS}}/\text{S.S316L}$, and $\text{SiO}_2^{\text{TEM}}/\text{S.S316L}$) are presented in figure 4.14. As a fine particle, SiO_2 (see figure 4.14a) cannot avoid agglomeration because of the strong interparticle force. $\text{SiO}_2^{\text{LD}}/\text{S.S316L}$ (see figure 4.14c) presents a discontinuous coating but not uniform, which can be seen from one $\text{SiO}_2^{\text{LD}}/\text{S.S316L}$ particle (see figure 4.14c), most of the surface of S.S316L was covered but some parts were not. The surface morphologies of $\text{SiO}_2^{\text{DLS}}/\text{S.S316L}$ (see figure 4.14d) demonstrates a good coating. Compared with the surface morphologies of $\text{SiO}_2^{\text{LD}}/\text{S.S316L}$ (see figure 4.14c), fewer agglomerated particles were captured. Among these three coatings, $\text{SiO}_2^{\text{TEM}}/\text{S.S316L}$ (see figure 4.14e) absolutely gives the best coating with a very smooth and visible surface.

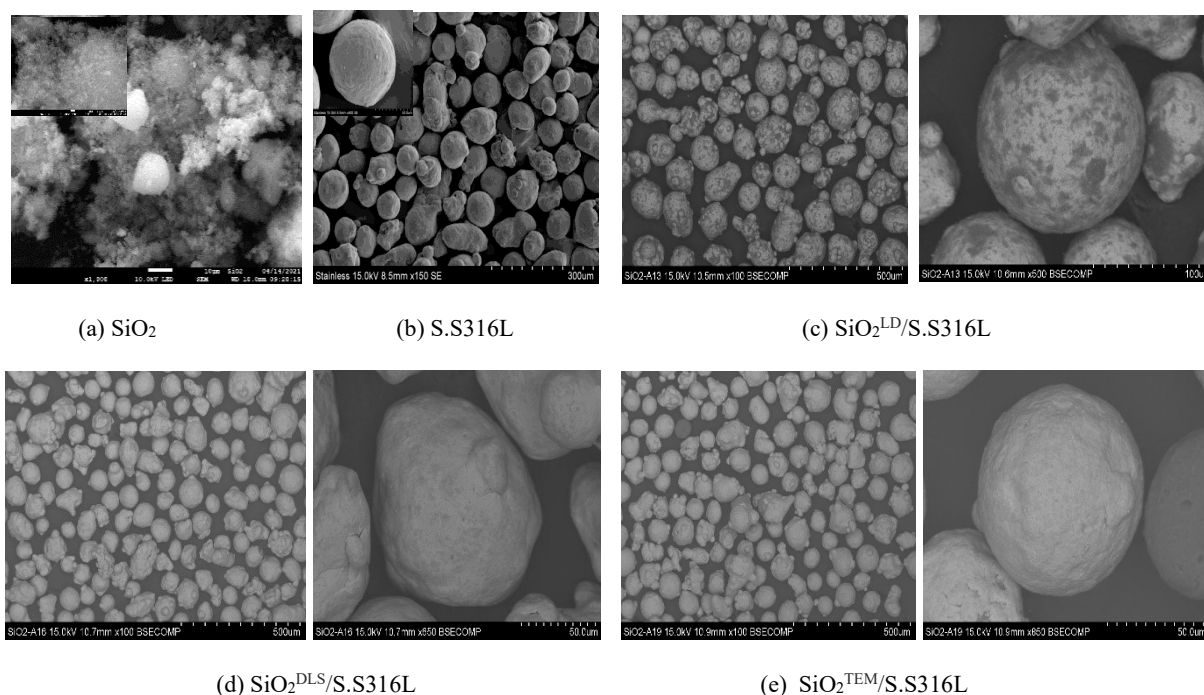


Fig. 4.14 SEM images of SiO₂ (a), S.S316L (b), and coated particles SiO₂^{LD}/S.S316L (c), SiO₂^{DLS}/S.S316L (d), SiO₂^{TEM}/S.S316L (e) under 3500rpm, 5min in Picomix.

The analysis of the SEM images of the coated particles showed that each host particle was coated by guests, but some of the coatings were uneven and discontinuous, such as Zeolite^{LD}/S.S316L, Zeolite^{DLS}/S.S316L, TiO₂^{LD}/S.S316L, SiO₂^{LD}/S.S316L, and SiO₂^{DLS}/S.S316L. This can be due to the different hardness of the particles, which leads to deformation, or due to the different mass of the guest particles that were used in the experiment (see Chapter 2, table 2.2). Meanwhile, for the same guest particle, such as Zeolite, three different measurement methods (LD (laser diffraction), DLS (dynamic light scattering), TEM (transmission electron microscope)) provide three different sizes, which means these three particle sizes correspond to three different masses (see Chapter 2, table 2.2). Therefore, the results of the coating are known as SEM images, LD size give a multiple layer coating and often is accompanied by a lot of agglomerated guest particle, this could be because the theoretical calculated mass of the guest particles is much more than the mass of requires to cover the host particles in one coating layer, such as Zeolite^{LD}/γ-Al₂O₃, TiO₂^{LD}/γ-Al₂O₃, Zeolite^{LD}/S.S316L.

4.5 Calculation of coating thickness

The previous sections have given us important information that not all of the masses of the theoretically calculated guests are 100% coated onto the host. Some guests' particles are not coated onto the host, these uncoated guests have been described in section 4.2. Some of the coatings are clearly observed as a thick layer of coating, such as Zeolite^{LD}/ γ -Al₂O₃, TiO₂^{LD}/ γ -Al₂O₃, and Zeolite^{LD}/S.S316L, which indicated more than one layer of coating, hence it is necessary to know the thickness of the coating and built the correlation with the mass fraction of uncoated guest particles and coating consequence.

In this study, in order to know the thickness of the coating, cross-section samples were prepared to make the direct observation of the thickness of the coating layer possible. The preparation process includes two parts: resin sample preparation and polishing process (see figure 4.15), the detailed preparation process is as follows:

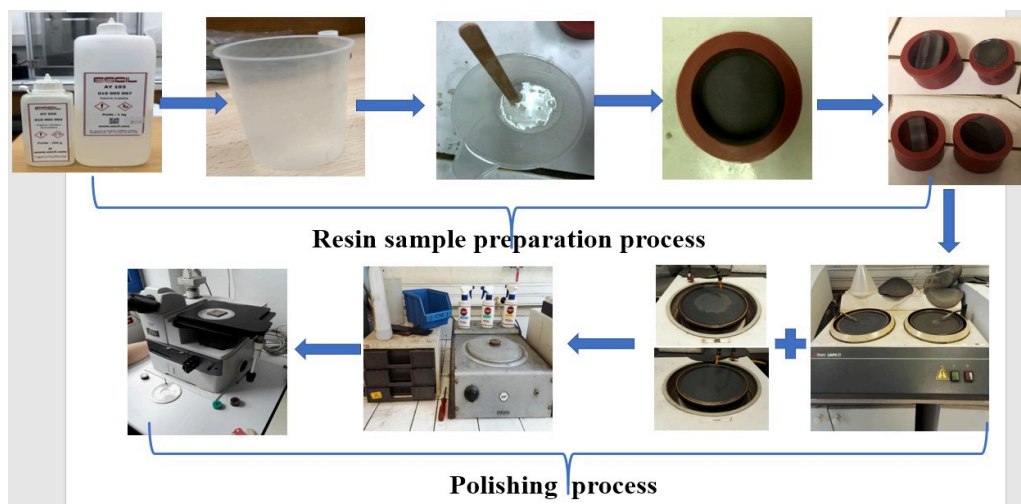


Fig.4.15 Schematic of the preparation of resin cross-section samples.

- 1) Prepared a solution: 25 ml resin + 5 ml stiffening agent (ratio of resin/stiffening agent should be 5);
- 2) Poured the solution into a 100ml white plastic cup and used a wood stick to stir the solution until there are no bubbles in the resin;
- 3) Put the sample into a mold (the sample has to cover the bottom of the mold) and poured the prepared mixture into the mold;

- 4) After more than 8 hours, took the prepared resin sample to polish;
- 5) Used a polisher (Struers LaboPol-21, Denmark) to polish the characterize surface. Polishing Machines with sanding discs grit 240, 400, 600, 1000, and 1200;
- 6) Continued polishing process in a micron-level polisher (6, 3, and 1 μ m) with the help of diamond slurry of 6, 3, and 1 μ m;
- 7) Used a photo-microscopy to check whether the polishing was enough.

When the resin samples were polished, they were characterized by SEM (see Chapter 2, paragraph 2.3.3). After obtaining the characterized SEM images, the thickness of the coating was measured directly using a ruler according to the size of the scale used for the characterization, and different thicknesses on one coated particle were measured as much as possible to reduce the error. The standard deviation was calculated by the following equation:

$$\sigma = \sqrt{\frac{\sum_{i=1}^n (X_i - \bar{X})^2}{N_t - 1}} \quad (\text{Eq. 4.10})$$

Where N_t = the number of data points, that is the points for different coating thicknesses; X_i = each of the value of the thickness, \bar{X} = the average thickness of X_i .

But, for some coated particles, the coating was assumed to be perfectly uniform because it was very homogeneous, therefore, no standard deviation was given in the next descriptions. However, in this study, only one or two particles were generally used for the evaluation of the thickness of the coating, thus, the next claim of the thickness may deviate from the actual thickness.

4.5.1 Thickness of Zeolite/ γ -Al₂O₃, TiO₂/ γ -Al₂O₃, and SiO₂/ γ -Al₂O₃

Figure 4.16 shows the SEM images of cross-section samples of Zeolite^{LD}/ γ -Al₂O₃, Zeolite^{DLS}/ γ -Al₂O₃, and Zeolite^{TEM}/ γ -Al₂O₃. It can be seen that each γ -Al₂O₃ particle is covered by Zeolite^{LD} particle (see figure 4.16-a1). The thickness of the coating is basically uniform (see figures 4.16-b1 and -c1) but somewhere can be seen a very thick layer (see figure 4.16-b1), which indicates agglomerated Zeolite^{LD} because of strong interparticle force. This result is corresponding to figure 4.9-c1. Figure 4.16-c1 was labeled based on its basic scale of 10 μ m and it shows in figure 4.16-d1. The thickness of Zeolite^{LD}/ γ -Al₂O₃ = 4.1 \pm 1.50 μ m. In order to decrease the deviation of assessment, different coating thicknesses of one particle were selected as much as possible.

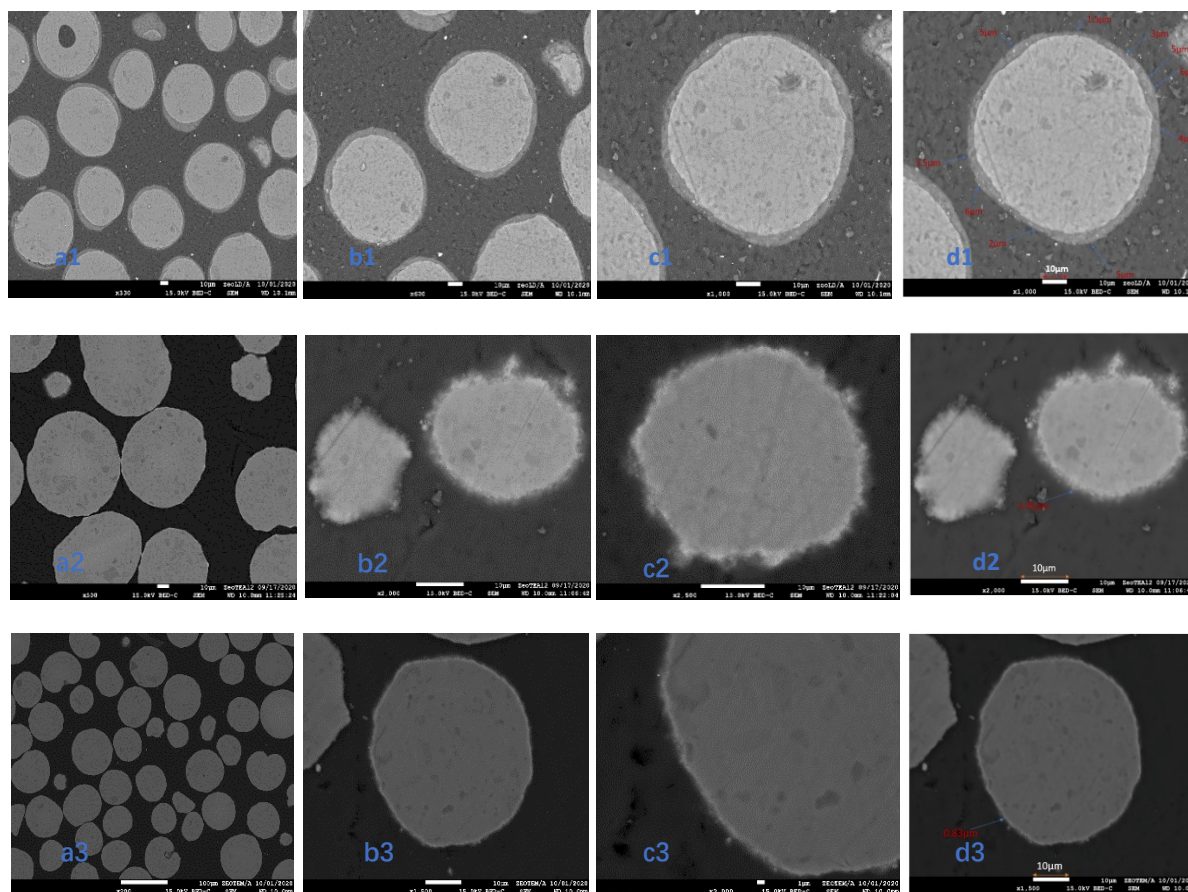


Fig.4.16 SEM images of cross-section samples of Zeolite^{LD}/γ-Al₂O₃ (a1-d1), Zeolite^{DLS}/γ-Al₂O₃ (a2-d2), and Zeolite^{TEM}/γ-Al₂O₃ (a3-d3) under 3500rpm, 5min of operating conditions.

From figure 4.16(a2-d2), we can observe that a thin layer of Zeolite^{DLS} particles covered all the γ-Al₂O₃ particles. However, the images (see figures 4.16-b2 and-c2) of increased magnification of the microscope do not give us very clear information on coating thickness, which is probably because Zeolite^{DLS} particles are not tightly coated on the surface of γ-Al₂O₃ particles, or maybe due to the too long time spend or strength on polishing, lead to damaged thin coated of Zeolite^{DLS} particles. Therefore, its thickness deviation is not considered and given as $1.05 \pm 0 \mu\text{m}$ (see figure 4.16-d2).

Figure 4.16(a3-d3) show a thin and very uniform coating of Zeolite^{TEM}/γ-Al₂O₃, this result is consistent with the surface morphologies of Zeolite^{TEM}/γ-Al₂O₃ (see figure 4.9e). Since the coating layer is very thin, and it is regarded as a homogeneous coating, no deviation will be given here, therefore, the thickness of the coating of Zeolite^{TEM}/γ-Al₂O₃ = $0.83 \pm 0 \mu\text{m}$.

Overall, the thickness of the coating of Zeolite^{LD}/ γ -Al₂O₃, Zeolite^{DLS}/ γ -Al₂O₃, and Zeolite^{TEM}/ γ -Al₂O₃, respectively, are $4.1 \pm 1.50 \mu\text{m}$, $1.05 \pm 0 \mu\text{m}$, $0.83 \pm 0 \mu\text{m}$. The results of this thickness assessment are in general agreement with the results of the SEM images (see figure 4.9c-e) and size distribution analysis (see figure 4.7a and table 4.5) in the previous part.

Figure 4.17 provides the SEM images of cross-section samples of TiO₂^{LD}/ γ -Al₂O₃, TiO₂^{DLS}/ γ -Al₂O₃, and TiO₂^{TEM}/ γ -Al₂O₃.

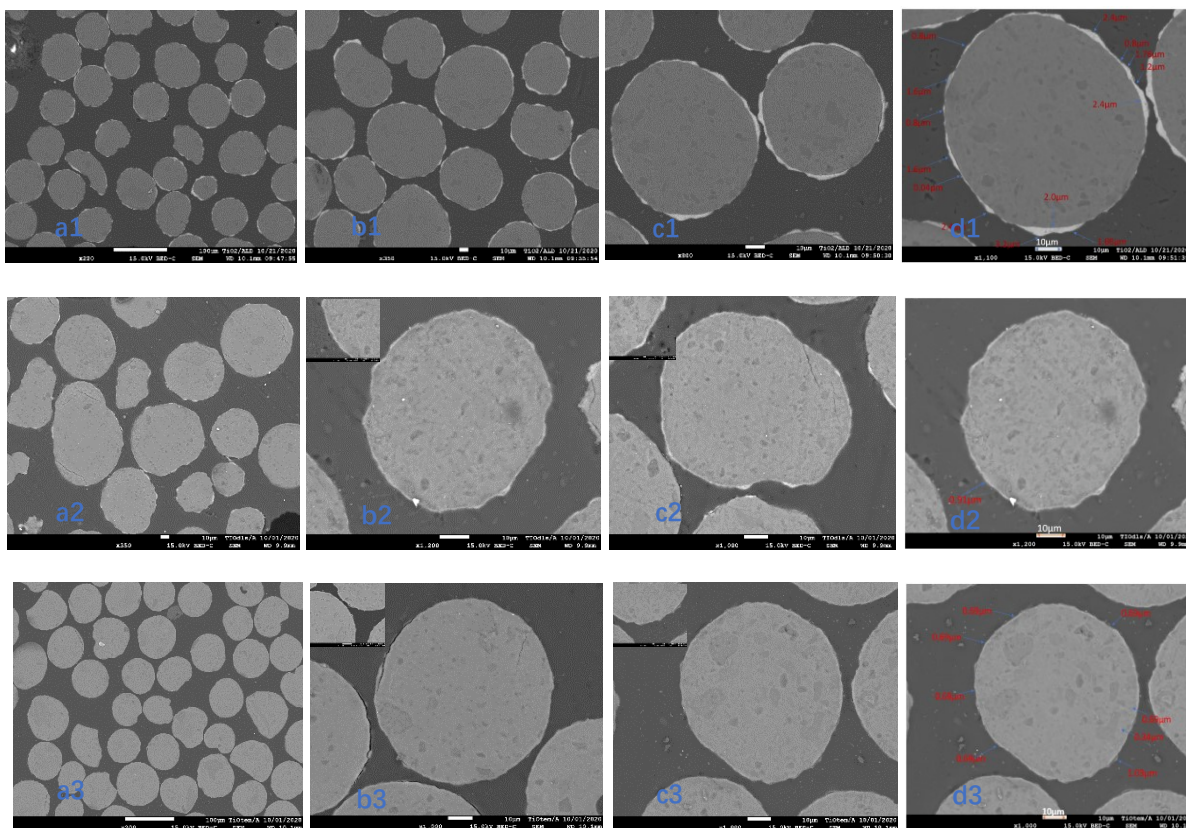


Fig.4.17 SEM images of cross-section samples of TiO₂^{LD}/ γ -Al₂O₃ (a1-d1), TiO₂^{DLS}/ γ -Al₂O₃ (a2-d2), and TiO₂^{TEM}/ γ -Al₂O₃ (a3-d3) under 3500rpm, 5min of operating conditions.

It was found that each γ -Al₂O₃ particle is covered with TiO₂^{LD} particle (see figure 4.17-a1), but some particles of γ -Al₂O₃ with more TiO₂^{LD} particles distributed on the surface, and some with less (see figures 4.17-b1 and-c1), which indicates that the coating is not very uniform. The reason for this phenomenon could be the agglomerated TiO₂^{LD} particles. The thickness of TiO₂^{LD}/ γ -Al₂O₃ = $1.68 \pm 0.81 \mu\text{m}$ (see figure 4.17d1), this value may differ a bit from the real thickness of TiO₂^{LD}/ γ -Al₂O₃ particle because one particle's thickness was estimated.

As for the SEM images of cross-section samples of $\text{TiO}_2^{\text{DLS}}/\gamma\text{-Al}_2\text{O}_3$, there are some white small fragments that can be observed (see figure 4.17a2). It is possible that these fragments were not originally coated $\text{TiO}_2^{\text{DLS}}$ particles or the coated $\text{TiO}_2^{\text{DLS}}$ particle was removed during the polishing process because of over polishing time or strength. A thin coating layer can be seen from figures 4.17b2 and c2, since this thickness looks very uniform, $\text{TiO}_2^{\text{DLS}}/\gamma\text{-Al}_2\text{O}_3$ is considered as a uniform coating. The thickness of the coating of $\text{TiO}_2^{\text{DLS}}/\gamma\text{-Al}_2\text{O}_3 = 0.91 \pm 0 \mu\text{m}$ was presented in figure 4.17d2.

A very thin coating layer was observed (see figures 4.17b3 and c3). It is noted that some chips are next to the $\text{TiO}_2^{\text{TEM}}/\gamma\text{-Al}_2\text{O}_3$ particle (see figure 4.17c3). These chips could be the uncoated $\text{TiO}_2^{\text{TEM}}$ particle or were removed $\text{TiO}_2^{\text{DLS}}$ particle during the polishing. The thickness of the coating of $\text{TiO}_2^{\text{TEM}}/\gamma\text{-Al}_2\text{O}_3$ is estimated at $0.69 \pm 0.17 \mu\text{m}$ (see figure 4.17d3).

To sum up, here, the thickness of the coatings of $\text{TiO}_2^{\text{LD}}/\gamma\text{-Al}_2\text{O}_3$, $\text{TiO}_2^{\text{DLS}}/\gamma\text{-Al}_2\text{O}_3$, and $\text{TiO}_2^{\text{TEM}}/\gamma\text{-Al}_2\text{O}_3$ respectively are $1.68 \pm 0.81 \mu\text{m}$, $0.91 \pm 0 \mu\text{m}$, and $0.69 \pm 0.17 \mu\text{m}$. The results of this thickness evaluation can be linked to the results of the SEM analysis (see figure 4.10c-e) and size analysis (see figure 4.7b and table 4.5) in the previous section, and justify the analysis of size and SEM.

Figure 4.18 presents the SEM images of cross-section samples of $\text{SiO}_2^{\text{LD}}/\gamma\text{-Al}_2\text{O}_3$, $\text{SiO}_2^{\text{DLS}}/\gamma\text{-Al}_2\text{O}_3$, and $\text{SiO}_2^{\text{TEM}}/\gamma\text{-Al}_2\text{O}_3$. A very thin coating layer can be observed in figure 4.18. Due to unavoidable SiO_2^{LD} particle agglomeration, the dispersion of SiO_2^{LD} particles was not uniform (see figure 4.18b1-d1). One particle was used to estimate the thickness of the coating of SiO_2^{LD} particles, different thickness was selected to finish the assessment of the thickness of the coated SiO_2^{LD} particle. This value is $1.42 \pm 0.48 \mu\text{m}$.

Some pieces of $\text{SiO}_2^{\text{DLS}}$ particles were captured (see figure 4.18a2-d2). It could be an uncoated $\text{SiO}_2^{\text{DLS}}$ particle or a destroyed part of the coating of $\text{SiO}_2^{\text{DLS}}/\gamma\text{-Al}_2\text{O}_3$ that led to $\text{SiO}_2^{\text{DLS}}$ particles staying next to the $\gamma\text{-Al}_2\text{O}_3$ particle. Unlike the cross-section sample of $\text{SiO}_2^{\text{LD}}/\gamma\text{-Al}_2\text{O}_3$, the coating of $\text{SiO}_2^{\text{DLS}}/\gamma\text{-Al}_2\text{O}_3$ has better uniformity, probably because less mass of $\text{SiO}_2^{\text{DLS}}$ particles were used compared with the mass of SiO_2^{LD} particles. Due to a very thin coating layer can be observed, the coating of $\text{SiO}_2^{\text{DLS}}/\gamma\text{-Al}_2\text{O}_3$ was considered as a very homogeneous coating, no deviation will be shown here. After evaluation, the thickness of the coating of $\text{SiO}_2^{\text{DLS}}/\gamma\text{-Al}_2\text{O}_3$ is given as $0.61 \pm 0 \mu\text{m}$,

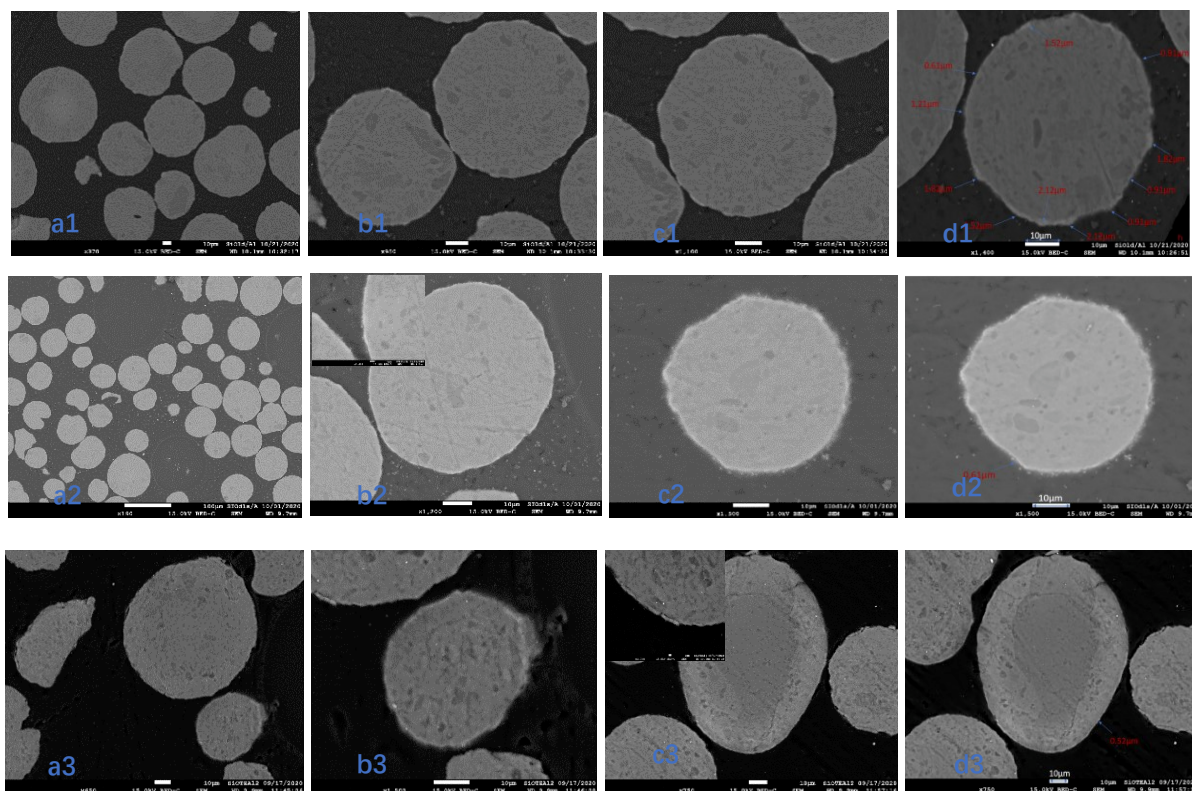


Fig.4.18 SEM images of cross-section samples of $\text{SiO}_2^{\text{LD}}/\gamma\text{-Al}_2\text{O}_3$ (a1-d1), $\text{SiO}_2^{\text{DLS}}/\gamma\text{-Al}_2\text{O}_3$ (a2-d2), and $\text{SiO}_2^{\text{TEM}}/\gamma\text{-Al}_2\text{O}_3$ (a3-d3) under 3500rpm, 5min of operating conditions.

Since the $\text{SiO}_2^{\text{TEM}}$ particle has a small size (nano-level), even though the magnification of the microscope is large, able to clearly and visibly capture the coating, it faced certain challenges. Therefore, in the cross-section samples of $\text{SiO}_2^{\text{TEM}}/\gamma\text{-Al}_2\text{O}_3$, few clear and visible particles are presented here (see figure 4.18a3-d3), which is a very thin and coating layer is taken into account to be a very uniform coating. The thickness of the coating of $\text{SiO}_2^{\text{TEM}}/\gamma\text{-Al}_2\text{O}_3$ is assessed as $0.52 \pm 0 \mu\text{m}$. The thickness of the coatings of $\text{SiO}_2^{\text{LD}}/\gamma\text{-Al}_2\text{O}_3$, $\text{SiO}_2^{\text{DLS}}/\gamma\text{-Al}_2\text{O}_3$, and $\text{SiO}_2^{\text{TEM}}/\gamma\text{-Al}_2\text{O}_3$ respectively are $1.42 \pm 0.48 \mu\text{m}$, $0.61 \pm 0 \mu\text{m}$, and $0.5 \pm 0 \mu\text{m}$. The results of this evaluation were correlated with their particle size analysis (see figure 4.7c) and SEM analysis (see figure 4.11c-d).

4.5.2 Thickness of Zeolite/S.S316L, $\text{TiO}_2/\text{S.S316L}$, and $\text{SiO}_2/\text{S.S316L}$

SEM images of cross-section samples of coated Zeolite^{LD}/S.S316L, Zeolite^{DLS}/S.S316L, and Zeolite^{DLS}/S.S316L are shown in figure 4.19. Obviously, every S.S316L particle has been covered by Zeolite^{LD} particles and revealed a heavy coating layer (see figure 4.19a1-c1), the main reason may be due

to the excessive quantity of the Zeolite^{LD} mass being used (see Chapter 2, table 2.2). Nevertheless, this coating layer is not uniform because of the agglomeration of Zeolite^{LD} particles. The results of the estimation of the coating thickness of Zeolite^{LD}/S.S316L (see figure 4.19-d1, thickness = $4.06 \pm 2.40 \mu\text{m}$) proved the non-uniformity of the coating as a big standard deviation was obtained.

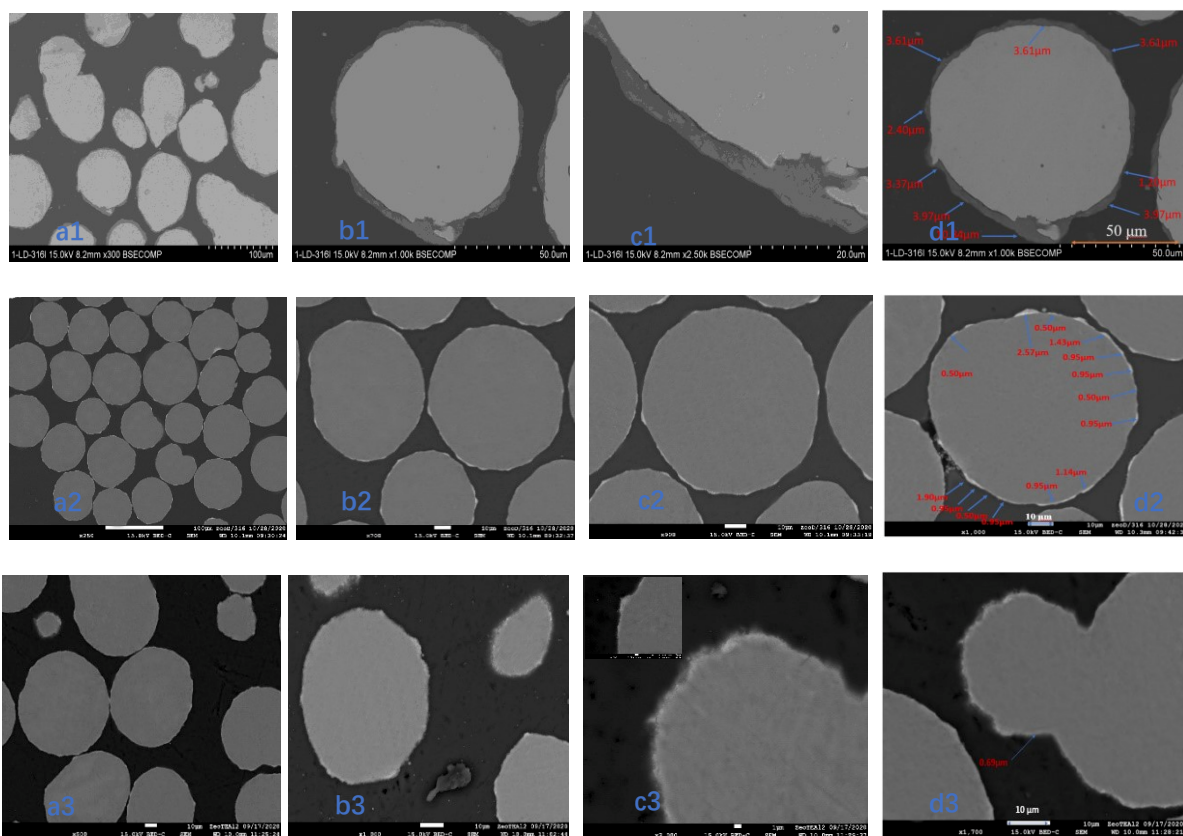


Fig.4.19 SEM images of cross-section samples of Zeolite^{LD}/S.S316L (a1-d1), Zeolite^{DLS}/S.S316L (a2-d2), and Zeolite^{TEM}/S.S316L (a3-d3) under 3500rpm, 5min of operating conditions.

As can be seen from figure 4.19a1, Zeolite^{DLS} particles are relatively uniformly distributed on the surface of S.S316L particle. The captured three particles (see figure 4.19-b2 and -c2) display a relatively thin coating layer. The thickness of the coating of Zeolite^{DLS}/S.S316L (see figure 4.19-d2) was estimated to be $1.05 \pm 0.56 \mu\text{m}$.

A thin coating layer can be seen in the figure 4.19-b3 and -c3. Compared to the other two types of coated particle (Zeolite^{LD}/S.S316L and Zeolite^{DLS}/S.S316L), the coating of Zeolite^{TEM}/S.S316L is not very obvious (see figure 4.19-a3) because less agglomeration gives a smaller size. There is a big debris that can be seen in figure 4.19-b3, which should be uncoated Zeolite^{TEM} particles or the Zeolite^{TEM} particles that

were removed from the surface of Zeolite^{TEM}/S.S316L particles during the polishing process. Since the thickness of the coating is very thin, the deviation is ignored and is given around $0.69 \pm 0 \mu\text{m}$.

Respectively, the thickness of Zeolite^{LD}/S.S316L, Zeolite^{DLS}/S.S316L, and Zeolite^{TEM}/S.S316L are $4.06 \pm 2.40 \mu\text{m}$, $1.05 \pm 0.56 \mu\text{m}$, and $0.69 \pm 0 \mu\text{m}$. The value of this assessment is corresponding to their particle size analysis (see figure 4.8a) and SEM analysis (see figure 4.12c-d).

Figure 4.20 shows the SEM images of cross-section samples of TiO₂^{LD}/S.S316L, TiO₂^{DLS}/S.S316L, and TiO₂^{TEM}/S.S316L. It is found that each S.S316L particle was covered with TiO₂^{LD} particles (see figure 4.20a1-c1) and presents a very thick coating layer. However, this thick coating layer is not homogeneous (see figure 4.20-b1 and -d1), the thickness of the coating is assessed as $5.08 \pm 2.38 \mu\text{m}$, this value proves the non-uniformity of the coating layer, because of the big standard deviation.

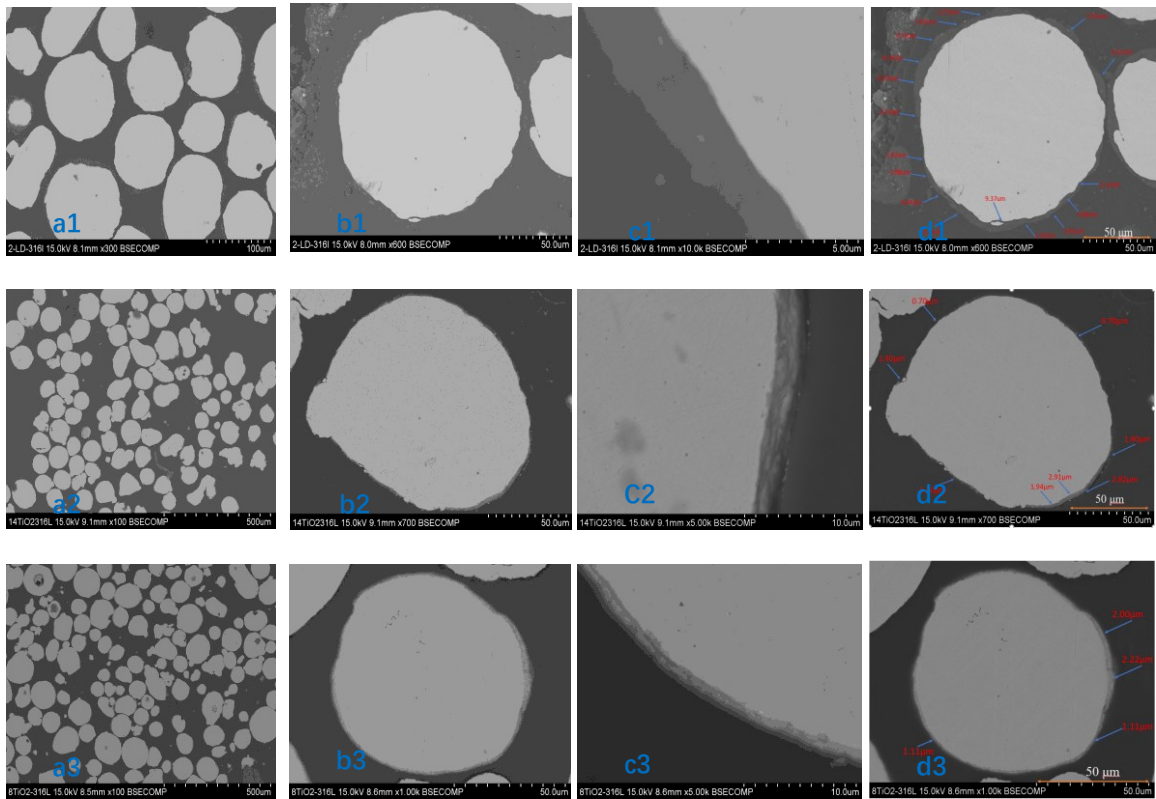


Fig.4.20 SEM images of cross-section samples of TiO₂^{LD}/S.S316L (a1-d1), TiO₂^{DLS}/S.S316L (a2-d2), and TiO₂^{TEM}/S.S316L (a3-d3) under 3500rpm, 5min of operating conditions.

Unlike TiO_2^{LD} particles, $\text{TiO}_2^{\text{DLS}}$ particle provides a smaller size. Therefore, the process of coating with the same mass of S.S316L requires less $\text{TiO}_2^{\text{DLS}}$ particles mass than TiO_2^{LD} particles (see Chapter 2, table 2.2). Theoretically, coated with S.S316L, $\text{TiO}_2^{\text{DLS}}$ particle's coating layer is thinner than that TiO_2^{LD} particle's coating layer. This theory can be proven from figure 4.20-c2, which provides a very thin coating layer. The thickness of the coating was roughly estimated as $1.66 \pm 0.79 \mu\text{m}$.

Compared to $\text{TiO}_2^{\text{LD}}/\text{S.S316L}$ and $\text{TiO}_2^{\text{DLS}}/\text{S.S316L}$ particles, the thickness of $\text{TiO}_2^{\text{TEM}}/\text{S.S316L}$ is harder to get because $\text{TiO}_2^{\text{TEM}}$ particle exhibits a small particle size (mean diameter $d_{p(3,2)}=19.79 \text{ nm}$, see Chapter 3, table 3.5). Thus, it is very difficult to visually observe the thickness of the coating of $\text{TiO}_2^{\text{TEM}}/\text{S.S316L}$ particles with a microscope. A $\text{TiO}_2^{\text{TEM}}/\text{S.S316L}$ particle (see figures 4.20-b3 and -c3) obtained gives a thin, tight, and relatively homogeneous coating. This particle was used to cursorily calculate the thickness of the coating of $\text{TiO}_2^{\text{TEM}}/\text{S.S316L}$, which is $1.61 \pm 0.5 \mu\text{m}$.

Totally, the thickness of the coating of $\text{TiO}_2^{\text{LD}}/\text{S.S316L}$, $\text{TiO}_2^{\text{DLS}}/\text{S.S316L}$, and $\text{TiO}_2^{\text{TEM}}/\text{S.S316L}$ respectively are $5.08 \pm 2.38 \mu\text{m}$, $1.66 \pm 0.79 \mu\text{m}$, and $1.61 \pm 0.5 \mu\text{m}$. The results of this rough evaluation are well related to the particle size (see figure 4.8b) and surface morphology (see figure 4.13c-d) of the three coated particles.

SEM images of cross-section samples of $\text{SiO}_2^{\text{LD}}/\text{S.S316L}$, $\text{SiO}_2^{\text{DLS}}/\text{S.S316L}$, and $\text{SiO}_2^{\text{TEM}}/\text{S.S316L}$ are presented in figure 4.21. As it can be seen, SiO_2^{LD} particles are more evenly dispersed on the S.S316L surface and formed a visible coating (see figures 4.21-b1 and -c1). The thickness of the coating of $\text{SiO}_2^{\text{LD}}/\text{S.S316L}$ is about $3.11 \pm 1.72 \mu\text{m}$ (see figure 4.21-d1).

A thin, tight coating layer but not uniform can be observed from figures 4.21b2 and c2. The thickness of the coating of $\text{SiO}_2^{\text{DLS}}/\text{S.S316L}$ is estimated as $1.86 \pm 0.61 \mu\text{m}$. Since $\text{SiO}_2^{\text{DLS}}$ has a small size of 119 nm (see Chapter 3, table 3.5), after the formation of the coating, it is difficult to observe the thin coating with the microscope even at a large magnification (see figure 4.21-a2).

In the previous study of the particle size analysis (see Chapter 3, table 3.5), it was obtained that $\text{SiO}_2^{\text{TEM}}$ presents the smallest particle size compared to SiO_2^{LD} and $\text{SiO}_2^{\text{DLS}}$ particles. Hence, compared to both $\text{SiO}_2^{\text{LD}}/\text{S.S316L}$ and $\text{SiO}_2^{\text{DLS}}/\text{S.S316L}$, it becomes more challenging and difficult to obtain the coating layer of $\text{SiO}_2^{\text{TEM}}/\text{S.S316L}$ particle. Only at the very high magnification of the microscope, a thin coating layer (see figure 4.21-d3) can be captured. All $\text{SiO}_2^{\text{TEM}}$ particles were assumed to be uniformly coated onto the surface of the S.S316L particle, as a result, the thickness of the coating of $\text{SiO}_2^{\text{TEM}}/\text{S.S316L}$ is $0.23 \pm 0 \mu\text{m}$.

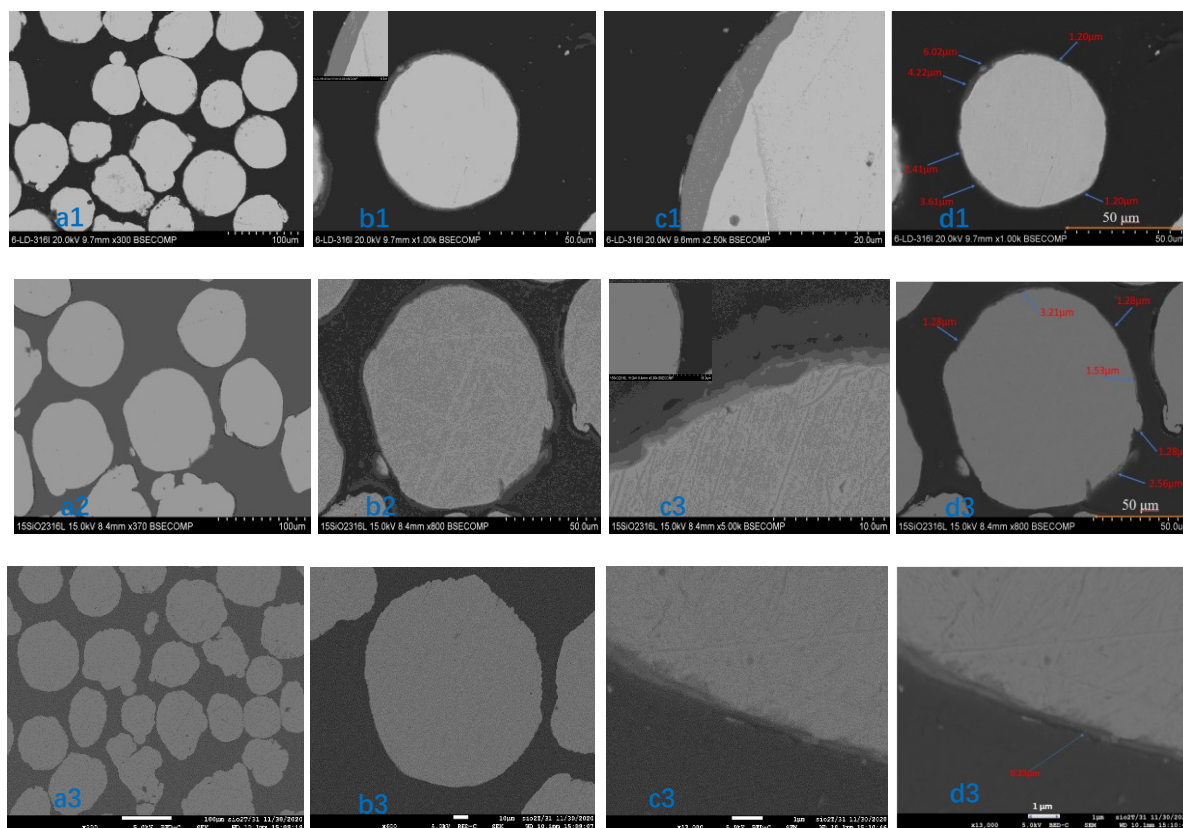


Fig.4.21 SEM images of cross-section samples of $\text{SiO}_2^{\text{LD}}/\text{S.S316L}$ (a1-d1), $\text{SiO}_2^{\text{DLS}}/\text{S.S316L}$ (a2-d2), and $\text{SiO}_2^{\text{TEM}}/\text{S.S316L}$ (a3-d3) under 3500rpm, 5min of operating conditions.

The thickness of the coating of $\text{SiO}_2^{\text{LD}}/\text{S.S316L}$, $\text{SiO}_2^{\text{DLS}}/\text{S.S316L}$, and $\text{SiO}_2^{\text{TEM}}/\text{S.S316L}$ respectively are $3.11 \pm 1.72 \mu\text{m}$, $1.86 \pm 0.61 \mu\text{m}$, and $0.23 \pm 0 \mu\text{m}$. The results of this evaluation were correlated with the particle size (see figure 4.8c) and surface morphologies (see figure 4.14c-e) of the three particles.

Table 4.6 summarizes all the thickness of coatings to get a clearer understanding. In the meantime, the size of all particles before the coating is also given as a reference value to analyze the results of the coating.

Theoretically, the thickness of the coating layer equals the size of the guest particle, this would be an ideal coating. However, it is often very difficult to achieve it in real experiments because the guest particles are often accompanied by agglomerates. Therefore, the analysis for the size of nanoparticles may also be the size of agglomerated particles (such as LD (laser diffraction) and DLS (dynamic light scattering) measurement).

Chapter 4: Dry Coating Results and Discussions

Table 4.6 Thickness of the coatings.

Host particles	Host particles ($dp_{(3,2)}$) (μm)	Guest particles	Guest particles ($dp_{(3,2)}$)	Coated particles	Coated particles ($dp_{(3,2)}$) (μm)	Thickness of coating layer (μm)
$\gamma\text{-Al}_2\text{O}_3$	67	Zeolite ^{LD}	7.79 μm	Zeolite ^{LD} / $\gamma\text{-Al}_2\text{O}_3$	79.4	4.1 ± 1.50
		Zeolite ^{DLS}	206.84 nm	Zeolite ^{DLS} / $\gamma\text{-Al}_2\text{O}_3$	76.9	1.05 ± 0
		Zeolite ^{TEM}	19.79 nm	Zeolite ^{TEM} / $\gamma\text{-Al}_2\text{O}_3$	74.2	0.83 ± 0
		TiO ₂ ^{LD}	2.67 μm	TiO ₂ ^{LD} / $\gamma\text{-Al}_2\text{O}_3$	76.5	1.68 ± 0.81
		TiO ₂ ^{DLS}	107 nm	TiO ₂ ^{DLS} / $\gamma\text{-Al}_2\text{O}_3$	74.4	0.91 ± 0
		TiO ₂ ^{TEM}	25.16 nm	TiO ₂ ^{TEM} / $\gamma\text{-Al}_2\text{O}_3$	73.9	0.69 ± 0.17
		SiO ₂ ^{LD}	0.45 μm	SiO ₂ ^{LD} / $\gamma\text{-Al}_2\text{O}_3$	75.9	1.42 ± 0.48
		SiO ₂ ^{DLS}	119 nm	SiO ₂ ^{DLS} / $\gamma\text{-Al}_2\text{O}_3$	71.8	0.61 ± 0
S.S316L	98.3	SiO ₂ ^{TEM}	17.39 nm	SiO ₂ ^{TEM} / $\gamma\text{-Al}_2\text{O}_3$	72.8	0.52 ± 0
		Zeolite ^{LD}	7.79 μm	Zeolite ^{LD} /S.S316L	115	4.06 ± 2.40
		Zeolite ^{DLS}	206.84 nm	Zeolite ^{DLS} /S.S316L	105	1.05 ± 0.56
		Zeolite ^{TEM}	19.79 nm	Zeolite ^{TEM} /S.S316L	99.9	0.69 ± 0
		TiO ₂ ^{LD}	2.67 μm	TiO ₂ ^{LD} /S.S316L	106	5.08 ± 2.38
		TiO ₂ ^{DLS}	107 nm	TiO ₂ ^{DLS} /S.S316L	104	1.66 ± 0.79
		TiO ₂ ^{TEM}	25.16 nm	TiO ₂ ^{TEM} /S.S316L	103	1.61 ± 0.5
		SiO ₂ ^{LD}	0.45 μm	SiO ₂ ^{LD} /S.S316L	103	3.11 ± 1.72
SiO ₂ ^{DLS}	119 nm	SiO ₂ ^{DLS} /S.S316L	102	1.86 ± 0.61		
SiO ₂ ^{TEM}	17.39 nm	SiO ₂ ^{TEM} /S.S316L	100	0.23 ± 0		

***Note:** LD (laser diffraction), DLS (dynamic light scattering), TEM (transmission electron microscope).

$dp_{(3,2)}$ is the mean diameter and the calculation of it can be found in Chapter 2, equation 2.3.

Table 4.6 demonstrates that the thickness of coated particles is less than the original particle size, e.g., the size of Zeolite^{LD} particle is 7.79 μm but the thickness of the coating of Zeolite^{LD}/ $\gamma\text{-Al}_2\text{O}_3$ is $4.1 \pm 1.50 \mu\text{m}$, apparently, the value of the thickness of Zeolite^{LD}/ $\gamma\text{-Al}_2\text{O}_3$ is smaller than that the size of Zeolite^{LD} particle. Three reasons may be used to explain this phenomenon, two of which are related to the preparation of the dry coating and are shown in figure 4.22.

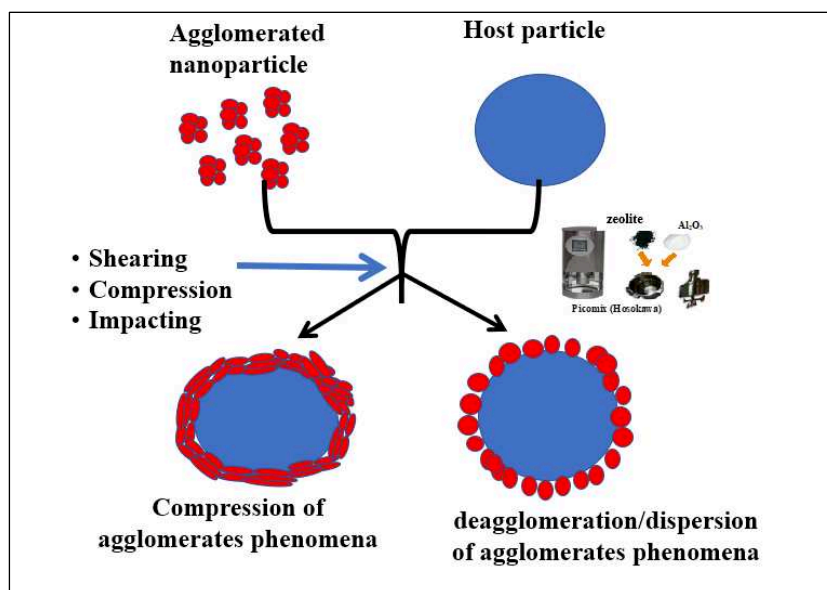


Fig. 4.22 The coating process.

Firstly, as described in Chapter 2, paragraph 2.2.2.2, the function of the top paddle (third paddle) of the rotor of Picomix is to separate the agglomerated particles and turn them into individual particles. These separated agglomerated particles are dispersed as a single particle on the surface of the host particles (see figure 4.22 (right)) so that the thickness of the coating is smaller than the size of the original agglomerated nanoparticle. Secondly, the agglomerated particles are compressed together under high-speed rotation due to the shearing/compression/impacting force, and the dispersed nanoparticle forms a multilayer coating (see figure 4.22 (left)).

A third possible reason is that in this coating thickness study, generally only one or two coating particles were used to assess the coating thickness, which can lead to some error between the assessed results and the actual thickness of the coating.

For some particles, after coating, the thickness of the coatings is bigger than the size of guest particles, e.g., the size of SiO_2^{LD} particle is $0.45 \mu\text{m}$ but the thickness of the coating of $\text{SiO}_2^{\text{LD}}/\gamma\text{-Al}_2\text{O}_3$ is $1.42 \pm 0.48 \mu\text{m}$, which possibly because only one or two particles are involved in the calculation of the thickness of the coating, it is also possible that because the destroyed agglomerates regrouped together and then formed a coating.

Some fragments were found (e.g., Zeolite^{DLS}/ γ -Al₂O₃) probably meaning Zeolite^{DLS} particles are not tightly coated on the surface of γ -Al₂O₃ particles, or maybe due to a too long time spent on polishing (or its strength).

We can say Zeolite^{TEM}, TiO₂^{TEM}, and SiO₂^{TEM} give the best coating because the SEM images of the cross-section of Zeolite^{TEM}/S.S316L, Zeolite^{TEM}/ γ -Al₂O₃, SiO₂^{TEM}/S.S316L, SiO₂^{TEM}/ γ -Al₂O₃, TiO₂^{TEM}/S.S316L, and TiO₂^{TEM}/ γ -Al₂O₃ present a thin, tight, and relatively homogeneous coating. The SEM images of cross-section samples of Zeolite^{LD}/S.S316L, Zeolite^{LD}/ γ -Al₂O₃, SiO₂^{LD}/S.S316L, SiO₂^{LD}/ γ -Al₂O₃, TiO₂^{LD}/S.S316L, and TiO₂^{LD}/ γ -Al₂O₃ provide a thick coating layer because too much mass of agglomerated Zeolite^{LD}, SiO₂^{LD}, and TiO₂^{LD} particles were used in the preparation process. This result is in general agreement with the analysis of particle size (see paragraph 4.4.1) after coating and the results of surface morphological analysis (see paragraph 4.4.2).

Overall, the SEM images of the cross-section of samples provided very useful information and allowed us to roughly compare the thickness of the coatings. Although the values of these thicknesses may deviate somewhat from the true values because only one or two particles were taken into account in the calculation of the thickness.

4.6 Conclusions

In this chapter, firstly, van der Waals' force between different particles was calculated to investigate the effect of adhesion on dry coating process. In the calculation of uncoated guest particle, it was found that all particles formed with the S.S316L show little uncoated guest particle (maximum the mass fraction of uncoated particle is Zeolite^{LD}/S.S316L 1.62%). However, in the coating with γ -Al₂O₃, the mass fraction of uncoated particles is relatively high regardless of the type of particles, with the mass fraction of uncoated Zeolite being as high as 11.41% (Zeolite^{LD}/ γ -Al₂O₃). When the host particles are the same, e.g., for γ -Al₂O₃ particles, uncoated guest particles of Zeolite^{LD} are more than Zeolite^{DLS} and Zeolite^{TEM}, this probably because the mass of Zeolite^{LD} particles required to coat 24.56g γ -Al₂O₃ particles is less than the theoretically calculated mass of the particles, which results in the excess mass sticking to the surface of the vessel and the rotor under strong forces. The percentage by mass of guest particles used in the coating experiment was calculated based on the assumption of 100% surface coverage of the host particles with a monolayer of guest particles (see Chapter 2 paragraph 2.2.2.3). Besides, because high rotation speed produced high energy to particles, and created drastic collisions for particle-particle and particle-wall, it

therefore caused an increase of local temperature of the powder. If this is the case, it is not only beneficial for the guest particles to coat on the host particles but it also promotes adhesion of the guest particles to adhere to the vessel and the rotor of Picomix.

For the effect of guest and host particles on coating, particle size distribution indicated that both S.S316L and γ -Al₂O₃ provided a good coating because the size of coated particles has all increased. Zeolite^{LD}/S.S316L gave a bigger size compared with Zeolite^{DLS}/S.S316L and Zeolite^{TEM}/S.S316L. TEM images (see Chapter 3, figure 3.3) have demonstrated that Zeolite has a lot of agglomeration, although, after 3500 rpm, 5 min, on the surface of Zeolite^{LD}/S.S316L might still have agglomerated Zeolite^{LD} particle. This may be the reason why Zeolite^{LD}/S.S316L presented the largest size compared with all coated particles. Meanwhile, the mass fraction of uncoated guest particles proved that only 1.62% of Zeolite^{LD} particles stayed on the surface of the mixer (the vessel and rotor)

The surface morphologies of SEM images indicated that for TiO₂^{LD}, SiO₂^{LD}, and Zeolite^{LD} particles, whether the coating is with S.S316L or γ -Al₂O₃, each host particle was covered by guest particles and formed a thick coating. Many agglomerated guest particles can be directly observed on the surface of the host particles. when TiO₂^{DLS}, SiO₂^{DLS}, Zeolite^{DLS}, coat with S.S316L or γ -Al₂O₃, a smooth surface was found but a small number of debris (agglomerated guest particles) can also be seen. As far as the images obtained by SEM are concerned, TEM provides the best coating because a smooth surface without any chips can be obtained, which means TiO₂^{TEM}/ γ -Al₂O₃, SiO₂^{TEM}/ γ -Al₂O₃, Zeolite^{TEM}/ γ -Al₂O₃, TiO₂^{TEM}/S.S316L, SiO₂^{TEM}/S.S316L, and Zeolite^{TEM}/S.S316L present the best coating. Because the particle size of the guest particles (TiO₂^{DLS}, SiO₂^{DLS}, Zeolite^{DLS}, TiO₂^{TEM}, SiO₂^{TEM}, and Zeolite^{TEM}) is at the nanometer level, the coated layer can only be observed at a relatively large microscope magnification.

Chapter 5: DEM Numerical Modelization

As mentioned in Chapter 1, the modeling of particle interactions has great importance for gaining a better understanding of the coating mechanism. DEM modeling is an ideal contact model for investigating the particle motions and collisions under the high shearing force in complex dry coating devices [196, 199, 251, 353, 354]. The objective of this study is to model the dry particle coating process and understand the behavior of particles in the Picomix by DEM numerical modelization.

Although DEM modeling is widely used, as reported in the literature [196, 199, 200, 202], it has been proved that DEM approaches are useful in developing a better understanding of particle motions and the mechanism of particulate processes. It is still relatively uncommon in the field of simulating dry particle coatings: at least two kinds of particles must be put in, namely the guest particles and host particles. In experimental studies, the particle size of the guest particles is generally at the nanometer level, and if DEM modeling wants to correlate with experimental results, the best way is to use nanoscale guest particles. However, this would undoubtedly put a lot of pressure on the simulation calculations. Therefore, in many simulation studies of dry particle coating, researchers [221, 227, 230] increase the particle size to reduce the computational time, or only one or two host particles [18, 232, 233, 235] are taken into account, and a limited number of guest particles are involved.

In this work, the numerical studies of dry particle coating in Picomix were performed using one commercial DEM simulation software EDEM 2018.3.0 and EDEM 2020.3.1 (Academic license for a CPU with 8 cores, DEM solutions Ltd., Edinburgh, UK) with Hertz-Mindlin (no slip) contact model and Hertz-Mindlin + JKR cohesive model. Three computers were used in this study, two are equipped with a processor of Intel(R) Core(TM) i7-4790 CPU@3.60Hz, and 8.0Go RAM; one is equipped with process of Intel(R) Xeon(R) CPU E5-1650 v2 @3.5GHz, and 32.0Go RAM.

5.1 Introduction to EDEM

EDEM software includes three main subsystems: the pre-processor - EDEM Creator, the solver - EDEM Simulator, and the post-processor – EDEM Analyst.

EDEM Creator (see figure 5.1) is used to create a representative model of bulk material. There are some tools to specify the components of the model, including contact physics parameters. In the selection of bulk material, the properties of materials, such as Poisson's ratio, solid density, shear modulus, young's

modulus, coefficient of restitution, etc. can be added, the size of particle and shape can be defined as well. In the selection of equipment materials, the properties of the equipment of the material used can be defined. In the selection of geometry, it can be selected from the software system or imported. At the same time, the number of particles and the motion of geometry (translation or rotational motion) can be added. The model types (such as Hertz-Mindlin (no-slip) contact model and Hertz-Mindlin + JKR cohesive model) can be chosen from the physics display.

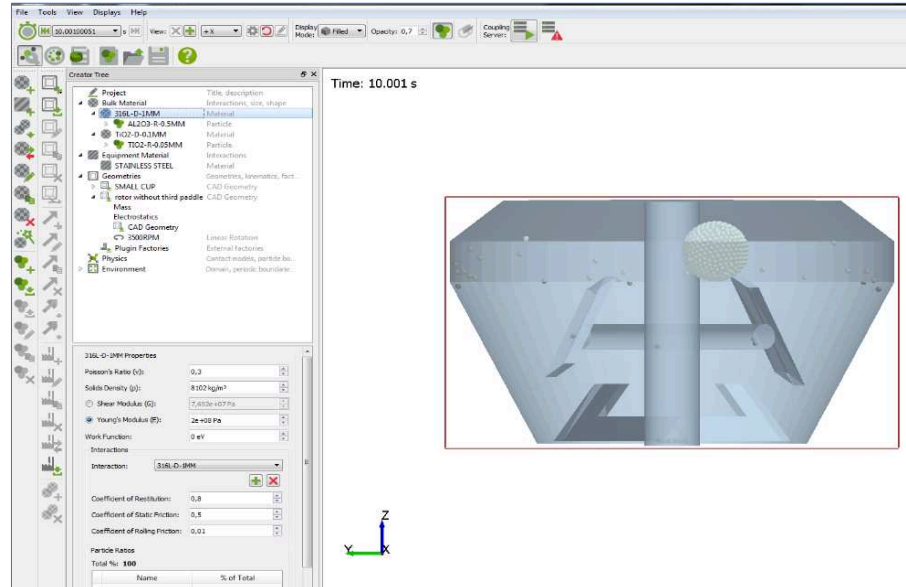


Fig. 5.1 The capture of EDEM creator.

EDEM Simulator (see Figure 5.2) is where it is possible to configure and control the operation of the EDEM simulation engine. Simulation time-step and data save intervals can be specified. Simulation status can be visualized and checked in the solve report. EDEM has rewind capability, allowing re-run of a simulation from any point with or without changes to the model. The main computational challenge in DEM simulation is the detection of contacts. By dividing the domain into grid cells, the simulator can check each cell and analyze only those that contain two or more elements (and therefore a possible contact), thus reducing processing time. As the grid length decreases, fewer elements are assigned to each grid cell and contacts become easier to resolve. The fewer particles per grid cell, the more efficient the simulator. If there is no more than one particle in each grid cell then no contact detection needs to take place so the simulation will progress faster. The idealized length of a grid cell is $2R_{\min}$ where R_{\min} is the minimum particle radius in the simulation.

Chapter 5: DEM Numerical Modelization

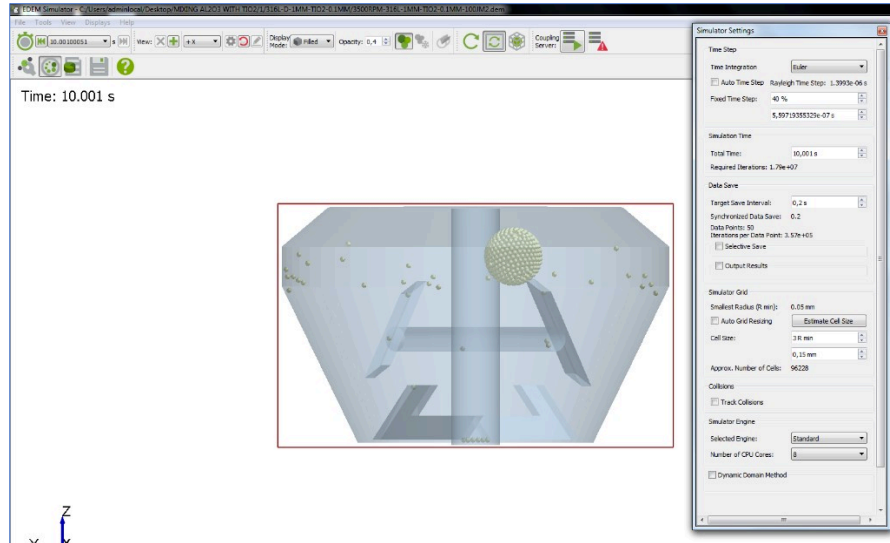


Fig. 5.2 The capture of EDEM simulator.

EDEM Analyst (see figure 5.3) provides a selection of post-processing tools for analysis, visualization, and export of simulation data. Bulk behavior metrics can be extracted from the particle-scale simulation data using a range of binning techniques with equipment geometry movement. EDEM provides 3D visualizations of the bulk particle system including cutaway views. Visualizations can be exported as images or videos. The data export function allows us to know the collisions, such as the number of collisions of particle-particle; the contacts, such as the normal contact forces between particles.

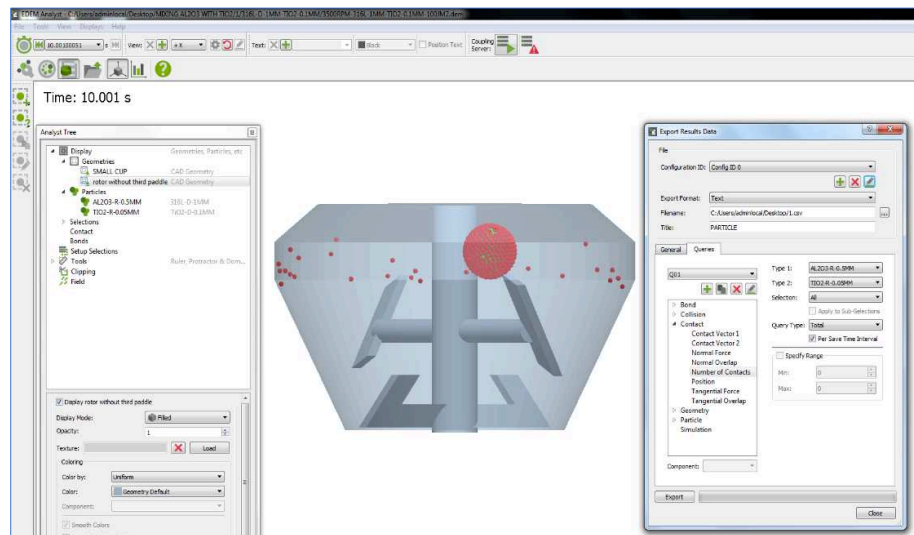


Fig. 5.3 The capture of EDEM analyst.

5.2 Modeling parameters

The material's property has significant effect on the particle motions and interaction, the definition of all of the parameters get involved in this study are presented in table 5.1.

Table 5.1 Definition of parameters are used in this study ^[250].

Parameters	Definition
Particle number (N_0)	The number of particles in the simulation is evaluated by: $N_0 = \frac{V_{total}}{V_0} = \frac{V_{total}}{\frac{4}{3}\pi R^3}$, Where V is the total volume of particles in the model system, V_0 is the volume of individual particle which equals to $\frac{4}{3}\pi R^3$, R is the sphere radius.
Sphere radius (R , mm)	The sphere radius of particles is assumed to be the soft sphere in the model.
Solid Density (ρ , kg/m ³)	The ratio of the mass of a substance to its volume of particles is known as the mass density or solid density.
Poisson's Ratio (ν)	Poisson's ratio is a measurement of the Poisson effect, that describes the expansion or contraction of material in directions perpendicular to the direction of loading. Most materials have Poisson's ratio values ranging between 0.0 and 0.5 ^[355] .
Young's Modulus (E , Pa)	Young's modulus is a mechanical property that measure the stiffness of a solid material. It defines the relationship between tense stress (force per unit area) and strain (proportional deformation) in a material in the linear elasticity regime of a uniaxial deformation. $E = \frac{T_\sigma}{\epsilon}$ where E is young's modulus, T_σ is the tense stress, ϵ is the strain or proportional deformation.
Shear modulus (G , Pa)	Shear modulus or modulus of rigidity is a measure of the elastic shear stiffness of a material and is defined as the ratio of shear stress to the shear strain. G can be calculated by $G = \frac{E}{2(1+\nu)}$ ^[250] . In the EDEM system, this value will be automatically calculated by this equation when the Poisson's Ratio and Young's Modulus are introduced.
Coefficient of Restitution (e)	Coefficient of restitution is the ratio of the final to initial relative velocity between two objects after they collide. It normally ranges from 0 to 1 where 1 would be a perfectly elastic collision. $e = \frac{v_{final}}{v_{initial}}$.
Coefficient of Static friction (μ_s)	Coefficient of static friction is the ratio of the force of friction between an object and a surface to the frictional force resisting the motion of object. The static friction force must be overcome by an applied force before an object can move. The proportionality factor between the maximum friction force (f_{max}) and the applied normal force (F_N) of two surfaces before sliding begins the static friction coefficient $\mu_s = \frac{f_{max}}{F_N}$, the Coefficient of static friction (μ_s) can be measured by sliding tests.

Chapter 5: DEM Numerical Modelization

Coefficient of Rolling friction (μ_f)	Coefficient of rolling friction is the indication of how great the rolling resistance (rolling friction torque ($\tau_{rolling}$) is for a given normal force (F_N) between the wheel and the surface upon which it is rolling. $\mu_f = \frac{\tau_{rolling}}{F_N}$ as the rolling resistance between smooth spheres is extremely weak, it is common in the DEM simulation that the μ_f between particles were assumed to be very small (e.g., 0.01) or sometimes can be ignored.
Rotation speed (Ω , rpm)	It is defined of the numbers of rotation conducted by the paddles per minutes, it is an important parameter in the dry coating experiments. The relation between rotation speed (Ω , rpm) and angular velocity of (ω , rad/s) the paddle is: $\omega = 2 \pi \Omega / 60$.
Time-step (ΔT , s)	In EDEM software, the DEM algorithms are concerned with solving equilibrium equations at discrete time intervals for the particle systems. It is known as time-step (ΔT). In the software, Rayleigh wave method is using for calculation $\Delta T \approx (0.1 \sim 0.5) t_{Rayleigh} = \pi \left(\frac{R}{0.163\nu + 0.8766} \sqrt{\frac{\rho}{G}} \right)$ R is radius of particle; ν is Poisson's ratio of particle ; ρ is the solid density of particle; G is the shear modulus of particle.
Running/calculation time ($t_{run\ time}$, s)	Running/calculation time (t) is decided by operator. Generally, few seconds will be enough to study the particle motions. The spent calculation time ($t_{run\ time}$) can be given by: $t_{run\ time} = \vartheta N_0 \frac{t}{\Delta T}$, N_0 is the number of particles, ϑ is a factor which depends on the hardware of computer (typical ranges from 0.5 to 1.5 μ s).

The parameters of the material should be chosen very carefully, because there are some parameters that have a particularly large impact on the calculation time such as density (ρ), young's modulus (E), particle size. Figure 5.4 presents the effect of young's modulus/shear modulus on the simulation time.

The time step, ΔT , can be calculated by ^[250]:

$$\Delta T = \pi \left(\frac{R}{0.163\nu + 0.877} \sqrt{\frac{G}{\rho}} \right) \quad (Eq.5.1)$$

Where R is radius of particle; ν is Poisson's ratio of particle ; ρ is the solid density of particle; G is the shear modulus of particle. Shear modulus or modulus of rigidity is a measure of the elastic shear stiffness of a material and is defined as the ratio of shear stress to the shear strain. G can be calculated by

$$G = \frac{E}{2(1+\nu)} \quad [250].$$

$$t_{run\ time} = \vartheta N_0 \frac{t}{\Delta T} \quad (Eq.5.2)$$

Where t is the modeling time, N is the number of particles employed in the modeling, ϑ is Per Iteration Per Particle depends on hardware and number of licenses (depends on computer, normally the value range is 0.5-1.5 μ s).

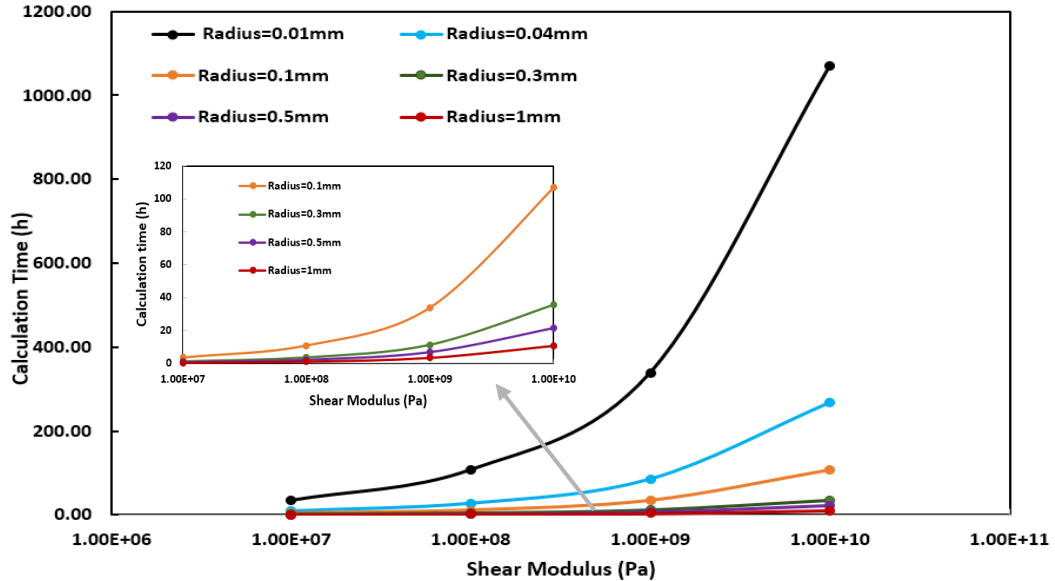


Fig. 5.4 The relation of the running/calculation time and shear modulus (Equation 5.1 and 5.2 were used to calculate the time step, solid density $\rho=3258 \text{ kg/m}^3$; $\nu=0.25$; modeling time $t = 1 \text{ s}$, modeling number $N_0 = 10000$, $\vartheta = 1.0 \mu\text{s}$) with different particle radius of $\gamma\text{-Al}_2\text{O}_3$

Figure 5.4 shows that when the shear modulus increases to $G = 1.0 \times 10^{10} \text{ Pa}$, modeling 10000 $\gamma\text{-Al}_2\text{O}_3$ spherical particles with a diameter of 10 μm , modeling 1 s, will take 1069 h (44.6 days), which is obviously impractical. Therefore, it is very important to choose the feasible parameters for the simulation.

5.3 Geometry

Figure 5.5 shows the dimension of the high shear mixer (Picomix, Hosokawa Micron B.V) used for DEM modeling, which has been drawn in a three-dimension software “Onshape”. The geometry information was provided by Hosokawa Micron (shown in Appendix 1). The dimensions of the Picomix have been introduced in Chapter 2, paragraph 2.2.2.2. The clearance gap between the wall of the vessel and paddles is $1.3 \pm 0.3 \text{ mm}$, the distance between the bottom to the bottom paddle is 1 mm. In the simulation study, since the maximum particle size is 2 mm, the clearance gap between the wall of the vessel and paddles, the distance between the bottom to the bottom paddle was increased by 1.3 times. That is, the clearance

gap between the wall of the vessel and paddles is 3 mm, the distance between the bottom to the bottom paddle is 2.3 mm. The other dimensions are the same as the Picomix used in the experiment.

The Picomix model is comprised of a conical shaped vessel with 100 mL volume, three pairs of mixed paddles, and a centered rotor. The clearance between paddles to the wall of the vessel plays an important role in the movement of the particles. This rotor will be given a rotational speed to learn the contact between particles and their collisions by changing the speed in subsequent simulations.

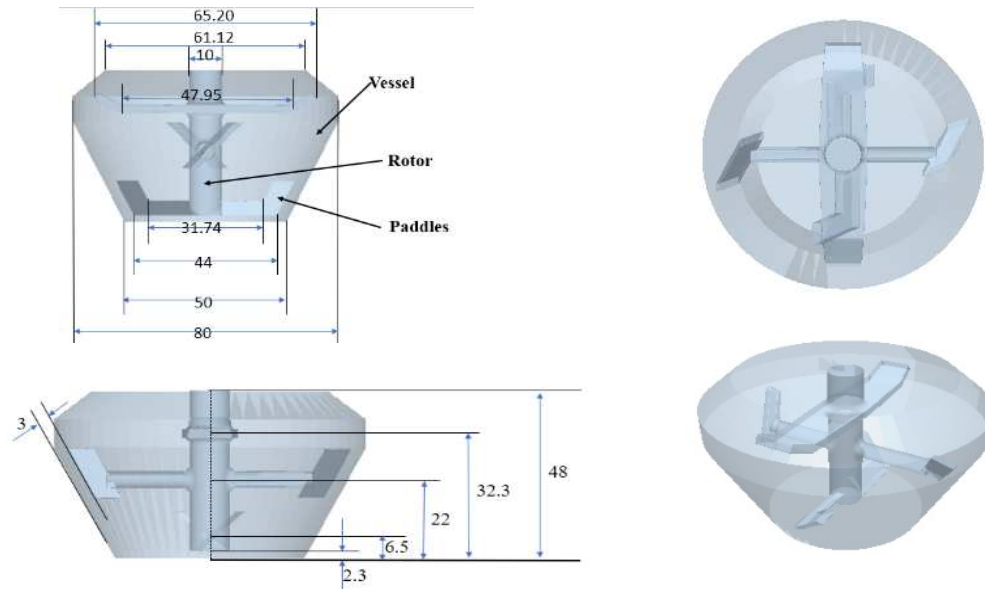


Fig. 5.5 Geometry of the high-shear mixer (Picomix) model with different views.

5.3.1 Parameters analysis of Al_2O_3

In EDEM simulation, young's modulus, Poisson's ratio, coefficient of restitution, coefficient of static friction, and coefficient of rolling friction are necessary to be added. However, these parameters are normally difficult to be measured precisely in experiments. Therefore, it is necessary to do a literature analysis and find these values before conducting numerical modeling. The density (ρ) measurements were performed using a Helium pycnometer (AccuPyc 1330, micromeritics Instrument Corp). Table 5.2 presents the parameter analysis of $\gamma-Al_2O_3$ from the literature.

It was reported ^[104, 354] that the friction coefficient affected the particle transition from the static to the dynamic state more significantly and the restitution coefficient has a greater influence on the behavior of

Chapter 5: DEM Numerical Modelization

the moving particles. The variation of friction coefficient and restitution coefficient will give different predictions in the DEM modeling of particle interactions.

Table 5.2 parameter analysis of γ -Al₂O₃

Parameters	Authors /Suppliers	Values	Conditions in literature	Ref.
Density (kg/m³)	Sasol-Germany	3258	Density measured by the AccuPyc 1330 Pycnometer (in our team)	[356]
Young's modulus (E, GPa)	MemPro Ceramics (USA)	11.3 ± 2.3	Investigated the mechanical and structural characterizations of α -Al ₂ O ₃ and γ -Al ₂ O ₃ nanofibers.	[357]
	Zhao et al.	15.1-22.5	Studied the mechanical properties of lumina (α -Al ₂ O ₃ and γ -Al ₂ O ₃) nanofibers.	[358]
	Zhang et al.	23.8	Studied the fabrication of flexible alumina fibers composed of nanosheets were studied	[359]
	Tamei Chemical Co., Nagano, Japan	17	The microstructure and mechanical properties of porous alumina ceramics was investigated.	[360]
	Kováčik J	17	Studied the correlation between young's modulus and porosity in porous materials.	[361]
Poisson's ratio (ν)	International Syalons	0.22	International Syalons is one of the UK's foremost technical ceramics suppliers and manufacturers.	[362]
	Degussa AG (Frankfurt, Germany)	0.24 ± 0.2	The mechanical properties of dense, bulk, γ -Al ₂ O ₃ from nanosize particles were studied.	[363]
	Roberts and Jjot	0.2	The finite-element method was used to study the influence of porosity and pore shape on the elastic properties of model porous ceramics.	[364]
	Alcoa a16sg powder	0.15-0.25	Presented a study on the influence of the porosity level on young's modulus and Poisson's ratio of alumina.	[365]
Coefficient restitution (e)	Müller et al.	0.735	Investigated the restitution coefficient of granules.	[366]
	Mueller et al.	0.82	Three different types of granules have been used as model granules: γ -Al ₂ O ₃ and Zeolite 4a and the dominant plastic sodium benzoate to study the restitution coefficient	[367]
	Mueller et al.	0.82	Presented the normal and oblique impact of three types of wet granules γ -Al ₂ O ₃ and Zeolite 4a and the dominant plastic sodium benzoate.	[368]
	Michels	0.8	This work presents the numerical simulation of flexural tests in metal ceramic composites.	[369]
Static Friction Coefficient (μ_s)	Michels	0.1	Numerical simulation of flexural tests in metal ceramic composites were investigated.	[369]
	Berman et al.	0.48	Described the results of microtribological studies of an industrially important surface-alumina (gamma and alpha), both untreated and treated with a specially synthesized chemisorbed surfactant layer.	[370]
	F99.7 alumina (Friatec, Germany)	0.16	Studied the frictional behavior both static and sliding friction of steel/steel, steel/alumina and alumina/alumina pairs under unlubricated or oil lubricated conditions.	[371]
Rolling Friction Coefficient (μ_r)	Teffo et al.	0.01 or 0	It is common in DEM simulations that the rolling friction coefficient between particles were assumed to be very small (e.g.,0.01) or sometimes can be ignored.	[372]
	Michels et al.	0.01	Numerical simulation of flexural tests in metal ceramic composites were investigated.	[369]

5.3.2 Parameters analysis of stainless steel (S.S316L) powders

The properties analysis of S.S316L from literature is summarized in table 5.3. The S.S316L used in the experiments was provided by Höganäs Belgium; the density (8102 kg/m^3) was performed using a helium pycnometer (AccuPyc 1330, Micromeritics Instrument Corp.) in our team.

Table 5.3 Parameters analysis of S.S 316L.

Parameters	Authors /suppliers	Values	Conditions in literature	Ref.
Young's modulus (E, GPa)	ASM Aerospace Specification Metals, Ltd. USA	193	Company provides different type of stainless steel and use for chemical processing, food processing, marine exterior firm etc.	[373]
	Höganäs Belgium	198	The one we used in our experiments to prepare the new supports	[374]
	Li et al.	190-200	Investigated the deformation process and stress/strain evolution of micro- lattice structures produced by selective laser melting (SLM) techniques. Some methods were used to measure the constitutive properties of S.S316L, including Young's modulus, yield stress, hardness etc.	[375]
	Gu et al.	190	Studied the influences of energy density on porosity and microstructure of S.S316L.	[376]
	Lee et al.	206-224	The temperature was changed to study the impact on the mechanical of S.S316L.	[377]
	Song et al.	196	S.S316L were used to simulate the sintering step, meanwhile sintering experiments were carried out in a batch furnace to verify the numerical model and simulations on S.S316L.	[378]
	Michels	200	Simulated the production process (compaction and sintering) and flexural tests in a metal ceramic composite.	[369]
Poisson's ratio (v)	Lee et al.	0.16-0.45	The temperature was changed to study the impact on the mechanism of S.S316L.	[377]
	Li et al.	0.3	Investigated the deformation process and stress/strain evolution of micro- lattice structures produced by selective laser melting (SLM) techniques.	[379]
	Mott et al.	0.3	Used different quadratic formulae that from the classical theory to study the material's Poisson's ratio of three possible ranges.	[380]
	Gu et al.	0.3	Studied the influences of energy density on porosity and microstructure of S.S316L. Experiments were carried out by varying processing parameters to change energy density.	[376]
	Song et al.	0.28	S.S316L were used to simulate the sintering step.	[378]
	Michels	0.3	Simulated the production process (compaction and sintering) with EDEM software and flexural tests in a metal ceramic composite.	[369]

Chapter 5: DEM Numerical Modelization

Coefficient restitution (e)	Michels	0.8	Simulated the production process (compaction and sintering) with EDEM software and flexural tests in a metal ceramic composite.	[369]
	United States Patent	0.81	In this patent, golf club was seeking a head face that can have good stiffness with a high coefficient of restitution. By comparing the material's elastic modulus, thickness, coefficient of restitution etc.	[381]
	Liu et al.	0.7	DEM was used to describe the relationship between the relative density of the powder bed of S.S316L and its thickness.	[382]
Static Friction Coefficient (μ_s)	Michels	0.5	Simulated the production process (compaction and sintering) with EDEM software and flexural tests in a metal ceramic composite.	[369]
	Liu et al.	0.2	DEM was used to describe the relationship between the relative density of the powder bed of S.S316L and its thickness.	[382]
	Iwasaki et al.	0.1	Studied the efficiency of tooth movement associated with some orthodontic mechanics that can be compromised by friction between S.S316L and bracket.	[383]
Rolling Friction Coefficient (μ_r)	Michels	0.01	DEM was used to describe the relationship between the relative density of the powder bed of S.S316L and its thickness.	[369]
	Liu et al.	0.01	DEM was used to describe the relationship between the relative density of the powder bed of S.S316L and its thickness.	[382]
	Teffo et al.	0.01	The aim of this study was to experimentally determine the coefficients of restitution and static and rolling friction of coal and S.S316L for discrete element modelling (DEM).	[372]

The analysis of literature demonstrated that young's modulus of S.S316L has a range of 190 - 200 GPa, the Poisson's ratio of S.S316L is 0.3. The coefficient of restitution of S.S316L could be 0.7- 0.8, the coefficient of static friction of S.S316L can be chosen between 0.1 to 0.5, the coefficient of rolling friction of S.S316L is 0.01.

5.3.3 Parameters used for modelisation

Since the study of this simulation includes the study of mixing of host particles (γ -Al₂O₃ and S.S316L) and dry coating (coating of γ -Al₂O₃ with TiO₂), the parameters used may be different and are summarized in a different table (see table 5.4 and 5.5).

Table 5.4 presents the parameters used in the simulation of the two host particles. The parameters were found in the literature and part of them that have been used in this work.

Chapter 5: DEM Numerical Modelization

5.4 Parameters have been used to study the host particle behavior.

Parameters	Properties of particle $\gamma\text{-Al}_2\text{O}_3$	Properties of particles S.S316L	Properties of picomix (steel)
Density (ρ , kg/m ³)	3258	8102	7990 [384, 385]
Sphere diameter (D , mm)	0.6, 1, 2		
Poisson's ratio (ν)	0.15-0.44 [362-365]	0.16-0.45 [369, 376-380]	0.25 [369]
Young's Modulus (E , Pa)	$1.13\text{-}2.3 \times 10^{10}$ [357-361]	$1.9\text{-}2.0 \times 10^{11}$ [369, 373-378]	1.9×10^{11} [369]
Filling ratio	10 - 40% filling ratio of picomix volume (100 mL)		
Coefficient of Restitution coefficient (e)	$\gamma\text{-Al}_2\text{O}_3$ - $\gamma\text{-Al}_2\text{O}_3$	0.735-0.82 [366-369]	
	$\gamma\text{-Al}_2\text{O}_3$ - wall	0.8 [369]	
	S.S316L - S.S316L	0.7-0.81 [369, 381, 382]	
	S.S316L - wall	0.8	
Coefficient of Static friction (μ_s)	$\gamma\text{-Al}_2\text{O}_3$ - $\gamma\text{-Al}_2\text{O}_3$	0.1-0.48 [369-371]	
	$\gamma\text{-Al}_2\text{O}_3$ - wall	0.5 [369]	
	S.S316L - S.S316L	0.1-0.5 [369, 382, 383]	
	S.S316L - wall	0.5	
Coefficient of Rolling friction (μ_r)	$\gamma\text{-Al}_2\text{O}_3$ - $\gamma\text{-Al}_2\text{O}_3$	0 or 0.01 [369, 372]	
	$\gamma\text{-Al}_2\text{O}_3$ - wall	0.3 [369]	
	S.S316L - S.S316L	0 or 0.01 [369, 372, 382]	
	S.S316L - wall	0.01	
Number of particles	2867(2 mm) - 22918(1 mm)- 106103(0.6 mm)		
Rotation speed (Ω , rpm)	1500, 3500, 5000		
Modeling time (t , s)	1.0		
Rayleigh time-step (ΔT)	40%		
*The Picomix refers to the vessel (100 mL) and paddles			

Considering the calculation time, the size of the host and guest particles have been scaled up in this simulation. Young's modulus of $\gamma\text{-Al}_2\text{O}_3$ used in the mixing section is $1.7\text{e}+10$ Pa [357-359, 361], Young's modulus of TiO_2 reported in the literature is $1.19 - 2.82\text{e}+11$ Pa [386-391]. In this study Young's modulus is reduced and summarized in table 5.5.

Chapter 5: DEM Numerical Modelization

Table 5.5 The parameters have been used to study dry particle coating.

Parameters	Properties of particles		Properties of Picomix (steel)
	$\gamma\text{-Al}_2\text{O}_3$	TiO_2	
Density (ρ , kg/m^3)	3528	3955	7990
Sphere diameter (D , mm)	1	0.1/0.04	
Number of particles	1	484/2704	
Poisson's ratio (ν)	0.25	0.28 ^[389, 390]	0.25
Shear Modulus (G , Pa)	6.80×10^7	5.859×10^7	7.60×10^{10}
Young's Modulus (E , Pa)	1.70×10^8	1.50×10^8	1.90×10^{11}
Coefficient of Restitution (e)	$\gamma\text{-Al}_2\text{O}_3 - \gamma\text{-Al}_2\text{O}_3$		0.7
	$\gamma\text{-Al}_2\text{O}_3 - \text{wall}$		0.8
	$\gamma\text{-Al}_2\text{O}_3 - \text{TiO}_2$		0.6
	$\text{TiO}_2 - \text{TiO}_2$		0.8 ^[392]
	$\text{TiO}_2 - \text{wall}$		0.8
Coefficient of Static friction (μ_s)	$\gamma\text{-Al}_2\text{O}_3 - \gamma\text{-Al}_2\text{O}_3$		0.1
	$\gamma\text{-Al}_2\text{O}_3 - \text{wall}$		0.5
	$\gamma\text{-Al}_2\text{O}_3 - \text{TiO}_2$		0.1
	$\text{TiO}_2 - \text{TiO}_2$		0.3 ^[393]
	$\text{TiO}_2 - \text{wall}$		0.3
Coefficient of Rolling friction (μ_f)	$\gamma\text{-Al}_2\text{O}_3 - \gamma\text{-Al}_2\text{O}_3$		0.01
	$\gamma\text{-Al}_2\text{O}_3 - \text{wall}$		0.3
	$\gamma\text{-Al}_2\text{O}_3 - \text{TiO}_2$		0.01
	$\text{TiO}_2 - \text{TiO}_2$		0.03 ^[394, 395]
	$\text{TiO}_2 - \text{wall}$		0.01
Rotation speed (Ω , rpm)			3500
Modeling time (t , s)			10
Surface energy (J/m^2)	$\gamma\text{-Al}_2\text{O}_3 - \gamma\text{-Al}_2\text{O}_3$: 1.5 ^[396-398] ; $\text{TiO}_2 - \text{TiO}_2$: 0 and 0.9 ^[399, 400]		
Rayleigh time-step (ΔT)			40%

5.4 Data analysis

EDEM Analyst provides a selection of post-processing tools for analysis, visualization and export of simulation data. EDEM provides fast, parallelized 3D visualizations of the bulk particle system including cutaway views. Visualizations can be exported as images or videos. In this study, the particle motion has been investigated as the particle translational velocity, angular velocity, collision force, collision number,

Chapter 5: DEM Numerical Modelization

collision frequency, translational kinetic energy, rotational energy, potential energy, and impact energy. Table 5.6 presents the definitions of all exported data attributes.

Table 5.6 Definition of parameters will be used in DEM models [250].

Exported data	Definition/Equation
Average particle velocity (\bar{v}_p , m/s)	<p>The particle velocity reveals the particle motions in the picomix, as the higher as the velocity, the more rapidly the particle move. The average particle velocity magnitude in the DEM modeling is given by: $\bar{v}_p = \frac{\sum_{i=1}^{N_0} v_{i(trans.)}}{N_0}$; $v_{i(trans.)} = \sqrt{v_{xi(trans.)}^2 + v_{yi(trans.)}^2 + v_{zi(trans.)}^2}$</p> <p>Where $v_{i(trans.)}$ is the translational velocity magnitude of particle i and N_0 is the total number of particles in the simulation, respectively, $v_{xi(trans.)}$, $v_{yi(trans.)}$, $v_{zi(trans.)}$ are the translational velocity magnitude of particle i, j in X, Y and Z axis direction.</p>
Angular velocity (v_{ang} , m/s)	<p>Angular velocity refers to how fast an object rotates or revolves relative to another point, i.e., how fast the angular position or orientation of an object changes with time. For a particle (radius R) rotating at velocity (ω, rad/s), the angular velocity $v_{ang.} = R\omega$ and the magnitude of $v_{i(ang.)} = \sqrt{v_{xi(ang.)}^2 + v_{yi(ang.)}^2 + v_{zi(ang.)}^2}$ Where $v_{i(ang.)}$ is the angular velocity magnitude of particle i, respectively, $v_{xi(ang.)}$, $v_{yi(ang.)}$, $v_{zi(ang.)}$ are the angular velocity magnitude of particle i, j in X, Y and Z axis direction.</p>
Normal contact force ($F_{n,ij}$, N)	<p>The particle contact force describes the interparticle force acting at the contact point. The contact force which derived from the deformed overlap of particles is normally decomposed into normal and tangential direction for analysis. The normal contact force is supposed to contribute to the translational motions of particles. The normal contact force is calculated</p> $F_{n,i,j} = \frac{4}{3} E^* (R^*)^{1/2} \delta_n^{3/2} \text{ (Hertz-Mindlin (no slip) model)}$ <p>Where E^* and R^* is the equivalent Young's modulus and the equivalent radius, δ_n is the normal overlap between the contacting particle i and j. $F_{n,ij} = -4\sqrt{\pi\gamma E^* a^3} + \frac{4E^*}{3R^*} a^3$ (when the Hertz-Mindlin + JKR contact model is applied. γ is the surface energy of particles.</p>
Tangential contact force (F_t , N)	<p>The tangential contact force facilitates the rotational motions of particles. The tangential contact force is calculated $F_t = -K_t \delta_t$, Where K_t is the tangential stiffness; δ_t is the tangential overlap.</p>
Number of collisions ($N_{collision}$)	<p>When two particles collide, it will count as one collision, no matter how long the particles stay in contact, only the completed collisions are counted.</p>
Number of contacts	<p>The total number of contacts of particle-particle are the impacts occurring between all particles at data write-out points. In other words, the contact is in progress when the write-out takes place.</p>
Collision frequency (f_n , s ⁻¹)	<p>Collision numbers per particle per second is defined as the collision frequency, it is given by $f_n = \frac{N_{collision}}{N_0 T}$, Where the $N_{collision}$ is the accumulative collision numbers during the simulation period time T, N_0 is the total simulated number. The collision frequency is a very important factor in the dry particle coating process, as it represents the degree of particle.</p>
Particle kinetic energy (\bar{E}_k , J)	<p>In physics, the kinetic energy of an object is the energy that it possesses due to its motion. The kinetic energy is defined by $\bar{E}_k = 0.5mv^2$, where m is the particle mass, v is the velocity magnitude ($v = \sqrt{v_x^2 + v_y^2 + v_z^2}$ of the particle.</p>
	<p>It was reported that the rotational kinetic energy acted in the direction for the growth of a granule in the particle granulation process, when granules with high speed collide to other granules, they would be broken into pieces, in</p>

Chapter 5: DEM Numerical Modelization

Rotational kinetic energy (\bar{E}_r , J)	order to avoid breaking granules, the rotational kinetic energy is important to understand the behavior. The rotational kinetic energy is defined as $\bar{E}_r = \sum_{i=1}^{N_0} \frac{1}{2} I v_{ang}^2 / N_0$, Where I is the moment of inertia, v_{ang} is the angular velocity magnitude of particle i , N_0 is the total number of particles in the modeling; for a sphere, the moment of inertia $I = 2/5 m R^2$, where m is the particle mass, R is the particle radius, ρ is the solid density.
Translational kinetic energy (\bar{E}_t , J)	When the particle moves from one location to another, it will produce energy, this energy is named as translational kinetic energy. The translational kinetic energy is defined by ($\bar{E}_t = \frac{1}{2} m v_{trans}^2$, where m is the mass of particle, v_{trans} is the translational velocity magnitude of particle.
Potential energy (\bar{E}_p , J)	The potential energy of particles presents quantitatively the position, which is defined as $\bar{E}_p = mgh$, Where m is the particle mass, g is acceleration of gravity ($g=9.81 \text{ m/s}^2$) and h is the distance between the center mass of the particle and the defined 'ground' level (i.e. coordinate plan $Z=0$). Therefore, the value of particle potential energy displays the state of particle, the larger the potential energy, the higher positions of the particle will be during the motions.
Impact energy (E_i , J)	The impact energy is the energy required to break the material, the maximum kinetic energy of the drop weight that at the time of impact into the sample ^[401] . It is calculated by $E_i = \frac{1}{2} m v_i^2 f_n$, Where m is the particle mass, f_n is collision frequency, v_i is the velocity magnitude ($v_i = \sqrt{v_{xi}^2 + v_{yi}^2 + v_{zi}^2}$ of the particle i .
Total energy (E_t , J)	The total energy of a particle is the sum of the translational kinetic energy, rotational kinetic energy and potential energy of a particle, i.e. $E_t = E_r + E_k + E_p$
Total force (F_t , N)	Total force is the sum of contact force (normal force and tangential force) non-contact force (van der Waal force and electrostatic force) and gravity force
Adhesion force (F_{ad} , J)	In DEM JKR model, the adhesion force is calculated by $F_{pullout/ad} = -\frac{3}{2} \pi \gamma R^*$.

5.5 Conclusion

In this chapter, firstly, the commercial DEM simulation software EDEM was introduced (Academic license with 8 CPU, DEM solutions Ltd., Edinburgh, UK) to investigate the dry particle coating process of host particles (e.g., $\gamma\text{-Al}_2\text{O}_3$) and guest particles (TiO_2) in the ‘‘Picomix’’. Secondly, the definition of all of the parameters was involved in this study were summarized. Thirdly, described the dimension of the high shear mixer (Picomix, Hosokawa Micron B.V) used for DEM modeling.

As an important part of EDEM simulation, the selection of material parameters is the first step at the beginning of the simulation. Therefore, the parameters of $\gamma\text{-Al}_2\text{O}_3$, S.S316L and TiO_2 were analyzed and summarized by extensive literature. Then there are some parameters that were used in this simulation study.

The host particles used in the experiments are at the micron level and the guest materials are at the nanometer level. However, it is not realistic to use real particle sizes as in the experiment in the simulation because it would consume a lot of computation time, even if the calculation time is the only 1s (see figure

5.4, modeling 10000 γ -Al₂O₃ spherical particles with a diameter of 10 μ m, modeling 1s, will take 1069 h). Considering this reason, the size of the host and guest particles have been scaled up in this simulation. Then the influence of particle size, filling ratio, young's modulus as well as rotation speed of the rotor of picomix on the particle behavior have been studied to understand the particle's interactions during the dry particle coating process.

Chapter 6: Simulation Results and Discussions

During the experimental study of the dry coating in the picomix, it was found that $\gamma\text{-Al}_2\text{O}_3$ and S.S316L were coated with three types of nanopowder (TiO_2 , SiO_2 , and Zeolite) respectively. The coating happened because of the collision of particle to particle, and of particles with the wall of the vessel of picomix. However, little has been reported in literature about particle collisions and particle motion in the picomix, because intuitively obtaining the correlation between particles and geometry is very complex and challenging. DEM modeling can be used to track particle motion, collision and to analyze contact force, energy, and velocity, etc. ^[104, 186]. This numerical modeling work will allow us to understand the particle behavior during the dry particle coating process.

The numerical DEM modeling results will be presented in this chapter. The numerical studies of dry particle coating in the picomix were performed using one commercial DEM simulation software EDEM 2018.3.0 and EDEM 2020.3.1 (Academic license a CPU with 8 cores, DEM solutions Ltd., Edinburgh, UK) with Hertz-Mindlin (no-slip) contact model and Hertz-Mindlin + JKR cohesive model. The Hertz-Mindlin (no-slip) contact model was used to study the mixing of the host particles. The Hertz-Mindlin with JKR cohesion model allows us to represent the cohesion between fine and host particles. Considering the calculation time, the size of the host and the guest particles have been scaled up in this simulation. This simulation work includes two main sections:

1. Modelization of the particle in the picomix: study of the Mixing of $\gamma\text{-Al}_2\text{O}_3$ and S.S316L respectively. Analysis of the effects of particle size, filling ratio, rotation speed, and young's modulus on particle behavior.
2. The modeling of the adhesion of host particles ($\gamma\text{-Al}_2\text{O}_3$ particles) and guest particles (TiO_2 particles) was conducted, and the influence of surface energy of host/guest particles was investigated by the Hertz-Mindlin with JKR cohesion model.

6.1 Modeling the behavior of powders in the picomix: Mixing analysis of $\gamma\text{-Al}_2\text{O}_3$ and S.S316L

As a result of the experimental work on dry coating and the preparation of supports, S.S316L was considered to give a better coating than $\gamma\text{-Al}_2\text{O}_3$ under the same experimental conditions. In order to

Chapter 6: Simulation Results and Discussions

explain this phenomenon, a numerical study was considered to investigate the influence of intrinsic material properties on the dry particle coating.

Table 6.1 The parameters have been used to study the particle behavior.

Parameters	Properties of particle $\gamma\text{-Al}_2\text{O}_3$	Properties of particles S.S316L	Properties of picomix (steel)
Fixed parameters			
Density (ρ , kg/m ³)	3258	8102	7990 [384, 385]
Sphere diameter (D , mm)	0.6, 1, 2		
Poisson's ratio (ν)	0.25 [360, 363-365]	0.3 [369, 375-377, 380]	0.25 [369]
Young's Modulus (E , Pa)	1.7×10^{10} [357-359, 361]	2.0×10^{11} [369, 374, 375]	1.9×10^{11} [369]
Coefficient of Restitution coefficient (e)	$\gamma\text{-Al}_2\text{O}_3$ - $\gamma\text{-Al}_2\text{O}_3$	0.7 [366, 368]	
	$\gamma\text{-Al}_2\text{O}_3$ - wall	0.8 [369]	
	S.S316L - S.S316L	0.8 [366, 369]	
	S.S316L - wall	0.8	
Coefficient of Static friction (μ_s)	$\gamma\text{-Al}_2\text{O}_3$ - $\gamma\text{-Al}_2\text{O}_3$	0.1 [369]	
	$\gamma\text{-Al}_2\text{O}_3$ - wall	0.5 [369]	
	S.S316L - S.S316L	0.5 [369]	
	S.S316L - wall	0.5	
Coefficient of Rolling friction (μ_r)	$\gamma\text{-Al}_2\text{O}_3$ - $\gamma\text{-Al}_2\text{O}_3$	0.01 [369, 375]	
	$\gamma\text{-Al}_2\text{O}_3$ - wall	0.3 [369]	
	S.S316L - S.S316L	0.01 [369, 372, 375]	
	S.S316L - wall	0.01	
Modeling/simulation time (t , s)	1.0		
Rayleigh time-step (ΔT)	40% ΔT		
Variated parameters			
Number of particles (Diameter of particles)	2867 (2 mm) – 22918 (1 mm) – 106103 (0.6 mm)		
Filling ratio	10-40% filling ratio of picomix volume (100 mL)		
Young's modulus (E , Pa)	$\gamma\text{-Al}_2\text{O}_3$: 1.7×10^7 to 1.7×10^{10} S.S316L: 2.0×10^7 to 2.0×10^{11}		
Rotation speed (Ω , rpm)	1500, 3500, 5000		
<p>* $\Delta T = \pi \left(\frac{R}{0.163\nu + 0.877} \sqrt{\frac{G}{\rho}} \right)$, where R is radius of particle; ν is Poisson's ratio of particle ; ρ is the solid density of particle; G is the shear modulus of particle. G can be calculated by $G = \frac{E}{2(1+\nu)}$.</p>			

The objective of this study is to visualize and compare the possible effects on coating by mixing two types of host particles ($\gamma\text{-Al}_2\text{O}_3$ and S.S316L) separately. As described in Chapter 5, paragraph 5.2, the choice of material parameter plays a crucial role in the study of simulation because some parameters have a particularly large impact on calculation time. These parameters include density (ρ), young's modulus (E),

coefficient of restitution (e), coefficient of rolling friction (μ_f), coefficient of static friction (μ_s), diameters of host and guest particles, but these parameters are uneasily measured precisely in experiments. Therefore, before conducting numerical modeling, these values were obtained through an extensive literature analysis (see Chapter 5, paragraph 5.3.1).

In the current study, the main parameters for simulation regarding particles are particle density, young's modulus, Poisson's ratio, coefficient of restitution, coefficient of static friction, and coefficient of rolling friction. The value of particle density was measured by using a Helium pycnometer (AccuPyc1330, micromeritics Instrument Corp, see Chapter 2, paragraph 2.3.2). Except for this parameter, all other parameters are from the analysis of the literature. The clearance between paddles to the wall of the vessel is 1.3 ± 0.3 mm. However, in this study, this clearance was extended to 3 mm (as shown in figure 5.5, Chapter 5) because the largest particle size was 2 mm. Meanwhile, the distance between the rotor and the bottom paddles should be 1 mm (see Chapter 2, figure 2.2) in order to avoid the particles getting stuck at the bottom of the vessel and not being able to move. Hence, we had to increase the clearance between the paddles and the wall of the vessel: the distance between the rotor and the bottom paddles is increased by the same multiplying factor (1.3 times) as well.

This work was accomplished based on γ -Al₂O₃ and S.S316L particulate systems, and the setting of the parameters is based on the analysis in Chapter 5 and table 5.4. Notably, in each simulation, only one parameter is varied, the other parameters are fixed. This is the way to reach the study of the effect of a parameter on particle motion. The values of the parameters used in this work are summarized in table 6.1.

6.1.1 Analysis of stability calculation

Rajesh et al. ^[220] proved that collision frequency is an important factor in the dry coating process, because it presents the degree of particle interactions in the system. The larger the collision frequency, the more efficient interactions will happen between the guest particle and the host particle. Their simulation study showed that the collision frequency will reach a stable value after a certain time. In this study, collision frequency is introduced to study the interactions between particles ^[104, 186, 220]. Cumulative collision numbers acting on a single particle per second is defined as the collision frequency (f_n)

$$f_n = \frac{N_{collision}}{N_0 T_s} \quad (Eq. 6.1)$$

Where $N_{collision}$ is the cumulative collision numbers, T_s is the simulation time period and N_0 is the total simulated number. The simulation time (see figure 6.1) is chosen based on the stability of the collision frequency.

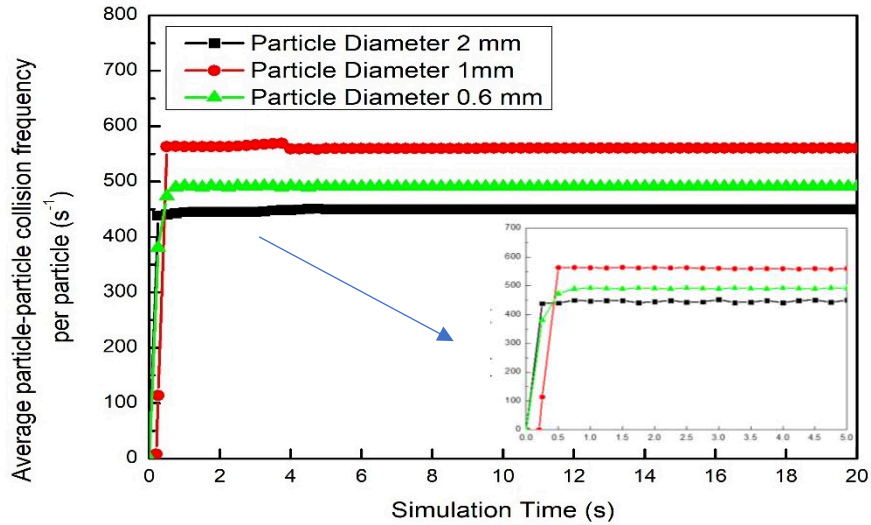


Fig. 6.1. Average particle-particle collision frequency per particle in 20 s as a function of simulation/modeling time at 3500 rpm, filling ratio at 20%, the diameter of γ - Al_2O_3 is 0.6 mm, 1 mm, and 2 mm (other parameters see table 6.1).

Figure 6.1 shows that the collision frequency reaches a steady state after 0.5 s even if the simulation time is extended to 20 s. Therefore, the simulation time of the DEM modeling in this study was set to 1s.

6.1.2 The effect of young's modulus/shear modulus

As described in Chapter 5, paragraph 5.2, it is difficult to complete a large number of simulations using the same parameters as in the experiments, because it takes a lot of computational time to complete a single simulation (see Chapter 5, figure 5.4). The calculation time of the simulation is related to four parameters, radius of the particle, Poisson's ratio of the particle, the solid density of the particle, and young's modulus of the particle, of which young's modulus, mainly affects the calculation time.

Young's modulus is a mechanical property that measures the stiffness of a solid material. In DEM modeling, reducing the young's modulus to increase the rayleigh time step and decrease the calculation cost is a common acceptable approach [20, 21]. However, some articles [402, 403] reported that the powder behaviour changes drastically with reducing the young's modulus (particle stiffness).

The purpose of this study is to investigate the effect of young's modulus on the behavior of particles. The Hertz-Mindlin (no-slip) contact model was applied in this study. The radius of the particles was set at 1 mm, the rotation speed was fixed at 3500 rpm, the filling ratio was kept at 20%, modeling time was 1 s (others parameters see table 6.1). Young's modulus was changed from 2.0×10^7 to 2.0×10^{11} Pa for S.S316L, for γ -Al₂O₃, the range of variation of young's modulus is from 1.7×10^7 to 1.7×10^{10} Pa.

6.1.2.1 Images snapshots analysis

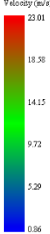
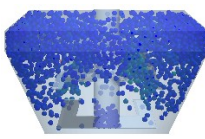
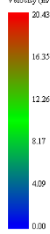
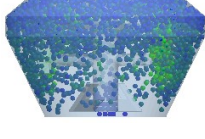
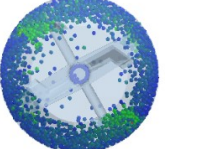
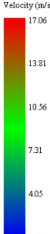
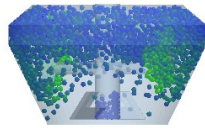
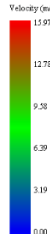
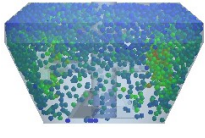
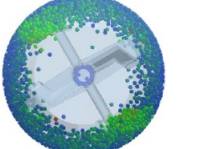
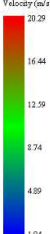
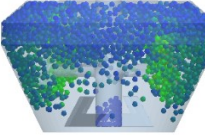
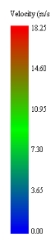
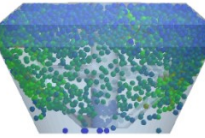
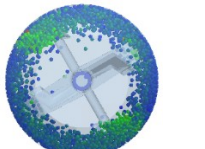
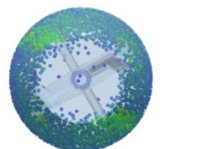
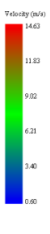
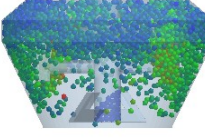
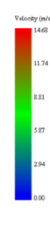
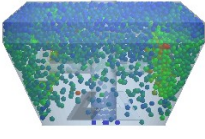
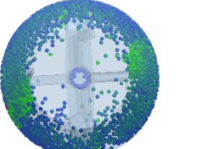
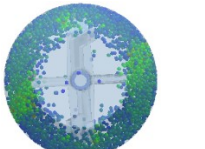
Image snapshots can be exported at a single time step or over a range of time steps in the modeling. This allows us to directly observe the movement of particles and it is very useful in understanding particle interactions. The particles are colored by the magnitude of particle velocity. The highest velocity particles are colored in red. The blue color represents the minimum velocity of the particles. The particles below the highest speed and above the minimum speed were marked in green.

Table 6.2 shows the snapshot of S.S316L and γ -Al₂O₃ particle motion at 1 s modeling time with the increase of young's modulus, the filling ratio was fixed at 20%, the rotation speed was 3500 rpm, the diameter of two particles was 2 mm (others parameters see table 6.1).

As it can be seen in the table 6.2, when the modeling time is 1 s, most particles stay at the upper end of the vessel with relatively high velocities. The influence of the variation of young's modulus on the state of particle motion is not obvious. However, with the same modeling conditions (rotation speed, filling ratio, and particle size), the S.S316L particles move at a relatively high site compared to γ -Al₂O₃ particles, as almost no S.S316L particles are seen at the bottom of the vessel but there are few γ -Al₂O₃ particles that can be found on the bottom of the vessel. This phenomenon can be related to the property of the particles themselves, as shown in Table 6.1. The density of S.S316L is larger than that of γ -Al₂O₃, and the mass of S.S316L is larger than that of γ -Al₂O₃ in the case of same particle size.

Chapter 6: Simulation Results and Discussions

Table 6.2 The snapshot of S.S316L and $\gamma\text{-Al}_2\text{O}_3$ particle motion at 1 s modeling time with the increase of young's modulus, the filling ratio was fixed at 20%, the rotation speed was 3500 rpm, the diameter of two particles was 2 mm (others parameters see table 6.1).

S.S316L		$\gamma\text{-Al}_2\text{O}_3$			
Different young's modulus (Pa) and snapshots of x and z views (at 1 s of modeling time)					
Young's Modulus: 2.0×10^7 Pa 	X view		Young's Modulus: 1.7×10^7 Pa 	X view	
	Z view			Z view	
Young's Modulus: 2.0×10^8 Pa 	X view		Young's Modulus: 1.7×10^8 Pa 	X view	
	Z view			Z view	
Young's Modulus: 2.0×10^9 Pa 	X view		Young's Modulus: 1.7×10^9 Pa 	X view	
	Z view			Z view	
Young's Modulus: 2.0×10^{10} Pa 	X view		Young's Modulus: 1.7×10^{10} Pa 	X view	
	Z view			Z view	

6.1.2.2 Analysis of particle contact force and overlap

Particle contact force is the force that acts between two solids that are physically touching each other [404]. Generally, contact between two particles occurs in the finite area due to the deformation of the particle, the contact force acting on particles is divided into two types of components-normal and tangential. When two particles collide, there is an area or range in common, called the overlap. The overlap consists of two components: normal and tangential. Figure 6.2 presents the effect of young's modulus on particle contact force and overlap.

It can be seen that the average contact force rises with the increase of young's modulus (see figure 6.2a-normal contact force and figure 6.2b-tangential contact force). As has been written in Chapter 1, paragraph 1.7.1.2, when two spherical particles are in elastic contact, the normal contact force between the two particles is $F_{n,i,j} = \frac{4}{3}E^*(R^*)^{1/2}\delta_n^{3/2}$. Respectively, $E^* \left(\frac{1}{E^*} = \frac{1-\nu_i^2}{E_i} + \frac{1-\nu_j^2}{E_j} \right)$ and $R^* \left(R^* = \frac{1}{\left(\frac{1}{R_i} + \frac{1}{R_j} \right)} \right)$ are the equivalent young's modulus and the equivalent radius. Here δ_n is the normal overlap between the contacting particle i and j ; The tangential contact force $F_{t,ij} = -K_t\delta_t$, here δ_t is the tangential overlap between the contacting particles i and j ; K_t the tangential spring constant. K_t is determined by [20, 104, 403]:

$$K_t = 8G^*/R^*\delta_n \quad (Eq. 6.2)$$

The relation between shear modulus and young's modulus is $G = \frac{E}{2(1+\nu)}$, where G^* is the equivalent shear modulus. Therefore, when the Poissio's ratio and the particles' radius are fixed, the tangential spring constant K_t rises with the increase of the young's modulus. The tangential contact force will surge with the increase of the young's modulus (see figure 6.2b).

As has been described in the beginning of this section, young's modulus is a mechanical property that measures the stiffness of solid material, stiffness is the extent to which an object resists deformation in response to an applied force. The higher young's modulus, the harder the particle, therefore the overlap will become smaller and smaller (see figure 6.2c and 6.2d).

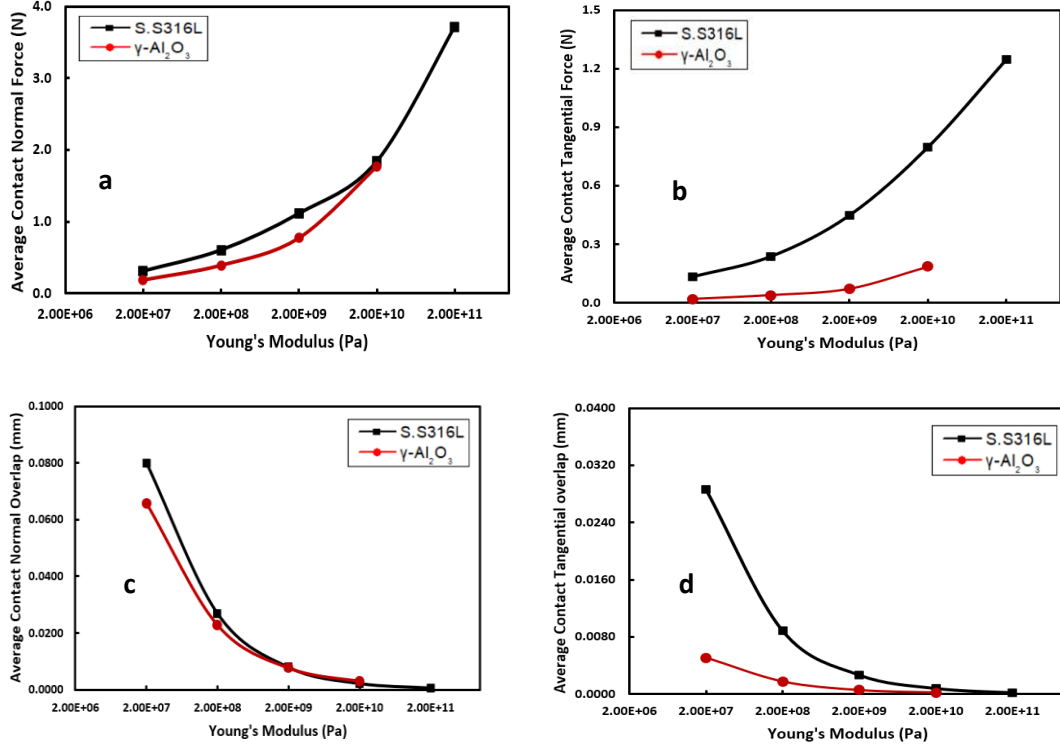


Fig.6.2 The variation of average particle contacts force (a-normal contact force and b-tangential contact force) and average overlap (c-normal overlap and d-tangential overlap) with the increasing of young's modulus. Rotation speed fixed at 3500 rpm, the filling ratio was set at 20%, the diameter of two particles is 2 mm, at 1 s modeling time (others parameters see table 6.1).

Both the normal contact force and the tangential force are related to the overlap and young's modulus, but since the value of the overlap is usually small, the normal/tangential contact force grows with the increase of young's modulus (see figures 6.2a and 6.2b).

6.1.2.3 Particle velocity

The magnitude of particle velocity can reveal the particle motions in the Picomix. The higher the particle velocity, the faster the particle movement. The average particle velocity in DEM modeling is given by:

$$\bar{v}_p = \sum_{i=1}^{N_0} v_{i(trans.)} / N_0 \quad (Eq. 6.3)$$

$$v_{i(trans.)} = \sqrt{v_{xi(trans.)}^2 + v_{yi(trans.)}^2 + v_{zi(trans.)}^2} \quad (Eq. 6.4)$$

Where $v_{i(trans.)}$ is the translational velocity magnitude of particle i , N_0 is the total number of particles in the simulation. Respectively, $v_{xi(trans.)}$ $v_{yi(trans.)}$ $v_{zi(trans.)}$ are the translational velocity magnitudes of particle i,j in X, Y and Z axis direction.

Figure 6.3 presents the average particle velocity of S.S316L and γ -Al₂O₃ as a function of young's modulus with 3500 rpm rotational speed, the diameter of particle 2 mm, filling ratio 20%, and modeling time 1 s.

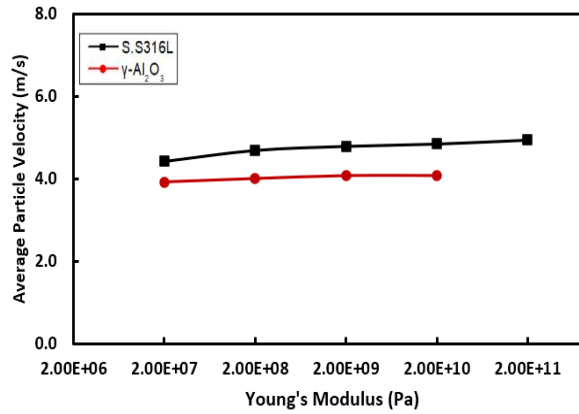


Fig.6.3 The variation of average particle velocity with the increase of young's modulus. Rotational speed fixed at 3500 rpm, filling ratio set at 20%, diameter of two particles is 2 mm, modeling time at 1 s (Other's parameters see table 6.1).

It can be seen from figure 6.3 that young's modulus does not seem to have any significant effect on the average particle velocity. Under the same simulation conditions, the average velocity of S.S316L is larger than that of γ -Al₂O₃, which may be mainly related to the property of the particles themselves, as shown in Table 6.1. The density of S.S316L is larger than that of γ -Al₂O₃, and the mass of S.S316L is larger than that of γ -Al₂O₃ in the case of the same particle size.

6.1.2.4 Kinetic energy

The kinetic energy of a solid is the energy that it possesses due to its motion^[405], in a rotational system, the kinetic energy splits into the sum of the translational kinetic energy and the rotational kinetic energy:

$$E_k = \bar{E}_t + \bar{E}_r \quad (Eq. 6.5)$$

Where E_k is the total kinetic energy, \bar{E}_t is the translational kinetic energy, \bar{E}_r is the rotational kinetic energy.

When the particle moves from one location to another, the energy produced during its movement is called translational kinetic energy. The average translational kinetic energy in the DEM modeling is given by the following equation:

$$\bar{E}_t = \sum_{i=1}^{N_0} \frac{1}{2} m v_{i(trans.)}^2 / N_0 \quad (Eq. 6.6)$$

Where m is the mass of particle, $v_{i(ang.)}$ is the translational velocity magnitude of particle i , N_0 is the total number of particles in the modeling.

Energy associated with the rotational motion is not a new form of energy; rather, it is the energy associated with rotational motion, the same as kinetic energy in translational motion. This value in the DEM modeling can be obtained by the following equation:

$$\bar{E}_r = \sum_{i=1}^{N_0} \frac{1}{2} I v_{ang.}^2 / N_0 \quad (Eq. 6.7)$$

Where I is the moment of inertia, $v_{ang.}$ is the angular velocity magnitude of particle i , N_0 is the total number of particles in the modeling; for a sphere, the moment of inertia $I = 2/5 m R^2$, where m is the particle mass, R is the particle radius, ρ is the solid density. Angular velocity is defined as the speed at which an object rotates, $v_{ang} = R\omega$.

Figure 6.4 shows the trend of the particle kinetic energy of S.S316L and γ -Al₂O₃ with the increase of young's modulus.

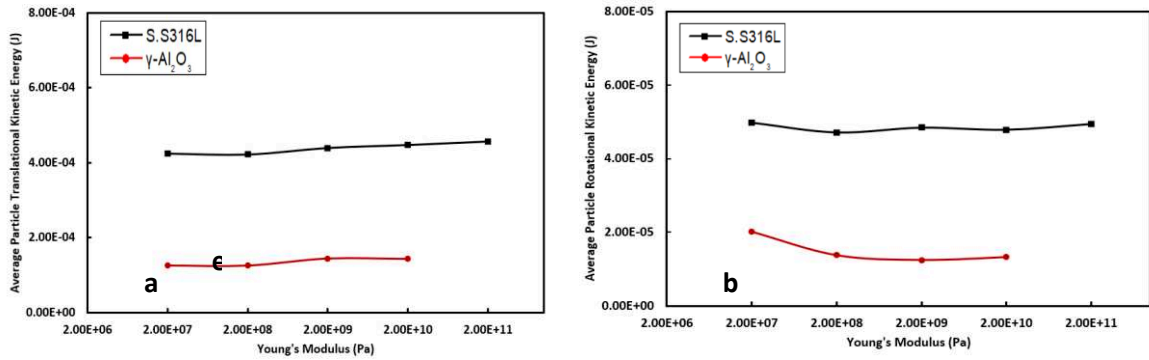


Fig.6.4 The variation of average kinetic energy (a-translational kinetic energy and b-rotational kinetic energy) with the increasing of young's modulus. Rotational speed fixed at 3500 rpm, the filling ratio was set at 20%, the diameter of two particles is 2 mm, at 1 s modeling time (others parameters see table 6.1).

It is found that young's modulus does not seem to have any significant effect on the average kinetic energy (see figure 6.4a- average particle translational kinetic energy and figure 6.4b- average particle rotational

kinetic energy). According to equations 6.6 and 6.7, the kinetic energy of the particle is determined by the velocity (translational and angular) and mass. In the above section, the average velocity was essentially unchanged with increasing young's modulus (see figure 6.3). Therefore, the increase in young's modulus has little effect on the kinetic energy of the particles.

6.1.2.5 Particle potential energy

Potential energy is a kind of energy stored in a physical system and is a physical quantity used to describe the magnitude of an object's ability to do work in a conservative force field. In a physical sense, potential energy represents the energy stored in an object at a given position and describes the magnitude of the work capability. Under the right circumstances, potential energy can be converted into other energy such as kinetic energy [405]. In the DEM modeling, the particle potential energy is given by the following equation:

$$\bar{E}_p = mgh \quad (Eq. 6.8)$$

Where m is the particle mass, g is the acceleration of gravity ($g = 9.81 \text{ m/s}^2$) and h is the distance between the center mass of the particle and the defined 'ground' level (i.e., coordinate plan $h=0$). Therefore, the magnitude of particle potential energy displays the state of a particle, the larger the potential energy, the higher the positions of the particle will be during the motions.

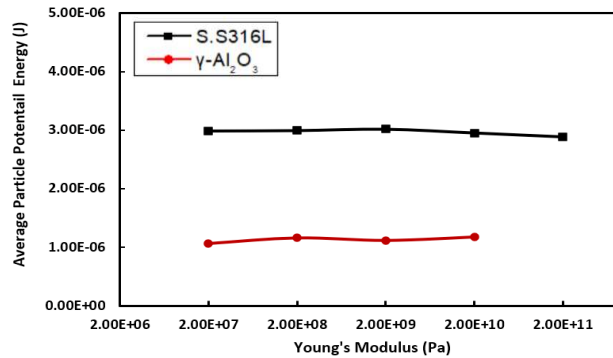


Fig.6.5 Average kinetic energy as a function of young's modulus. Rotational speed fixed at 3500 rpm, the filling ratio was set at 20%, the diameter of two particles is 2 mm, at 1 s modeling time (others parameters see table 6.1).

Figure 6.5 presents the variation of potential energy of S.S316L and γ -Al₂O₃ with the increase of young's modulus. As it can be seen, the increase in young's modulus of the particles does not seem to have any significant effect on the potential energy of the particles.

6.1.3 The effect of particle size

As presented in Chapter 5, paragraph 5.1, it is not practical to use the same particle size during the experiment. This would impose a large computational burden on the simulation. Therefore, we decided to enlarge the size of the particles to reduce the calculation time and tried to do as many simulations as possible to study particle behavior.

To learn the effect of particle size on particle behavior, the radius of the particles was varied from 0.3 to 1 mm. Filling ratio fixed at 20%, with 3500 rpm rotational speed at 1 s modeling time (others parameters see table 6.1). The interval for data saving was set at 0.25 s to avoid excessive time or storage for this feature. The results were analyzed and exported as data values, images, or videos for investigating the particles' motions and interactions. The Hertz-Mindlin (no-slip) contact model was applied in this study. Two particles (γ -Al₂O₃ and S.S316L) with different radius (0.3, 0.5, and 1 mm) were conducted to study particle behavior.

In the previous section (see paragraph 6.1.2) we have found that the reduction of young's modulus has essentially no effect on the energy of the particles and their velocities. In the study (this section), because of the small size (radius is 0.3 mm) involved, 106103 particles will be used, and in order to reduce the calculation time, the young's modulus of γ -Al₂O₃ and S.S316L are respectively 1.7×10^8 Pa and 2.0×10^8 Pa.

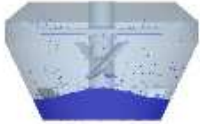
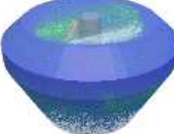
6.1.3.1 Image snapshots analysis

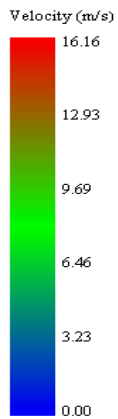
Table 6.3 shows the snapshots of S.S316L particles in picomix under 3500 rpm by DEM modeling, with 0.6-2.0 mm in particle diameter, 20% filling ratio, the particles are colored by the magnitude of particle velocity, the highest velocity-colored particles are red, the blue color ones represent the minimum velocity of the particles, the particles below the highest speed and above the minimum speed were marked as green.

As it can be seen in the initial state, in the 0-0.25 s of modeling time, the particles lift up along the wall of the vessel up to the upper side of the picomix. As the modeling time increases from 0.25 s to 1 s, the particles reach the top and become steady and move on the upper side of the picomix. There are a lot of S.S316L with a radius of 0.3 mm that can be observed that stayed at the bottom of the vessel of the picomix. By contrast, there are no 2 mm S.S316L particles that can be found at the bottom of the picomix's vessel.

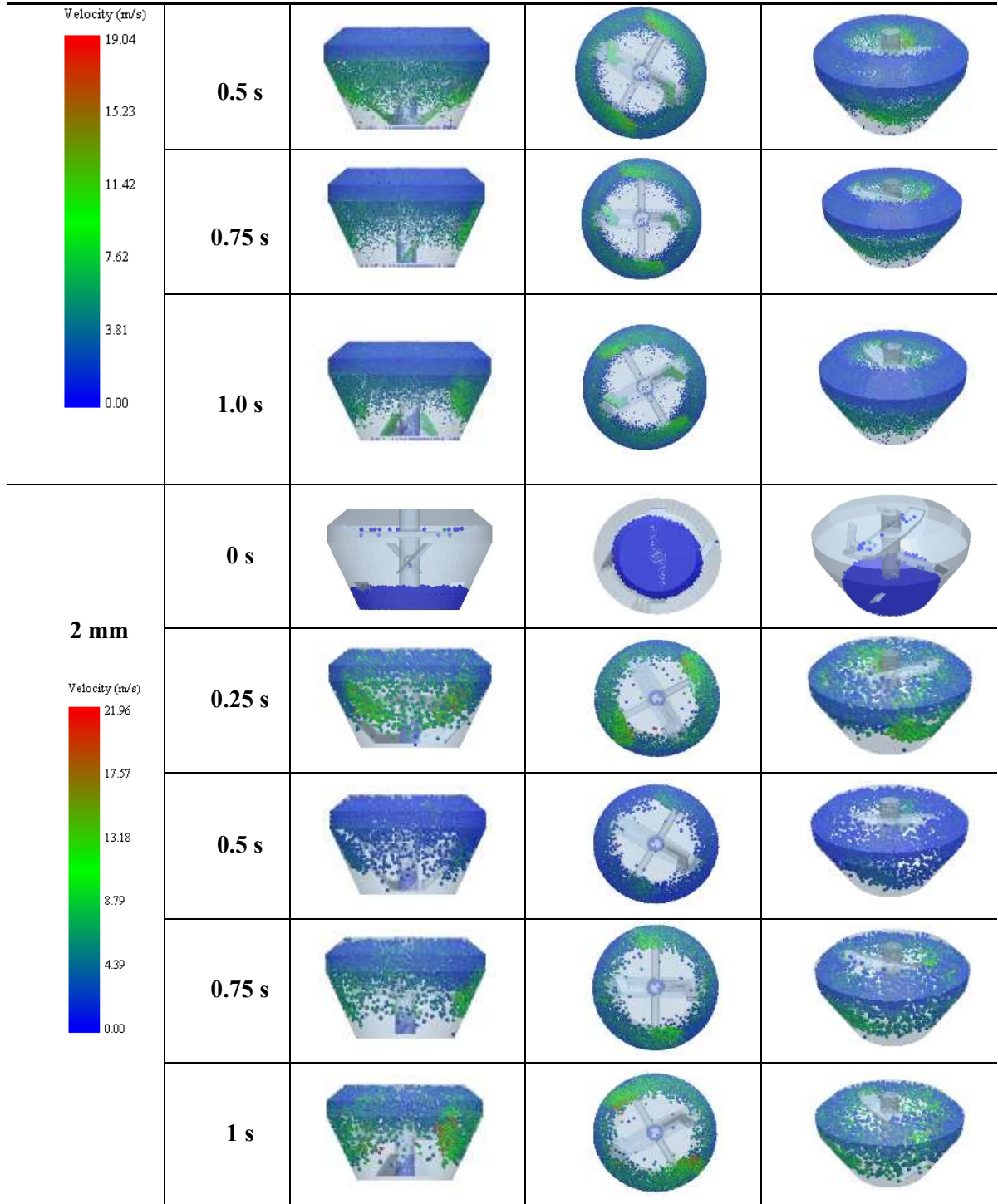
Chapter 6: Simulation Results and Discussions

Table 6.3 The snapshot of S.S316L particle motion in the Picomix at 3500 rpm, 1 s with different particle size at fixed filling ratio 20% (others parameters see table 6.1).

Particle diameter	Modeling time (s)	X-axis view	Z-axis view	3D view
0.6 mm	0 s			
	0.25 s			
	0.5 s			
	0.75 s			
	1.0 s			
	1 mm	0 s		
0.25 s				



Chapter 6: Simulation Results and Discussions



The magnitude of particle distribution revealed that the particles exhibited the highest velocity around the middle paddle of the rotor, which were colored as red spheres. Green particles that represent the average velocity (between the highest velocity in red and the minimum velocity in blue) can be found along the

walls or in the center of Picomix. At the same modeling conditions, it was noted that particles with a particle radius of 0.3 mm were also moving around the wall under the centrifugal force, but very few red particles were captured, indicating that the small size particles were moving along the wall at a low speed.

6.1.3.2 Analysis of particle contact force and overlap

In the current study, the average normal force between two particles $F_{n,ij}$ is calculated by

$$F_{n,ij} = \frac{4}{3}E^*(R^*)^{1/2}\delta_n^{3/2}, \text{ The average tangential force } F_{t,ij} \text{ is calculated by } F_{t,ij} = -K_t\delta_t.$$

Figure 6.6 presents average normal contact force, tangential contact force, average normal overlap, and average tangential overlap at 3500 rpm, 1 s modeling time with different particle diameters.

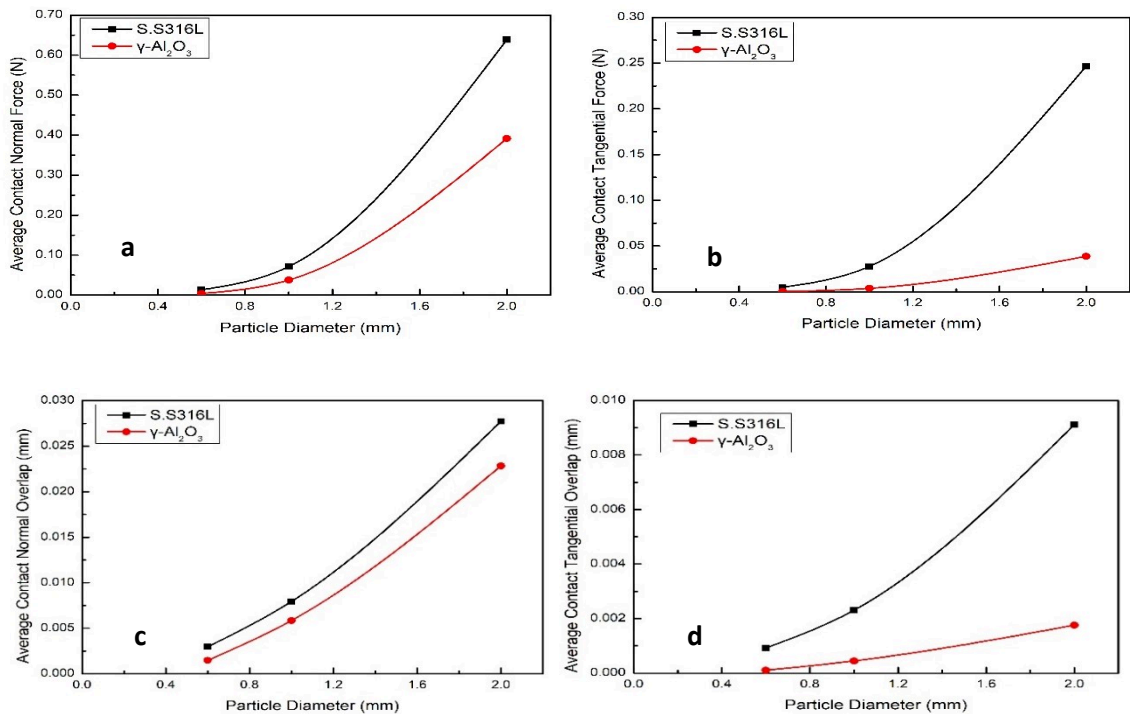


Fig. 6.6 Average contact normal force (a), average contact tangential force (b), average contact normal overlap (c), and average contact tangential overlap (d) as a function of particle diameters with filling ratio fixed at 20%, with 3500 rpm rotational speed at 1 s modeling time (others parameters see table 6.1).

It was found that both average normal contact force and tangential contact force increased with the particle diameter from 0.6 mm to 2 mm. Taking into account the same particle diameter (e.g., the particle diameter

is 1mm), S.S316L gives bigger force than γ -Al₂O₃. This phenomenon can be explained by the intrinsic material properties. As it can be seen, the contact normal force relates to equivalent young's modulus (calculated by Eq.1.10), equivalent particle radius (is calculated by Eq.1.11), and overlap (calculated by Eq.1.8). For a 1 mm diameter, the equivalent particle radius will be the same (0.25 mm calculated by Eq.1.11) for S.S316L and γ -Al₂O₃. Based on some literature analysis^[357-359, 361], S.S316L has a higher young's modulus and Poisson's ratio than γ -Al₂O₃.

Figures 6.6(c) and 6.6(d) show that the normal/tangential contact overlap increases with the particle diameter, apparently, figure 6.6(d) gives the same trends as figure 6.6(b), because tangential force is given by $F_{t,ij} = -K_t \delta_t$. When the particle size of S.S316L and γ -Al₂O₃ is the same, the contact overlap of S.S316L is higher than γ -Al₂O₃. This can be explained by Newton's second law, which has been written in Eq.1.24 ($m_i \frac{dV_i}{dt} = \sum F_i$). Mass is calculated by solid density ($\rho_{\gamma-Al_2O_3} = 3258 \text{ kg/m}^3$, $\rho_{S.S316L} = 7990 \text{ kg/m}^3$) and volume. When particle diameter is the same, denser materials provide larger mass (because in the DEM modeling, the volume is calculated without considering the porosity of material).

6.1.3.3 Particle velocity and energy

The magnitude of particle velocity was calculated by equations 6.3 and 6.4, the translational kinetic energy, rotational kinetic energy, and potential energy respectively were calculated by equations 6.6, 6.7, and 6.8.

Figure 6.7 presents the average particle velocity, the translational kinetic energy, the rotational kinetic energy, and the potential energy of S.S316L and γ -Al₂O₃ as a function of particles diameter with 3500 rpm rotational speed, filling ratio 20%, and modeling time 1 s, other parameters can see table 6.1.

It was found that the average particle velocity increases with particle diameter (see figure 6.7a), the images of the snapshot in table 6.2 have already proved that the velocity increases with an increase in particle size. The average particle potential energy increases in correlation with the particle size (see figure 6.7b). Since S.S316L has a higher solid density than γ -Al₂O₃, at the same particle diameter, S.S316L will provide higher potential energy. Meanwhile, the snapshot (see table 6.2) demonstrated that the particles with a radius of 2 mm were moving around the wall of the vessel of the piocmix at a relatively high position.

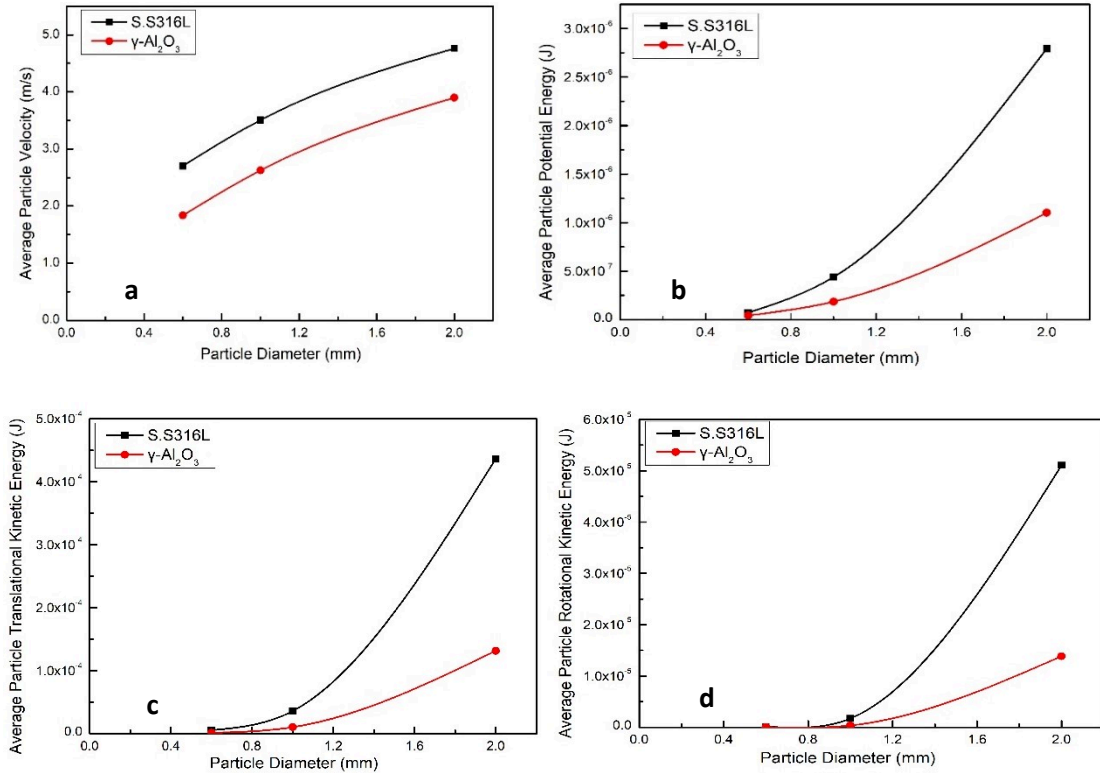


Fig. 6.7 Average particle velocity(a), average particle potential energy(b), average particle translational kinetic energy(c), and average particle rotational kinetic energy(d) as a function of particle diameters with filling ratio fixed at 20%, with 3500 rpm rotational speed at 1s modeling time (others parameters see table 6.1)

It illustrates that as the particles increase, the average particle translational kinetic energy (see figure 6.7c), and the average particle rotational kinetic energy (see figure 6.7d) will increase as well. According to equations 6.6 and 6.7, the average translational kinetic energy is related to the velocity. The velocity rises with the increase of particle size (see figure 6.7a). Therefore, the average translational kinetic energy grows along with particle size.

6.1.4 The effect of rotational speed

In our team, Lu ^[132] and Liu ^[104] have studied the effect of rotational speed on dry particle coating. Through numerical experimental studies, they proved that the rotational speed is an important parameter for dry particle coating.

The purpose of this part of the study is to learn how the rotational speed influences the two different particles ($\gamma\text{-Al}_2\text{O}_3$ and S.S316L) behavior in a simulation. The radius of the particles was set to 1 mm, the

filling ratio fixed at 20%, the rotational speed was varied from 1500 rpm to 5000 rpm, modeling time was at 1 s. Because only 2867 particles were used for the simulation when the particle diameter was 2 mm, the young's modulus of γ -Al₂O₃ and S.S316L were respectively 1.7×10^{10} Pa and 2.0×10^{11} Pa. (others parameters see table 6.1).

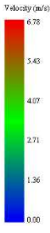
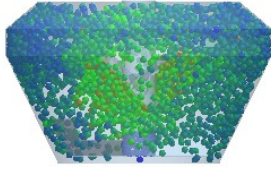
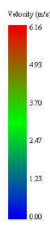
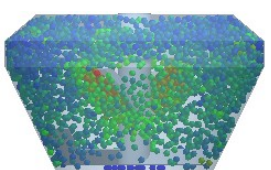
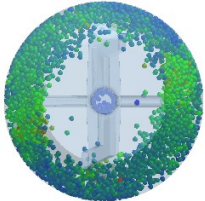
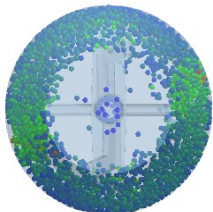
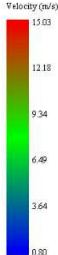
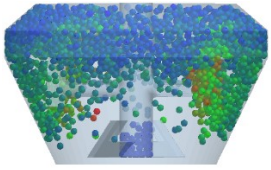
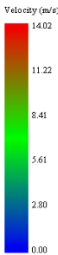
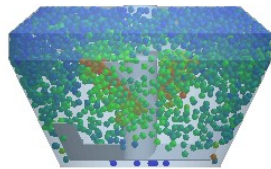
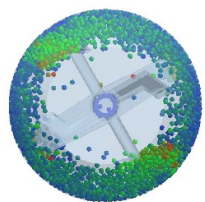
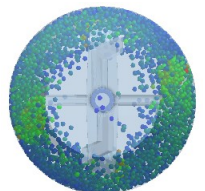
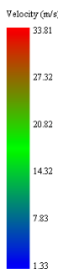
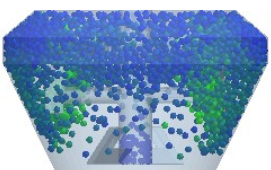
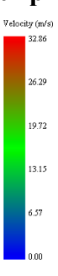
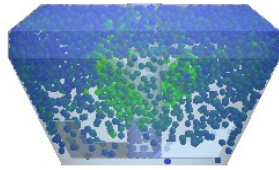
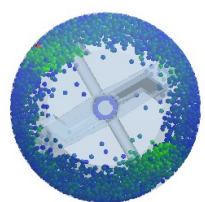
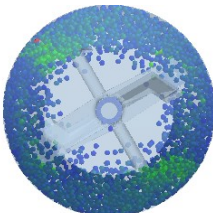
6.1.4.1 Images snapshot analysis

Table 6.4 shows the snapshots of particle motion in the picomix at 1 s with a different rotational speed at a fixed filling ratio of 20%, the diameter of the two particles is 2 mm (others parameters see table 6.1). The particle in the table on the left shows all particles colored by velocity. The particles with the highest velocity were colored in red; those with the lowest particles were colored in blue. From the study of the effect of particle size on particle motion in the previous section, we knew that in the initial of mixing, the particles went up from the bottom to the top of the vessel of the picomix. 0.5 s into the simulation, the motion of the particles was basically in a stable state.

The snapshot of S.S316L and γ -Al₂O₃ particle motion reveals that the particles exhibited the highest velocity around the middle paddle. As the rotational speed increases, fewer and fewer particles can be seen at the bottom. The fact is that when the rotational speed rises to 3500 rpm, there are no S.S316L particles present at the bottom of the vessel. Nevertheless, there are several γ -Al₂O₃ particles that can be seen even if the rotational speed is increased to 5000 rpm. The snapshot implies that the increase in rotational speed has a significant effect on both particles, but it seems to have a greater effect on the S.S316L particles. This may be related to the property of S.S316L itself. When the diameter of S.S316L and γ -Al₂O₃ and filling ratio are the same, the density of the S.S316L particles is higher than that of the γ -Al₂O₃ particles. Therefore, S.S316L has a bigger mass compared to that of γ -Al₂O₃, it can transmit more energy at the same rotational speed.

Chapter 6: Simulation Results and Discussions

Table 6.4 The snapshot of S.S316L and γ -Al₂O₃ particle motion at 1 s with different rotational speeds at fixed filling ratio 20%, the diameter of two particles is 2 mm (others parameters see table 6.1).

		S.S316L			γ -Al ₂ O ₃
Different rotational speed/rpm and snapshot of x and z views (at 1s)					
Rotational speed : 1500 rpm 	X view		Rotational speed : 1500 rpm 	X view	
	Z view			Z view	
Rotational speed : 3500 rpm 	X view		Rotational speed : 3500 rpm 	X view	
	Z view			Z view	
Rotational speed : 5000 rpm 	X view		Rotational speed : 5000 rpm 	X view	
	Z view			Z view	

6.1.4.2 Particle force, velocity, and energy analysis

Figure 6.8 shows the variation of the average particle's normal/tangential contacts force, the average normal/tangential overlap, the average kinetic energy, the average potential energy, and the average particle velocity with an increasing rotational speed, the filling ratio was fixed at 20%, the diameter of two particles was 2 mm, at 1 s modeling time (others parameters see table 6.1).

It was found that the velocity (see figure 6.8h) of both particles increases with rise of rotational speed, because more energy was provided by the picomix and transmitted to the particles. When $\gamma\text{-Al}_2\text{O}_3$ and S.S316L have the same filling ratio and diameter, the denser S.S316L particles have a higher mass compared to $\gamma\text{-Al}_2\text{O}_3$ particles. Therefore, the velocity and energy of S.S316L will always be higher compared to $\gamma\text{-Al}_2\text{O}_3$. The important thing is that the higher the rotational speed, the larger the gap between S.S316L and $\gamma\text{-Al}_2\text{O}_3$ (figure 6.8h). Due to low speeds, both S.S316L and $\gamma\text{-Al}_2\text{O}_3$ particles are moving at a relatively low level. But as the rotational speed increases, S.S316L particles with large masses will move faster and faster. This will make the velocity gap between S.S316L and $\gamma\text{-Al}_2\text{O}_3$ become wider and wider.

Since the average particle translational and rotational kinetic energy are related to the particle's velocity, both the average particle translational (see figure 6.8e) and rotational kinetic energy (see figure 6.8f) increase in correlation with rotational speed.

The image snapshot analysis (see table 6.4) has demonstrated that as velocity increases, the particles move at relatively high positions of the vessel. Since the magnitude of particle potential energy is related to the magnitude of particle mass and the particle's position in the picomix, thus the average particle potential energy (see figure 6.8g) increases with velocity.

In DEM modeling, the normal overlap represents the normal deformation of a particle ($\delta_{n,ij}$) between two particles i and j at positions P_i and P_j with radius R_i and R_j . The overlap is defined as ^[406]:

$$\delta_{n,ij} = (R_i + R_j) - (P_i + P_j) \quad (\text{Eq. 6.9})$$

or, alternatively, at any time,

$$\delta_{n,ij} = - \int_{t=t_{c,ij}}^t V_{n,ij} dt \quad (\text{Eq. 6.10})$$

$V_{n,ij}$ is the normal relative velocity between particles i and j , $t_{c,ij}$ is the time at the onset of the collision process.

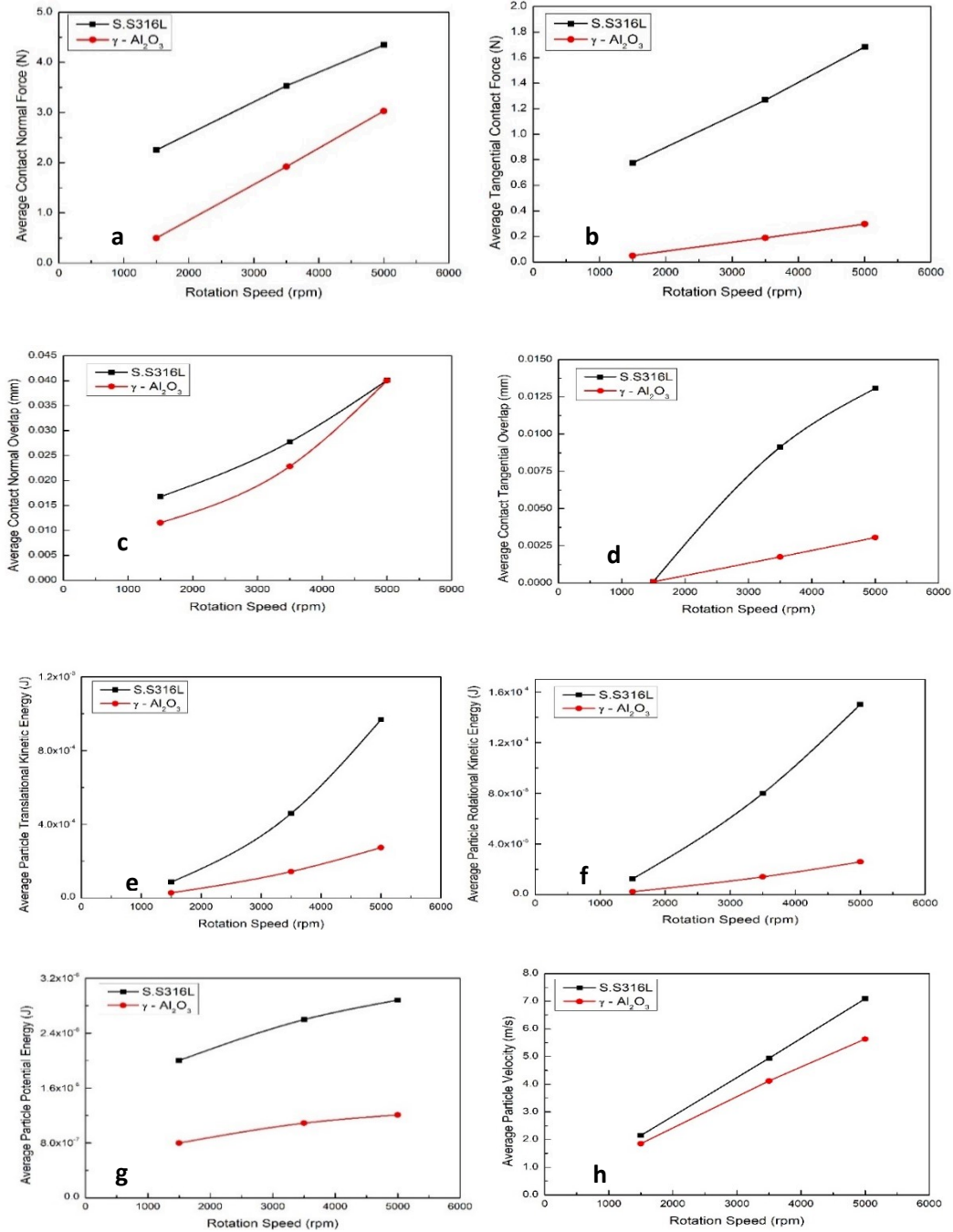


Fig.6.8 The variation of average particle contacts force (a-normal contact force and b-tangential contact force), average overlap (c-normal overlap and d-tangential overlap), average kinetic energy (e-translational kinetic energy and f-rotational kinetic energy), average potential energy (g), average particle velocity (h) with the growth of rotational speed, the filling ratio was fixed at 20%, the diameter of two particles was 2 mm, at 1 s simulation time (others parameters see table 6.1).

The tangential overlap ($\delta_{t,ij}$) of the contact points up to the point at which the contact ends or the particle begins to roll or slip. It can be calculated by ^[407]

$$\delta_{t,ij} = \int_{t=t_{c,ij}}^t V_{t,ij} dt \quad (\text{Eq. 6.11})$$

$t_{c,ij}$ is the time at the onset of the collision process, $V_{t,ij}$ is equal to the difference between the relative velocity and the normal relative velocity: $V_{t,ij} = V_{ij} - V_{n,ij}$.

According to equation 6.11, the tangential overlap rises with increasing velocity (see figure 6.8d), therefore, the average contact tangential force shows a growing trend (see figure 6.8b). The normal overlap can be calculated by equation 6.10, it shows an increasing trend with increasing rotational speed (see figure 6.8c). However, as it can be seen, the gap of the normal contact overlap between S.S316L and γ -Al₂O₃ becomes narrower and narrower, because the overlap consists of two components, normal and tangential (the overlap between two particles i and j, $\delta_{ij} = \delta_{n,ij} + \delta_{t,ij}$). The overlap of particles is increasing, but due to the gap of tangential overlap between S.S316L and γ -Al₂O₃, it gets wider and wider. Thus, it is reasonable to conclude that the normal overlap gap between S.S316L and γ -Al₂O₃ becomes narrower.

According to the following equation $F_n = \frac{4}{3}E^*(R^*)^{1/2}\delta_n^{3/2}$, the normal contact force (see figure 6.8a) relates to the equivalent radius and the equivalent young's modulus. When the diameters of S.S316L and γ -Al₂O₃ are the same, the equivalent radius will be the same, the magnitude of normal contact force will be directly relying on the magnitude of equivalent young's modulus and the normal overlap. Consequently, the normal contact force grows with the rise of rotational speed, like the normal overlap, the gap of normal contact force between S.S316L and γ -Al₂O₃ narrows.

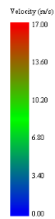
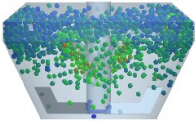
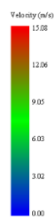
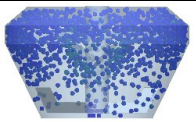
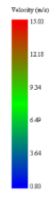
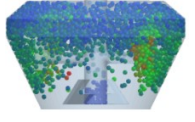
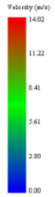
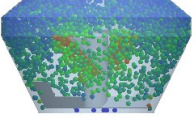
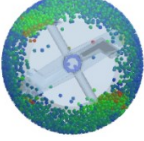
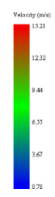
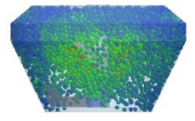
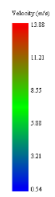
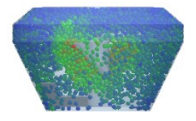
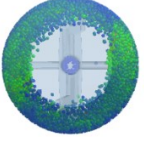
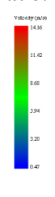
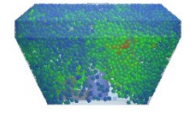
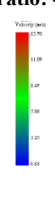
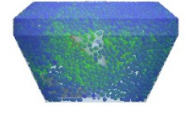
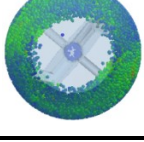
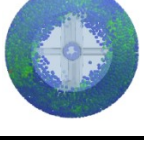
6.1.5 The effect of filling ratio

The effect of the filling ratio on particle motion has been reported by Sato ^[186] and Liu ^[104] in their modeling studies. The effects of rotational speed and particle size have been investigated in the previous section. This part aims at learning how the filling ratio influences the two different host particles (γ -Al₂O₃ and S.S316L) behavior in the simulation. The radius of the particles was set at 1 mm, the rotational speed was fixed at 3500 rpm, the filling ratio was 10%, 20%, 30%, and 40%, modeling time was 1 s (others parameters see table 6.1).

6.1.5.1 Images snapshot analysis

Table 6.5 shows the snapshot of S.S316L and γ -Al₂O₃ particle motion at 1s with the increase of filling ratio. The radius of the particles was set at 1mm, the rotational speed was fixed at 3500 rpm, the filling ratio was 10%, 20%, 30%, and 40%, modeling time was 1s (others parameters see table 6.1).

Table 6.5 The snapshot of S.S316L and γ -Al₂O₃ particle motion at 1 s simulation time with the increase of filling ratio at fixed rotation speed 3500 rpm, the diameter of two particles is 2 mm (others parameters see table 6.1).

S.S316L			γ -Al ₂ O ₃		
Different filling ratio/% and snapshot of x and z views (at 1s of simulation time)					
Filling ratio: 10% 	X view		Filling ratio: 10% 	X view	
	Z view			Z view	
Filling ratio: 20% 	X view		Filling ratio: 20% 	X view	
	Z view			Z view	
Filling ratio: 30% 	X view		Filling ratio: 30% 	X view	
	Z view			Z view	
Filling ratio: 40% 	X view		Filling ratio: 40% 	X view	
	Z view			Z view	

When the particle filling ratio is 10%, the particle has a lot of free space to move, the movement of the particles is mainly concentrated in the middle and upper middle of the vessel but as the filling rate increases, more particles are involved in the vessel. Therefore, the particles can be seen in the whole vessel. At the same filling ratio, e.g., at a filling ratio of 40%, more $\gamma\text{-Al}_2\text{O}_3$ particles are spread to the bottom of the vessel compared to the S.S316L particles. This is the same reason, as has been explained before, related to the property of the two particles themselves, the main influencing factor should be the density of the particles.

6.1.5.2 Particle force, velocity, and kinetic analysis

Figure 6.9 shows the effect of the filling ratio on the motion of two types of host particles ($\gamma\text{-Al}_2\text{O}_3$ and S.S316L). The effect was assessed by the average particle normal/tangential contact force, the average particle normal/tangential overlap, the average particle translational/rotational kinetic energy, the average particle potential energy, and the average particle velocity.

It was found that the average velocity (see figure 6.9i) has a slightly increasing trend but remains in a relatively stable state with the increase of the filling ratio from 10-40%. It indicated that the filling ratio exhibits a very small influence on both particles. An increase in the filling ratio causes an increase in the number of particles, which move in the middle part of the vessel at low filling ratios (see table 6.5, the images of the snapshot of S.S316L and $\gamma\text{-Al}_2\text{O}_3$). At low filling ratios (such as filling ratio 10%), all particles move in the middle part of the vessel. More particles mean the space for movement becomes less available and the picomix becomes more crowded. The particles appear at the bottom and the top of the vessel. Therefore, the change in average velocity with increasing filling ratio is not very significant.

The average translational kinetic energy in DEM modeling is given by equation 6.6, and it relates to velocity. Therefore, it is logical that the average translational kinetic energy (see figure 6.9e) remains in a relatively stable state as well.

Both the average contact normal force (see figure 6.9a) and the average normal overlap (see figure 6.9c) boost with the growth of the filling ratio, which due to the increase in filling ratio means that more particles are involved in the movement. The more particles there are in the same space, the more chances for them to run into each other. Thus, it is reasonable that the average contact normal force and the average normal overlap tend to increase with the increase of the filling ratio.

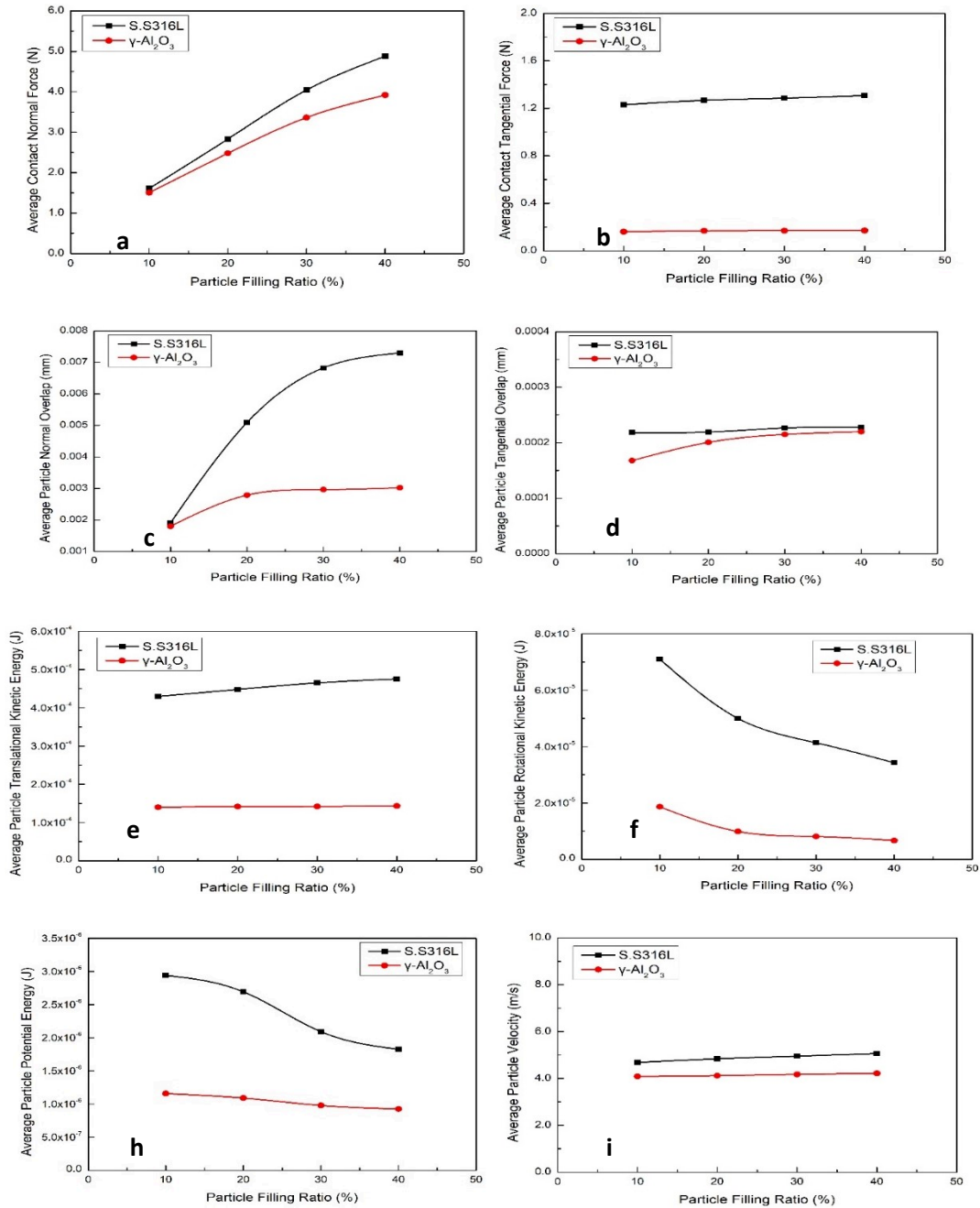


Fig.6.9 The variation of average particle contacts force (a-normal contact force and b-tangential contact force), average overlap (c-normal overlap and d-tangential overlap), average kinetic energy (e-translational kinetic energy and f-rotational kinetic energy), average potential energy (g), average particle velocity (h) with a rise of the filling ratio. The rotational speed was fixed at 3500 rpm, the diameter of the two particles is 2 mm, at 1s modeling time (others parameters see table 6.1).

For the average contact tangential force (see figure 6.9b) and the average tangential overlap (see figure 6.9d), the increase in filling ratio does not seem to have an obvious effect on them. According to equation 6.11, it is clear that the tangential overlap refers to the particle velocity. However, the particle velocity is not very sensitive to the increase of the filling ratio. That's why both the average contact tangential force and the average tangential overlap are insensitive to the filling ratio as well.

Looking at the average particle rotational kinetic energy (see figure 6.9f), it presents a mild decrease tendency with the increase of the filling ratio. As we claimed earlier, kinetic energy has two aspects- translational kinetic energy and rotational kinetic energy. The velocity of the particles can be divided into normal and tangential directions as well. But the particle velocity does not respond positively to change in the filling ratio, thus theoretically there is no change in the average kinetic energy. When the average particle translational kinetic energy increases slightly with a rise of the filling ratio, it is reasonable to conclude that the average rotational kinetic energy has a slight tendency to decrease as the filling ratio increases.

Accordingly, the particle potential energy is directly relying on the particle mass and the particle position. As the filling ratio increases, the number of particles also increases significantly, the movement of the particles becomes restricted (this phenomenon can be clearly seen in table 6.5), thus the average particle potential energy has a tendency to decrease (see figure 6.9h).

6.1.6 Partial conclusion

In this section, the effect of particle size, rotational speed, filling ratio, and young's modulus on the particle's motions and interactions in the Picomix have been investigated via DEM modeling. The choice of particle parameters, except for the density of the particles, was obtained from previous literature analyses. The effect of these values (particle size, rotational speed, filling ratio, and young's modulus) on particle behavior was evaluated in terms of contact forces, kinetic energy, velocity between particles, and some snapshots have contributed to this evaluation as well. The degree of correlation between the variation of parameters and the particle behaviors in the DEM modeling is summarized in table 6.6.

The studies demonstrate that particle size and rotational speed have a significant effect on contact forces (normal/tangential contact force), overlap (normal/tangential overlap), velocity, and energy (potential, translational/rotational kinetic energy).

Chapter 6: Simulation Results and Discussions

Table 6.6 The degree of correlation between the variation of parameters and particle behaviors in DEM modeling of γ -Al₂O₃ and S.S316L particles in the picomix.

Particles	Evaluation of particle behaviors	Variation of parameters			
		Particle radius (0.3-1 mm)	Rotational speed (1500-5000 rpm)	Filling ratio (10 - 40%)	Young's modulus (2.0×10^7 - 2.0×10^{11} Pa)
S.S316L	Particle velocity (m/s)	●●●	●●●	●	●
	Particle normal contact force (N)	●●●	●●●	●●●	●●●
	Particle tangential contact force (N)	●●●	●●●	●	●●●
	Particle normal overlap (mm)	●●●	●●●	●●●	●●●
	Particle tangential overlap (mm)	●●●	●●●	●	●●●
	Particle translational kinetic energy (J)	●●●	●●●	●	●
	Particle rotational kinetic energy (J)	●●●	●●●	●●	●
	Particle potential energy (J)	●●●	●●●	●●	●
γ -Al ₂ O ₃	Particle velocity (m/s)	●●●	●●●	●	●
	Particle normal contact force (N)	●●●	●●●	●●●	●●●
	Particle tangential contact force (N)	●●●	●●●	●	●●●
	Particle normal overlap (mm)	●●●	●●●	●●●	●●●
	Particle tangential overlap (mm)	●●●	●●●	●	●●●
	Particle translational kinetic energy (J)	●●●	●●●	●	●
	Particle rotational kinetic energy (J)	●●●	●●●	●●	●
	Particle potential energy (J)	●●●	●●●	●●	●

Notes: ●●● means a very big influence of the parameters on the a certain value of the particles;
 ●● means a moderate influence of the parameters on the a certain value of the particles;
 ● means a mild or no influence of the parameters on the a certain value of the particles.

Unlike particle size and rotational speed, the filling ratio and young's modulus only have an effect on some of the values. E.g., the normal contact force and normal overlap reacted very dramatically with the growth

of the filling ratio, but the particle's velocity didn't show an obvious change with a variation of the filling ratio. Since the magnitude of young's modulus represents the magnitude of stiffness, the normal/tangential contact forces and normal/tangential overlap are associated with stiffness and have a significant effect.

It is worth mentioning that a variation of all parameters (particle size, rotational speed, filling ratio, and young's modulus) has a greater effect on the S.S316L particles than on the γ -Al₂O₃ particles. This may be mainly related to the property of the particles themselves, as shown in Table 6.1.

6.2 Modeling of the adhesion between particles: simulation of the coating phenomenon

In the previous section on mixing, it was observed that when young's modulus is greater than $1.7 \cdot 10^8$ Pa and when the filling ratio is greater than 20%, there is no significant effect on the particle motion. Nevertheless, particle size and rotational speed are two important parameters.

In this section, guest particles have been taken into account to get a better understanding of dry particle coating. As it has been mentioned in Chapter 1, paragraph 1.7.1.3. JKR cohesion model allows us to represent the cohesive nature of fine and host materials. In this study, Hertz-Mindlin with JKR (Johnson-Kendall-Roberts) cohesion model (see Chapter 1, paragraph 1.7.1.3) has been applied to model the coating between fine and host particles.

6.2.1 Modeling parameters

In the simulation of dry particle coating, it is very impractical to use a large number of host particles and guest particles to complete the simulation because it will cost a massive amount of time. In DEM modeling, the calculation time is based on the smallest radius of the particle. In Chapter 5, paragraph 5.2 (see figure 5.4), we have investigated the effect of young's modulus and particle size on calculation time. It was found that both of them have a great influence on calculation time. In addition, according to equations 5.1 and 5.2, the number of particles and the modeling time also have a great influence on the calculation time. Figure 6.10 shows the number of particles versus calculation time. The calculation of the number of guest particles required to coat 1-7 host particles is based on equation 2.1 (see Chapter 2, paragraph 2.2.2.3) and equations 5.1 and 5.2 (see Chapter 5, paragraph 5.2).

As it can be seen on the graph, the radius of the host ($\gamma\text{-Al}_2\text{O}_3$) and the guest (TiO_2) are 0.5 mm and 0.02 mm, respectively. The guest particle of TiO_2 has the following properties: density $\rho = 3955 \text{ kg/m}^3$; $\nu = 0.28$; young's modulus $E = 1.50 \times 10^9 \text{ Pa}$ (the real young's modulus $E = 1.50 \times 10^{11} \text{ Pa}$ [386-391]); modeling time $t = 10 \text{ s}$. When the number of hosts ($\gamma\text{-Al}_2\text{O}_3$) is 1, coat one layer of one host ($\gamma\text{-Al}_2\text{O}_3$) requires 2704 of guest (TiO_2) particles, a modeling simulation of 10 s will take 124 h (more than 5 days). If the number of hosts is 5, coat one layer of 5 hosts ($\gamma\text{-Al}_2\text{O}_3$) needs 13520 of guest (TiO_2) particles and will cost 743 h (30 days). The results of this evaluation suggest that it is not realistic to use a large number of host particles to investigate dry coatings in the picomix. According to literature reports [222, 224, 225, 229], we found that only one or two host particles are generally used in a simulation to save simulation time during a study of coatings.

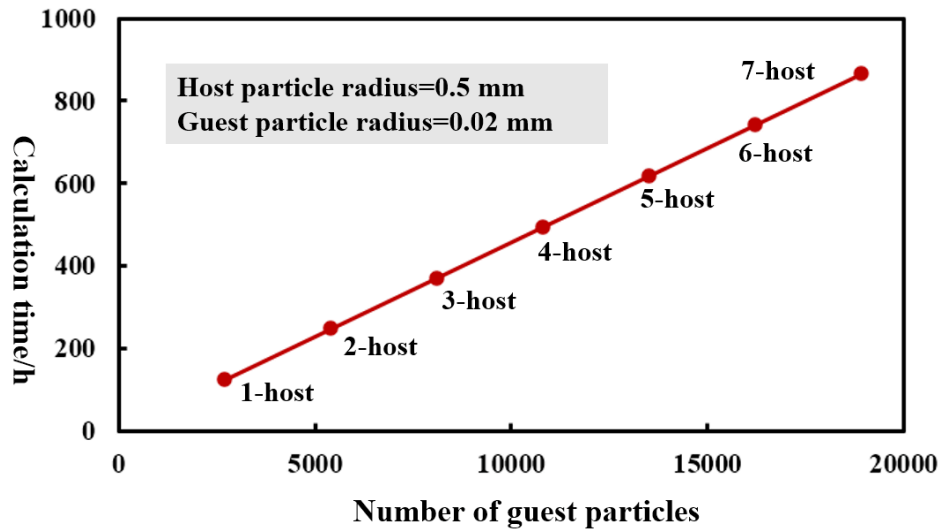


Fig.6.10 Calculation time with number of guest particles (Equations 5.1 and 5.2 were used to calculate the time step, solid density $\rho=3955 \text{ kg/m}^3$; $\nu=0.28$; young's modulus $E=1.50 \times 10^9 \text{ Pa}$; $\vartheta = 1.0 \mu\text{s}$; Rayleigh time step: 20%; modeling time $t = 10 \text{ s}$).

Therefore, in this study, only one host particle was used to study the coating process (see table 6.7), the calculation of the number of guest particles was calculated by equation 2.1 (see Chapter 2, paragraph 2.2.2.3). Because of the large amount of time required for simulation, only one type of coating behavior of the host particle ($\gamma\text{-Al}_2\text{O}_3$) and the guest particles (TiO_2) was studied. In the previous analytical study of nanoparticles, we found that among the three nanoparticles (SiO_2 , TiO_2 , and Zeolite), the TEM images (see Chapter 3, figure 3.3) of TiO_2 showed very clear particles. Thus, we assumed that its particle analysis had few agglomerated particles and provided a relatively accurate particle size. Therefore, TiO_2 was

Chapter 6: Simulation Results and Discussions

chosen as the guest particle to study in the coating modeling. As for the choice of host, compared to S.S316L, the young's modulus of γ -Al₂O₃ is smaller and less dense, which will save calculation time.

The size of the host and guest were scaled up in this simulation order to save on calculation time. Young's modulus of γ -Al₂O₃ from literature is 1.7×10^{10} Pa [357-359, 361], and young's modulus of TiO₂ reported in the literature is $1.19 - 2.82 \times 10^{11}$ Pa [386-391]. Before the official simulation started, we tried to launch a simulation of γ -Al₂O₃ and TiO₂ on coating and found that the number of coated guest particles (TiO₂) increases with modeling time. That is to say, a modeling time of 1 s to study the coating is not enough. In order to obtain good coating modeling, it is necessary to have a relatively long simulation time of more than 1 s.

Table 6.7 The parameters have been used to study dry particle coating.

Parameters	Properties of particles		Properties of Picomix (steel)
	γ -Al ₂ O ₃	TiO ₂	
Density (ρ , kg/m ³)	3528	3955	7990
Sphere diameter (D_m , mm)	1	0.1/0.04	
Number of particles	1	484/2704	
Poisson's ratio (ν)	0.25	0.28 [389, 390]	0.25
Shear Modulus (G , Pa)	6.80×10^7	5.859×10^7	7.60×10^{10}
Young's Modulus (E , Pa)	1.7×10^8	1.5×10^8	1.90×10^{11}
Coefficient of Restitution (e)	γ -Al ₂ O ₃ – γ -Al ₂ O ₃		0.7
	γ -Al ₂ O ₃ – wall		0.8
	γ -Al ₂ O ₃ – TiO ₂		0.6
	TiO ₂ – TiO ₂		0.8 [392]
	TiO ₂ – wall		0.8
Coefficient of Static friction (μ_s)	γ -Al ₂ O ₃ – γ -Al ₂ O ₃		0.1
	γ -Al ₂ O ₃ – wall		0.5
	γ -Al ₂ O ₃ – TiO ₂		0.1
	TiO ₂ – TiO ₂		0.3 [393]
	TiO ₂ – wall		0.3
Coefficient of Rolling friction (μ_r)	γ -Al ₂ O ₃ – γ -Al ₂ O ₃		0.01
	γ -Al ₂ O ₃ – wall		0.3
	γ -Al ₂ O ₃ – TiO ₂		0.01
	TiO ₂ – TiO ₂		0.03 [394, 395]
	TiO ₂ – wall		0.01
Rotation speed (Ω , rpm)			3500
Modeling time (t , s)			10
Surface energy (J/m ²)	γ -Al ₂ O ₃ – γ -Al ₂ O ₃ : 1.5 [396-398]; TiO ₂ – TiO ₂ : 0 and 0.9 [399, 400]		
Rayleigh time-step (ΔT , s)			40% ΔT

Table 6.7 summarizes the parameters that have been used in this study. As has been described in Chapter 1, paragraph 1.7.4.3, surface energy is one of the important parameters when the JKR cohesive modeling is carrying out as it determines the adhesion between the two phases. In this study, the choice of surface energy was taken from literature reports and can be seen in table 6.7.

6.2.2 Geometry of the used picomix

Putting a host particle and one coating layer of the guest particle in a 100 mL vessel for simulation will be a burden to the grid cell. The fewer particles per grid cell, the more efficient the simulator. We tried to put 10 γ -Al₂O₃ particles with a 2 mm diameter and 27040 TiO₂ particles with a 0.08 mm diameter for 1 layer coating, rotational speed was 3500 rpm, simulated 1 s, the surface energy of γ -Al₂O₃ – γ -Al₂O₃: 1.5 J/m² [396-398]; TiO₂ – TiO₂: 0.9 J/m² [399, 400], the interfacial energy between γ -Al₂O₃ and TiO₂ is 0.076 J/m² (calculated based on equation 1.38, see Chapter 1, paragraph 1.7.4.3), other parameters see table 6.7.

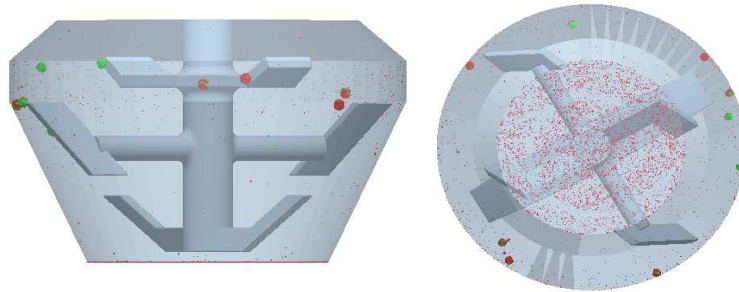


Fig.6.11 Snapshot of 10 host particles with a 2 mm diameter and 27040 guest particles with a 0.08 mm diameter under 3500 rpm rotational speed at 1 s, γ -Al₂O₃ – γ -Al₂O₃: 1.5 J/m²; TiO₂ – TiO₂: 0.9 J/m², the interfacial energy between γ -Al₂O₃ and TiO₂ is 0.076 J/m².

We found that it was difficult to capture the coating phenomenon clearly (see figure 6.11). Since the distance between the bottom of the vessel and the first paddle was too far, maybe the rotor could not contact with all the TiO₂ particles when it rotated. This results in many TiO₂ particles staying at the bottom of the picomix they cannot be in contact with the γ -Al₂O₃ particles, and therefore there was no good coating for this simulation. Or perhaps because the speed of agitation was too low, the small particles went to the bottom since they had too little energy to move to the top of the vessel.

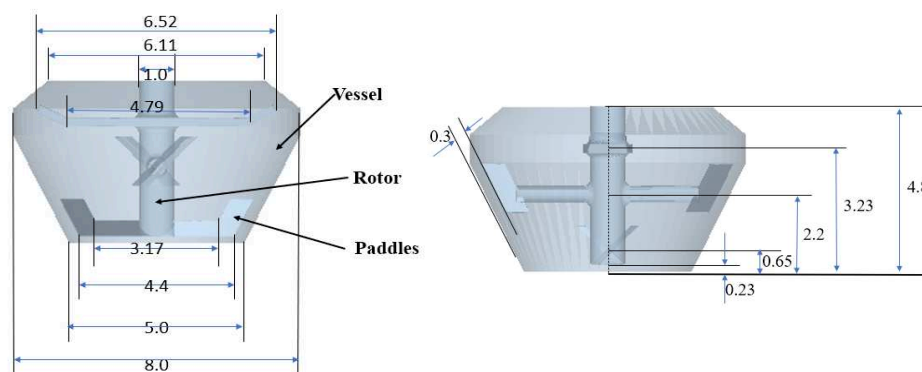


Fig. 6.12 Dimension of the reduced geometry of the original picomix with different views (The unit of the dimension is mm).

For these reasons, two approaches can be used to improve this phenomenon. One way is to increase the agitation speed/rotation speed; the other way is to reduce the size of the picomix.

In this study, the dimension of the vessel was reduced by 10 times from figure 5.5 (see Chapter 5, paragraph 5.3). The dimension of the reduced geometry of the original picomix is shown in Figure 6.12.

6.2.3 Analysis of the modeling by adhesion phenomenon between Al_2O_3 and TiO_2 particles

In this section, the particle motion of the host particle ($\gamma-Al_2O_3$) and guest particle (TiO_2) were simulated in the reduced picomix (10 mL) via the JKR cohesion model (see Chapter 1, paragraph 1.7.1.3). The size ratio of the host to guest is considered to be an important factor in the dry particle coating process. As described in Chapter 3, paragraph 3.5, the results of three nanoanalytical techniques were used in experimental studies and were named LD (laser diffraction/diffusion), TEM (transmission electronic microscope), and DLS (dynamic light scattering). Since LD gave the largest size among these three techniques because it always measures the agglomerates, TEM gave the smallest size. If we use the size of TiO_2^{TEM} , the size ratio of the host ($\gamma-Al_2O_3$) and guest particle (TiO_2^{TEM}) will be 2669 ($D_{mhost}/D_{mquest} = 2669$). This means that if the size of the host ($\gamma-Al_2O_3$) is 1 mm then the size of the guest (TiO_2^{TEM}) has to be 3.72×10^{-5} mm, coating a 1 mm host ($\gamma-Al_2O_3$) will require around 7.2×10^{10} guest of TiO_2^{TEM} particles, which is obviously unrealistic to use such a large number of particles for the simulation. Therefore, in this study, we respected the size ratio of the host particle ($\gamma-Al_2O_3$) and guest particle (TiO_2^{LD}) that is 25 ($D_{mhost}/D_{mquest} = 25$).

This section can be divided into three parts depending on the size of the particles.

1. The diameter of γ -Al₂O₃ was 2.5 mm (number of γ -Al₂O₃ is 1), the diameter of TiO₂ was set to 0.1 mm (requires 2704 TiO₂ for coating one γ -Al₂O₃, calculated by equation 2.2), that is $D_{mhost}/D_{mguest} = 25$.

2. The diameter of γ -Al₂O₃ was 1.0 mm (number of γ -Al₂O₃ is 1), the diameter of TiO₂ was 0.1 mm (requires 484 TiO₂ for coating one γ -Al₂O₃, calculated by equation 2.2), $D_{mhost}/D_{mguest} = 10$. (*the choice of this diameter will be detailed in paragraph 6.2.3.3)

3. The diameter of γ -Al₂O₃ was 1.0 mm (number of γ -Al₂O₃ is 1), the diameter of TiO₂ was 0.04 mm (requires 2704 TiO₂ for coating one γ -Al₂O₃, calculated by equation 2.2), that is $D_{mhost}/D_{mguest} = 25$.

6.2.3.1 Analysis of the modeling: Host particle: Al₂O₃-D_m-2.5 mm and guest particle: TiO₂-D_m-0.1 mm

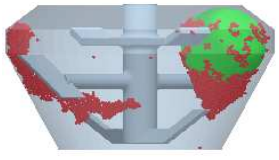
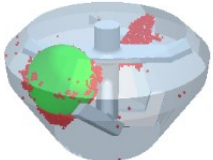
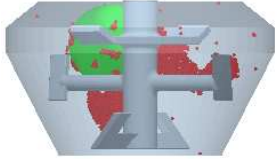
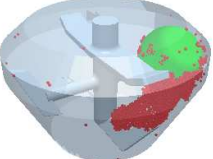
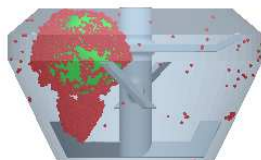
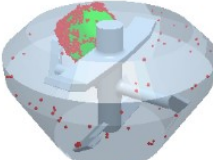
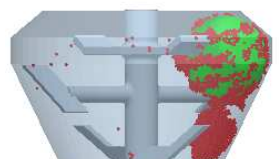
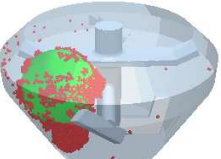
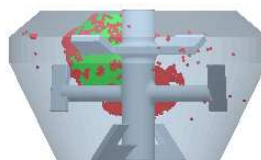
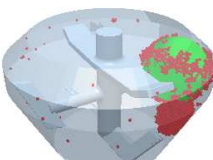
In this modeling, the ratio of host to guest particle was respected ($D_{mhost}/D_{mguest} = 25$). Considering the calculation time, the particle size of guest was assumed to be 0.1 mm and then the particle size of host to be 2.5 mm.

The picomix shown in figure 6.12 was used in this section study, the diameter of γ -Al₂O₃ was 2.5 mm (number of γ -Al₂O₃ was 1), the diameter of TiO₂ was set to 0.1 mm (number of TiO₂ was 2704). The rotational speed was 3500 rpm, the simulation time was 1 s, the surface energy of γ -Al₂O₃, TiO₂ respectively are 1.5 J/m² [396-398] and 0.9 J/m² [399, 400], the interfacial energy between γ -Al₂O₃ and TiO₂ is 0.076 J/m² (calculated based on equation 1.38, see Chapter 1, paragraph 1.7.4.3), other parameters can be found in table 6.7. The snapshot of in γ -Al₂O₃ and TiO₂ particles in the picomix under these conditions is shown in Figure 6.13.

It was found that as the modeling time went from 0.2 s to 1 s, more and more TiO₂ particles were coated onto the surface of the γ -Al₂O₃ particle. Meanwhile, a large number of TiO₂ particles stuck together and formed an agglomeration. Even TiO₂ particles coated on the surface of the γ -Al₂O₃ particle have a small agglomeration phenomenon. Because the interfacial force between the TiO₂ particles is greater than the gravity of the particles, it made the particles agglomerate together, that is, the surface energy between the TiO₂ particles is quite large.

Chapter 6: Simulation Results and Discussions

Fig. 6.13 Snapshot of γ -Al₂O₃ (2.5 mm in diameter, green in color) and TiO₂ (1.0 mm in diameter, red in color) particles in picomix during simulation time of 0.2-1.0 s.

Modeling time (s)	X-axis views	3D views
0.2		
0.4		
0.6		
0.8		
1.0		

In order to avoid the agglomeration of TiO₂ particles, we assumed that the surface energy of TiO₂ particles is 0 to see if all TiO₂ particles may be able to be coated on the surface of the γ -Al₂O₃ particle. The rotational speed was 3500 rpm, the simulation time was 2 s, the surface energy of the γ -Al₂O₃, TiO₂ respectively are 1.5 J/m² and 0 J/m², the interfacial energy between γ -Al₂O₃ and TiO₂ is 1.5 J/m² (calculated based on equation 1.38, see Chapter 1, paragraph 1.7.4.3), other parameters can be found in the table 6.7. The initial modeling time was set to 1 s, but it was found that not all TiO₂ particles were coated on the surface of the γ -Al₂O₃ particle, therefore, the modeling time was extended to 2 s to see if all TiO₂ particles have adhered

Chapter 6: Simulation Results and Discussions

on the surface of $\gamma\text{-Al}_2\text{O}_3$ particle. The snapshot of the $\gamma\text{-Al}_2\text{O}_3$ and TiO_2 particles in the picomix under these conditions is shown in figure 6.14.

Fig. 6.14 Snapshot of the $\gamma\text{-Al}_2\text{O}_3$ (2.5 mm in diameter, green in color) and TiO_2 (1.0 mm in diameter, red in color) particles in Picomix during simulation time of 0.2-2.0 s.

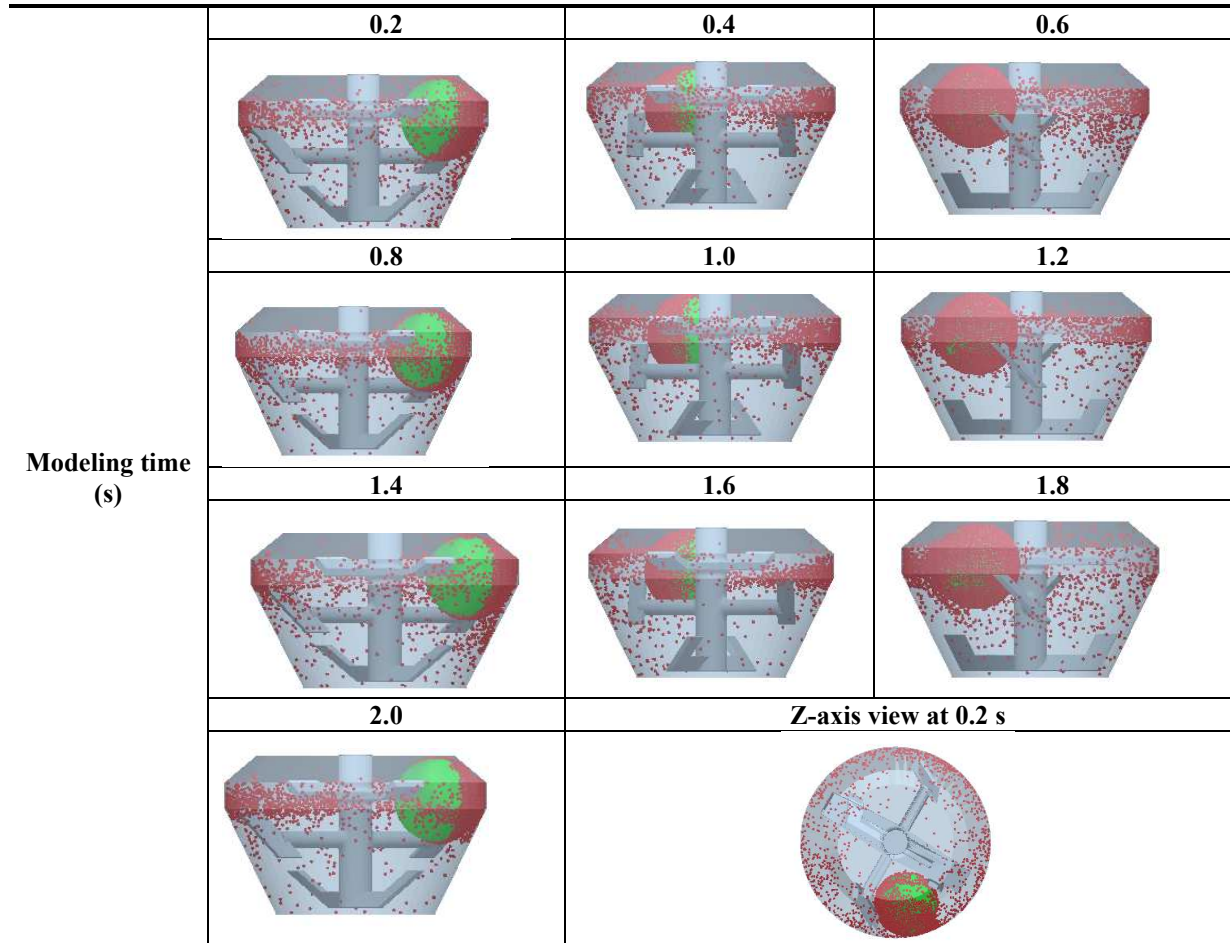
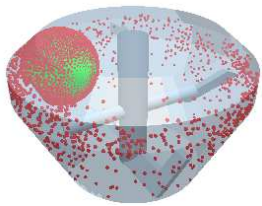
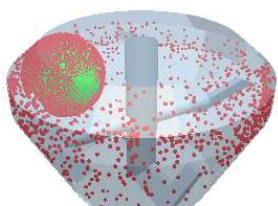
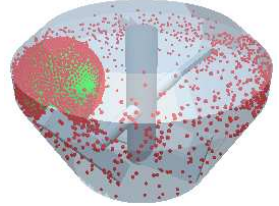


Figure 6.14 revealed the fact that TiO_2 particles of the coating do increase with time, but some of the TiO_2 particles were not fully coated on the surface of the $\gamma\text{-Al}_2\text{O}_3$ particle. It was observed that there are no TiO_2 particles stuck to the surface of the $\gamma\text{-Al}_2\text{O}_3$ particle near the rotor. On the last graph from a z – axis view at 0.2 s in Figure 6.14 we can see that the $\gamma\text{-Al}_2\text{O}_3$ particle was probably too large and it was stuck in the middle of the second and third of paddles and cannot move. Therefore, the $\gamma\text{-Al}_2\text{O}_3$ particle close to the rotor did not have the opportunity to meet with TiO_2 particles, resulting in no coating formation.

As claimed in Chapter 2, paragraph 2.2.2.2, the function of the third paddle (top paddle) of the rotor is to deagglomerate the agglomerated particles. The size of the third paddle (see figure 6.12) of the new reduced

picomix is 6.52 mm and the width of the picomix is 8 mm, thus, there is 0.71 mm left on both sides, a diameter of a particle of 2.5 mm will not move because of lack of space. Therefore, we decided to remove the third paddle to allow the particle to move. In order to explore whether the $\gamma\text{-Al}_2\text{O}_3$ particle was not fully coated because the $\gamma\text{-Al}_2\text{O}_3$ particle was stuck, the third paddle of the rotor was removed in the next study. Figure 6.15 presents a snapshot of the coating without the third paddle of the rotor, the rotation speed was 3500 rpm, the simulation time was 2 s, the surface energy of the $\gamma\text{-Al}_2\text{O}_3$, TiO_2 respectively were 1.5 J/m^2 and 0 J/m^2 , the interfacial energy between $\gamma\text{-Al}_2\text{O}_3$ and TiO_2 was 1.5 J/m^2 , other parameters can be found in the table 6.7.

Fig. 6.15 Snapshot of $\gamma\text{-Al}_2\text{O}_3$ (2.5 mm in diameter, green in color) and TiO_2 (1.0 mm in diameter, red in color) particles in picomix (without third paddle of the rotor) during modeling time of 0.4-2.0 s.

	0.4	1.0	2.0
Modeling time (s)			

It can be seen that without the third paddle of the rotor, there are 2104 out of 2704 TiO_2 particles coated on the surface of the $\gamma\text{-Al}_2\text{O}_3$ particle. But it is a little disappointing that the $\gamma\text{-Al}_2\text{O}_3$ particles near the rotor was not completely coated; maybe because of the lack of modeling time, or probably because the $\gamma\text{-Al}_2\text{O}_3$ particle was so close to the rotor that it did not have enough space to move. Therefore, in the next study, the diameter of the $\gamma\text{-Al}_2\text{O}_3$ particle was reduced to 1 mm and the modeling time was extended to 10 s.

6.2.3.2 Analysis of the modeling: Host particle: $\text{Al}_2\text{O}_3\text{-}D_m\text{-}1.0 \text{ mm}$ and guest particle: $\text{TiO}_2\text{-}D_m\text{-}0.1 \text{ mm}$

In the previous part of the simulation study, we knew that even if the third paddle of the picomix was removed, there were still no TiO_2 particles sticking to the $\gamma\text{-Al}_2\text{O}_3$ particle near the rotor part, and we consider that it may be because the diameter of the host particles is too large. Therefore, in this study, the diameter of the host was reduced to 1.0 mm.

The rotor without the third paddle of reduced picomix was used to study the dry particle coating with the diameter of $\gamma\text{-Al}_2\text{O}_3$ set to 1.0 mm (number of $\gamma\text{-Al}_2\text{O}_3$ was 1) and the diameter of TiO_2 set to 0.1 mm

(number of TiO₂ was 484). The rotational speed was 3500 rpm, the surface energy of γ -Al₂O₃, TiO₂ respectively was fixed at 1.5 J/m² and 0 J/m².

6.2.3.2.1 Effect of interfacial energy

Figure 6.15 presents a γ -Al₂O₃ particle that was not completely covered by TiO₂. One of the possible reasons for that was that there was not enough interfacial energy between γ -Al₂O₃ and TiO₂. However, no reports on the interfacial energy between γ -Al₂O₃ and TiO₂ have been found in the literature. In this study, the interfacial energy between γ -Al₂O₃ and TiO₂ was varied from 1.5 to 100 J/m² in order to investigate the effect of interfacial energy on the coating.

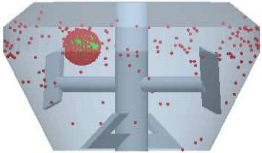
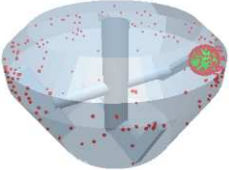
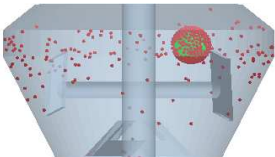
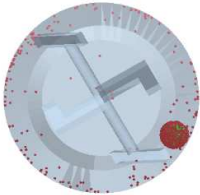
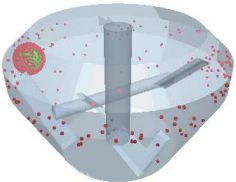
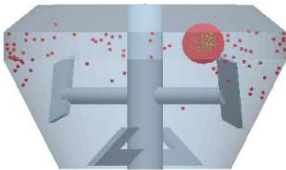
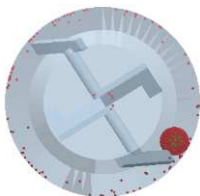
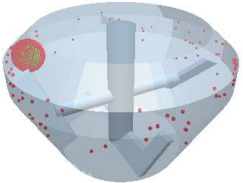
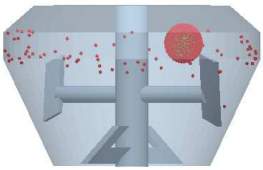
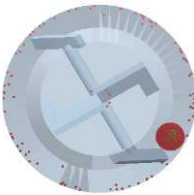
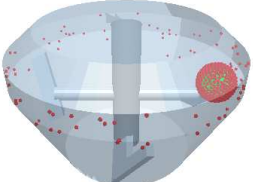
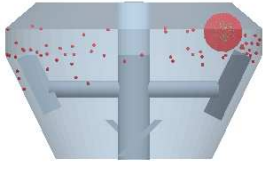
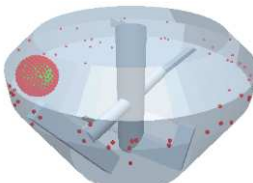
The rotor without the third paddle of the reduced picomix (see figure 6.12) was used to study the dry particle coating with the diameter of γ -Al₂O₃ set to 1.0 mm (number of γ -Al₂O₃ was 1), the diameter of TiO₂ set to 0.1 mm (number of TiO₂ was 484). The rotational speed was 3500 rpm, the modeling time was 10 s, the surface energy of the γ -Al₂O₃, TiO₂ respectively was fixed at 1.5 J/m² and 0 J/m², the interfacial energy between γ -Al₂O₃ and TiO₂ was varied from 1.5 to 100 J/m², other parameters can be found in table 6.7. The snapshot of in γ -Al₂O₃ and TiO₂ particles in Picomix under these conditions is shown in Figure 6.16.

It was shown in the X-axis views and Z-axis views of figure 6.16 that as the interfacial energy of γ -Al₂O₃-TiO₂ increases, more and more TiO₂ particles were coating onto the surface of the γ -Al₂O₃ particle. However, it can be seen that after the interfacial energy of γ -Al₂O₃-TiO₂ reached 20 J/m², the coating seems to reach a stable state, as the change in the number of TiO₂ particles coatings starts to become less pronounced. At the same time, some uncoated gaps of the γ -Al₂O₃ particle can be seen in the 3D views of figure 6.16.

TiO₂ particles were coated onto the surface of the γ -Al₂O₃ particle. As soon as a guest particle contacts a host particle, this guest particle would stick on the surface of the host particle because of its strong adhesion force (van der Waals' force). The number of TiO₂ particles coated onto the surface of the γ -Al₂O₃ particle and the fraction of coated number with the variation of interfacial energy of γ -Al₂O₃ and TiO₂ is shown in figure 6.17. The number of guest particles required to coat a host particle was calculated by equation 2.1 (see Chapter 2, paragraph 2.2.2.3), it shows that 484 TiO₂ particles are required to coat a γ -Al₂O₃ particle.

Chapter 6: Simulation Results and Discussions

Fig. 6.16 Snapshot of $\gamma\text{-Al}_2\text{O}_3$ (1.0 mm in diameter, green in color) and TiO_2 (0.1 mm in diameter, red in color) particles in the picomix under different interfacial energy of $\gamma\text{-Al}_2\text{O}_3$ and TiO_2 at 10 s of modeling time.

Interfacial energy of $\gamma\text{-Al}_2\text{O}_3\text{-TiO}_2$ (J/m^2)	X-axis views	Z-axis views	3D views
1.5			
2.0			
20			
50			
100			

In order to know compare with the theoretical calculated number of coatings, the fraction of coated number of (see equation 6.12) guest particles are proposed here. The coated number is the number of guests that adhere to the surface of the host particle in the modeling. The calculated number of guests is the number that has been used in the modeling. The results are presented in the figure 6.17.

$$\text{Fraction of coated number \%} = \frac{\text{coated number of guest particles}}{\text{the calculated number of guest particle}} \times 100\% \text{ (Eq.6.12)}$$

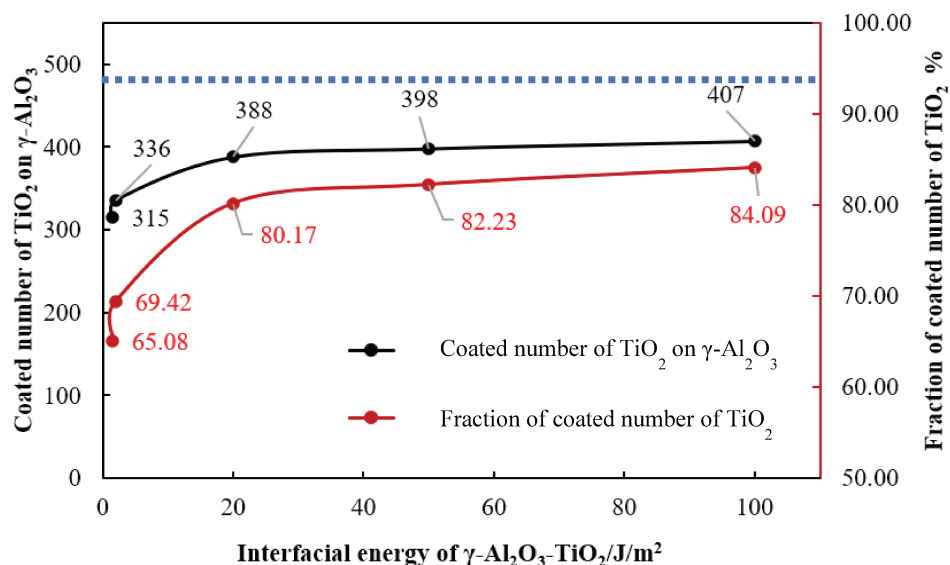


Fig.6.17 The relationship between the coated number of TiO₂ particles and the variation of interfacial energy of γ-Al₂O₃ and TiO₂ (the blue line is the baseline that represents 484 number of TiO₂ particles, 484 TiO₂ particles are required to coat a γ-Al₂O₃ particle in theoretical calculation (see Chapter 2, equation 2.2)).

Figure 6.17 illustrates the interfacial energy of γ-Al₂O₃-TiO₂ is 1.5 J/m² and 2 J/m², the coated number of TiO₂ particles are respectively, 315 and 336. This number represents only 65% and 69% of the total number of TiO₂ particles coated. As the energy increases, more and more TiO₂ particles stick to the surface of the γ-Al₂O₃ particle, this phenomenon can also be observed in the snapshot in figure 6.16. When the interfacial energy of γ-Al₂O₃-TiO₂ reaches 20 J/m², and the interfacial energy of γ-Al₂O₃-TiO₂ continues to increase to 50 J/m² or 100 J/m², the tendency of increasing TiO₂ particles sticking to the surface of the γ-Al₂O₃ particle is becoming lower.

To some extent, the fraction of the coated number exhibits that not all TiO₂ particles are adhered to the surface of the γ-Al₂O₃ (see figure 6.18a). But theoretically, all TiO₂ particles should stick to the surface of the γ-Al₂O₃ particle because the calculation was made according to one layer of guest particles to a host particle (see figure 6.18 of ideal coating). This may be because the coating is random and not every TiO₂ particle has the opportunity to coat on the surface of γ-Al₂O₃ because the gaps of γ-Al₂O₃ surface are not enough to accommodate a TiO₂ particle (see figure 6.18b).

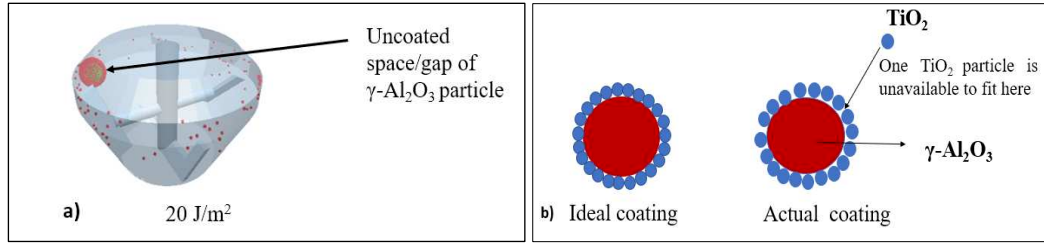


Fig.6.18 An explanation images of uncoated number of TiO_2 particles to $\gamma\text{-Al}_2\text{O}_3$ particle.

If this was the reason that not all TiO_2 particles stuck to the $\gamma\text{-Al}_2\text{O}_3$ surface, we hypothesized that when the interfacial energy of $\gamma\text{-Al}_2\text{O}_3\text{-TiO}_2$ is 20 J/m^2 , the rotational speed is 3500 rpm and the simulation time is 10 s (other parameters see table 6.7), only 388 TiO_2 particles are in fact needed to coat one $\gamma\text{-Al}_2\text{O}_3$ particle. To verify whether all 388 TiO_2 particles would stick to the $\gamma\text{-Al}_2\text{O}_3$ surface, a new simulation was launched, the results can be seen in figure 6.19.

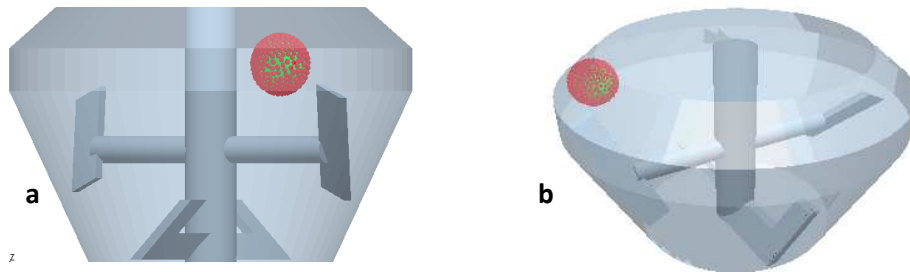


Fig.6.19 Snapshot of $\gamma\text{-Al}_2\text{O}_3$ (1.0 mm in diameter, green in color) and TiO_2 (0.1 mm in diameter, red in color) particles in the picomix when the interfacial energy of $\gamma\text{-Al}_2\text{O}_3\text{-TiO}_2$ is 20 J/m^2 at 10 s of modeling time.

In fact, when there were 388 TiO_2 particles, only 358 of them stuck to the $\gamma\text{-Al}_2\text{O}_3$ surface, which means that there were still 30 particles that did not participate in the coating, and these were found around the paddle near the bottom (see figure 6.19b).

Based on this, another simulation was done in which 358 TiO_2 particles were put with one $\gamma\text{-Al}_2\text{O}_3$ particle under the following conditions: interfacial energy of $\gamma\text{-Al}_2\text{O}_3\text{-TiO}_2$ is 20 J/m^2 , rotational speed 3500 rpm, and the modeling time 10 s (other parameters see table 6.7). We wanted to know if all 358 TiO_2 particles would adhere to $\gamma\text{-Al}_2\text{O}_3$ surface. The results of the simulation are shown in figure 6.20.



Fig.6.20 Snapshot of $\gamma\text{-Al}_2\text{O}_3$ (1.0 mm in diameter, green in color) and TiO_2 (0.1 mm in diameter, red in color) particles in picomix when the interfacial energy of $\gamma\text{-Al}_2\text{O}_3\text{-TiO}_2$ is 20 J/m^2 at 9.8-10 s of modeling time.

In this simulation where 358 TiO_2 particles were involved, only four (figure 6.20a, when the modeling time at 9.8 s) or five (figure 6.20a, when the modeling time at 10 s) of TiO_2 particles did not coat to the surface of the $\gamma\text{-Al}_2\text{O}_3$ particle. These four or five TiO_2 particles that did not stick to the surface of the $\gamma\text{-Al}_2\text{O}_3$ particle could be captured at the bottom of the rotor.

Two reasons were taken into account: firstly, these TiO_2 particles were stuck in the space between the first paddle of the rotor and the bottom of the vessel, making them unable to move to the upper part of the vessel to collide with $\gamma\text{-Al}_2\text{O}_3$ and form a coating; secondly, as previously considered and explained, there was not enough space on the surface of $\gamma\text{-Al}_2\text{O}_3$ to accommodate TiO_2 particles because their size was too large.

Therefore, in the next section study, the diameter of the TiO_2 particles was set to 0.04 mm. The choice of the diameter of TiO_2 particles also respected the same size ratio ($D_{mhost}/D_{mquest} = 25$) as the experiment.

6.2.3.3 Analysis of the modeling: Host particle: $\text{Al}_2\text{O}_3\text{-}D_m\text{-}1.0 \text{ mm}$ and guest particle: $\text{TiO}_2\text{-}D_m\text{-}0.04 \text{ mm}$

After the study in the previous two sections and the analysis of its results, a decision was made to use a reduced picomix (10 mL, see figure 6.12) without the third paddle to complete the simulation of the dry particle coating. The goal of this study is to see if all of the guest particles with a smaller size would stick to the host particles while maintaining the same size ratio ($D_{mhost}/D_{mquest} = 25$) as the experiment.

Simulation conditions precisely as follows: the diameter of $\gamma\text{-Al}_2\text{O}_3$ was 1.0 mm (number of $\gamma\text{-Al}_2\text{O}_3$ was 1), the diameter of TiO_2 was 0.04 mm (number of TiO_2 was 2704), the rotational speed was 3500 rpm, the modeling time was 10 s, the surface energy of $\gamma\text{-Al}_2\text{O}_3$ and TiO_2 respectively were fixed at 1.5 J/m^2 and 0 J/m^2 , the interfacial energy between $\gamma\text{-Al}_2\text{O}_3$ and TiO_2 was varied from 1.5 to 100 J/m^2 , other parameters

Chapter 6: Simulation Results and Discussions

can be found in table 6.7. The snapshot of the $\gamma\text{-Al}_2\text{O}_3$ and TiO_2 particles in the picomix under these conditions in different views is shown in Figure 6.21.

Fig.6.21 Snapshot of $\gamma\text{-Al}_2\text{O}_3$ (1.0 mm in diameter, green in color) and TiO_2 (0.04 mm in diameter, red in color) particles in picomix under different interfacial energy of $\gamma\text{-Al}_2\text{O}_3$ and TiO_2 at 10 s of modeling time.

Interfacial energy of $\gamma\text{-Al}_2\text{O}_3\text{-TiO}_2$ (J/m^2)	X-axis view	Z-axis view	3D view
1.5			
2.0			
20			
50			
100			

From the X-axis view (see figure 6.21), it can be seen that the surface coverage of the γ -Al₂O₃ particle increased as the interfacial energy of γ -Al₂O₃-TiO₂ rose from 1.5 to 20 J/m², which indicates that more TiO₂ particles were bonded to the surface of the γ -Al₂O₃ particle as the interfacial energy of γ -Al₂O₃-TiO₂ rose. But it can be clearly seen that a part the γ -Al₂O₃ particle was uncovered when the interfacial energy of γ -Al₂O₃-TiO₂ was raised from 20 to 100 J/m². Meanwhile, it's become apparent that there were some TiO₂ particles staying at the bottom of the vessel or next to the bottom of the rotor and moving at a very slow speed.

From the Z-axis (see figure 6.21), it was obtained that the movement of the TiO₂ particles was around the center of the rotor, but mainly near the edge of the vessel. The 3D view (see figure 6.21) revealed the fact that the γ -Al₂O₃ particle near the rotor part did not have TiO₂ particles attached to it. This could be explained by the fact that because some TiO₂ particles moved at a low speed at the bottom, but the γ -Al₂O₃ particle has been moving around the edge of the vessel at the top. This will result in no possibility of collision between these TiO₂ particles moving at low speed at the bottom and the γ -Al₂O₃ particle, thus, γ -Al₂O₃ particle cannot be completely covered.

Why is the γ -Al₂O₃ particle near the rotor showing no coverage? It may be because the γ -Al₂O₃ particle is in a steady state doing the rotational movement, and in the part near the rotor, TiO₂ particles are few. This would lead to reasoning that the γ -Al₂O₃ particle near the rotor does not have more opportunities to contact with TiO₂ particles.

The number of TiO₂ particles coated onto the surface of the γ -Al₂O₃ particle and the fraction of coated number with the variation of interfacial energy of γ -Al₂O₃ and TiO₂ is shown in figure 6.22.

Figure 6.22 indicates that at interfacial energy of γ -Al₂O₃ -TiO₂ 1.5 J/m², with a total number of TiO₂ particles of 2704, the number of TiO₂ particles adhered to γ -Al₂O₃ was only 1859, which means that only 69% of all TiO₂ particles achieved coating. However, the number of TiO₂ particles coated on the γ -Al₂O₃ particle increased with the rise of the interfacial energy of γ -Al₂O₃ -TiO₂ and reached a maximum at interfacial energy of γ -Al₂O₃ -TiO₂ 20 J/m². The number of TiO₂ particles adhering to the γ -Al₂O₃ particle is 2442 at interfacial energy of γ -Al₂O₃ -TiO₂ 20 J/m², and this coating accounted for 90% of the total number of TiO₂ particles. Subsequently, the number of TiO₂ particles adhering to the γ -Al₂O₃ particle did not rise with the increasing interfacial energy of γ -Al₂O₃ -TiO₂. The trend of the value of coated TiO₂ particles was consistent with the results presented in figure 6.21.

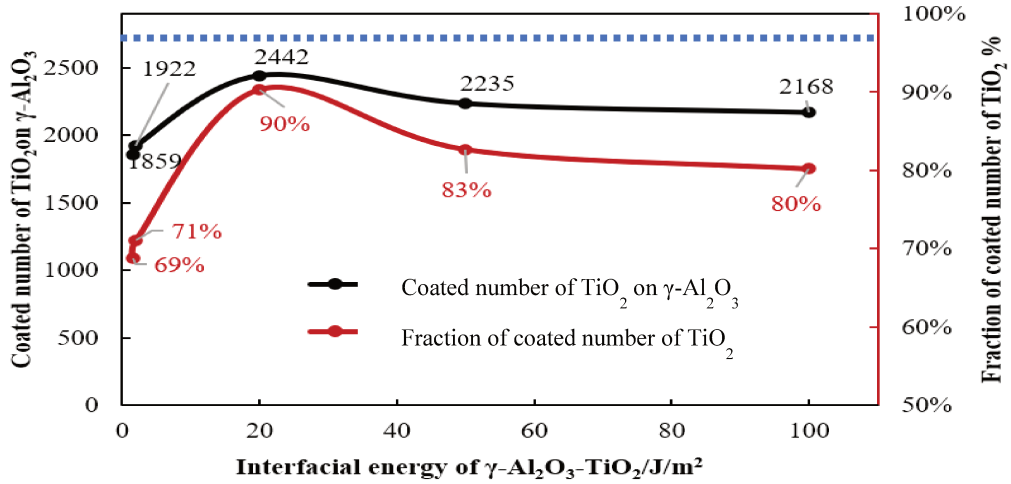


Fig.6.22 The relationship between the coated number of TiO₂ particles on the surface of the γ-Al₂O₃ particle and the fraction of coated number of TiO₂ particles with the variation of interfacial energy of γ-Al₂O₃-TiO₂ (the blue line is the baseline that represents 2704 number of TiO₂ particles, 2704 of TiO₂ particles are needed to coat one γ-Al₂O₃ particle by theoretical calculation)

In the JKR contact model, the adhesion force is calculated as the following equation dictates ^[251]:

$$F_{adhesion} = \frac{3}{2}\pi\gamma R^* \quad (Eq. 6.13)$$

γ is the surface energy between two particles, in this study, it refers to interfacial energy of γ-Al₂O₃-TiO₂. Figure 6.23 presents the adhesion force between different size ratios with different interfacial energy of γ-Al₂O₃-TiO₂.

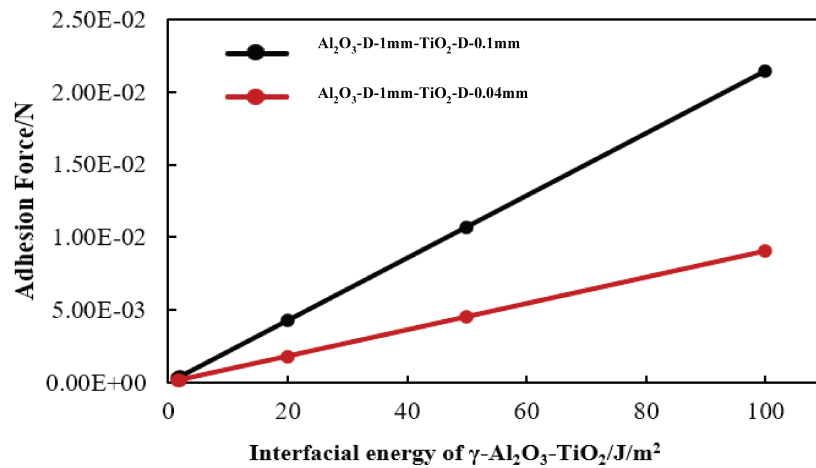


Fig.6.23 Effect of the interfacial energy of γ-Al₂O₃-TiO₂ on adhesion force at different size ratios.

As it can be seen (see equation 6.13), the magnitude of adhesion force depends on the surface energy and the equivalent radius. Therefore, at the same interfacial energy of $\gamma\text{-Al}_2\text{O}_3\text{-TiO}_2$, the adhesion force between a diameter of 1.0 mm for the $\gamma\text{-Al}_2\text{O}_3$ particle and a diameter of 0.1 mm for the TiO_2 is higher than the adhesion force when the diameter of $\gamma\text{-Al}_2\text{O}_3$ is 1.0 mm and the diameter of TiO_2 is 0.04 mm (see figure 6.23).

The following values were applied for the simulation conditions: rotational speed 3500, simulation time 10 s, other parameters can be seen in table 6.7, the trends of particle velocity, potential energy, overlap, contact force, and kinetic energy with the interfacial energy of $\gamma\text{-Al}_2\text{O}_3\text{-TiO}_2$ and size ratio variations are presented in figure 6.24.

As mentioned in Chapter 1, paragraph 1.7.1.3. The normal overlap between two particles can be calculated by Eq.1.14 ($\delta_n = \frac{a^2}{R^*} - \left(\frac{4\pi\gamma a}{E^*}\right)^{1/2}$). For the normal overlap of TiO_2 particles (figure 6.24a), at the same diameter as the $\gamma\text{-Al}_2\text{O}_3$ particle, when the size ratio $D_{host}/D_{guest} = 25$ (the diameter of $\gamma\text{-Al}_2\text{O}_3$ was 1.0 mm, the diameter of TiO_2 was 0.04 mm), the average normal overlap started to increase with a rise of the interfacial energy of $\gamma\text{-Al}_2\text{O}_3\text{-TiO}_2$, and the average normal overlap reached a maximum when the interfacial energy of $\gamma\text{-Al}_2\text{O}_3\text{-TiO}_2$ reached 20 J/m^2 . After this, it started to decrease as the interfacial energy of $\gamma\text{-Al}_2\text{O}_3\text{-TiO}_2$ rose, which indicated that the interfacial energy of $\gamma\text{-Al}_2\text{O}_3\text{-TiO}_2$ 20 J/m^2 is the maximum interfacial energy required for the coating of $\gamma\text{-Al}_2\text{O}_3$ and TiO_2 when the diameter of $\gamma\text{-Al}_2\text{O}_3$ was 1.0 mm, the diameter of TiO_2 was 0.04 mm. Figure 6.22 has already proved this indication. When the size ratio $D_{host}/D_{guest} = 25$, the normal overlap kept increasing as the interfacial energy of $\gamma\text{-Al}_2\text{O}_3\text{-TiO}_2$ increased, but the tendency to rise became less apparent, this phenomenon matched perfectly with the results shown in Figure 6.17.

In the JKR model, the calculation of the tangential overlap still uses the same as the Hertz-Mindlin model. It relates to the diameter of the particles; large diameter particles provide a large tangential overlap (figure 6.24b). The trend of the tangential overlap determines the magnitude of the tangential contact force and its trend so that the tangential force increases with a rise of the interfacial energy of $\gamma\text{-Al}_2\text{O}_3\text{-TiO}_2$ (figure 6.24d).

The normal contact force is related to the interfacial energy between two particles and is given as equation 1.15 ($F_{n,ij} = -4\sqrt{\pi\gamma E^*} a^{\frac{3}{2}} + \frac{4E^*}{3R^*} a^3$). As it can be seen the normal contact force (figure 6.24c) showed an increasing trend with the increase of the interfacial energy of $\gamma\text{-Al}_2\text{O}_3\text{-TiO}_2$. The effect of increasing

interfacial energy of γ -Al₂O₃-TiO₂ on the velocity, potential energy, and translational kinetic energy was not very obvious.

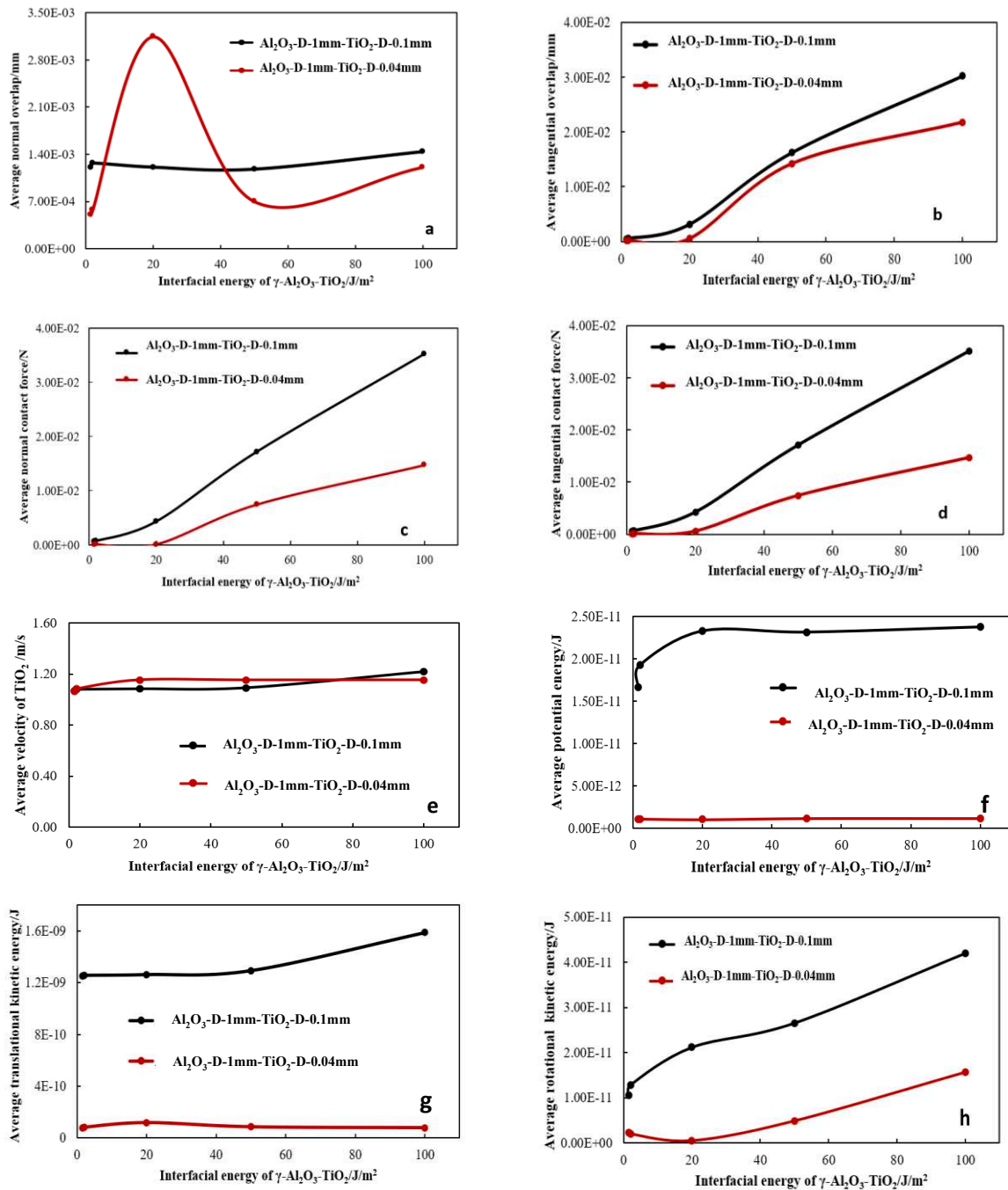


Fig.6.24 Average overlap (a-normal, b-tangential), the average velocity of TiO₂ (e), average potential energy (f), average contact force (c-normal, d-tangential), kinetic energy (g-translational, h-rotational) as a function of the interfacial energy of γ -Al₂O₃-TiO₂ at different size ratios of γ -Al₂O₃/TiO₂ with 3500 rpm, 10 s.

6.3 Conclusion

In this chapter, firstly, the effect of the particle size (the diameter 0.6 -1 mm), the rotation speeds (1500 - 5000 rpm), the filling ratio (10 - 40%), and the young's modulus (2.0×10^7 - 2.0×10^{11} Pa) on particles' motions of two host particle γ -Al₂O₃ and S.S316L were simulated via Hertz-Mindlin (no-slip) contact model by a commercial software EDEM. Secondly, the JKR cohesion model was applied to model the dry particle coating of host particles (γ -Al₂O₃ particles) with different sizes (1.0 and 2.5 mm) and guest particles (TiO₂ particles) with different sizes (0.04 and 0.1mm). The influence of interfacial energy of host/guest particles on particle interaction was also investigated.

The conclusions obtained from the above study were summarized as follows:

1. It was found that in the initial state, that is 0-0.25 s of modeling time, the particles were lifted up from the bottom to the roof of the picomix, this process ran along the wall of the vessel. As the simulation time increases from 0.25 s to 1 s, the particles reached the top and became steady and began moving on the top part of the picomix.
2. The simulation data showed that the contact force, the kinetic energy, the potential energy, and the velocity of γ -Al₂O₃ and S.S316L increased with an increase in the particle size. Under the same simulated conditions, S.S316L always presents a higher value than γ -Al₂O₃, this has to do with the property of the material itself, since the density of S.S316L and the hardness of S.S316L are higher than that of γ -Al₂O₃. The rotation speed also showed a very significant impact on particle motion.
3. Numerous simulation data demonstrated that the filling ratio and young's modulus only have an effect on some of the values. E.g., the normal contact force and normal overlap reacted very dramatically with a growth of the filling ratio, but particle velocity didn't show an obvious change in the filling ratio. Since the magnitude of young's modulus represents the magnitude of stiffness, the normal/tangential contact forces and normal/tangential overlap are associated with stiffness and have a significant effect.
4. When using the JKR model for simulation to investigate the coating process, the choice of surface energy and the number of particles is very important. The simulation of the γ -Al₂O₃ particle with a diameter of 2.5 mm and a surface energy of 1.5 J/m² and TiO₂ particles with the diameter of 1 mm and the surface energy 0.9 J/m² indicated that a large number of TiO₂ particles stuck together and formed an agglomeration. Even TiO₂ particles coated on the surface of the γ -Al₂O₃ particle have a small agglomeration phenomenon.

5. Without having considered the surface energy of TiO₂ particles (was set as 0), there was a part of the surface of γ -Al₂O₃ (the part near to the center of the rotor) that was not covered by TiO₂ particles. This could be caused by two reasons: 1, the interfacial energy of γ -Al₂O₃-TiO₂ was not enough; 2, the γ -Al₂O₃ particle was stuck in the middle of the second paddle and the third paddle of the rotor.

6. Unlike mixing, a simulation time of 1 s for the coating process was not sufficient because the particles coated to the surface of γ -Al₂O₃ increase as time increases. For example, in the beginning, the surface of γ -Al₂O₃ started to get covered by TiO₂ within 1-5 s, but as time was extended, only a few particles may have stuck to the surface of γ -Al₂O₃.

7. When the size ratio $D_{mhost}/D_{mquest} = 10$ (the diameter of γ -Al₂O₃ was 1.0 mm, the diameter of TiO₂ was 0.1 mm), the contact force, overlap, kinetic energy, potential energy, and velocity all increased to different degrees matching with the increase of the interfacial energy of γ -Al₂O₃-TiO₂. When the size ratio $D_{mhost}/D_{mquest} = 25$ (the diameter of γ -Al₂O₃ was 1.0 mm, the diameter of TiO₂ was 0.04 mm), the average normal overlap started to increase with a rise of the interfacial energy of γ -Al₂O₃-TiO₂, and the overlap reached a maximum when the interfacial energy of γ -Al₂O₃-TiO₂ reached 20 J/m². After that it started to decrease as the interfacial energy of γ -Al₂O₃-TiO₂ rose, which indicated that the interfacial energy of γ -Al₂O₃-TiO₂ 20 J/m² is the maximum interfacial energy required for the coating between γ -Al₂O₃ and TiO₂ when the diameter of γ -Al₂O₃ was 1.0 mm, the diameter of TiO₂ was 0.04 mm. The number of coated TiO₂ particles on the γ -Al₂O₃ particle also proved that when the interfacial energy of γ -Al₂O₃-TiO₂ is at 20 J/m², then 90% of TiO₂ particles adhere to the γ -Al₂O₃ particle (2442 TiO₂ particles adhered onto the γ -Al₂O₃ particle out of 2704).

8. The effect of increasing interfacial energy of γ -Al₂O₃-TiO₂ on the velocity, potential energy, and translational kinetic energy were not very obvious.

In summary, the use of two DEM modeling techniques (Hertz-Mindlin no-slip model and JKR model) gave us very valuable information to better understand dry coating. The results of the modelization demonstrated that it isn't the highest level of the interfacial energy of γ -Al₂O₃-TiO₂ that gives the best coating of γ -Al₂O₃ and TiO₂. The optimal value was found when the diameter of γ -Al₂O₃ was 1.0 mm, the diameter of TiO₂ was 0.04 mm, the interfacial energy of γ -Al₂O₃-TiO₂ of 20 J/m². However, even though the interfacial energy of γ -Al₂O₃-TiO₂ was at the optimum value of 20 J/m², it is a bit unfortunate that we did not get a completely coated γ -Al₂O₃ particle. Therefore, there is still room for more exploration and improvement, and it's possible to discover more details in future dry coating simulations.

Conclusions

In this work, both experimental and modelization work has been done to investigate dry particle coating and the interactions between particles during the coating process. The objective of the experimental part was to prepare new supports of catalysts for a methanation reaction via a high shear mixer called “Picomix”. As a result of this experimental work on dry coating and the preparation of supports and catalysts, many questions have arisen about the phenomena of collision and the adhesion of the particles in the picomix, as well as the variation of the different forces applied to the particle surfaces and the particle velocities. Therefore, the modelization work aimed to reveal particle movement and help us to get a better understanding of dry coating process.

In the experimental part, new supports $\text{TiO}_2/\gamma\text{-Al}_2\text{O}_3$, $\text{SiO}_2/\gamma\text{-Al}_2\text{O}_3$, Zeolite/ $\gamma\text{-Al}_2\text{O}_3$, $\text{TiO}_2/\text{S.S316L}$, $\text{SiO}_2/\text{S.S316L}$, and Zeolite/ S.S316L were prepared via mechanical force (impacting/compression/shearing force) in the picomix (Hosokawa Micro B.V) under the following conditions: 3500 rpm, 5 mins, filling ratio 40% (40 mL out of 100 mL). However, these powders (Zeolite, SiO_2 , TiO_2) were very cohesive and formed agglomerates with uncontrollable sizes. The coating process requires the size of the primary particles and not of the agglomerated particle size. Therefore, 5 techniques were included: LD (laser diffraction), TEM (transmission electron microscope), DLS (dynamic light scattering), SAXS (small-angle X-ray scattering), BET (specific surface area) to measure the nanosize. The other three (LD, TEM, DLS) provided results which were used to accomplish the preparation of new supports. Since BET is only valid for spherical, non-porous, monodisperse powders with a smooth surface. This is not the case for our three powders TiO_2 , SiO_2 , and Zeolite. Thus, BET size was not applied in the experimental study. SAXS theoretically gives very accurate measurements of nanopowder, since we do not have this instrument in our group, the results got from other analyzing place were late and additional software was needed to analyze the results of size distribution, it was not used to prepare new supports as well.

The new prepared supports were characterized by various methods to indicate the performance of the dry coating.

In the numerical part, DEM modeling was used to explore particle interaction in the high shear mixer “Picomix”. The numerical modeling of dry particle coating in the picomix was performed using one commercial DEM simulation software EDEM 2018.3.0 and EDEM 2020.3.1 (Academic license with 8 CPU, DEM solutions Ltd., Edinburgh, UK) with the Hertz-Mindlin (no-slip) contact model and the Hertz

Mindlin + JKR cohesive model. Three computers were used in this study, two of which are equipped with a Intel(R) Core(TM) i7-4790 [CPU@3.60Hz processor](#), and 8.0Go RAM; one is equipped with a Intel(R) Xeon(R) CPU E5-1650 v2 @3.5GHz processor, and 32.0Go RAM. The Hertz-Mindlin (no-slip) contact model was used to study the mixing of the two host particles (γ -Al₂O₃ and S.S316L) respectively. The Hertz-Mindlin with JKR cohesion model was used to model the cohesion between guest (TiO₂ particles) and host particles (γ -Al₂O₃ particles).

Firstly, the effects of particle size, filling ratio, rotational speed, young's modulus were simulated on two host particles γ -Al₂O₃ and S.S316L, with the help of the Hertz-Mindlin (no-slip) contact model.

Secondly, the modeling of host particles (γ -Al₂O₃ particles) and guest particles (TiO₂ particles) was conducted, and the influence of surface energy of host/guest particles was investigated by the Hertz-Mindlin with JKR cohesion model.

The results of the experimental study

1) It was found that among the five techniques for nanopowder analysis, the LD technique provided the largest particle size for the same amount of nanopowder, because it measured the agglomerates. The DLS gave a smaller size but the particles still form agglomerates. The TEM indicated the smallest diameter because the technique allows us to see the particles and measure them by image processing. It was worth noting that differences in the size of nanoparticles were determined by the use of different techniques. This is not caused by measurement errors, but in fact by the specificity of each technique. TEM measures the geometric size of the nanoparticles deposited on the surface; therefore, the advantage of TEM is that it can directly observe the morphology and determine the size of the particle, which offers certain intuitiveness and credibility. However, this method is the result of observation of local areas, so it has certain contingency and statistical errors. The average size of nanoparticles can be obtained by measuring and statistical analysis of particle size with a certain number of photos. Consequently, the difference between nanoparticle sizes for the same particle due to the agglomerates was discussed earlier. Moreover, it is important to be aware that each particle size characterization technique will measure a different property of a particle and therefore will give a different value from another technique that measures an alternative dimension. This leads to many approaches to data analysis which can affect the information obtained regarding particle size. As a result, each technique is not wrong, they are all correct; it is simply that a different property of nanoparticles is being measured.

2) Particle size distribution indicated that the guest particles were attached to the host particles, because the newly prepared supports provided almost the same peak as the host particles. No small peak was found because the prepared particles were sieved before analyzing the size. The particle size of the new supports seems to follow the order of Zeolite^{LD}/S.S316L > Zeolite^{DLS}/S.S316L > Zeolite^{TEM}/S.S316L, which was a very good result, as it corresponds with the original size of the guest particles Zeolite^{LD} > Zeolite^{DLS} > Zeolite^{TEM}.

3) The surface morphologies of SEM images demonstrated that for TiO₂^{LD}, SiO₂^{LD}, and Zeolite^{LD} particles, whether the coating was with S.S316L or γ -Al₂O₃, each host particle was covered by guest particles and formed a thick coating layer. Many agglomerated guest particles (because of strong interparticle force) can be directly observed on the surface of the host particles. When TiO₂^{DLS}, SiO₂^{DLS}, and Zeolite^{DLS}, coated with S.S316L or γ -Al₂O₃, a smooth surface was found but a small number of debris (agglomerated guest particles) can also be observed. As far as the images obtained by SEM are concerned, TEM size provided the best coating because a smooth surface without any chips can be obtained. That is to say, TiO₂^{TEM}/S.S316L, SiO₂^{TEM}/S.S316L, Zeolite^{TEM}/S.S316L, TiO₂^{TEM}/ γ -Al₂O₃, SiO₂^{TEM}/ γ -Al₂O₃, and Zeolite^{TEM}/ γ -Al₂O₃ presented the best coating.

4) The calculation of coating thickness again directly validated the results of SEM images and the analysis of particle size distribution that TiO₂^{TEM}/S.S316L, SiO₂^{TEM}/S.S316L, Zeolite^{TEM}/S.S316L, TiO₂^{TEM}/ γ -Al₂O₃, SiO₂^{TEM}/ γ -Al₂O₃, and Zeolite^{TEM}/ γ -Al₂O₃ presented the best coating. Nonetheless, one or two particles were taken into account in the evaluation of the coating thickness. These values lacked a certain degree of reliability, and perhaps there was some error between them and the real coating thickness.

5) In the calculation of uncoated guest particles, it was found that not all guest particles adhered onto the host particles, but the assessment of uncoated guest particles showed that there were much fewer little uncoated guest particles for S.S316L (maximum mass fraction for an uncoated particle is Zeolite^{LD}/S.S316L 1.62%). However, in the coating with γ -Al₂O₃, the mass fraction of uncoated particles was relatively high regardless of the type of particles with which they were coated, with the mass fraction of uncoated zeolite being as high as 11.48% (Zeolite^{LD}/ γ -Al₂O₃). This phenomenon can be explained by the behavior of materials and their structure, it would be interesting to develop and analyze this part in the work of the next PhD.

The results of the modeling study

In the investigation of modelization, the value of particle density was measured using a Helium pycnometer (AccuPyc1330, micromeritics Instrument Corp). Except for this parameter, all other parameters were taken from the literature.

1) Snapshot of mixing host particles modeling revealed that at the beginning of the mixing process, the particles rose from the bottom to the roof of the picomix, this process ran along the wall of the vessel. With time, the particles reached the top and became steady and moved to the top of picomix. For the same material used, under the same simulation conditions, particles with a small size still have some particles moving at the bottom of the vessel even at a high rotation speed of 3500 rpm. Such as, the motion of S.S316L particles in the picomix at 3500 rpm, 1 s with different particle sizes at a fixed filling ratio of 20%, the snapshot of the X views showed that at 0.5 s simulation time, there were no 2 mm S.S316L particles observed on the bottom of the vessel, but there were several 0.6 mm S.S316L particles that can be seen on the bottom of the vessel. For the different materials with the same simulation conditions, the snapshot showed that S.S316L always moves at relatively higher position at the same time frame of simulation time. Such as, when the rotational speed was fixed at 3500 rpm, the filling ratio was fixed at 20%, the diameter of the particles was set at 2 mm, the snapshot of the X views of S.S316L particles and the γ -Al₂O₃ particles showed that at 0.5 s of simulation time, no S.S316L particles were observed on the bottom of the vessel, but there were several γ -Al₂O₃ particles found on the bottom of the vessel.

2) Modeling data has demonstrated that particle size and rotational speed have a significant effect on both the velocity, the contact forces (normal/tangential contact force), the overlap (normal/tangential overlap), and the energy (potential, translational/rotational kinetic energy). The effect of the filling ratio and young's modulus on particle behavior seemed to be partial. E.g., the normal contact force and normal overlap reacted very dramatically to the growth of the filling ratio, but the particle velocity didn't show an obvious change with the variation of the filling ratio. Since the magnitude of young's modulus represents the magnitude of stiffness, the normal/tangential contact forces and normal/tangential overlap associated with stiffness and have a significant effect. It is worth mentioning that the variation of all parameters (particle size, rotational speed, filling ratio, and young's modulus) has a greater effect on the S.S316L particles than on the γ -Al₂O₃ particles. This could be caused by the property of the material itself, such as the density of S.S316L and the hardness of S.S316L, which are higher than that of γ -Al₂O₃.

- 3) The surface energy of the particle is a key parameter to estimate and above all it has a great impact on the Hertz-Mindlin JKR cohesive model to investigate the coating process. The value of the surface energy in this study was chosen from the literature. The goal was to speed up the calculation time and simulate more parameters. There were two measures that were taken to actualize: firstly, the diameter of the host particle $\gamma\text{-Al}_2\text{O}_3$ and the guest particle TiO_2 were scaled up; secondly, a picomix that has been reduced in dimension by ten times was used (original picomix: 100 mL in volume, reduced picomix: 10 mL in volume).
- 4) The simulation of the $\gamma\text{-Al}_2\text{O}_3$ particle with a diameter of 2.5 mm and a surface energy 1.5 J/m^2 and TiO_2 particles with a diameter of 1 mm and a surface energy 0.9 J/m^2 presented a coating whose surface was not completely covered with $\gamma\text{-Al}_2\text{O}_3$ particle. Meanwhile, a large number of TiO_2 particles bonded together and formed numerous agglomerations. Even TiO_2 particles coated on the surface of the $\gamma\text{-Al}_2\text{O}_3$ particle had a small agglomeration phenomenon. When the surface energy of TiO_2 particles was set as 0, no agglomeration was observed anymore, but a part of the surface of $\gamma\text{-Al}_2\text{O}_3$ (the part near to the center of the rotor) was not covered by TiO_2 particles.
- 5) Unlike mixing, the simulation time of 1 s for the coating process was not sufficient, because the particles coated onto the surface of the $\gamma\text{-Al}_2\text{O}_3$ particle increase as the time increases. For example, in the beginning, the surface of $\gamma\text{-Al}_2\text{O}_3$ quickly started to become covered with TiO_2 within 1 – 5 s, but as the time was extended, only a few particles could stick to the surface of $\gamma\text{-Al}_2\text{O}_3$.
- 6) When the size ratio $D_{host}/D_{guest} = 10$ (the diameter of $\gamma\text{-Al}_2\text{O}_3$ was 1.0 mm, the diameter of TiO_2 was 0.1 mm), the average normal/tangential contact force, the average normal/tangential overlap, the average translational/rotational kinetic energy, the average potential energy, and the average velocity all increased with the rise of the interfacial energy of $\gamma\text{-Al}_2\text{O}_3\text{-TiO}_2$. When the size ratio $D_{host}/D_{guest} = 25$ (the diameter of $\gamma\text{-Al}_2\text{O}_3$ was 1.0 mm, the diameter of TiO_2 was 0.04 mm), the average normal overlap started to increase with the rise of the interfacial energy of $\gamma\text{-Al}_2\text{O}_3\text{-TiO}_2$, and the average normal overlap reached a maximum when the interfacial energy of $\gamma\text{-Al}_2\text{O}_3\text{-TiO}_2$ reached 20 J/m^2 . After that it started to decrease as the interfacial energy of $\text{TiO}_2\text{-}\gamma\text{-Al}_2\text{O}_3$ rose, which indicated that the interfacial energy of $\gamma\text{-Al}_2\text{O}_3\text{-TiO}_2$ 20 J/m^2 is the maximum interfacial energy required for the coating between $\gamma\text{-Al}_2\text{O}_3$ and TiO_2 when the diameter of $\gamma\text{-Al}_2\text{O}_3$ was 1.0 mm and the diameter of TiO_2 was 0.04 mm. The number of coated TiO_2 particles onto the $\gamma\text{-Al}_2\text{O}_3$ particle also proved that when the interfacial energy of $\gamma\text{-Al}_2\text{O}_3\text{-TiO}_2$ 20 J/m^2 , 90% of TiO_2 particles adhering to $\gamma\text{-Al}_2\text{O}_3$ particle (2442 TiO_2 particles adhered onto the $\gamma\text{-Al}_2\text{O}_3$ particle

out of 2704). The effect of increasing interfacial energy of γ -Al₂O₃-TiO₂ on the velocity, the potential energy, and the translational kinetic energy was not very obvious.

7) Using two DEM modeling (Hertz-Mindlin no-slip model and JKR model) definitely provided very valuable information for us to better understand the dry coating process. The results of the modeling demonstrated that the higher the interfacial energy of γ -Al₂O₃-TiO₂, did not lead to a better coating of γ -Al₂O₃ and TiO₂. For example, when the diameter of γ -Al₂O₃ was 1.0 mm, the diameter of TiO₂ was 0.04 mm, then the interfacial energy of γ -Al₂O₃-TiO₂ of 20 J/m² was the optimal value. However, even though the interfacial energy of γ -Al₂O₃-TiO₂ was at the optimal value of 20 J/m², it was a bit disappointing that no completely coated γ -Al₂O₃ particles were obtained. Therefore, there is still a lot of room and possibilities to explore and discover more details in the simulation of the dry coating.

In a way, the data from the simulations were correlated with the results of the experiments. Under the same experimental conditions, the same guest particles, the coating of γ -Al₂O₃ was not as good as that of S.S316L. In the simulation study, it was found that that the variation of all parameters (particle size, rotational speed, filling ratio, and young's modulus) has a greater effect on the S.S316L particles than on the γ -Al₂O₃ particles. This could be caused by the property of the material itself, such as the density of the S.S316L and the hardness of S.S316L, which are higher than that of γ -Al₂O₃. Or it could be, because the material of the picomix is steel, which means S.S316L particles and the picomix are equally attractive to particles.

Perspectives

This work investigated the preparation of new supports of catalysts for methanation via a dry coating method in a high shear mixer "Picomix". DEM modeling of dry coating in a picomix was applied to explore the interactions and collisions between particles. The results of these two studies have laid a lot of foundation for future experimental and simulation studies on the dry coating method.

1) The newly prepared supports can be directly added promoters during the preparation of catalysts. Ni/NiO could be a very good option, because of the high efficiency in CH₄ production and low cost of CO₂ methanation, Ni catalysts are the most widely investigated material. Carry out the methanation reaction in a micro reactor to validate the studied supports.

- 2) A transparent picomix can be used to track particle motions and establish the connections between experimental and DEM modelization.
- 3) In DEM modeling, more parameters (density, coefficient of restitution) can be considered to vary to change its effect on the dry coating. More importantly, the coating modeling of S.S316L with TiO_2 particle should be launched to check if it will have a higher coated number of TiO_2 particles compare with $\gamma\text{-Al}_2\text{O}_3$.
- 4) The coating of two host particles or more than two host particles with guest particles can be launched to check the stability of the coating.
- 5) Consider making the size of the guest particles smaller in order to avoid the gap above the host particle which is too small to accommodate them (see figure 5.17).
- 6) The surface energy of the guest particles can be considered to simulate the agglomeration phenomenon, because agglomeration is an unavoidable phenomenon in the dry particle coating process.

References

- [1] M. Thema, T. Weidlich, M. Hörl, A. Bellack, F. Mörs, F. Hackl, M. Kohlmayer, J. Gleich, C. Stabenau, T. Trabold, Biological CO₂-methanation: an approach to standardization, *Energies*, **12** (2019) 1670.
- [2] M. Naseem, M. Usman, S. Lee, A parametric study of dehydrogenation of various Liquid Organic Hydrogen Carrier (LOHC) materials and its application to methanation process, *International Journal of Hydrogen Energy*, **46** (2021) 4100-4115.
- [3] M. Yunyu, S. Chuanxun, A Study on CO₂ Methanization Reduction Technology [J], *SPACE MEDICINE & MEDICAL ENGINEERING*, **2** (1994).
- [4] F. Wang, S. He, H. Chen, B. Wang, L. Zheng, M. Wei, D.G. Evans, X. Duan, Active site dependent reaction mechanism over Ru/CeO₂ catalyst toward CO₂ methanation, *Journal of the American Chemical Society*, **138** (2016) 6298-6305.
- [5] M. Boudart, Heterogeneous catalysis by metals, *Journal of molecular catalysis*, **30** (1985) 27-38.
- [6] Y. Zhao, Y.-x. Pan, Y. Xie, C.-j. Liu, Carbon dioxide reforming of methane over glow discharge plasma-reduced Ir/Al₂O₃ catalyst, *Catalysis Communications*, **9** (2008) 1558-1562.
- [7] T.M. Onn, S. Zhang, L. Arroyo-Ramirez, Y.-C. Chung, G.W. Graham, X. Pan, R.J. Gorte, Improved thermal stability and methane-oxidation activity of Pd/Al₂O₃ catalysts by atomic layer deposition of ZrO₂, *ACS Catalysis*, **5** (2015) 5696-5701.
- [8] X. Zhu, P. Huo, Y.-p. Zhang, D.-g. Cheng, C.-j. Liu, Structure and reactivity of plasma treated Ni/Al₂O₃ catalyst for CO₂ reforming of methane, *Applied Catalysis B: Environmental*, **81** (2008) 132-140.
- [9] K. Yatagai, Y. Shishido, R. Gemma, T. Boll, H.-H. Uchida, K. Oguri, Mechanochemical CO₂ methanation over LaNi-based alloys, *International Journal of Hydrogen Energy*, **45** (2020) 5264-5275.
- [10] P. Shafiee, S.M. Alavi, M. Rezaei, Solid-state synthesis method for the preparation of cobalt doped Ni–Al₂O₃ mesoporous catalysts for CO₂ methanation, *International Journal of Hydrogen Energy*, **46** (2021) 3933-3944.
- [11] P. Shafiee, S.M. Alavi, M. Rezaei, Mechanochemical synthesis method for the preparation of mesoporous Ni–Al₂O₃ catalysts for hydrogen purification via CO₂ methanation, *Journal of the Energy Institute*, **96** (2021) 1-10.
- [12] L. Qu, D. AV Morton, Particle engineering via mechanical dry coating in the design of pharmaceutical solid dosage forms, *Current pharmaceutical design*, **21** (2015) 5802-5814.
- [13] R. Pfeffer, R.N. Dave, D. Wei, M. Ramlakhan, Synthesis of engineered particulates with tailored properties using dry particle coating, *Powder Technology*, **117** (2001) 40-67.

References

- [14] J.S. Koner, E.Z. Dahmash, D.A. Wyatt, A. Mohammed, Dry particle coating-a unique solution for pharmaceutical formulation, *Pharmaceutical Technology*, **42** (2018) 26-30.
- [15] J.A. Hersey, Ordered mixing: a new concept in powder mixing practice, *Powder Technology*, **11** (1975) 41-44.
- [16] B. Chaudhuri, Simulation and modeling of magnetically-assisted impaction coating (MAIC) process for dry particle coating, New Jersey Institute of Technology. (2000).
- [17] D. Nguyen, A. Rasmuson, I. Niklasson Bjorn, K. Thalberg, Mechanistic time scales in adhesive mixing investigated by dry particle sizing, *Eur J Pharm Sci*, **69** (2015) 19-25.
- [18] S. Sarangi, K. Thalberg, G. Frenning, Numerical modeling of collision of adhesive units: Stability and mechanical properties during handling, *Chemical Engineering Science: X*, **6** (2020).
- [19] T.S. Ward, W. Chen, M. Schoenitz, R.N. Dave, E.L. Dreizin, A study of mechanical alloying processes using reactive milling and discrete element modeling, *Acta Materialia*, **53** (2005) 2909-2918.
- [20] K. Washino, E.L. Chan, T. Tanaka, DEM with attraction forces using reduced particle stiffness, *Powder Technology*, **325** (2018) 202-208.
- [21] S. Lommen, D. Schott, G. Lodewijks, DEM speedup: Stiffness effects on behavior of bulk material, *Particuology*, **12** (2014) 107-112.
- [22] S. Rönsch, J. Schneider, S. Matthischke, M. Schlüter, M. Götz, J. Lefebvre, P. Prabhakaran, S. Bajohr, Review on methanation—From fundamentals to current projects, *Fuel*, **166** (2016) 276-296.
- [23] S.N.F.M. Rudin, Z. Ab Muis, H. Hashim, W.S. Ho, Techno-economic assessment of integrated power plant with methanation, *Chemical Engineering Transactions*, **63** (2018) 451-456.
- [24] R. Hayes, W. Thomas, K. Hayes, A study of the nickel-catalyzed methanation reaction, *Journal of Catalysis*, **92** (1985) 312-326.
- [25] P. Sabatier, J. Senderens, Comptes Rendus Des Séances De L'Académie Des Sciences, Section VI—Chimie, Paris: Imprimerie Gauthier-Villars, (1902).
- [26] X. Su, J. Xu, B. Liang, H. Duan, B. Hou, Y. Huang, Catalytic carbon dioxide hydrogenation to methane: A review of recent studies, *Journal of Energy Chemistry*, **25** (2016) 553-565.
- [27] T. Schaaf, J. Grünig, M.R. Schuster, T. Rothenfluh, A. Orth, Methanation of CO₂-storage of renewable energy in a gas distribution system, *Energy, Sustainability and Society*, **4** (2014) 1-14.
- [28] E. Meloni, M. Martino, V. Palma, A short review on Ni based catalysts and related engineering issues for methane steam reforming, *Catalysts*, **10** (2020) 352.
- [29] B. Miao, S.S.K. Ma, X. Wang, H. Su, S.H. Chan, Catalysis mechanisms of CO₂ and CO methanation, *Catalysis Science & Technology*, **6** (2016) 4048-4058.

References

- [30] H. Yang, Z. Xu, M. Fan, R. Gupta, R.B. Slimane, A.E. Bland, I. Wright, Progress in carbon dioxide separation and capture: A review, *Journal of environmental sciences*, **20** (2008) 14-27.
- [31] S. Rönsch, Optimierung und bewertung von Anlagen zur Erzeugung von Methan, Strom und Wärme aus biogenen Festbrennstoffen, Deutsches Biomasseforschungszentrum gemeinnützige GmbH, (2011).
- [32] P. Li, F. Yu, N. Altaf, M. Zhu, J. Li, B. Dai, Q. Wang, Two-dimensional layered double hydroxides for reactions of methanation and methane reforming in C1 chemistry, *Materials*, **11** (2018) 221.
- [33] A. Iulianelli, S. Liguori, J. Wilcox, A. Basile, Advances on methane steam reforming to produce hydrogen through membrane reactors technology: A review, *Catalysis Reviews*, **58** (2016) 1-35.
- [34] M. Götz, A.M. Koch, F. Graf, State of the art and perspectives of CO₂ methanation process concepts for power-to-gas applications, International Gas Union Research Conference, International Gas Union Fornebu, Norway, 2014.
- [35] L. Falbo, M. Martinelli, C.G. Visconti, L. Lietti, C. Bassano, P. Deiana, Kinetics of CO₂ methanation on a Ru-based catalyst at process conditions relevant for Power-to-Gas applications, *Applied Catalysis B: Environmental*, **225** (2018) 354-363.
- [36] I.U.o.P.a.A.C.c. nomenclature, <http://goldbook.iupac.org/S06147.html>., 5 August 2021.
- [37] L. Lloyd, Handbook of industrial catalysts, Springer Science & Business Media. (2011).
- [38] R.-P. Ye, L. Liao, T.R. Reina, J. Liu, D. Chevella, Y. Jin, M. Fan, J. Liu, Engineering Ni/SiO₂ catalysts for enhanced CO₂ methanation, *Fuel*, **285** (2021) 119151.
- [39] T.A. Le, J.K. Kang, E.D. Park, Active Ni/SiO₂ catalysts with high Ni content for benzene hydrogenation and CO methanation, *Applied Catalysis A: General*, **581** (2019) 67-73.
- [40] R.-P. Ye, W. Gong, Z. Sun, Q. Sheng, X. Shi, T. Wang, Y. Yao, J.J. Razink, L. Lin, Z. Zhou, Enhanced stability of Ni/SiO₂ catalyst for CO₂ methanation: Derived from nickel phyllosilicate with strong metal-support interactions, *Energy*, **188** (2019) 116059.
- [41] J. Gao, Q. Liu, F. Gu, B. Liu, Z. Zhong, F. Su, Recent advances in methanation catalysts for the production of synthetic natural gas, *Rsc Advances*, **5** (2015) 22759-22776.
- [42] Z. Zhang, Y. Tian, L. Zhang, S. Hu, J. Xiang, Y. Wang, L. Xu, Q. Liu, S. Zhang, X. Hu, Impacts of nickel loading on properties, catalytic behaviors of Ni/ γ -Al₂O₃ catalysts and the reaction intermediates formed in methanation of CO₂, *International Journal of Hydrogen Energy*, **44** (2019) 9291-9306.
- [43] S. Rahmani, F. Meshkani, M. Rezaei, Preparation of Ni-M (M: La, Co, Ce, and Fe) catalysts supported on mesoporous nanocrystalline γ -Al₂O₃ for CO₂ methanation, *Environmental Progress & Sustainable Energy*, **38** (2019) 118-126.
- [44] T.A. Le, J.K. Kang, S.H. Lee, E.D. Park, CO and CO₂ Methanation over Ni/ γ -Al₂O₃ prepared by deposition-precipitation method, *Journal of nanoscience and nanotechnology*, **19** (2019) 3252-3262.

References

- [45] P. Panagiotopoulou, D.I. Kondarides, X.E. Verykios, Mechanistic aspects of the selective methanation of CO over Ru/TiO₂ catalyst, *Catalysis today*, **181** (2012) 138-147.
- [46] R. Zhou, N. Rui, Z. Fan, C.-j. Liu, Effect of the structure of Ni/TiO₂ catalyst on CO₂ methanation, *International Journal of Hydrogen Energy*, **41** (2016) 22017-22025.
- [47] W.L. Vrijburg, E. Moioli, W. Chen, M. Zhang, B.J. Terlingen, B. Zijlstra, I.A. Filot, A. Züttel, E.A. Pidko, E.J. Hensen, Efficient base-metal NiMn/TiO₂ catalyst for CO₂ methanation, *ACS Catalysis*, **9** (2019) 7823-7839.
- [48] G.D. Lee, M.J. Moon, J.H. Park, S.S. Park, S.S. Hong, Raney Ni catalysts derived from different alloy precursors Part II. CO and CO₂ methanation activity, *Korean Journal of Chemical Engineering*, **22** (2005) 541-546.
- [49] A. Westermann, B. Azambre, M. Bacariza, I. Graça, M. Ribeiro, J. Lopes, C. Henriques, Insight into CO₂ methanation mechanism over NiUSY zeolites: An operando IR study, *Applied Catalysis B: Environmental*, **174** (2015) 120-125.
- [50] L. Wei, N. Kumar, W. Haije, J. Peltonen, M. Peurla, H. Grénman, W. de Jong, Can bi-functional nickel modified 13X and 5A zeolite catalysts for CO₂ methanation be improved by introducing ruthenium?, *Molecular Catalysis*, **494** (2020) 111115.
- [51] A. Quindimil, U. De-La-Torre, B. Pereda-Ayo, J.A. Gonzalez-Marcos, J.R. Gonzalez-Velasco, Ni catalysts with La as promoter supported over Y-and BETA-zeolites for CO₂ methanation, *Applied Catalysis B: Environmental*, **238** (2018) 393-403.
- [52] L. Wei, W. Haije, N. Kumar, J. Peltonen, M. Peurla, H. Grenman, W. de Jong, Influence of nickel precursors on the properties and performance of Ni impregnated zeolite 5A and 13X catalysts in CO₂ methanation, *Catalysis Today*, **362** (2021) 35-46.
- [53] L. Zhu, S. Yin, Q. Yin, H. Wang, S. Wang, Biochar: a new promising catalyst support using methanation as a probe reaction, *Energy Science & Engineering*, **3** (2015) 126-134.
- [54] X. Wang, Y. Liu, L. Zhu, Y. Li, K. Wang, K. Qiu, N. Tippayawong, P. Aggarangsi, P. Reubroycharoen, S. Wang, Biomass derived N-doped biochar as efficient catalyst supports for CO₂ methanation, *Journal of CO₂ Utilization*, **34** (2019) 733-741.
- [55] X. Wang, M. Yang, X. Zhu, L. Zhu, S. Wang, Experimental study and life cycle assessment of CO₂ methanation over biochar supported catalysts, *Applied Energy*, **280** (2020) 115919.
- [56] J. Cusumano, R. Dalla Betta, R. Levy, Scientific resources relevant to the catalytic problems in the conversion of coal. Final report.[Approximately 1000 references], (1976).
- [57] F. Fischer, H. Tropsch, P. Dilthey, Reduction of carbon monoxide to methane in the presence of various metals, *Brennst. Chem*, **6** (1925) 265-271.
- [58] M. Vannice, The catalytic synthesis of hydrocarbons from carbon monoxide and hydrogen, *Catalysis Reviews—Science and Engineering*, **14** (1976) 153-191.

References

- [59] G.A. Mills, F.W. Steffgen, Catalytic methanation, *Catalysis Reviews*, **8** (1974) 159-210.
- [60] G. Garbarino, D. Bellotti, P. Riani, L. Magistri, G. Busca, Methanation of carbon dioxide on Ru/Al₂O₃ and Ni/Al₂O₃ catalysts at atmospheric pressure: catalysts activation, behaviour and stability, *International journal of hydrogen energy*, **40** (2015) 9171-9182.
- [61] S. Tada, R. Kikuchi, K. Urasaki, S. Satokawa, Effect of reduction pretreatment and support materials on selective CO methanation over supported Ru catalysts, *Applied Catalysis A: General*, **404** (2011) 149-154.
- [62] F. Solymosi, I. Tombacz, M. Kocsis, Hydrogenation of CO on supported Rh catalysts, *Journal of Catalysis*, **75** (1982) 78-93.
- [63] A. Borodziński, G.C. Bond, Selective hydrogenation of ethyne in ethene-rich streams on palladium catalysts. Part 1. Effect of changes to the catalyst during reaction, *Catalysis Reviews*, **48** (2006) 91-144.
- [64] O.A. Ojelade, S.F. Zaman, A Review on Pd Based Catalysts for CO₂ Hydrogenation to Methanol: In-Depth Activity and DRIFTS Mechanistic Study, *Catalysis Surveys from Asia*, **24** (2020) 11-37.
- [65] J. Ashok, S. Pati, P. Hongmanorom, Z. Tianxi, C. Junmei, S. Kawi, A review of recent catalyst advances in CO₂ methanation processes, *Catalysis Today*, **356** (2020) 471-489.
- [66] M.A. Vannice, R.L. Garten, Supported palladium catalysts for methanation, *Industrial & Engineering Chemistry Product Research and Development*, **18** (1979) 186-191.
- [67] M. prices, <https://rockawayrecycling.com/scrap-metal-prices/>, 5, August 2021.
- [68] M. prices, <http://www.infomine.com/investment/metalprices/>, 5, August 2021.
- [69] E. Kok, J. Scott, N. Cant, D. Trimm, The impact of ruthenium, lanthanum and activation conditions on the methanation activity of alumina-supported cobalt catalysts, *Catalysis today*, **164** (2011) 297-301.
- [70] C. De Vries, M. Claeys, G. Schaub, Chemical energy storage in gaseous hydrocarbons via iron Fischer–Tropsch synthesis from H₂/CO₂—kinetics, selectivity and process considerations, *Catalysis Today*, **242** (2015) 184-192.
- [71] Z. Zhang, X.E. Verykios, Carbon dioxide reforming of methane to synthesis gas over Ni/La₂O₃ catalysts, *Applied Catalysis A: General*, **138** (1996) 109-133.
- [72] Q. Miao, G. Xiong, S. Sheng, W. Cui, L. Xu, X. Guo, Partial oxidation of methane to syngas over nickel-based catalysts modified by alkali metal oxide and rare earth metal oxide, *Applied Catalysis A: General*, **154** (1997) 17-27.
- [73] M.A. Nieva, M.M. Villaverde, A. Monzón, T.F. Garetto, A.J. Marchi, Steam-methane reforming at low temperature on nickel-based catalysts, *Chemical Engineering Journal*, **235** (2014) 158-166.

References

- [74] S. Kawi, Y. Kathiraser, J. Ni, U. Oemar, Z. Li, E.T. Saw, Progress in synthesis of highly active and stable nickel-based catalysts for carbon dioxide reforming of methane, *ChemSusChem*, **8** (2015) 3556-3575.
- [75] S. Tada, T. Shimizu, H. Kameyama, T. Haneda, R. Kikuchi, Ni/CeO₂ catalysts with high CO₂ methanation activity and high CH₄ selectivity at low temperatures, *International Journal of Hydrogen Energy*, **37** (2012) 5527-5531.
- [76] D.C. da Silva, S. Letichevsky, L.E. Borges, L.G. Appel, The Ni/ZrO₂ catalyst and the methanation of CO and CO₂, *International Journal of Hydrogen Energy*, **37** (2012) 8923-8928.
- [77] N. Laosiripojana, S. Assabumrungrat, Methane steam reforming over Ni/Ce–ZrO₂ catalyst: Influences of Ce–ZrO₂ support on reactivity, resistance toward carbon formation, and intrinsic reaction kinetics, *Applied Catalysis A: General*, **290** (2005) 200-211.
- [78] S. Abate, K. Barbera, E. Giglio, F. Deorsola, S. Bensaid, S. Perathoner, R. Pirone, G. Centi, Synthesis, characterization, and activity pattern of Ni–Al hydrotalcite catalysts in CO₂ methanation, *Industrial & Engineering Chemistry Research*, **55** (2016) 8299-8308.
- [79] W. Wang, W. Chu, N. Wang, W. Yang, C. Jiang, Mesoporous nickel catalyst supported on multi-walled carbon nanotubes for carbon dioxide methanation, *international journal of hydrogen energy*, **41** (2016) 967-975.
- [80] N. Bion, F. Epron, M. Moreno, F. Marino, D. Duprez, Preferential oxidation of carbon monoxide in the presence of hydrogen (PROX) over noble metals and transition metal oxides: advantages and drawbacks, *Topics in Catalysis*, **51** (2008) 76.
- [81] D. Hu, J. Gao, Y. Ping, L. Jia, P. Gunawan, Z. Zhong, G. Xu, F. Gu, F. Su, Enhanced investigation of CO methanation over Ni/Al₂O₃ catalysts for synthetic natural gas production, *Industrial & Engineering Chemistry Research*, **51** (2012) 4875-4886.
- [82] E. Jwa, S. Lee, H. Lee, Y. Mok, Plasma-assisted catalytic methanation of CO and CO₂ over Ni–zeolite catalysts, *Fuel processing technology*, **108** (2013) 89-93.
- [83] T.A. Le, J.K. Kang, E.D. Park, CO and CO₂ methanation over Ni/SiC and Ni/SiO₂ catalysts, *Topics in Catalysis*, **61** (2018) 1537-1544.
- [84] T.A. Le, M.S. Kim, S.H. Lee, T.W. Kim, E.D. Park, CO and CO₂ methanation over supported Ni catalysts, *Catalysis Today*, **293** (2017) 89-96.
- [85] C. Guo, Y. Wu, H. Qin, J. Zhang, CO methanation over ZrO₂/Al₂O₃ supported Ni catalysts: A comprehensive study, *Fuel processing technology*, **124** (2014) 61-69.
- [86] J. Ren, H. Li, Y. Jin, J. Zhu, S. Liu, J. Lin, Z. Li, Silica/titania composite-supported Ni catalysts for CO methanation: effects of Ti species on the activity, anti-sintering, and anti-coking properties, *Applied Catalysis B: Environmental*, **201** (2017) 561-572.

References

- [87] X. Yan, Y. Liu, B. Zhao, Z. Wang, Y. Wang, C.-j. Liu, Methanation over Ni/SiO₂: effect of the catalyst preparation methodologies, *International Journal of Hydrogen Energy*, **38** (2013) 2283-2291.
- [88] N. Czuma, K. Zarebska, M. Motak, M.E. Galvez, P. Da Costa, Ni/zeolite X derived from fly ash as catalysts for CO₂ methanation, *Fuel*, **267** (2020) 117139.
- [89] T.A. Le, J. Kim, J.K. Kang, E.D. Park, CO and CO₂ methanation over Ni/Al@ Al₂O₃ core-shell catalyst, *Catalysis Today*, **356** (2020) 622-630.
- [90] M. Aziz, A. Jalil, S. Triwahyono, R. Mukti, Y. Taufiq-Yap, M. Sazegar, Highly active Ni-promoted mesostructured silica nanoparticles for CO₂ methanation, *Applied Catalysis B: Environmental*, **147** (2014) 359-368.
- [91] S. Tada, R. Kikuchi, K. Wada, K. Osada, K. Akiyama, S. Satokawa, Y. Kawashima, Long-term durability of Ni/TiO₂ and Ru-Ni/TiO₂ catalysts for selective CO methanation, *Journal of Power Sources*, **264** (2014) 59-66.
- [92] K. Urasaki, Y. Tanpo, Y. Nagashima, R. Kikuchi, S. Satokawa, Effects of preparation conditions of Ni/TiO₂ catalysts for selective CO methanation in the reformat gas, *Applied Catalysis A: General*, **452** (2013) 174-178.
- [93] B. Zhao, Z. Chen, Y. Chen, X. Ma, Syngas methanation over Ni/SiO₂ catalyst prepared by ammonia-assisted impregnation, *International journal of hydrogen energy*, **42** (2017) 27073-27083.
- [94] B. Zhao, P. Liu, S. Li, H. Shi, X. Jia, Q. Wang, F. Yang, Z. Song, C. Guo, J. Hu, Bimetallic Ni-Co nanoparticles on SiO₂ as robust catalyst for CO methanation: Effect of homogeneity of Ni-Co alloy, *Applied Catalysis B: Environmental*, **278** (2020) 119307.
- [95] B.A. Mehrabadi, S. Eskandari, U. Khan, R.D. White, J.R. Regalbuto, A review of preparation methods for supported metal catalysts, *Advances in Catalysis*, **61** (2017) 1-35.
- [96] J. Regalbuto, Catalyst preparation: science and engineering, CRC press. (2016).
- [97] J.D. Wright, N.A. Sommerdijk, Sol-gel materials: chemistry and applications, CRC press.(2018).
- [98] K. Polychronopoulou, A.F. Zedan, M. Katsiotis, M. Baker, A. AlKhoori, S.Y. AlQaradawi, S. Hinder, S. AlHassan, Rapid microwave assisted sol-gel synthesis of CeO₂ and CexSm_{1-x}O₂ nanoparticle catalysts for CO oxidation, *Molecular Catalysis*, **428** (2017) 41-55.
- [99] S. Esposito, "Traditional" sol-gel chemistry as a powerful tool for the preparation of supported metal and metal oxide catalysts, *Materials*, **12** (2019) 668.
- [100] M. Lu, N. Fatah, A.Y. Khodakov, Optimization of solvent-free mechanochemical synthesis of Co/Al₂O₃ catalysts using low-and high-energy processes, *Journal of Materials Science*, **52** (2017) 12031-12043.

References

- [101] M. Lu, N. Fatah, A.Y. Khodakov, New shearing mechanical coating technology for synthesis of alumina-supported cobalt Fischer–Tropsch solid catalysts, *Journal of Materials Chemistry A*, **5** (2017) 9148-9155.
- [102] M. Lu, N. Fatah, A.Y. Khodakov, Solvent-free synthesis of alumina supported cobalt catalysts for Fischer–Tropsch synthesis, *Journal of Energy Chemistry*, **25** (2016) 1001-1007.
- [103] X. Liu, N. Fatah, M. Touzin, Dry coating process for high activity Co/Al₂O₃ Fischer-Tropsch catalysts, (2017).
- [104] X. Liu, Conception en voie sèche de catalyseurs propres Co/Al₂O₃ pour la synthèse Fischer-Tropsch et modélisation numérique DEM, Ecole centrale de Lille, 2018.
- [105] Y. Ouabbas, J. Dodds, L. Galet, A. Chamayou, M. Baron, Particle–particle coating in a cyclomix impact mixer, *Powder Technology*, **189** (2009) 245-252.
- [106] J.S.K.E.Z. Dahmash, D.A.W.A. Mohammed, Dry Particle Coating—A Unique Solution for Pharmaceutical Formulation, (2018).
- [107] L.E. Beach, Effect of dry particle coating on the properties of cohesive pharmaceutical powders, (2011).
- [108] M. Ramlakhan, C.Y. Wu, S. Watano, R.N. Dave, R. Pfeffer, Dry particle coating using magnetically assisted impaction coating: modification of surface properties and optimization of system and operating parameters, *Powder Technology*, **112** (2000) 137-148.
- [109] J. Scicolone, A. Mujumdar, S. Sundaresan, R.N. Davé, Environmentally benign dry mechanical mixing of nano-particles using magnetically assisted impaction mixing process, *Powder technology*, **209** (2011) 138-146.
- [110] K. Zheng, K. Kunnath, Z. Ling, L. Chen, R.N. Davé, Influence of guest and host particle sizes on dry coating effectiveness: When not to use high mixing intensity, *Powder Technology*, **366** (2020) 150-163.
- [111] K. Al-Hamdani, J. Murray, T. Hussain, A. Kennedy, A. Clare, Cold sprayed metal-ceramic coatings using satellited powders, *Materials Letters*, **198** (2017) 184-187.
- [112] E. Alizadeh, H. Hajhashemi, F. Bertrand, J. Chaouki, Experimental investigation of solid mixing and segregation in a tetrapodal blender, *Chemical Engineering Science*, **97** (2013) 354-365.
- [113] V. Karde, S. Panda, C. Ghoroi, Surface modification to improve powder bulk behavior under humid conditions, *Powder Technology*, **278** (2015) 181-188.
- [114] Azonano, <https://www.azonano.com/equipment-details.aspx?EquipID=638>, 5, August 2021.
- [115] M. Kumon, M. Suzuki, A. Kusai, E. Yonemochi, K. Terada, Novel approach to DPI carrier lactose with mechanofusion process with additives and evaluation by IGC, *Chemical and pharmaceutical bulletin*, **54** (2006) 1508-1514.

References

- [116] M. Kumon, S. Machida, M. Suzuki, A. Kusai, E. Yonemochi, K. Terada, Application and mechanism of inhalation profile improvement of DPI formulations by mechanofusion with magnesium stearate, *Chemical and Pharmaceutical Bulletin*, **56** (2008) 617-625.
- [117] R. Sharma, G. Setia, Mechanical dry particle coating on cohesive pharmaceutical powders for improving flowability-A review, *Powder Technology*, **356** (2019) 458-479.
- [118] L. Nara Machinery Co., <https://www.rs.kagu.tus.ac.jp/~honda/hyb2.html>, 5, August 2021.
- [119] A. Böhm, T. Büttner, T. Weißgärber, B. Kieback, W. Pieper, Powder Manufacturing and Processing: Particle Modification and Powder Design using the NARA-Hybridizer, European Congress and Exhibition on Powder Metallurgy. European PM Conference Proceedings, The European Powder Metallurgy Association, 2004, pp. 1-7.
- [120] M. Gera, V.A. Saharan, M. Kataria, V. Kukkar, Mechanical methods for dry particle coating processes and their applications in drug delivery and development, *Recent patents on drug delivery & formulation*, **4** (2010) 58-81.
- [121] C.L. Burcham, P.C. Collins, D.J. Jarmer, K.D. Seibert, Reduction of particle size of drug substance for low-dose drug products, *Formulation and Analytical Development for Low-Dose Oral Drug Products*, (2009) 205.
- [122] F.D. Conforti, Cake manufacture, *Bakery products: Science and technology*, **22** (2006) 393-410.
- [123] KEMUTEC, <https://www.kemutec.com/revolution-cone-mill-performance/#.YEc2o2hKg2w>, 5, August 2021.
- [124] G. Ning, P. Li, T. Zhang, Z. Zhou, D. Li, Hydrophobic Nano-Silica for the Surface Modification of Graphite Flake, *Propellants, Explosives, Pyrotechnics*, **38** (2013) 520-524.
- [125] B.M.J. Tan, L.W. Chan, P.W.S. Heng, Milling and Blending: Producing the Right Particles and Blend Characteristics for Dry Powder Inhalation, *Pharmaceutical Inhalation Aerosol Technology*, (2019) 273.
- [126] Azom, <https://www.azom.com/equipment-details.aspx?EquipID=1462>, 5, August 2021.
- [127] K. Brockbank, T. Freeman, W. Hendrickson, C. Bowman, J. Clayton, Comparison of Magnetically Assisted Impaction Coating (MAIC) with Traditional Mixing Techniques for the Addition of a Silica Flow Aid, AIChE Annual Meeting, 2016.
- [128] P. Singh, T. Solanky, R. Mudryy, R. Pfeffer, R. Dave, Estimation of coating time in the magnetically assisted impaction coating process, *Powder technology*, **121** (2001) 159-167.
- [129] C. Mayer-Laigle, C. Gatumel, H. Berthiaux, Mixing dynamics for easy flowing powders in a lab scale Turbula® mixer, *Chemical Engineering Research and Design*, **95** (2015) 248-261.
- [130] Shaker-mixer, <https://www.wab-group.com/en/mixing-technology/3d-shaker-mixer/product/turbula/>, (5, August 2021).

References

- [131] M. Lu, N. Fatah, A.Y. Khodakov, Optimization of solvent-free mechanochemical synthesis of Co/Al₂O₃ catalysts using low- and high-energy processes, *Journal of Materials Science*, **52** (2017) 12031-12043.
- [132] M. Lu, New technology development for advanced" Clean" solid catalysts for Fischer-Tropsch synthesis, Lille 1, 2015.
- [133] HOSOKAWA.co.uk, <https://www.hosokawa.co.uk/products/picomix/>, (5, August 2021).
- [134] Y. Hoashi, Y. Tozuka, H. Takeuchi, Solventless dry powder coating for sustained drug release using mechanochemical treatment based on the tri-component system of acetaminophen, carnauba wax and glidant, *Drug development and industrial pharmacy*, **39** (2013) 259-265.
- [135] Q. Zhou, L. Shi, S. Chatteraj, C.C.J.J.o.p.s. Sun, Preparation and characterization of surface-engineered coarse microcrystalline cellulose through dry coating with silica nanoparticles, **101** (2012) 4258-4266.
- [136] Q. Zhou, B. Armstrong, I. Larson, P.J. Stewart, D.A. Morton, Improving powder flow properties of a cohesive lactose monohydrate powder by intensive mechanical dry coating, *Journal of pharmaceutical sciences*, **99** (2010) 969-981.
- [137] A. Sato, E. Serris, P. Grosseau, G. Thomas, A. Chamayou, L. Galet, M. Baron, Effect of operating conditions on dry particle coating in a high shear mixer, *Powder technology*, **229** (2012) 97-103.
- [138] Q. Zhou, L. Shi, S. Chatteraj, C.C. Sun, Preparation and characterization of surface-engineered coarse microcrystalline cellulose through dry coating with silica nanoparticles, *Journal of pharmaceutical sciences*, **101** (2012) 4258-4266.
- [139] Y. Ouabbas, A. Chamayou, L. Galet, M. Baron, G. Thomas, P. Grosseau, B. Guilhot, Surface modification of silica particles by dry coating: Characterization and powder ageing, *Powder Technology*, **190** (2009) 200-209.
- [140] M. Cai, L.L. Feng, M.S. Ruthkosky, J.D. Rogers, Nanostructured catalyst particle/catalyst carrier particle system, Google Patents, 2004.
- [141] A. Trovarelli, F. Zamar, J. Llorca, C. De Leitenburg, G. Dolcetti, J.T. Kiss, Nanophase fluorite-structured CeO₂-ZrO₂ Catalysts prepared by high-energy mechanical milling, *Journal of Catalysis*, **169** (1997) 490-502.
- [142] U. Kamolphop, S.F. Taylor, J.P. Breen, R. Burch, J.J. Delgado, S. Chansai, C. Hardacre, S. Hengrasmee, S.L. James, Low-Temperature Selective Catalytic Reduction (SCR) of NO_x with n-Octane Using Solvent-Free Mechanochemically Prepared Ag/Al₂O₃ Catalysts, *ACS Catalysis*, **1** (2011) 1257-1262.
- [143] F. Jentoft, H. Schmelz, H. Knözinger, Preparation of selective catalytic reduction catalysts via milling and thermal spreading, *Applied Catalysis A: General*, **161** (1997) 167-182.

References

- [144] R. Zhang, A. Villanueva, H. Alamdari, S. Kaliaguine, Cu-and Pd-substituted nanoscale Fe-based perovskites for selective catalytic reduction of NO by propene, *Journal of Catalysis*, **237** (2006) 368-380.
- [145] D.W. Kwon, K.H. Park, S.C. Hong, The influence on SCR activity of the atomic structure of V₂O₅/TiO₂ catalysts prepared by a mechanochemical method, *Applied Catalysis A: General*, **451** (2013) 227-235.
- [146] Y. Dimitriev, M. Gancheva, R. Iordanova, Synthesis of ZnO by mechanochemical decomposition of zinc carbonate hydroxide, *Journal of the University of Chemical Technology and Metallurgy*, **46** (2011) 243-248.
- [147] J. Šubrt, J.M. Criado, L. Szatmáry, M.J. Diánez-Millán, N. Murafa, L.A. Pérez-Maqueda, V. Brezová, Mechanochemical synthesis of visible light sensitive titanium dioxide photocatalyst, *International Journal of Photoenergy*, **2011** (2011).
- [148] T.K. Ghorai, M. Chakraborty, P. Pramanik, Photocatalytic performance of nano-photocatalyst from TiO₂ and Fe₂O₃ by mechanochemical synthesis, *Journal of Alloys and Compounds*, **509** (2011) 8158-8164.
- [149] C. Shifu, C. Lei, G. Shen, C. Gengyu, The preparation of nitrogen-doped photocatalyst TiO₂- xNx by ball milling, *Chemical Physics Letters*, **413** (2005) 404-409.
- [150] B. mill, <https://www.pharmapproach.com/ball-mill/>, 5, August 2021.
- [151] Q. Wu, W.-s. Miao, H.-j. Gao, D. Hui, Mechanical properties of nanomaterials: A review, *Nanotechnology Reviews*, **9** (2020) 259-273.
- [152] M. Vert, Y. Doi, K.-H. Hellwich, M. Hess, P. Hodge, P. Kubisa, M. Rinaudo, F. Schué, Terminology for biorelated polymers and applications (IUPAC Recommendations 2012), *Pure and Applied Chemistry*, **84** (2012) 377-410.
- [153] C. Buzea, I.I. Pacheco, K. Robbie, Nanomaterials and nanoparticles: sources and toxicity, *Biointerphases*, **2** (2007) MR17-MR71.
- [154] K. Seshan, Handbook of thin film deposition processes and techniques, William Andrew 2001.
- [155] C.A.S. Batista, R.G. Larson, N.A. Kotov, Nonadditivity of nanoparticle interactions, *Science*, **350** (2015).
- [156] R. Yang, A. Yu, S. Choi, M.S. Coates, H.-K. Chan, Agglomeration of fine particles subjected to centripetal compaction, *Powder Technology*, **184** (2008) 122-129.
- [157] S. Tsantilis, S.E. Pratsinis, Soft-and hard-agglomerate aerosols made at high temperatures, *Langmuir*, **20** (2004) 5933-5939.
- [158] B. Inkson, Scanning electron microscopy (SEM) and transmission electron microscopy (TEM) for materials characterization, Materials characterization using nondestructive evaluation (NDE) methods, Elsevier 2016, pp. 17-43.

References

- [159] B.A. Korgel, D. Lee, T. Hanrath, M.J. Yacaman, A. Thesen, M. Matijevic, R. Kilaas, C. Kisielowski, A.C. Diebold, Application of aberration-corrected TEM and image simulation to nanoelectronics and nanotechnology, *IEEE transactions on semiconductor manufacturing*, **19** (2006) 391-396.
- [160] J.S. Pedersen, Analysis of small-angle scattering data from colloids and polymer solutions: modeling and least-squares fitting, *Advances in colloid and interface science*, **70** (1997) 171-210.
- [161] H. Borchert, E.V. Shevchenko, A. Robert, I. Mekis, A. Kornowski, G. Grübel, H. Weller, Determination of nanocrystal sizes: a comparison of TEM, SAXS, and XRD studies of highly monodisperse CoPt₃ particles, *Langmuir*, **21** (2005) 1931-1936.
- [162] A. paar, <https://wiki.anton-paar.com/ca-fr/analyse-de-la-nanostructure-saxs/>, 5, August 2021.
- [163] J. Stetefeld, S.A. McKenna, T.R. Patel, Dynamic light scattering: a practical guide and applications in biomedical sciences, *Biophysical reviews*, **8** (2016) 409-427.
- [164] W.I. Goldberg, Dynamic light scattering, *American Journal of Physics*, **67** (1999) 1152-1160.
- [165] M. Kaszuba, D. McKnight, M.T. Connah, F.K. McNeil-Watson, U. Nobbmann, Measuring sub nanometre sizes using dynamic light scattering, *Journal of Nanoparticle Research*, **10** (2008) 823-829.
- [166] A. paar, <https://wiki.anton-paar.com/tw-zh/the-principles-of-dynamic-light-scattering/>, 5, August 2021.
- [167] S.K. Velu, M. Yan, K.-P. Tseng, K.-T. Wong, D.M. Bassani, P. Terech, Spontaneous formation of artificial vesicles in organic media through hydrogen-bonding interactions, *Macromolecules*, **46** (2013) 1591-1598.
- [168] K. Raj, B. Viswanathan, Effect of surface area, pore volume and particle size of P25 titania on the phase transformation of anatase to rutile, *India Journal of Chemistry*, **9** (2009) 991-992.
- [169] G. Fagerlund, Determination of specific surface by the BET method, *Matériaux et Construction*, **6** (1973) 239-245.
- [170] N.M. Shamhari, B.S. Wee, S.F. Chin, K.Y. Kok, Synthesis and characterization of zinc oxide nanoparticles with small particle size distribution, *Acta Chimica Slovenica*, **65** (2018) 578-585.
- [171] N. Hwang, A.R. Barron, BET surface area analysis of nanoparticles, *The Connexions project*, (2011) 1-11.
- [172] J.M. Antúnez Domínguez, Y. Ramaye, M. Dabrio, V. Kestens, Validation of a homogeneous incremental centrifugal liquid sedimentation method for size analysis of silica (nano) particles, *Materials*, **13** (2020) 3806.
- [173] I. Laidlaw, M. Steinmetz, Introduction to differential sedimentation, *Analytical ultracentrifugation: Techniques and methods*, **31** (2005) 270-290.

References

- [174] O. Couteau, J. Charoud-Got, H. Rauscher, F. Franchini, F. Rossi, V. Kestens, K. Franks, G. Roebben, A colloidal silica reference material for nanoparticle sizing by means of dynamic light scattering and centrifugal liquid sedimentation, *Particle & Particle Systems Characterization*, **27** (2010) 112-124.
- [175] A.F. microscope, https://simple.wikipedia.org/wiki/Atomic_force_microscope, 5, August 2021.
- [176] E.L. Blundell, L.J. Mayne, E.R. Billinge, M. Platt, Emergence of tunable resistive pulse sensing as a biosensor, *Analytical Methods*, **7** (2015) 7055-7066.
- [177] J. Gross-Rother, M. Blech, E. Preis, U. Bakowsky, P. Garidel, Particle Detection and Characterization for Biopharmaceutical Applications: Current Principles of Established and Alternative Techniques, *Pharmaceutics*, **12** (2020) 1112.
- [178] AZONANO, <https://www.azonano.com/article.aspx?ArticleID=4062>, 5, August 2021.
- [179] L. Diffraction, <https://www.sympatec.com/en/particle-measurement/sensors/laser-diffraction/>, 5, August 2021.
- [180] T.G. Souza, V.S. Ciminelli, N.D.S. Mohallem, A comparison of TEM and DLS methods to characterize size distribution of ceramic nanoparticles, *Journal of physics: conference series*, IOP Publishing, 2016, pp. 012039.
- [181] I. Laidlaw, M.J.A.u.T. Steinmetz, methods, Introduction to differential sedimentation, **31** (2005) 270-290.
- [182] A. Braun, O. Couteau, K. Franks, V. Kestens, G. Roebben, A. Lamberty, T. Linsinger, Validation of dynamic light scattering and centrifugal liquid sedimentation methods for nanoparticle characterisation, *Advanced Powder Technology*, **22** (2011) 766-770.
- [183] R.D. Boyd, S.K. Pichaimuthu, A. Cuenat, New approach to inter-technique comparisons for nanoparticle size measurements; using atomic force microscopy, nanoparticle tracking analysis and dynamic light scattering, *Colloids and Surfaces A: Physicochemical and Engineering Aspects*, **387** (2011) 35-42.
- [184] Z.H. Chen, C. Kim, X.-b. Zeng, S.H. Hwang, J. Jang, G. Ungar, Characterizing size and porosity of hollow nanoparticles: SAXS, SANS, TEM, DLS, and adsorption isotherms compared, *Langmuir*, **28** (2012) 15350-15361.
- [185] P.E. Petrochenko, N. Pavurala, Y. Wu, S.Y. Wong, H. Parhiz, K. Chen, S.M. Patil, H. Qu, P. Buoniconti, A. Muhammad, Analytical considerations for measuring the globule size distribution of cyclosporine ophthalmic emulsions, *International journal of pharmaceutics*, **550** (2018) 229-239.
- [186] A. Sato, Etude numérique et expérimentale de l'enrobage en voie sèche dans un mélangeur à fort taux de cisaillement, Ecole Nationale Supérieure des Mines de Saint-Etienne, 2012.
- [187] P.A. Cundall, O.D. Strack, A discrete numerical model for granular assemblies, *geotechnique*, **29** (1979) 47-65.

References

- [188] H. Zhu, Z. Zhou, R. Yang, A. Yu, Discrete particle simulation of particulate systems: theoretical developments, *Chemical Engineering Science*, **62** (2007) 3378-3396.
- [189] T. Zykova-Timan, J. Horbach, K. Binder, Monte Carlo simulations of the solid-liquid transition in hard spheres and colloid-polymer mixtures, *The Journal of chemical physics*, **133** (2010) 014705.
- [190] C. Wassgren, J.S. Curtis, The application of computational modeling to pharmaceutical materials science, *MRS bulletin*, **31** (2006) 900-904.
- [191] D. Kremer, B. Hancock, Process simulation in the pharmaceutical industry: a review of some basic physical models, *Journal of pharmaceutical sciences*, **95** (2006) 517-529.
- [192] S.B. Yeom, E.-S. Ha, M.-S. Kim, S.H. Jeong, S.-J. Hwang, D.H. Choi, Application of the discrete element method for manufacturing process simulation in the pharmaceutical industry, *Pharmaceutics*, **11** (2019) 414.
- [193] P. Pandey, R. Bharadwaj, Predictive Modeling of Pharmaceutical Unit Operations, Woodhead Publishing 2016.
- [194] C.T. Jayasundara, M. Khanal, D. Adhikary, Application of Discrete Element Method in Grinding Mills and Composite Particle Breakage, *Neural, Parallel, and Scientific Computations*, **22** (2014) 341-358.
- [195] M.A. Hopkins, M.Y. Louge, Inelastic microstructure in rapid granular flows of smooth disks, *Physics of Fluids A: Fluid Dynamics*, **3** (1991) 47-57.
- [196] R.P. Jensen, T.B. Edil, P.J. Bosscher, M.E. Plesha, N.B. Kahla, Effect of particle shape on interface behavior of DEM-simulated granular materials, *International Journal of Geomechanics*, **1** (2001) 1-19.
- [197] U. Puri, T. Uomoto, Characterization of distinct element modeling parameters for fresh concrete and its application in shotcrete simulations, *Journal of materials in civil engineering*, **14** (2002) 137-144.
- [198] T. Chen, K. Mao, X. Huang, M.Y. Wang, Dissipation mechanisms of nonobstructive particle damping using discrete element method, *Smart Structures and Materials 2001: Damping and Isolation*, International Society for Optics and Photonics, 2001, pp. 294-301.
- [199] B. Mishra, C. Murty, On the determination of contact parameters for realistic DEM simulations of ball mills, *Powder Technology*, **115** (2001) 290-297.
- [200] Y. Xu, K. Kafui, C. Thornton, G. Lian, Effects of material properties on granular flow in a silo using DEM simulation, *Particulate Science and Technology*, **20** (2002) 109-124.
- [201] R. Venugopal, R. Rajamani, 3D simulation of charge motion in tumbling mills by the discrete element method, *Powder Technology*, **115** (2001) 157-166.
- [202] T.G. Sitharam, S. Dinesh, N. Shimizu, Micromechanical modelling of monotonic drained and undrained shear behaviour of granular media using three-dimensional DEM, *International Journal for Numerical and Analytical Methods in Geomechanics*, **26** (2002) 1167-1189.

References

- [203] O. Hlungwani, J. Rikhotso, H. Dong, M. Moys, Further validation of DEM modeling of milling: effects of liner profile and mill speed, *Minerals Engineering*, **16** (2003) 993-998.
- [204] S. Limtrakul, A. Boonsrirat, T. Vatanatham, DEM modeling and simulation of a catalytic gas–solid fluidized bed reactor: a spouted bed as a case study, *Chemical Engineering Science*, **59** (2004) 5225-5231.
- [205] Q.-M. Gong, J. Zhao, Y.-Y. Jiao, Numerical modeling of the effects of joint orientation on rock fragmentation by TBM cutters, *Tunnelling and underground space technology*, **20** (2005) 183-191.
- [206] K. Mao, M.Y. Wang, Z. Xu, T. Chen, DEM simulation of particle damping, *Powder Technology*, **142** (2004) 154-165.
- [207] B. Cook, M. Lee, A. DiGiovanni, D. Bronowski, E. Perkins, J. Williams, Discrete element modeling applied to laboratory simulation of near-wellbore mechanics, *International Journal of Geomechanics*, **4** (2004) 19-27.
- [208] F. Bertrand, L.-A. Leclaire, G. Levecque, DEM-based models for the mixing of granular materials, *Chemical Engineering Science*, **60** (2005) 2517-2531.
- [209] J.A. Gantt, I.T. Cameron, J.D. Litster, E.P. Gatzke, Determination of coalescence kernels for high-shear granulation using DEM simulations, *Powder Technology*, **170** (2006) 53-63.
- [210] J. Doucet, N. Hudon, F. Bertrand, J. Chaouki, Modeling of the mixing of monodisperse particles using a stationary DEM-based Markov process, *Computers & Chemical Engineering*, **32** (2008) 1334-1341.
- [211] R. Hemph, B. van Wachem, A.-E. Almstedt, DEM modeling of hopper flows: comparison and validation of models and parameters, World Conference on Particle Technology, Orlando, FL, 2006.
- [212] J.A. Gantt, E.P. Gatzke, A stochastic technique for multidimensional granulation modeling, *AIChE journal*, **52** (2006) 3067-3077.
- [213] B. Chaudhuri, F.J. Muzzio, M.S. Tomassone, Modeling of heat transfer in granular flow in rotating vessels, *Chemical Engineering Science*, **61** (2006) 6348-6360.
- [214] Y. Tan, D. Yang, Y. Sheng, Discrete element method (DEM) modeling of fracture and damage in the machining process of polycrystalline SiC, *Journal of the European ceramic society*, **29** (2009) 1029-1037.
- [215] Y. Lu, D. Frost, Three-dimensional DEM modeling of triaxial compression of sands, Soil behavior and geo-micromechanics2010, pp. 220-226.
- [216] L. Fries, S. Antonyuk, S. Heinrich, S. Palzer, DEM–CFD modeling of a fluidized bed spray granulator, *Chemical Engineering Science*, **66** (2011) 2340-2355.
- [217] W.R. Ketterhagen, Modeling the motion and orientation of various pharmaceutical tablet shapes in a film coating pan using DEM, *International journal of pharmaceutics*, **409** (2011) 137-149.

References

- [218] J.M. Boac, M.E. Casada, R.G. Maghirang, J.P. Harner, Material and interaction properties of selected grains and oilseeds for modeling discrete particles, 2009 Reno, Nevada, June 21-June 24, 2009, American Society of Agricultural and Biological Engineers, 2009, pp. 1.
- [219] B. Chaudhuri, Simulation and modeling of magnetically-assisted impactation coating (MAIC) process for dry particle coating, (2000).
- [220] R. Dave, W. Chen, A. Mujumdar, W. Wang, R. Pfeffer, Numerical simulation of dry particle coating processes by the discrete element method, *Advanced Powder Technology*, **14** (2003) 449-470.
- [221] X. Deng, J. Scicolone, X. Han, R.N. Davé, Discrete element method simulation of a conical screen mill: A continuous dry coating device, *Chemical Engineering Science*, **125** (2015) 58-74.
- [222] M.R. Tamadondar, L. de Martín, K. Thalberg, I.N. Björn, A. Rasmuson, The influence of particle interfacial energies and mixing energy on the mixture quality of the dry-coating process, *Powder Technology*, **338** (2018) 313-324.
- [223] A. Sato, E. Serris, P. Grosseau, G. Thomas, L. Galet, A. Chamayou, M. Baron, Experiment and simulation of dry particle coating, *Chemical engineering science*, **86** (2013) 164-172.
- [224] J. Yang, C.-Y. Wu, M. Adams, DEM analysis of particle adhesion during powder mixing for dry powder inhaler formulation development, *Granular Matter*, **15** (2013) 417-426.
- [225] S. Sarangi, K. Thalberg, G. Frenning, Numerical modeling of collision of adhesive units: Stability and mechanical properties during handling, *Chemical Engineering Science: X*, **6** (2020) 100051.
- [226] Q. Zhang, P. Wang, S. Teng, Z. Qian, L. Zhu, C.G. Gogos, Simultaneous milling and coating of inorganic particulates with polymeric coating materials using a fluid energy mill, *Polymer Engineering & Science*, **50** (2010) 2366-2374.
- [227] E. Sahni, J. Hallisey, B. Morgan, J. Strong, B. Chaudhuri, Quantifying drying performance of a filter dryer: Experiments and simulations, *Advanced Powder Technology*, **23** (2012) 239-249.
- [228] B. Remy, T.M. Canty, J.G. Khinast, B.J. Glasser, Experiments and simulations of cohesionless particles with varying roughness in a bladed mixer, *Chemical Engineering Science*, **65** (2010) 4557-4571.
- [229] D. Nguyen, A. Rasmuson, K. Thalberg, I.N. Bjo, Numerical modelling of breakage and adhesion of loose fine-particle agglomerates, *Chemical Engineering Science*, **116** (2014) 91-98.
- [230] V. Vignali, F. Mazzotta, C. Sangiorgi, A. Simone, C. Lantieri, G. Dondi, Incorporation of rubber powder as filler in a new dry-hybrid technology: Rheological and 3D DEM mastic performances evaluation, *Materials*, **9** (2016) 842.
- [231] X. Deng, K. Zheng, R.N. Davé, Discrete element method based analysis of mixing and collision dynamics in adhesive mixing process, *Chemical Engineering Science*, **190** (2018) 220-231.
- [232] D. Nguyen, A. Rasmuson, K. Thalberg, I. Niklasson Björn, A breakage and adhesion regime map for the normal impact of loose agglomerates with a spherical target, *AIChE Journal*, **61** (2015) 4059-4068.

References

- [233] D. Nguyen, J. Remmelgas, I.N. Björn, B. van Wachem, K. Thalberg, Towards quantitative prediction of the performance of dry powder inhalers by multi-scale simulations and experiments, *International journal of pharmaceutics*, **547** (2018) 31-43.
- [234] K. Kunnath, L. Chen, K. Zheng, R.N. Davé, Assessing predictability of packing porosity and bulk density enhancements after dry coating of pharmaceutical powders, *Powder Technology*, **377** (2021) 709-722.
- [235] B. van Wachem, K. Thalberg, J. Remmelgas, I. Niklasson-Björn, Simulation of dry powder inhalers: combining micro-scale, meso-scale and macro-scale modeling, *AIChE Journal*, **63** (2017) 501-516.
- [236] R. Moreno-Atanasio, Energy dissipation in agglomerates during normal impact, *Powder technology*, **223** (2012) 12-18.
- [237] G. Lefebvre, L. Galet, A. Chamayou, Dry coating of talc particles with fumed silica: Influence of the silica concentration on the wettability and dispersibility of the composite particles, *Powder Technology*, **208** (2011) 372-377.
- [238] M.K. Nazemi, S. Sheibani, F. Rashchi, V.M. Gonzalez-DelaCruz, A. Caballero, Preparation of nanostructured nickel aluminate spinel powder from spent NiO/Al₂O₃ catalyst by mechano-chemical synthesis, *Advanced Powder Technology*, **23** (2012) 833-838.
- [239] S.N. Hosseini, F. Karimzadeh, M.H. Enayati, Mechanochemical synthesis of Al₂O₃/Co nanocomposite by aluminothermic reaction, *Advanced Powder Technology*, **23** (2012) 334-337.
- [240] V.L. Popov, Contact mechanics and friction, Springer2010.
- [241] L. Vu-Quoc, X. Zhang, An elastoplastic contact force–displacement model in the normal direction: displacement–driven version, *Proceedings of the Royal Society of London. Series A: Mathematical, Physical and Engineering Sciences*, **455** (1999) 4013-4044.
- [242] A. Di Renzo, F.P. Di Maio, An improved integral non-linear model for the contact of particles in distinct element simulations, *Chemical engineering science*, **60** (2005) 1303-1312.
- [243] P. Attard, S.J. Miklavcic, Effective spring constant of bubbles and droplets, *Langmuir*, **17** (2001) 8217-8223.
- [244] C. Thornton, S.J. Cummins, P.W. Cleary, An investigation of the comparative behaviour of alternative contact force models during elastic collisions, *Powder Technology*, **210** (2011) 189-197.
- [245] K.F. Malone, B.H. Xu, Determination of contact parameters for discrete element method simulations of granular systems, *Particuology*, **6** (2008) 521-528.
- [246] S.G.W. Qicheng, Introduction to Particle Mechanics, *China Science Press*, (2009).
- [247] V. Aleshin, K. Van Den Abeele, Preisach analysis of the Hertz–Mindlin system, *Journal of the Mechanics and Physics of Solids*, **57** (2009) 657-672.

References

- [248] D. Maugis, B. Gauthier-Manuel, JKR-DMT transition in the presence of a liquid meniscus, *Journal of adhesion science and technology*, **8** (1994) 1311-1322.
- [249] K. Nanda, A. Maisels, F. Kruis, H. Fissan, S. Stappert, Higher surface energy of free nanoparticles, *Physical review letters*, **91** (2003) 106102.
- [250] E. Simulation, <https://www.edemsimulation.com/>, 5, August 2021.
- [251] J. Horabik, M. Molenda, Parameters and contact models for DEM simulations of agricultural granular materials: A review, *Biosystems Engineering*, **147** (2016) 206-225.
- [252] B.V. Derjaguin, V.M. Muller, Y.P. Toporov, Effect of contact deformations on the adhesion of particles, *Journal of Colloid and interface science*, **53** (1975) 314-326.
- [253] P. Prokopovich, S. Perni, Comparison of JKR-and DMT-based multi-asperity adhesion model: Theory and experiment, *Colloids and Surfaces A: Physicochemical and Engineering Aspects*, **383** (2011) 95-101.
- [254] G. Violano, G.P. Demelio, L. Afferrante, On the DMT adhesion theory: from the first studies to the modern applications in rough contacts, *Procedia Structural Integrity*, **12** (2018) 58-70.
- [255] O.R. Walton, Application of molecular dynamics to macroscopic particles, *International Journal of Engineering Science*, **22** (1984) 1097-1107.
- [256] P.W. Cleary, M.L. Sawley, DEM modelling of industrial granular flows: 3D case studies and the effect of particle shape on hopper discharge, *Applied Mathematical Modelling*, **26** (2002) 89-111.
- [257] G. Pereira, N. Tran, P. Cleary, Segregation of combined size and density varying binary granular mixtures in a slowly rotating tumbler, *Granular Matter*, **16** (2014) 711-732.
- [258] F. Elskamp, H. Kruggel-Emden, Review and benchmarking of process models for batch screening based on discrete element simulations, *Advanced Powder Technology*, **26** (2015) 679-697.
- [259] C. Thornton, S.J. Cummins, P.W. Cleary, An investigation of the comparative behaviour of alternative contact force models during inelastic collisions, *Powder technology*, **233** (2013) 30-46.
- [260] S. Adam, D. Suzzi, C. Radeke, J.G. Khinast, An integrated Quality by Design (QbD) approach towards design space definition of a blending unit operation by Discrete Element Method (DEM) simulation, *European Journal of Pharmaceutical Sciences*, **42** (2011) 106-115.
- [261] M. Börner, M. Michaelis, E. Siegmann, C. Radeke, U. Schmidt, Impact of impeller design on high-shear wet granulation, *Powder Technology*, **295** (2016) 261-271.
- [262] B. Peng, Discrete element method (DEM) contact models applied to pavement simulation, Virginia Tech, 2014.
- [263] B. Chaudhuri, A. Mehrotra, F.J. Muzzio, M.S. Tomassone, Cohesive effects in powder mixing in a tumbling blender, *Powder Technology*, **165** (2006) 105-114.

References

- [264] E. Sahni, R. Yau, B. Chaudhuri, Understanding granular mixing to enhance coating performance in a pan coater: Experiments and simulations, *Powder Technology*, **205** (2011) 231-241.
- [265] C. Thornton, Coefficient of restitution for collinear collisions of elastic-perfectly plastic spheres, (1997).
- [266] O. Kluth, G. Schöpe, J. Hüpkes, C. Agashe, J. Müller, B. Rech, Modified Thornton model for magnetron sputtered zinc oxide: film structure and etching behaviour, *Thin solid films*, **442** (2003) 80-85.
- [267] H. Abbasfard, G.M. Evans, R. Moreno-Atanasio, Effect of van der Waals force cut-off distance on adhesive collision parameters in DEM simulation, *Powder Technology*, **299** (2016) 9-18.
- [268] J. Knoll, H. Nirschl, Influence of the magnetic force on the van der Waals force of superparamagnetic composite particles, *Powder Technology*, **259** (2014) 30-36.
- [269] M. Capece, K.R. Silva, D. Sunkara, J. Strong, P. Gao, On the relationship of inter-particle cohesiveness and bulk powder behavior: Flowability of pharmaceutical powders, *International journal of pharmaceuticals*, **511** (2016) 178-189.
- [270] P. H., Zhu, and, Y. Z., Zhou, and, Y. R., Yang, and, B. A., Discrete particle simulation of particulate systems: Theoretical developments, *Chemical Engineering Science*, (2007).
- [271] Roberto, Moreno-Atanasio, Simon, J. Antony, Richard, A. Williams, Richard, A. Williams, Institute, of, Influence of interparticle interactions on the kinetics of self-assembly and mechanical strength of nanoparticulate aggregates, *Particuology*, **02** (2009) 21-28.
- [272] A.R. Golkarian, M. Jabbarzadeh, The density effect of van der Waals forces on the elastic modules in graphite layers, *Computational Materials Science*, **74** (2013) 138-142.
- [273] R.Y. Yang, R.P. Zou, A.B. Yu, Computer simulation of the packing of fine particles, *Phys Rev E Stat Phys Plasmas Fluids Relat Interdiscip Topics*, **62** (2000) 3900-3908.
- [274] T. Tanaka, Y. Tsuji], Numerical simulation of particulate flow with liquid bridge between particles (simulation of centrifugal tumbling granulator), *Powder Technology*, (2000).
- [275] S. Jr, Simons, and, J. Pk, Seville, and, J. M., Adams, An analysis of the rupture energy of pendular liquid bridges, *Chemical Engineering Science*, (1994).
- [276] Calculation of the Liquid Bridge Volume and Bulk Saturation from the Half-filling Angle, *Particle & Particle Systems Characterization*, **16** (1999) 238-242.
- [277] C.D. Willett, M.J. Adams, S.A. Johnson, J. Seville, Capillary Bridges between Two Spherical Bodies, *Langmuir*, **16** (2000) 9396-9405.
- [278] C. Pei, C. Wu, D. England, S. Byard, H. Berchtold, M. Adams, DEM-CFD modeling of particle systems with long-range electrostatic interactions, *AIChE Journal*, **61** (2015).

References

- [279] M. Hogue, C.I. Calle, P.S. Weitzman, D.R. Curry, Calculating the trajectories of triboelectrically charged particles using Discrete Element Modeling (DEM), *Journal of Electrostatics*, **66** (2008) 32-38.
- [280] L.S. Lu, S.S. Hsiau, Mixing in vibrated granular beds with the effect of electrostatic force, *Powder Technology*, **160** (2005) 170-179.
- [281] S.W. Q, On the variation of vacuum permittivity in Friedmann universes, *The Astrophysical Journal*, **429** (1994) 491-498.
- [282] R.Y. Yang, R.P. Zou, K.J. Dong, X.Z. An, A. Yu, Simulation of the packing of cohesive particles, *Computer Physics Communications*, **177** (2007) 206-209.
- [283] J. M., Rhodes, and, S. X., Wang, and, M., Nguyen, and, P., Use of discrete element method simulation in studying fluidization characteristics: influence of interparticle force, *Chemical Engineering Science*, (2001).
- [284] Z. Peng, E. Doroodchi, G. Evans, DEM simulation of aggregation of suspended nanoparticles, *Powder Technology*, **204** (2010) 91-102.
- [285] T. Zou, G. Wu, D. Li, Q. Ren, J. Xin, Y. Peng, A numerical method for predicting O-forming gap in UOE pipe manufacturing, *International Journal of Mechanical Sciences*, **98** (2015) 39-58.
- [286] H.P. Zhu, Z.Y. Zhou, R.Y. Yang, A.B. Yu, Discrete particle simulation of particulate systems: Theoretical developments, *Chemical Engineering Science*, **62** (2007) 3378-3396.
- [287] P.P.T. Burns S J, Hanley K J. , Critical time step for DEM simulations of dynamic systems using a Hertzian contact model, *International Journal for Numerical Methods in Engineering*, **119(5)** (2019) 432-451.
- [288] H.K.J. Rackl M, A methodical calibration procedure for discrete element models, *Powder technology*, **307** (2017) 73-83.
- [289] E. Lytton, Application of Surface Energy Measurements to Evaluate Moisture Susceptibility of Asphalt and Aggregates, *Texas A&M University*, (2005).
- [290] K.L. Johnson, K. Roberts, Surface Energy and the Contact of Elastic Solid, *Proc. R. Soc. Lond*, **324** (1971) 301-313.
- [291] M.K. Chaudhury, Interfacial interaction between low-energy surfaces, *Materials Science and Engineering: R: Reports*, **16** (1996) 97-159.
- [292] R.J. Good, Contact angle, wetting, and adhesion: a critical review, *Journal of adhesion science and technology*, **6** (1992) 1269-1302.
- [293] A. Kozbial, Z. Li, C. Conaway, R. McGinley, S. Dhingra, V. Vahdat, F. Zhou, B. D'Urso, H. Liu, L. Li, Study on the surface energy of graphene by contact angle measurements, *Langmuir*, **30** (2014) 8598-8606.

References

- [294] D. Subedi, Contact angle measurement for the surface characterization of solids, *Himalayan Physics*, **2** (2011) 1-4.
- [295] M. Gindl, G. Sinn, W. Gindl, A. Reiterer, S. Tschegg, A comparison of different methods to calculate the surface free energy of wood using contact angle measurements, *Colloids and Surfaces A: Physicochemical and Engineering Aspects*, **181** (2001) 279-287.
- [296] S.J. Marshall, S.C. Bayne, R. Baier, A.P. Tomsia, G.W. Marshall, A review of adhesion science, *Dental materials*, **26** (2010) e11-e16.
- [297] A.E. Bangera, K. Appaiah, A conditional justification for the determination of surface energy of solids using contact angle methods, *Materials Chemistry and Physics*, **234** (2019) 168-171.
- [298] D. Li, A. Neumann, Contact angles on hydrophobic solid surfaces and their interpretation, *Journal of colloid and interface science*, **148** (1992) 190-200.
- [299] R.H. Castro, S.V. Ushakov, L. Gengembre, D. Gouvêa, A. Navrotsky, Surface energy and thermodynamic stability of γ -alumina: Effect of dopants and water, *Chemistry of materials*, **18** (2006) 1867-1872.
- [300] S.F. Energy, <https://www.nanoscience.com/techniques/tensiometry/surface-free-energy/>, 5, August 2021.
- [301] L. Girifalco, R.J. Good, A theory for the estimation of surface and interfacial energies. I. Derivation and application to interfacial tension, *The Journal of Physical Chemistry*, **61** (1957) 904-909.
- [302] S.H.D.H.H. Ying, Theoretic fundcation of Young-Good-Girifalco-Fowkes equation use for solid surface energy calculation [J], *TECHNOLOGY ON ADHESION & SEALING*, **5** (2000).
- [303] D. Kwok, D. Li, A. Neumann, Fowkes' surface tension component approach revisited, *Colloids and Surfaces A: Physicochemical and Engineering Aspects*, **89** (1994) 181-191.
- [304] M. Mantel, J. Wightman, Influence of the surface chemistry on the wettability of stainless steel, *Surface and Interface analysis*, **21** (1994) 595-605.
- [305] J.N. Israelachvili, Intermolecular and surface forces, Academic press 2011.
- [306] H.-J. Butt, M. Kappl, Surface and interfacial forces, Wiley Online Library 2010.
- [307] R. Yang, R. Zou, A. Yu, Computer simulation of the packing of fine particles, *Physical review E*, **62** (2000) 3900.
- [308] J. Yang, A. Sliva, A. Banerjee, R.N. Dave, R. Pfeffer, Dry particle coating for improving the flowability of cohesive powders, *Powder technology*, **158** (2005) 21-33.
- [309] N. Fatah, Study and comparison of micronic and nanometric powders: Analysis of physical, flow and interparticle properties of powders, *Powder Technology*, **190** (2009) 41-47.

References

- [310] C. Rochas, E.J.M. Geissler, Measurement of dynamic light scattering intensity in gels, **47** (2014) 8012-8017.
- [311] J. Stetefeld, S.A. McKenna, T.R.J.B.r. Patel, Dynamic light scattering: a practical guide and applications in biomedical sciences, **8** (2016) 409-427.
- [312] O. Couteau, J. Charoud-Got, H. Rauscher, F. Franchini, F. Rossi, V. Kestens, K. Franks, G.J.P. Roebben, P.S. Characterization, A colloidal silica reference material for nanoparticle sizing by means of dynamic light scattering and centrifugal liquid sedimentation, **27** (2010) 112-124.
- [313] A. Meller, R. Bar-Ziv, T. Tlusty, E. Moses, J. Stavans, S. Safran, Localized dynamic light scattering: a new approach to dynamic measurements in optical microscopy, *Biophysical journal*, **74** (1998) 1541-1548.
- [314] R.J. Aguerre, C. Suarez, P.E. Viollaz, New BET type multilayer sorption isotherms, *Part II: Modelling water sorption in foods. Lebensm. _Wiss. a. Technol*, **22** (1989) 192-195.
- [315] M. Sultan, T. Miyazaki, S. Koyama, Optimization of adsorption isotherm types for desiccant air-conditioning applications, *Renewable Energy*, **121** (2018) 441-450.
- [316] E.O. Timmermann, Multilayer sorption parameters: BET or GAB values?, *Colloids and Surfaces A: Physicochemical and Engineering Aspects*, **220** (2003) 235-260.
- [317] V. Gómez-Serrano, C. González-García, M. González-Martín, Nitrogen adsorption isotherms on carbonaceous materials. Comparison of BET and Langmuir surface areas, *Powder Technology*, **116** (2001) 103-108.
- [318] M. Khalfaoui, S. Knani, M. Hachicha, A.B. Lamine, New theoretical expressions for the five adsorption type isotherms classified by BET based on statistical physics treatment, *Journal of colloid and interface science*, **263** (2003) 350-356.
- [319] H.-M. Lee, H.-G. Kim, S.-J. Kang, S.-J. Park, K.-H. An, B.-J. Kim, Effects of pore structures on electrochemical behaviors of polyacrylonitrile (PAN)-based activated carbon nanofibers, *Journal of Industrial and Engineering Chemistry*, **21** (2015) 736-740.
- [320] K.S.W. Sing, Reporting physisorption data for gas/solid systems with special reference to the determination of surface area and porosity (Provisional), *Pure and Applied Chemistry*, **54** (1982) 2201-2218.
- [321] S. Pabisch, B. Feichtenschlager, G. Kickelbick, H. Peterlik, Effect of interparticle interactions on size determination of zirconia and silica based systems—A comparison of SAXS, DLS, BET, XRD and TEM, *Chemical physics letters*, **521** (2012) 91-97.
- [322] M. Peleg, Flowability of food powders and methods for its evaluation—a review, *Journal of Food Process Engineering*, **1** (1977) 303-328.

References

- [323] C. Nwajiobi, J. Otaigbe, O. Oriji, Physicochemical, spectroscopic and tableting properties of microcrystalline cellulose obtained from the African breadfruit seed hulls, *African Journal of Biotechnology*, **18** (2019) 371-382.
- [324] D. Schulze, Flow properties of powders and bulk solids, *Braunschweig/Wolfenbu ttel, Germany: University of Applied Sciences*, (2006).
- [325] R. Gopinath, R. Naidu, Pharmaceutical preformulation studies–current review, *International Journal of Pharmaceutical and Biological Archives*, **2** (2011) 1391-1400.
- [326] J. Cain, An alternative technique for determining ANSI/CEMA Standard 550 flowability ratings for granular materials, *Powder Handling and Processing*, **14** (2002) 218-220.
- [327] S. Otlés, O. Lecoq, J.A. Dodds, Dry particle high coating of biopowders: An energy approach, *Powder technology*, **208** (2011) 378-382.
- [328] D. Turki, N. Fatah, M. Saidani, The impact of consolidation and interparticle forces on cohesive cement powder, *International Journal of Materials Research*, **106** (2015) 1258-1263.
- [329] J.A. von Fraunhofer, Adhesion and cohesion, *International journal of dentistry*, **2012** (2012).
- [330] H. Wei, J. Xia, W. Zhou, L. Zhou, G. Hussain, Q. Li, K.K. Ostrikov, Adhesion and cohesion of epoxy-based industrial composite coatings, *Composites Part B: Engineering*, **193** (2020) 108035.
- [331] L.-O. Heim, J. Blum, M. Preuss, H.-J. Butt, Adhesion and friction forces between spherical micrometer-sized particles, *Physical Review Letters*, **83** (1999) 3328.
- [332] M. Takeuchi, Adhesion forces of charged particles, *Chemical Engineering Science*, **61** (2006) 2279-2289.
- [333] H.-J. Butt, B. Cappella, M. Kappl, Force measurements with the atomic force microscope: Technique, interpretation and applications, *Surface science reports*, **59** (2005) 1-152.
- [334] D. Turki, N. Fatah, Description of consolidation forces on nanometric powders, *Brazilian Journal of Chemical Engineering*, **27** (2010) 555-562.
- [335] E.M. Lifshitz, M. Hamermesh, The theory of molecular attractive forces between solids, *Perspectives in Theoretical Physics*, (1992) 329-349.
- [336] D. Bargeman, F. van Voorst Vader, Van der Waals forces between immersed particles, *Journal of Electroanalytical Chemistry and Interfacial Electrochemistry*, **37** (1972) 45-52.
- [337] G. Lefevre, A. Jolivet, Calculation of Hamaker constants applied to the deposition of metallic oxide particles at high temperature, *Proceedings of International Conference on Heat Exchanger Fouling and Cleaning*, **8** (2009) 120-124.
- [338] C. Sanchez, B. Wood, R. Green, J. Liard, D. Inglis, A determination of Planck's constant using the NRC watt balance, *Metrologia*, **51** (2014) S5.

References

- [339] A.S. Jbara, Z. Othaman, H. Aliabad, M. Saeed, Electronic and Optical Properties of γ - and β -Alumina by First Principle Calculations, *Advanced Science, Engineering and Medicine*, **9** (2017) 287-293.
- [340] D.B. Hough, L.R. White, The calculation of Hamaker constants from Lifshitz theory with applications to wetting phenomena, *Advances in Colloid and Interface Science*, **14** (1980) 3-41.
- [341] Z. Feng, X. Cheng, C. Dong, L. Xu, X. Li, Effects of dissolved oxygen on electrochemical and semiconductor properties of 316L stainless steel, *Journal of nuclear materials*, **407** (2010) 171-177.
- [342] H. Xu, L. Wang, D. Sun, H. Yu, The passive oxide films growth on 316L stainless steel in borate buffer solution measured by real-time spectroscopic ellipsometry, *Applied Surface Science*, **351** (2015) 367-373.
- [343] R.J. Kuo, E. Matijevic, Particle adhesion and removal in model systems: III. Monodispersed ferric oxide on steel, *Journal of Colloid and Interface Science*, **78** (1980) 407-421.
- [344] M. Sun, W. Maichen, R. Pophale, Y. Liu, R. Cai, C.M. Lew, H. Hunt, M.W. Deem, M.E. Davis, Y. Yan, Dielectric constant measurement of zeolite powders by time-domain reflectometry, *Microporous and mesoporous materials*, **123** (2009) 10-14.
- [345] Cameo, <http://cameo.mfa.org/wiki/Zeolite>, 5, August 2021.
- [346] M. Kimura, M. Komaki, T. Nakajima, Effect of Zeolite on the Dispersion Stability of Particles, *Textile Research Journal*, **57** (1987) 82-87.
- [347] A. Wypych, I. Bobowska, M. Tracz, A. Opasinska, S. Kadlubowski, A. Krzywania-Kaliszewska, J. Grobelny, P. Wojciechowski, Dielectric properties and characterisation of titanium dioxide obtained by different chemistry methods, *Journal of Nanomaterials*, **2014** (2014).
- [348] K. Dutta, S. De, Electrical conductivity and dielectric properties of SiO₂ nanoparticles dispersed in conducting polymer matrix, *Journal of Nanoparticle Research*, **9** (2007) 631-638.
- [349] I.H. Malitson, Interspecimen comparison of the refractive index of fused silica, *Josa*, **55** (1965) 1205-1209.
- [350] T. Wen, J. Zhang, T.P. Chou, S.J. Limmer, G. Cao, Template-based growth of oxide nanorod arrays by centrifugation, *Journal of sol-gel science and technology*, **33** (2005) 193-200.
- [351] H. Krupp, G. Sperling, Theory of adhesion of small particles, *Journal of Applied Physics*, **37** (1966) 4176-4180.
- [352] J. Visser, On Hamaker constants: A comparison between Hamaker constants and Lifshitz-van der Waals constants, *Advances in colloid and interface science*, **3** (1972) 331-363.
- [353] A. Khazeni, Z. Mansourpour, Influence of non-spherical shape approximation on DEM simulation accuracy by multi-sphere method, *Powder Technology*, **332** (2018) 265-278.

References

- [354] H. Kuo, P. Knight, D. Parker, Y. Tsuji, M. Adams, J. Seville, The influence of DEM simulation parameters on the particle behaviour in a V-mixer, *Chemical engineering science*, **57** (2002) 3621-3638.
- [355] G.N. Greaves, A. Greer, R.S. Lakes, T. Rouxel, Poisson's ratio and modern materials, *Nature materials*, **10** (2011) 823-837.
- [356] Sasolgermany, <https://www.sasolgermany.de/ueber-uns/>, 5, August 2021.
- [357] M. Vahtrus, M. Umalas, B. Polyakov, L. Dorogin, R. Saar, M. Tamme, K. Saal, R. Löhmus, S. Vlassov, Mechanical and structural characterizations of gamma-and alpha-alumina nanofibers, *Materials Characterization*, **107** (2015) 119-124.
- [358] Z. Zhao, X. Shen, H. Yao, J. Wang, J. Chen, Z. Li, Alumina nanofibers obtained via electrospinning of pseudo-boehmite sol/PVP solution, *Journal of Sol-Gel Science and Technology*, **70** (2014) 72-80.
- [359] P. Zhang, D. Chen, X. Jiao, Fabrication of Flexible α -Alumina Fibers Composed of Nanosheets, *European Journal of Inorganic Chemistry*, **2012** (2012) 4167-4173.
- [360] Z.Y. Deng, T. Fukasawa, M. Ando, G.J. Zhang, T. Ohji, Microstructure and mechanical properties of porous alumina ceramics fabricated by the decomposition of aluminum hydroxide, *Journal of the American Ceramic Society*, **84** (2001) 2638-2644.
- [361] J. Kováčik, Correlation between Young's modulus and porosity in porous materials, *Journal of materials science letters*, **18** (1999) 1007-1010.
- [362] Syalons, <https://www.syalons.com/materials/alumina/>, 5, August 2021.
- [363] M.R. Gallas, G.J. Piermarini, Bulk modulus and Young's modulus of nanocrystalline γ -alumina, *Journal of the American Ceramic Society*, **77** (1994) 2917-2920.
- [364] A.P. Roberts, E.J. Garboczi, Elastic properties of model porous ceramics, *Journal of the American Ceramic Society*, **83** (2000) 3041-3048.
- [365] M. Asmani, C. Kermel, A. Leriche, M. Ourak, Influence of porosity on Young's modulus and Poisson's ratio in alumina ceramics, *Journal of the European ceramic society*, **21** (2001) 1081-1086.
- [366] P. Müller, S. Antonyuk, J. Tomas, S. Heinrich, Investigations of the restitution coefficient of granules, *Micro-Macro-interaction*, **21** (2008) 235-241.
- [367] P. Mueller, J. Tomas, S. Antonyuk, S. Heinrich, The restitution coefficient of three characteristic granules, *Abstracts and Proceedings, WCPT6*, (2010).
- [368] P. Mueller, S. Antonyuk, M. Stasiak, J. Tomas, S. Heinrich, The normal and oblique impact of three types of wet granules, *Granular Matter*, **13** (2011) 455-463.
- [369] R. Michels, Numerical simulation of flexural tests in metal ceramic composites, CURSO DE ENGENHARIA NAVAL, UNIVERSIDADE FEDERAL DE SANTA CATARINA, 2015.

References

- [370] A. Berman, S. Steinberg, S. Campbell, A. Ulman, J. Israelachvili, Controlled microtribology of a metal oxide surface, *Tribology letters*, **4** (1998) 43-48.
- [371] D.-H. Hwang, K.-H. Zum Gahr, Transition from static to kinetic friction of unlubricated or oil lubricated steel/steel, steel/ceramic and ceramic/ceramic pairs, *Wear*, **255** (2003) 365-375.
- [372] V. Teffo, N. Naudé, Determination of the coefficients of restitution, static and rolling friction of Eskom-grade coal for discrete element modelling, *Journal of the Southern African Institute of Mining and Metallurgy*, **113** (2013) 351-356.
- [373] A.S.A. Metals, <http://asm.matweb.com/search/SpecificMaterial.asp?bassnum=MQ316Q>, 5, August 2021.
- [374] Hogan, <https://www.hoganas.com/en/about-hoganas/our-history/>, 5, August 2021.
- [375] P. Li, Z. Wang, N. Petrinic, C. Siviour, Deformation behaviour of stainless steel microlattice structures by selective laser melting, *Materials Science and Engineering: A*, **614** (2014) 116-121.
- [376] H. Gu, H. Gong, D. Pal, K. Rafi, T. Starr, B. Stucker, Influences of energy density on porosity and microstructure of selective laser melted 17-4PH stainless steel, *2013 Solid Freeform Fabrication Symposium*, **474** (2013) 113-118.
- [377] S.S. Lee, U.-S. Min, B. Ahn, S.H. Yoo, Elastic constants determination of thin cold-rolled stainless steels by dynamic elastic modulus measurements, *Journal of materials science*, **33** (1998) 687-692.
- [378] J. Song, J.C. Gelin, T. Barrière, B. Liu, Experiments and numerical modelling of solid state sintering for 316L stainless steel components, *Journal of Materials Processing Technology*, **177** (2006) 352-355.
- [379] P. Li, Z. Wang, N. Petrinic, C.R. Siviour, Deformation behaviour of stainless steel microlattice structures by selective laser melting, *Materials Science and Engineering: A*, **614** (2014) 116-121.
- [380] P. Mott, C. Roland, Limits to Poisson's ratio in isotropic materials, *Physical review B*, **80** (2009) 132104.
- [381] L.C. Bissonnette, N.M. Nardacci, R.L. Poynor, Golf club head with a high coefficient of restitution, USA, 2003.
- [382] L. Liu, M. Huang, Y. Ma, M. Qin, T. Liu, Simulation of Powder Packing and Thermo-Fluid Dynamic of 316L Stainless Steel by Selective Laser Melting, *Journal of Materials Engineering and Performance*, **29** (2020) 7369-7381.
- [383] L.R. Iwasaki, M.W. Beatty, C.J. Randall, J.C. Nickel, Clinical ligation forces and intraoral friction during sliding on a stainless steel archwire, *Am J Orthod Dentofacial Orthop*, **123** (2003) 408-415.
- [384] R. Morgan, C. Sutcliffe, W. O'Neill, Density analysis of direct metal laser re-melted 316L stainless steel cubic primitives, *Journal of materials science*, **39** (2004) 1195-1205.

References

- [385] M. Yakout, M. Elbestawi, S.C. Veldhuis, Density and mechanical properties in selective laser melting of Invar 36 and stainless steel 316L, *Journal of Materials Processing Technology*, **266** (2019) 397-420.
- [386] A. Bendavid, P. Martin, H. Takikawa, Deposition and modification of titanium dioxide thin films by filtered arc deposition, *Thin solid films*, **360** (2000) 241-249.
- [387] O. Çomaklı, T. Yetim, A. Çelik, The effect of calcination temperatures on wear properties of TiO₂ coated CP-Ti, *Surface and Coatings Technology*, **246** (2014) 34-39.
- [388] T. Shibata, H. Irie, D.A. Tryk, K. Hashimoto, Effect of residual stress on the photochemical properties of TiO₂ thin films, *The Journal of Physical Chemistry C*, **113** (2009) 12811-12817.
- [389] M. Mayo, R. Siegel, A. Narayanasamy, W. Nix, Mechanical properties of nanophase TiO₂ as determined by nanoindentation, *Journal of Materials Research*, **5** (1990) 1073-1082.
- [390] P. Soares, A. Mikowski, C.M. Lepienski, E. Santos Jr, G.A. Soares, V.S. Filho, N.K. Kuromoto, Hardness and elastic modulus of TiO₂ anodic films measured by instrumented indentation, *Journal of Biomedical Materials Research Part B: Applied Biomaterials: An Official Journal of The Society for Biomaterials, The Japanese Society for Biomaterials, and The Australian Society for Biomaterials and the Korean Society for Biomaterials*, **84** (2008) 524-530.
- [391] H. Li, K. Khor, P. Cheang, Impact formation and microstructure characterization of thermal sprayed hydroxyapatite/titania composite coatings, *Biomaterials*, **24** (2003) 949-957.
- [392] C.J. Reagle, Technique for measuring the coefficient of restitution for microparticle sand impacts at high temperature for turbomachinery applications, Virginia Tech, 2012.
- [393] Y.-f. Fu, J. Li, F.-q. Zhang, K. Xu, The preparation and the friction and wear behaviours of TiO₂/CNT/PI composite film, *Journal of Experimental Nanoscience*, **11** (2016) 459-469.
- [394] K. Hu, Y. Xu, E. Hu, J. Guo, X. Hu, Rolling friction performance and functional conversion from lubrication to photocatalysis of hollow spherical nano-MoS₂/nano-TiO₂, *Tribology International*, **104** (2016) 131-139.
- [395] L. Chang, Z. Zhang, Tribological properties of epoxy nanocomposites: Part II. A combinative effect of short carbon fibre with nano-TiO₂, *Wear*, **260** (2006) 869-878.
- [396] A.H. Tavakoli, P.S. Maram, S.J. Widgeon, J. Rufner, K. Van Benthem, S. Ushakov, S. Sen, A. Navrotsky, Amorphous alumina nanoparticles: structure, surface energy, and thermodynamic phase stability, *The Journal of Physical Chemistry C*, **117** (2013) 17123-17130.
- [397] J. McHale, A. Auroux, A. Perrotta, A. Navrotsky, Surface energies and thermodynamic phase stability in nanocrystalline aluminas, *Science*, **277** (1997) 788-791.
- [398] R.H. Castro, D.V. Quach, Analysis of anhydrous and hydrated surface energies of gamma-Al₂O₃ by water adsorption microcalorimetry, *The Journal of Physical Chemistry C*, **116** (2012) 24726-24733.

References

- [399] D.R. Hummer, J.D. Kubicki, P.R. Kent, J.E. Post, P.J. Heaney, Origin of nanoscale phase stability reversals in titanium oxide polymorphs, *The Journal of Physical Chemistry C*, **113** (2009) 4240-4245.
- [400] A.L. Da Silva, D. Hotza, R.H. Castro, Surface energy effects on the stability of anatase and rutile nanocrystals: A predictive diagram for Nb₂O₅-doped-TiO₂, *Applied Surface Science*, **393** (2017) 103-109.
- [401] M.R.I. Muthukumar Chandrasekar, Mohammad Jawaid, S.M. Sapuan, Z. Leman, Low velocity impact properties of natural fiber-reinforced composite materials for aeronautical applications, *Composites Science and Engineering*, **14** (2018) 293-313.
- [402] T. Kobayashi, T. Tanaka, N. Shimada, T. Kawaguchi, DEM–CFD analysis of fluidization behavior of Geldart Group A particles using a dynamic adhesion force model, *Powder technology*, **248** (2013) 143-152.
- [403] J. Hærvig, U. Kleinhans, C. Wieland, H. Spliethoff, A.L. Jensen, K. Sørensen, T.J. Condra, On the adhesive JKR contact and rolling models for reduced particle stiffness discrete element simulations, *Powder Technology*, **319** (2017) 472-482.
- [404] I.H. Shames, G.K.M. Rao, Engineering mechanics: statics and dynamics, Prentice-Hall Englewood Cliffs 1967.
- [405] M. Avadhanulu, A textbook of engineering physics, S. Chand Publishing 1992.
- [406] J. Marshall, Discrete-element modeling of particulate aerosol flows, *Journal of Computational Physics*, **228** (2009) 1541-1561.
- [407] V.D. Blais B, Bertrand F, et al., Experimental methods in chemical engineering: Discrete element method—DEM, *The Canadian Journal of Chemical Engineering*, **97(7)** (2019) 1964-1973.

Appendix

1. Nanosize analysis: BET

As described in Chapter 2, the literature show that from the measurement of the BET specific surface one can estimate a particle size but this under conditions that the particle is not porous, spherical, smooth and has a monomodal size distribution. If a powder is not porous, spherical, and smooth, the following equation can be used to calculate the size of particle.

$$D = \frac{\text{surface of sphere}}{\text{volume of sphere} * \text{density of particles}} = \frac{6}{S * \rho}$$

Where D is the diameter of particle and ρ is the density of materials. This equation was carried out to estimate the diameter of particle in this study and the results show as following table (the surface area and density can be found in Chapter 3).

Samples	Diameter (nm)
Zeolite	5.81
TiO ₂	6.87
SiO ₂	58.09

However, as has been presented in Chapter 3, the isotherms indicated that zeolite and SiO₂ are porous, which means the diameter of these powders obtained by above equation can deviate with the real size. And for TiO₂, the isotherm demonstrated it is non-porous but the size calculated by this equation has a big difference with the size that has been measured by other devices. Therefore, the BET diameter was not used to prepare the new supports.

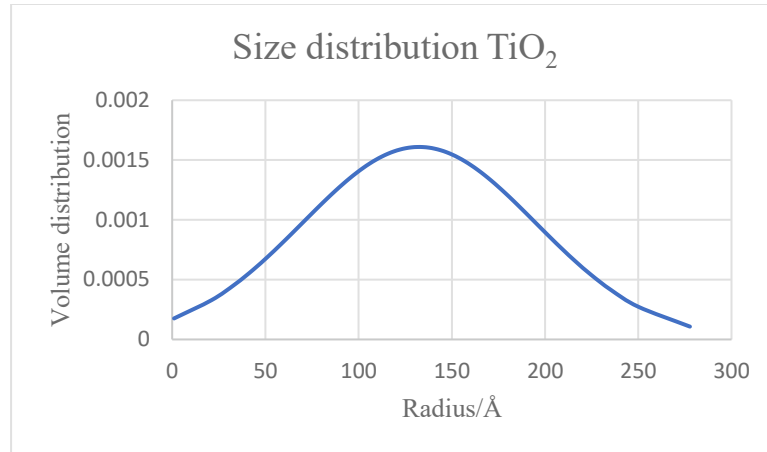
2. Nanosize analysis: SAXS

SAXS results was processed in IGORPRO. The below figures represent the size distribution of each powder. The x-axis gives us the radius (in Å) of the particles. The results seem to correspond to the TEM images.

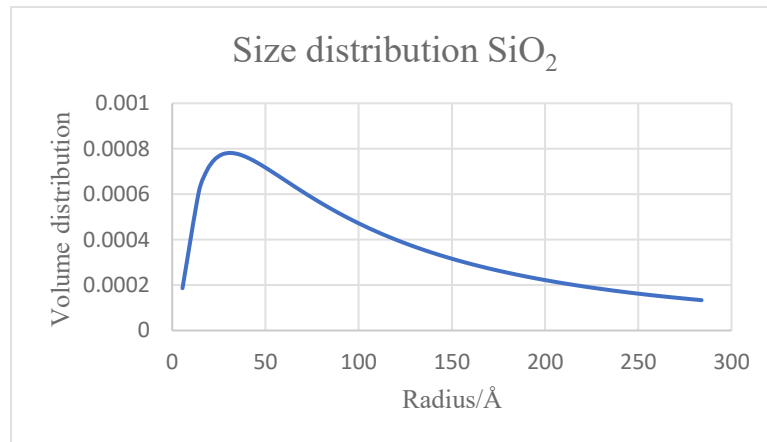
Appendix

However, the large size distribution of the powders and the formation of agglomerates give us SAXS results that are not very accurate.

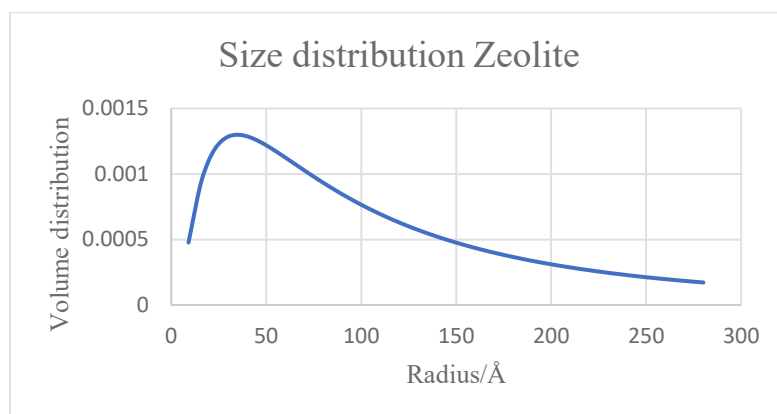
TiO₂ : Radius= 132Å =13.2nm



SiO₂: Radius = 125Å = 12.5nm



Zeolite: Radius = 101Å =10.1nm



Title: New process of dry particle coating and numerical modelisation: preparation of clean solid catalysis for methanation

The objective of this thesis is to propose a new methodology – dry particle coating technique to prepare catalyst supports for the methanation reaction. Dry particle coating is considered as an environmentally friendly and low-cost technique. However, it is crucial to understand the mechanism of the dry coating process, the factors affect the coating performance, the evaluation of the coating quality, the large-scale production as well as the exploration of new application fields.

In this work, the method of preparing new catalyst supports is to coat γ -Al₂O₃ and 316L steel (S.S316L) particles with TiO₂, SiO₂, and Zeolite nanoparticles. However, these powders (TiO₂, SiO₂, and Zeolite) are highly cohesive and form agglomerates of uncontrollable sizes, the nanoscale of the powders poses a major problem in the accuracy of size measurements. The coating process requires analysis of the nanoparticles. Four analytical techniques were applied and compared. The basic principle of the dry particle coating process is the mixing of particles under mechanical force (impact/compression/shear force). Host particle: γ -Al₂O₃ and S.S316L have an average diameter of about 67 μ m and 98.3 μ m will be used as host particles to prepare new carriers. The guest particles: TiO₂, SiO₂ and Zeolite with nanosize will be used to coat the surface of γ -Al₂O₃ and S.S316L to prepare the new substrates (such as TiO₂/S.S316L, SiO₂/S.S316L, Zeolite/S.S316L and TiO₂/ γ -Al₂O₃, SiO₂/ γ -Al₂O₃, Zeolite/ γ -Al₂O₃). The coating of particles in dry process is due to mechanical/shear forces and it depends on collisions, particle movements, interactions between particles and the impact of operating conditions (the rotation speed and coating time) in the mixer. A numerical modeling DEM (Discrete Element Method) has been implemented to answer and explain the phenomena and the coating process.

The results of the analysis of the nanoparticles showed that the technique of diffraction/laser scattering (LD) highlights a larger size of particle of the nanopowder (overestimation) on the other hand the dynamic diffusion of the light (DLS) shows a smaller size. Transmission electron microscopy (TEM) indicates the smaller diameter of the nanopowder. The coating results highlight a good coating by SiO₂, TiO₂, and Zeolite nanoparticles on the surface of γ -Al₂O₃ and S.S316L under 3500 rpm and 5 min. However, for the same guest particles with different host particles, the S.S316L coating shows excellent coating. Numerical modeling reveals that the main factors affecting the simulation are: rotational speed and particle size. Simulation of the coating indicates that the interfacial energy between the host and the guest is the main parameter affecting the coating.

Keywords: Dry particle coating, High-shearing force, Picomix, Nanopowder, DEM modeling.

Titre: Nouveau procédé d'enrobage de particules en voie sèche et modélisation numérique: préparation de catalyseur solide propre pour la méthanisation

L'objectif de ce travail de thèse est de proposer une nouvelle méthodologie pour préparer des supports de catalyseurs pour la réaction de méthanation. En particulier, l'application d'une technique d'enrobage de particules en voie sèche. L'enrobage à sec des particules est considéré comme une technique respectueuse de l'environnement et peu coûteuse. Cependant, il est crucial de comprendre le mécanisme du processus d'enrobage à sec, les facteurs qui affectent la performance de l'enrobage, l'évaluation de la qualité de l'enrobage, la production à grande échelle ainsi que l'exploration de nouveaux champs d'application.

Dans ce travail, la méthode de préparation de nouveaux supports de catalyseurs consiste à enrober des particules de γ -Al₂O₃ et d'acier 316L avec des nanoparticules de TiO₂, SiO₂, et Zeolite. Cependant, ces poudres (TiO₂, SiO₂, et Zeolite) sont très cohésives et forment des agglomérats de tailles incontrôlables, l'échelle nanométrique des poudres pose un problème majeur dans la précision des mesures de la taille. Le processus de revêtement nécessite une analyse des nanoparticules. Cinq techniques d'analyses ont été appliquées et comparées. Le principe de base du processus d'enrobage des particules en voie sèche consiste à mélanger des particules hôtes et invitées sous l'effet des forces mécaniques (impact/compression/force de cisaillement). Particules hôtes : γ -Al₂O₃ et l'acier 316L ont un diamètre moyen d'environ 67 μ m et 98.3 μ m seront utilisées comme particules hôtes pour préparer de nouveaux supports. Les particules invitées : TiO₂, SiO₂ et Zeolite de taille nanométrique seront utilisées pour revêtir la surface de γ -Al₂O₃ et d'acier 316L pour préparer les nouveaux supports (tels que TiO₂/ γ -Al₂O₃, SiO₂/ γ -Al₂O₃, zéolite/ γ -Al₂O₃, TiO₂/S316L, SiO₂/S.S316L, zéolite/S316L). L'enrobage des particules en voie sèche est dû aux forces mécaniques/cisaillements et il dépend des paramètres comme les mouvements des particules forces de collisions, interactions entre les particules et l'impact des conditions opératoires (la vitesse de rotation et le temps d'enrobage) dans le mélangeur. Ainsi, on a mis en place un programme de modélisation numérique par DEM (Discrete Element Method) qui semble indispensable pour permettre de répondre et d'expliquer les phénomènes et le mode d'enrobage.

Les résultats de l'analyse des nanoparticules ont montré que la technique de diffraction/diffusion laser (LD) met en évidence une plus grande taille de particules de nanopoudres (surestimation) par contre la diffusion dynamique de la lumière (DLS) montre une taille plus petite. La microscopie électronique à transmission (TEM) indique le plus petit diamètre des nanopoudres. Les résultats de l'enrobage met en évidence un bon enrobage par nanoparticules SiO₂, TiO₂, et Zeolite sur la surface des solides γ -Al₂O₃ et acier 316L sous 3500 rpm et 5 min. Cependant, pour les mêmes particules invitées avec différentes particules hôtes, le revêtement de l'acier 316L montre un enrobage excellent. La modélisation numérique révèle que les principaux facteurs affectant la simulation sont : la vitesse de rotation et la taille des particules. La simulation de l'enrobage, indique que l'énergie interfaciale entre l'hôte et l'invité s'est avérée être le principal paramètre affectant le revêtement.

Mots clefs : Enrobage en voie sèche, support de catalyseurs, forces de cisaillement, Picomix, nanopoudre, modélisation DEM.